POLITECNICO DI MILANO
Doctoral School (Ph.D.) in
Mathematical Models and Methods in Engineering
– XXIV cycle –

NON-CONFORMING HIGH ORDER METHODS FOR THE ELASTODYNAMICS EQUATION

Presented to Dipartimento di Matematica "F. Brioschi"
POLITECNICO DI MILANO

by

Ilario Mazzieri

ID number: 738629

Advisors

Prof. Alfio Quarteroni
Politecnico di Milano and
École Polytechnique Fédérale de Lausanne (EPFL)

Dr. Francesca Rapetti
Université de Nice Sophia Antipolis

Co-Advisor

Dr. Paola Francesca Antonietti
Politecnico di Milano

Ph.D. Coordinator: Prof. Paolo Biscari

Milan, March 2012

From I. to I.

Abstract

The study and development of high-order methods for simulating elastic wave propagation in seismic regions has been subjected to a tremendous growth, occurred in the past ten years. Recent developments in computational seismology have been based on numerical strategies as finite differences, boundary element methods and, more recently, spectral element (SE) methods. SE methods combine the flexibility of finite elements with the accuracy of spectral techniques. They handle naturally both interface continuity and free boundary conditions, allowing very accurate resolutions of evanescent interface and surface waves. Moreover, SE methods retain a high level parallel structure, thus are well suited for massively parallel computations. The main drawback of SE methods is that they require a uniform polynomial order on the whole computational domain, and this can lead to an unreasonably large computational effort, in particular in regions where a fine mesh grid is needed already to describe accurately the domain geometry. Therefore, it can be more adequate in some cases to use a lower order method in the small elements to reduce the CPU effort without loosing much accuracy.
Non-conforming high-order techniques, like the Discontinuous Galerkin Spectral Element (DGSE) or the Mortar Spectral Element (MSE) methods, allow to treat locally varying polynomial degrees of the basis functions, so-called p-adaptivity, as well as locally varying mesh size on the computational domain, h-adaptivity. The hp-adaptive version of these schemes is useful in complex 2 and 3-d models with small-scale features which have to be meshed with reasonably small elements to capture the necessary geometrical details of interest. In this thesis, we present a new discretization approach to combine the DGSE and MSE methods with suitable time advancing schemes for the simulation of wave propagations in heterogeneous media. To overcome the limitations of the existing approaches we will apply the non-conforming paradigm only at subdomain level (not elementwise). We will show that the resulting formulations are stable, provide optimal approximation properties, and suffer from low dispersion and dissipation errors. Applications of the DGSE and MSE methods to simulate realistic seismic wave propagation problems are also analyzed.

Keywords: High-order Discontinuous Galerkin and Mortar methods; Non-conforming domain decomposition techniques; Wave propagation; Numerical analysis.

Contents

Introduction

The study of wave propagation in elastic solids has a long and distinguished history. Indeed, since the middle of the 19^{th} century, great mathematicians as Poisson, Cauchy, Green, Lamé and Stokes developed what is now generally known as the theory of elasticity. In the latter part of the 19^{th} century the interest in the study of wave propagations in elastic solids has increased because of applications in the field of geophysics. Currently, wave propagation in solids is still a very active area of investigation in seismology because of the need for accurate informations on earthquake phenomena, and detection of nuclear explosions.

In this thesis we aim at proposing and analyzing a family of non-conforming numerical methods capable of simulating elastic wave propagations in two and three dimensional configurations, characterized by the presence of irregular interfaces, heterogeneous materials as well as the capability of predicting correctly soil-structure interaction phenomena.

The use of the elastodynamics equations to model the seismic response of heterogeneous earth media with irregular topography and internal interfaces is a subject that has been intensively investigated in recent years. The study and development of high-order methods for simulating elastic wave propagation in seismic regions has been subjected to a tremendous growth, occurred in the past ten years. Recent developments in computational seismology have been based on numerical strategies as finite differences, boundary element methods and, more recently, spectral element methods (see e.g. [46, 50, 41, 61, 104, 34, 57, 67]). Although the finite difference (FD) method still represents the most employed technique in computational seismology, it is well known that standard second order FD schemes suffer from grid dispersion employed on too coarse computational grids or when the wave field features large layers. Then, when FD schemes are employed in realistic applications is rather difficult to balance the trade-off

between numerical dispersion and computational cost [48, 87, 89]. However, it is possible to reduce grid dispersion, dissipation and anisotropy errors using the staggered-grid formulation [72, 115, 70], which is based on the symmetric first-order hyperbolic form of the elastodynamics equation [56], or using fourth-order centered schemes both in space and time, based on modified wave-equation techniques [37, 13].
An interesting overview focused on the stability condition and grid dispersion of the three dimensional fourth-order FD schemes is provided in [81, 80, 82], where important advances were obtained in the use of staggered-grid techniques. Other difficulties arising with FD methods are the implementation of free-surface or absorbing boundary conditions and their lack of geometrical flexibility. Even though some techniques have been incorporated to deal with surface topography using methods based on grid deformation combined with the staggered grid formulation, they remain limited to simple geometrical settings [99, 86]. For such reasons, FD methods are not able to describe accurately surface waves (e.g. Rayleigh and Love waves) and interface waves. On the other hand, despite the fact that finite element methods (FE) are able to deal with complex geometries (e.g. realistic basins) and strong heterogeneous materials, they exhibit poor dispersion and dissipation properties. Therefore, FE are not widely used for wave propagation problems [113, 76].

Numerical solutions to the wave equation can be obtained on the basis of the integral representations of the problem relating quantities on the physical boundaries. Direct boundary element (BE) methods formulate the problem in terms of unknown tractions and displacements [32, 33, 14], while indirect methods make use of a formulation in terms of force and moment boundary densities [100]. The main advantage of these techniques is that solutions are found over a surface that is one dimension lower than the original form of the problem, and that the radiation (Sommerfield) condition is a priori satisfied. On the other hand, BE methods are most often limited to linear and homogeneous problems. Moreover, the resulting linear systems of equations in these methods are very large, dense and in general non symmetric, making the solution of the resulting linear system of equations unaffordable from the computational point of view. The computational advantage in processing time and storage requirements that would intuitively be expected is therefore not always achieved in the case of realistic problem sizes.

Another possible approach is to enrich the approximation spaces with functions that well capture the characteristics of the solution. This is the idea adopted in [119, 77, 116]

with the discontinuous enrichment (DE) method or in [53, 83] with the plane wave (PW) method. In DE and PW approaches the standard finite element space (that represents the coarse scale of the solution) is enriched elementwise by free-space solutions of the homogeneous partial differential equation to be solved. This can reduce dramatically the computational cost of standard FE methods while preserving their accuracy and flexibility.

The other family of discretization methods widely used in computational seismology is the spectral element method. Spectral methods were firstly introduced in fluid dynamics around thirty years ago and successively applied to elastodynamic problems. The so-called global pseudo-spectral (PS) method was then introduced by replacing the original set of truncated Fourier series with a set of algebraic polynomials in space (of Chebyschev or Legendre type). The PS numerical solution satisfies the wave equation in differential form at some suitably chosen collocation points, and its accuracy is shown to depend strongly on this choice [65, 118, 58]. The main limitation of the PS methods is the difficulty to handle complex geometries, heterogeneous materials and realistic free-surface boundary conditions. To overcome such shortcomings in [28, 59] curvilinear coordinate systems have been proposed. However, this remains confined to smooth global mappings of little use in realistic geological models.

The spectral element (SE) method, introduced firstly in fluid dynamics by [88, 74], can be related to the $p-$ and $hp-$versions of the FE methods [11, 10]. SE methods are based on high-order Lagrangian interpolants sampled at the Gauss-Legendre-Lobatto quadrature points, and combine the flexibility of finite elements with the accuracy of spectral techniques. Since they are based on the weak formulation of the elastodynamics equations, they handle naturally both interface continuity and free boundary conditions, allowing very accurate resolutions of evanescent interface and surface waves. Moreover, SE methods retain a high level parallel structure, thus are well suited for massively parallel computations. Important recent applications, with SE techniques were provided for computational seismology applications [60, 110, 79, 35]. SE methods usually require a uniform polynomial order on the whole computational domain, and this can lead to an unreasonably large computational effort, in particular in regions where a fine mesh grid is needed already to describe accurately the domain geometry.

Non-conforming high-order techniques, like the Discontinuous Galerkin spectral element (DGSE) method [9, 95, 52] or the Mortar spectral element (MSE) method [19, 117, 21], allow to deal with a non uniform polynomial degree distribution ($p-$adaptivity),

as well as a locally varying mesh size ($h-$adaptivity). The built-in flexibility of these schemes is useful in complex two and three dimensional problems that feature multi-scale phenomena.
In [57] the $p-$version of the Discontinuous Galerkin approach have been studied for seismic wave propagation problem. This method combines DG discretizations with the so-called Cauchy-Kovalewski approach using repeatedly the governing partial differential equation itself, in order to guarantee arbitrary high-order accuracy in both space and time. Moreover, to further increase the computational efficiency, the authors have introduced a new local time stepping algorithm. Indeed, usual explicit time stepping schemes require stability (Courant-Friedrichs-Levy (CFL)) conditions that impose a time step which depends on the smallest element size. By using local time stepping, each element can use its optimal time step given by the local stability condition [44]. One of the main drawback of the techniques proposed in [57, 44] is that the DG approach is applied elementwise, and therefore the proliferation of degrees of freedom cannot be kept under control.

Here, we present a new discretization approach to combine the DGSE and MSE methods with suitable time advancing schemes for the simulation of wave propagations in heterogeneous media. To overcome the limitations of the existing approaches we will apply the non-conforming paradigm only at subdomain level. We will show that the resulting formulations are stable, provide optimal approximation properties, and suffer from low dispersion and dissipation errors. Some meaningful geophysical applications are also addressed. The results of this thesis are original and have been partially published or submitted for possible publication in [8, 78]

We describe in detail the subject addressed by summarizing the contents of the various chapters.

In Chapter 1 we describe the physical phenomenon governing seismic wave propagations and we derive the elastodynamics weak formulation.

The geometrical and functional discretization of the problem is presented in Chapter 2 in the context of non-conforming approximations and the Discontinuous Galerkin and the Mortar spectral element methods are derived starting from a common weak formulation. The computational domain is split into macro-regions called subdomains (usually associated to the earth's substrata, heterogeneous media, engineering structures) with

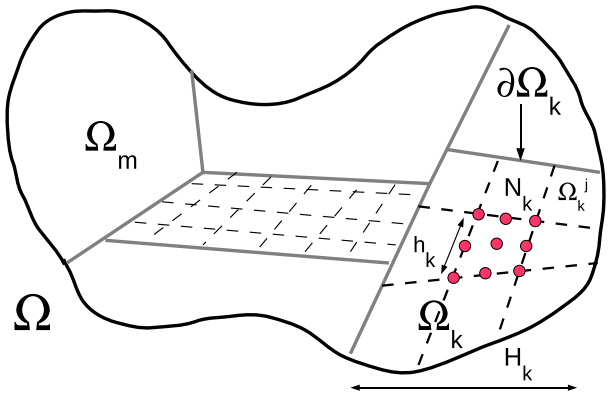

Figure 1: Non-conforming domain decomposition. The computational domain Ω is partitioned in subdomains Ω_k of characteristic (linear) size H_k. Conforming partition inside each Ω_k made by quadrilaterals/hexahedras of size h_k and polynomial approximation degree N_k. The non-conforming approach is employed across subdomains' boundary.

typical size H (see Figure 1), and the non-conforming approach is employed across subdomains' boundaries. The quadrilaterals/hexahedras do not have to match between neighbouring subdomains, and different spectral approximation degrees are allowed, see Figure 1. Therefore, the continuity of the solution at the skeleton $\mathcal{S} = \bigcup_k (\partial\Omega_k \setminus \partial\Omega)$ of the decomposition is imposed weakly, either by means of a Lagrange multiplier for the MSE method, or by penalizing the jumps of the displacement in the DGSE method. Then, in each non-overlapping subdomain a conforming spectral finite element discretization is employed.

Starting from a common displacement-based weak formulation of the elastodynamics equation, we prove *a priori* error bounds for the non-conforming semi-discrete formulations. A similar analysis is provided in the existing literature for a slightly different Discontinuous Galerkin formulation, for dynamic linear elasticity and viscoelasticity [98, 97]. In fact the above formulation involves an additional penalty term whose physical meaning is unclear. Yet, other authors refer to that analysis when discussing their Discontinuous Galerkin schemes [40, 39]. Here we modify and update the results of [98] to analyze the presented DGSE method. In the MSE method case, at the best of our knowledge, such analysis has never been carried out before in elastodynamics, but only for elliptic and parabolic equations [19, 5, 17, 49]. The algebraic aspects of the DGSE and MSE methods are then described at the end of Chapter 2. To ease the presentation,

the analysis is carried out in a two dimensional setting. The extension of the theoretical results to three dimensional problems is given at the end of Chapter 2 for the DGSE methods.

In Chapter 3 we describe three different time integration schemes that could be used for the discretization of the system of ordinary differential equations resulting from the semi-discrete approximations. In particular we study the leap-frog (LF) scheme, the implicit midpoint (IM) method and the fourth order Runge-Kutta (RK4) method. Moreover we present error estimates for the fully-discrete-problem, obtained combining the non-conforming discretizations with the previous time integration methods. The LF finite difference method, the most popular approach used in seismic modelling [61, 36, 35, 43, 30], is a special case of the Newmark methods [55] and is second order accurate, explicit and conditionally stable. The IM method belongs to the family of the Runge-Kutta methods [68] and it is still second order accurate but implicit and unconditionally stable. At the best of our knowledge, up to now, implicit time integration schemes have been coupled only with finite differences or collocation methods to solve acoustic [54] and elastic wave propagation problems [118]. The main advantage of this approach relies on their unconditioned stability, that allows to chose a time integration step ten times larger than the one in the explicit case [118]. The four stage RK4 method is explicit, fourth order accurate and conditionally stable. Runge-Kutta methods are studied and applied in wave propagation [54, 71] because they are highly accurate and feature low dispersion errors. Moreover, in the explicit case their absolute stability region is not more restrictive than the LF one.
Other high order methods proposed in the literature for time discretization are Taylor-Galerkin methods [39], the ADER-DG method [57, 41], the rapid expansion method [112, 64], and the symplectic method [105, 85, 112]. A comparison of these methods is beyond the scope of this present work and will be the subject of future research.

The semi-discrete and fully-discrete non-conforming formulations are analyzed in Chapter 4 from the point of view of the dispersion, dissipation and stability properties. For wave propagation problems, the grid dispersion/dissipation criterion determines the lowest number of nodes per wavelength such that the numerical solution has an acceptable level of accuracy, while the stability criterion determines the largest time step allowed for explicit time integration schemes. Here, we propose a new generalized eigenvalue

approach to determine sharp grid dispersion and dissipation errors as well as stability bounds for the LF and RK methods. This approach is based on the Von Neumann's method (plane wave analysis) and can be used to determine dispersion and dissipation properties for different space and time discretizations. First, we use this technique to derive dispersion and dissipation relations for the semi-discrete DGSE and MSE approximations. Then, we extend the analysis to the corresponding fully-discrete problems presented in Chapter 3, addressing the combined effect of the LF, RK4, IM time discretizations with DGSE and MSE approximations. A general framework to study the numerical dispersion for the SE methods has been developed in [36] and analyzed for the acoustic case up to polynomial approximation degree equal to three. In [103] a complete description for the elastic case is given, based on a Rayleigh quotient approximation of the eigenvalue problem characterizing the dispersion relation. For the DGSE method, grid dispersion has been analyzed in [3, 40]. In particular in [3] the dispersion and dissipation errors of the acoustic wave equation in one space dimension are derived using the flux formulation. The results include polynomial approximation degree equal to three and conjectures on the extension to higher orders are given. Making use of the plane wave analysis, in [40] a complete description of the grid dispersion properties is carried out for both the acoustic and the elastic case.
At the best of our knowledge, for the MSE method no results are available for the grid dispersion/dissipation properties regarding the elastic wave equation. The results obtained show that both DGSE and MSE methods feature low dispersive/dissipative errors.

Chapter 5 is devoted to the implementation aspects of the non-conforming approaches in a spectral element based code. Special emphasis is given to the description of the numerical strategies used for facing integral computations present in DGSE and the MSE discretizations. Moreover, we propose an efficient way (in term of low memory storage and executing program velocity) to code DGSE and MSE approaches for wave propagations.

Numerical results for test cases are presented in Chapter 6. Here, we validate the proposed schemes on two and three dimensional benchmarks available in literature. All the results are compared with analytical solutions or with the numerical solution obtained with the SE approximation.

Chapter 7 addresses some real geophysical applications. At first we show the seismic response of a remarkable railway masonry bridge, and soft soil amplifications occurring on alluvial basin. Then, we present relevant earthquake scenarios, i.e., the case of the Grenoble valley (France) and the Canterbury plains near Christchurch (New Zealand). The latter results represent the state of the art in computational seismology.

Finally, in Chapter 8 we draw some conclusions and we outline some future perspectives.

Chapter 1

Motivations and model formulation

1.1 The physical problem

Wave propagation in heterogeneous media is a problem arising in many scientific disciplines as acoustics, electro-magnetics, fracture mechanics and elastodynamics. Usually, when considering acoustic or electromagnetic waves we are interested on their refraction across an obstacle, while when dealing with elastic waves we observe their propagation within the examined body.
Seismic waves are elastic waves of energy that travel through the earth, and are a result of an earthquake, explosion, or a volcano that imparts low-frequency acoustic energy. The direct physical effect yielded by an earthquake in the region surrounding the source consists, essentially but not exclusively, of a vibratory (or seismic) ground motion varying from point to point. A fundamental seismological and engineering problem is that of quantifying the characteristics of such motion (e.g. amplitude, duration, frequency content) at a distant point, as a function of the characteristics of the source and of the portions of the earth crust traversed by the seismic waves.
The propagation velocity of the waves depends on density and elasticity of the medium. Velocity tends to increase with depth, and ranges from approximately 2 to 8 km/s in the earth's crust up to 13 km/s in the deep mantle. Earthquakes create various types of waves with different velocities; when reaching seismic observatories, their different travel time enables the scientists to locate the epicentre. There are two types of seismic waves, body wave and surface waves.
Body waves travel through the interior of the earth. They follow ray-paths refracted

by the varying density and modulus (stiffness) of the earth's interior. Body waves are divided into two categories: primary (P) waves and secondary (S) waves. P waves are longitudinal (pressure) waves that can travel through any type of material, and can travel at nearly twice the speed of shear waves. S-waves are transverse (shear) in nature. These waves typically follow P waves during an earthquake and displace the ground perpendicular to the direction of propagation. S waves can travel only through solids, since fluids (liquids and gases) do not support shear stresses.
Surface waves are analogous to water waves and travel along the earth's surface. They travel slower than body waves. Because of their low frequency, long duration, and large amplitude, they can be the most destructive type of seismic wave. There are two types of surface waves: Rayleigh waves and Love waves that are the cause of the rolling and circular shearing of the ground.
All these information are resumed and described by the following elastodynamics model as we are going to explain.

1.2 The mathematical model

We consider an elastic medium occupying a finite region $\Omega \subset \mathbb{R}^d$, for $d = 2, 3$, with boundary $\Gamma = \partial\Omega$ and unit outward normal $\mathbf{n} = \mathbf{n}(x_1, ..., x_d)$ at the point $(x_1, ..., x_d) \in \partial\Omega$. The boundary is assumed to be composed of portions Γ_D, where the displacement vector $\mathbf{u}$ is prescribed, Γ_N where external loads apply, and Γ_{NR} where suitable non-reflecting conditions are imposed. The portion Γ_{NR} is in fact a fictitious boundary of the computational domain which is introduced to bound the physical domain for the numerical approximation of wave propagation problems in unbounded media. We make the assumptions that Γ_D, Γ_N and Γ_{NR} are disjoint, i.e. $\Gamma_D \cap \Gamma_N = \emptyset$ and $\Gamma_N \cap \Gamma_{NR} = \emptyset$ and either Γ_D or Γ_N can be empty, .
Here and in the sequel, an underlying bar denotes matrix or tensor quantities, while vectors are typed in bold. Having fixed the temporal interval $[0, T]$, with T real and positive, the equilibrium equations for an elastic medium, subjected to an external force

$\mathbf{f}$ (seismic source) read:

$$\begin{cases} \rho\partial_{tt}\mathbf{u} - \nabla\cdot\underline{\sigma}(\mathbf{u}) = \mathbf{f}, & \text{in } \Omega\times(0,T], \\ \mathbf{u} = \mathbf{0}, & \text{on } \Gamma_D\times[0,T], \\ \underline{\sigma}(\mathbf{u})\cdot\mathbf{n} = \mathbf{t}, & \text{on } \Gamma_N\times[0,T], \\ \text{non reflecting boundary conditions} & \text{on } \Gamma_{NR}\times[0,T], \\ \partial_t\mathbf{u} = \mathbf{u}_1, & \text{in } \Omega\times\{0\}, \\ \mathbf{u} = \mathbf{u}_0, & \text{in } \Omega\times\{0\}, \end{cases} \tag{1.1}$$

where $\mathbf{u} = (u_1, ..., u_d)^\top$ is the medium displacement vector, $\underline{\sigma}$ the stress tensor, t the time variable and ρ the material density and where $\mathbf{u}_0, \mathbf{u}_1$ are given (smooth enough) functions. Here and after ∂_t denotes the partial derivative with respect to time, while $\nabla\cdot\underline{a} = \sum_{j=1}^{d}\frac{\partial\underline{a}_{ij}}{\partial x_j}$ represents the divergence of the tensor $\underline{a}$. Without loss of generality (see, for instance, [92]) we make the following further assumptions on Γ: on Γ_D the medium is rigidly fixed in the space and on Γ_N we prescribe surface tractions $\mathbf{t}$. Finally, on Γ_{NR} non-reflecting boundary conditions are imposed: from the mathematical point of view, the latter condition have the effect of introducing a fictitious traction $\mathbf{t}^*$, that will be defined later, which is a linear combination of space and time derivatives of the displacement $\mathbf{u}$ (cf. [107, 30], for example).

To complete the system in (1.1), we prescribe initial conditions $\mathbf{u}_0$ and $\mathbf{u}_1$ for the displacement and the velocity, respectively.

When we consider viscoelastic materials, see Chapter 6, we introduce in the system (1.1) an additional term in the form of volume forces

$$\mathbf{f}^{visc} = -2\rho\zeta\dot{\mathbf{u}} - \rho\zeta^2\mathbf{u}, \tag{1.2}$$

where $\zeta = \zeta(x_1, ..., x_d)$ is a suitable decay factor with dimension inverse of time. Correspondingly, the equation of motion becomes

$$\rho\partial_{tt}\mathbf{u} - \nabla\cdot\underline{\sigma}(\mathbf{u}) = \mathbf{f} + \mathbf{f}^{visc}. \tag{1.3}$$

The parameter ζ is supposed to be piecewise constant, as in [30], in order to model absorbing regions, thus providing an alternative or a complement to the absorbing boundary conditions. In other cases, like seismic wave propagation through heterogeneous media with strong elastic impedance, this model is used to prevent the onset of

non-physical oscillations of the numerical solution.

We define the strain tensor $\underline{\varepsilon}$ as the symmetric gradient of $\mathbf{u}$, i.e.,

$$\underline{\varepsilon}(\mathbf{u}) = \frac{1}{2}(\nabla\mathbf{u} + \nabla\mathbf{u}^\top),$$

or equivalently

$$\epsilon_{ij}(\mathbf{u}) = \frac{1}{2}(\frac{\partial u_j}{\partial x_i} + \frac{\partial u_i}{\partial x_j}) \quad \forall i,j = 1,...,d$$

since $(\nabla\mathbf{u})_{k\ell} = \frac{\partial u_k}{\partial x_\ell}$, for $\ell, k = 1,...,d$. The stress tensor is denoted by $\underline{\sigma}(\mathbf{u})$ such that $\sigma_{ii}(\mathbf{u})$ is the normal stress in the direction x_i and $\sigma_{ij}(\mathbf{u})$ for $i \neq j$ is the shear stress. The stress tensor satisfies the constitutive relation (Hooke's law)

$$\sigma_{ij}(\mathbf{u}) = \lambda \sum_{j=1}^{d} \frac{\partial u_j}{\partial x_j}\delta_{ik} + 2\mu\epsilon_{ij}(\mathbf{u}) = \sum_{k,\ell=1}^{d} D_{ijk\ell}\epsilon_{k\ell}(\mathbf{u}) \quad \forall i,j = 1,...,d$$

where where λ and μ are the Lamé elastic coefficients of the medium, δ_{ij} is the Kronecker delta and $D_{ijk\ell} = (\underline{\underline{\mathbf{D}}})_{i,j,k,\ell}$, is the fourth order Hooke's tensor, satisfying the symmetries

$$D_{ijk\ell} = D_{jik\ell} = D_{ij\ell k} = D_{k\ell ij}.$$

We assume that $\underline{\underline{\mathbf{D}}}$ is positive definite and bounded over Ω, i.e, $\exists\, D_0$ and D_1 s.t.

$$0 < D_0 \sum_{i,j} \chi_{ij}^2 \leq \sum_{i,j,k,\ell} \chi_{ij} D_{ijk\ell} \chi_{k\ell} \leq D_1 \sum_{i,j} \chi_{ij}^2 \quad \forall \underline{\chi} \neq \mathbf{0}.$$

Moreover, since for heterogeneous media we suppose ρ, λ and μ bounded functions of the spatial variable, not necessarily continuous, i.e., ρ, λ and $\mu \in L^\infty(\Omega)$, the stress tensor is also piecewise constant over Ω and by the Hooke's law, can be written as

$$\begin{bmatrix} \sigma_{11} \\ \sigma_{22} \\ \sigma_{12} \end{bmatrix} = \begin{bmatrix} \lambda+2\mu & \lambda & 0 \\ \lambda & \lambda+2\mu & 0 \\ 0 & 0 & \mu \end{bmatrix} \begin{bmatrix} \epsilon_{11} \\ \epsilon_{22} \\ \epsilon_{12} \end{bmatrix},$$

for $d = 2$ and similarly for $d = 3$.

The availability of accurate and reliable modelling of wave transmission along the boundaries of the discretized domain is a key issue in the simulation of wave propagation problems. While the representation of the free boundaries (typically free surfaces in geophysical application) do not present any difficulty, the modelling of continuous boundaries is a delicate issue. Ideally, such boundaries should be able to propagate any incident wave without reflections.

Let $\mathbf{n} = (n_1, n_2)$ be the unit normal to the point $(x_1, x_2) \in \partial\Omega$ and let $\boldsymbol{\tau} = (\tau_1, \tau_2)$ be the tangential unit vector at $(x_1, x_2) \in \partial\Omega$, the non-reflecting conditions on Γ_{NR} take the form [29]

$$\begin{cases} \dfrac{\partial}{\partial n}(\mathbf{u}\cdot\mathbf{n}) = -\dfrac{1}{c_P}\dfrac{\partial}{\partial t}(\mathbf{u}\cdot\mathbf{n}) + \dfrac{c_S - c_P}{c_P}\dfrac{\partial}{\partial \tau}(\mathbf{u}\cdot\boldsymbol{\tau}), \\ \dfrac{\partial}{\partial n}(\mathbf{u}\cdot\boldsymbol{\tau}) = -\dfrac{1}{c_S}\dfrac{\partial}{\partial t}(\mathbf{u}\cdot\boldsymbol{\tau}) + \dfrac{c_S - c_P}{c_P}\dfrac{\partial}{\partial \tau}(\mathbf{u}\cdot\mathbf{n}). \end{cases} \tag{1.4}$$

The quantities c_P and c_S appearing in (1.4) are the compressional and the shear wave velocities, respectively defined as

$$c_P = \sqrt{\frac{\lambda + 2\mu}{\rho}} \quad \text{and} \quad c_S = \sqrt{\frac{\mu}{\rho}}, \tag{1.5}$$

and they refer to the velocity of P and S body waves respectively. Primary (P) and Secondary (S) waves travel from the source through the interior of the elastic medium and they follow paths refracted by the varying density and modulus (stiffness) of the materials encountered. P waves are said compressional or longitudinal waves and they are very similar to acoustic waves, in particular the particles of the material invested by P waves move in the same direction of the P wave front. S waves are transversal waves and induce on the material oscillations perpendicular to their propagating direction. An important feature of S waves is that they can not propagate in fluids, for which the Lamé coefficient $\mu = 0$. Absorbing boundary conditions must be applied as natural boundary conditions, in other words Γ_{NR} is a boundary subjected to a stress state $\underline{\sigma}^*$ which satisfies equation (1.4). Then, to derive the explicit expression of the fictitious traction $\mathbf{t}^* = \underline{\sigma}^*(\mathbf{u})\cdot\mathbf{n}$ we proceed as follows.
We rewrite the stress tensor $\underline{\sigma}$ in the coordinate system $\{\boldsymbol{\tau}, \mathbf{n}\}$ as

$$\begin{bmatrix} \sigma_{11} \\ \\ \sigma_{22} \\ \\ \sigma_{12} \end{bmatrix} = \begin{bmatrix} \sigma_{\tau\tau} \\ \\ \sigma_{nn} \\ \\ \sigma_{\tau n} \end{bmatrix} = \begin{bmatrix} (\lambda + 2\mu)\frac{\partial u_\tau}{\partial \tau} + \lambda\frac{\partial u_n}{\partial n} \\ \\ (\lambda + 2\mu)\frac{\partial u_n}{\partial n} + \lambda\frac{\partial u_\tau}{\partial \tau} \\ \\ \mu(\frac{\partial u_\tau}{\partial \tau} + \frac{\partial u_n}{\partial \tau}) \end{bmatrix}. \tag{1.6}$$

We use equation (1.4) to express derivatives with respect to the normal direction as a combination of derivatives with respect to the tangential direction and with respect to

time so that equation (1.6) becomes

$$\begin{bmatrix} \sigma_{\tau\tau} \\ \\ \sigma_{nn} \\ \\ \sigma_{\tau n} \end{bmatrix} = \begin{bmatrix} (\lambda+2\mu)\frac{\partial u_\tau}{\partial \tau} + \lambda(-\frac{1}{c_P}\frac{\partial u_n}{\partial t} + \frac{c_S-c_P}{c_P}\frac{\partial u_\tau}{\partial \tau}) \\ \\ (\lambda+2\mu)(-\frac{1}{c_P}\frac{\partial u_n}{\partial t} + \frac{c_S-c_P}{c_P}\frac{\partial u_\tau}{\partial \tau}) + \lambda\frac{\partial u_\tau}{\partial \tau} \\ \\ \mu\frac{\partial u_\tau}{\partial \tau} + \mu(-\frac{1}{c_S}\frac{\partial u_n}{\partial t} + \frac{c_S-c_P}{c_S}\frac{\partial u_n}{\partial \tau}) \end{bmatrix}.$$

In this system of coordinates, the force for surface unit $\mathbf{t}^*$ is

$$\begin{bmatrix} t^*_\tau \\ \\ t^*_n \end{bmatrix} = \begin{bmatrix} \sigma_{\tau n} \\ \\ \sigma_{nn} \end{bmatrix} = \begin{bmatrix} \frac{\mu(2c_S-c_P)}{c_S}\frac{\partial u_n}{\partial \tau} - \frac{\mu}{c_S}\frac{\partial u_\tau}{\partial t} \\ \\ \frac{\lambda c_S+2\mu(c_S-c_P)}{c_P}\frac{\partial u_\tau}{\partial \tau} - \frac{\lambda+2\mu}{c_P}\frac{\partial u_n}{\partial t} \end{bmatrix}.$$

Computing in the above equation normal and tangential derivatives as $\frac{\partial}{\partial n} = n_1\frac{\partial}{\partial x_1} + n_2\frac{\partial}{\partial x_2}$ and $\frac{\partial}{\partial \tau} = \tau_1\frac{\partial}{\partial x_1} + \tau_2\frac{\partial}{\partial x_2} = n_2\frac{\partial}{\partial x_1} - n_1\frac{\partial}{\partial x_2}$ we obtain

$$\begin{bmatrix} t^*_\tau \\ \\ t^*_n \end{bmatrix} = \begin{bmatrix} \frac{\mu(2c_S-c_P)}{c_S}[n_1n_2(\frac{\partial u_1}{\partial x_1} - \frac{\partial u_2}{\partial x_2}) - n_1^2\frac{\partial u_1}{\partial x_2} + n_2^2\frac{\partial u_2}{\partial x_1}] - \frac{\mu}{c_S}(\frac{\partial u_1}{\partial t}n_2 - \frac{\partial u_2}{\partial t}n_1) \\ \\ \frac{\lambda c_S+2\mu(c_S-c_P)}{c_P}[n_2^2\frac{\partial u_1}{\partial x_1} - n_1n_2(\frac{\partial u_1}{\partial x_2} + \frac{\partial u_2}{\partial x_1}) + n_1^2\frac{\partial u_2}{\partial x_2}] - \frac{\lambda+2\mu}{c_P}(\frac{\partial u_1}{\partial t}n_1 + \frac{\partial u_2}{\partial t}n_2) \end{bmatrix}.$$

Finally, since $\mathbf{t}^*$ is expressed in the local coordinate system, we project it on the global coordinate system

$$\mathbf{t}^* = \begin{bmatrix} t^*_1 \\ t^*_2 \end{bmatrix} = \begin{bmatrix} t^*_\tau n_2 + t^*_n n_1 \\ t^*_n n_2 - t^*_\tau n_1 \end{bmatrix}. \tag{1.7}$$

For $d = 3$ non-reflecting boundary conditions are given by (see [30])

$$\begin{cases} \dfrac{\partial}{\partial n}(\mathbf{u}\cdot\mathbf{n}) = -\dfrac{1}{c_P}\dfrac{\partial}{\partial t}(\mathbf{u}\cdot\mathbf{n}) + \dfrac{c_S-c_P}{c_P}\left[\dfrac{\partial}{\partial \tau_1}(\mathbf{u}\cdot\boldsymbol{\tau_1}) + \dfrac{\partial}{\partial \tau_2}(\mathbf{u}\cdot\boldsymbol{\tau_2})\right], \\ \dfrac{\partial}{\partial n}(\mathbf{u}\cdot\boldsymbol{\tau_1}) = -\dfrac{1}{c_S}\dfrac{\partial}{\partial t}(\mathbf{u}\cdot\boldsymbol{\tau_1}) + \dfrac{c_S-c_P}{c_P}\dfrac{\partial}{\partial \tau_1}(\mathbf{u}\cdot\mathbf{n}), \\ \dfrac{\partial}{\partial n}(\mathbf{u}\cdot\boldsymbol{\tau_2}) = -\dfrac{1}{c_S}\dfrac{\partial}{\partial t}(\mathbf{u}\cdot\boldsymbol{\tau_2}) + \dfrac{c_S-c_P}{c_P}\dfrac{\partial}{\partial \tau_2}(\mathbf{u}\cdot\mathbf{n}), \end{cases} \tag{1.8}$$

where $\boldsymbol{\tau_1}$ and $\boldsymbol{\tau_2}$ are two arbitrary mutually orthogonal unit vectors on the plane orthogonal to $\boldsymbol{n}$, the normal to Γ_{NR}, such that $\{\boldsymbol{\tau_1}, \boldsymbol{\tau_2}, \boldsymbol{n}\}$ defines a right handed Cartesian system. Starting to (1.8) it is possible to deduce an analogous of (1.7) for the definition of absorbing boundary conditions on a three dimensional framework. We refer to [29] for a detailed description of the derivation along with the illustration of a procedure for the practical choice of the axes $\boldsymbol{\tau_1}$ and $\boldsymbol{\tau_2}$.

1.3 The variational formulation

Before recasting the problem in a variational form we introduce the following notation. We denote by $\mathbf{X}$ the d-direct product of the functional space X by itself and introduce the following product operators defined for scalar, vectorial and tensorial quantities:

$$a \cdot b = ab, \qquad (a,b)_\Omega = \int_\Omega a \cdot b \, d\Omega \qquad \forall\, a, b \in L^2(\Omega),$$

$$\mathbf{a} \cdot \mathbf{b} = \sum_{i=1}^{d} a_i b_i, \qquad (\mathbf{a},\mathbf{b})_\Omega = \int_\Omega \mathbf{a} \cdot \mathbf{b} \, d\Omega \qquad \forall\, \mathbf{a}, \mathbf{b} \in \mathbf{L}^2(\Omega),$$

$$\underline{a} : \underline{b} = \sum_{i,j=1}^{d} a_{ij} b_{ij}, \qquad (\underline{a},\underline{b})_\Omega = \int_\Omega \underline{a} : \underline{b} \, d\Omega \qquad \forall\, \underline{a}, \underline{b} \in [\mathbf{L}^2(\Omega)]^d,$$

respectively. By multiplying the first equation in (1.1) for a regular enough function $\mathbf{v}$ (candidate to represent an admissible displacement), integrating by parts over the domain Ω, using the Green's formula:

$$-\left(\nabla \cdot \underline{\sigma}(\mathbf{u}), \mathbf{v}\right)_\Omega = \left(\underline{\sigma}(\mathbf{u}), \underline{\varepsilon}(\mathbf{v})\right)_\Omega - \left(\mathbf{v}, \underline{\sigma}(\mathbf{u}) \cdot \mathbf{n}\right)_\Gamma,$$

and imposing the boundary conditions, the variational formulation of (1.1) reads: $\forall t \in (0,T]$ *find* $\mathbf{u} = \mathbf{u}(t) \in V$ *such that*

$$\mathrm{d}_{tt}\left(\rho\mathbf{u}, \mathbf{v}\right)_\Omega + \mathcal{A}(\mathbf{u}, \mathbf{v})_\Omega = \mathcal{L}(\mathbf{v}) \quad \forall\, \mathbf{v} \in V, \tag{1.9}$$

where the bilinear form $\mathcal{A} : V \times V \to \mathbb{R}^d$ is defined as

$$\mathcal{A}(\mathbf{u}, \mathbf{v})_\Omega = \left(\underline{\sigma}(\mathbf{u}), \underline{\varepsilon}(\mathbf{v})\right)_\Omega,$$

and the linear functional $\mathcal{L} : V \to \mathbb{R}^d$ as

$$\mathcal{L}(\mathbf{v}) = \left(\mathbf{t}, \mathbf{v}\right)_{\Gamma_N} + \left(\mathbf{t}^*, \mathbf{v}\right)_{\Gamma_{NR}} + \left(\mathbf{f}, \mathbf{v}\right)_\Omega.$$

Here V is the Sobolev space $V = \{\mathbf{v} \in \mathbf{H}^2(\Omega) : \mathbf{v} = \mathbf{0} \text{ on } \Gamma_D\}$, where $L^2(\Omega)$ is the space of square integrable functions over Ω and $H^2(\Omega)$ is the space of functions in $L^2(\Omega)$ such that for every multi-index α such that $|\alpha| \leq 2$ the weak partial derivative $\partial^\alpha u$ belongs to $L^2(\Omega)$. We recall that it can be proved that the bilinear form $\mathcal{A}(\cdot,\cdot)$ is symmetric, V-elliptic and continuous [94]. These conditions imply that problem (1.9) admits a unique solution $\mathbf{u} \in \mathcal{C}^0((0,T);V) \cap \mathcal{C}^1((0,T);\mathbf{L}^2(\Omega))$ satisfying suitable stability estimates [24, 94], provided that $\rho \in L^\infty(\Omega)$ is a strictly positive function, and

that $\mathbf{u}_0 \in V$, $\mathbf{u}_1 \in \mathbf{L}^2(\Omega)$ and $\mathbf{f} \in \mathbf{L}^2(\Omega \times (0,T))$.

By introducing a finite dimensional space V_δ which is a suitable approximation of V, the semi-discrete approximation of (1.9) reads : $\forall t \in (0,T]$ *find* $\mathbf{u}_\delta = \mathbf{u}_\delta(t) \in V_\delta$ *such that*

$$\mathrm{d}_{tt}\left(\rho \mathbf{u}_\delta, \mathbf{v}\right)_\Omega + \mathcal{A}(\mathbf{u}_\delta, \mathbf{v})_\Omega = \mathcal{L}(\mathbf{v}) \quad \forall\, \mathbf{v} \in V_\delta. \tag{1.10}$$

In the next section we will explain how to construct V_δ for two different families of non-conforming domain decomposition methods, namely, the Discontinuous Galerkin spectral element (DGSE) method and the Mortar spectral element (MSE) method.

The reasons for using non-conforming DGSE and MSE discretizations can be summarized in the following lines. Firstly, the flexibility in handling complex geometries, retaining the high order accuracy of spectral elements methods for locally smooth solutions.

Secondly, since they are based on the weak formulation of the elastodynamics equations, they handle naturally both interface continuity and free boundary conditions, allowing very accurate resolutions of evanescent interface and surface waves. Moreover, they guarantee geometrical and polynomial flexibility that is an important task for simulating correctly the wave-front field in complex wave phenomena such as soil-structure interaction problems or seismic response of sedimentary basins (cf. Chapters 6 and 7), accommodating discontinuities, not only in the parameters, but also in the wavefield.

Finally, they retain a high level parallel structure, thus well suited for parallel computations.

Chapter 2

Non-conforming Galerkin spectral formulations

We first introduce the non-conforming Galerkin spectral formulations in a $d = 2$ dimensional setting, to ease the presentation. The extension to three dimensional problems can be obtained similarly.

At the first level, we subdivide Ω into K non overlapping polygonal subdomains Ω_k, $k = 1, ..., K$, of size $H_j = diam(\Omega_j)$, with sufficiently smooth boundary $\partial\Omega_k$, such that $\overline{\Omega} = \bigcup_{k=1}^{K} \overline{\Omega}_k$ with $\Omega_k \cap \Omega_\ell = \emptyset$ if $k \neq \ell$ and we define the skeleton of this (macro) decomposition as $\mathcal{S} = \bigcup_{k=1}^{K} \partial\Omega_k \setminus \partial\Omega$.

Note that this (macro) decomposition can be geometrically non-conforming, *i.e.*, for two neighbouring subdomains Ω_k, Ω_ℓ, the interface $\gamma = \partial\Omega_k \cap \partial\Omega_\ell$ may not be a complete side of Ω_k or Ω_ℓ (see Figure 2.1).

Then problem (1.1) is solved in each Ω_k together with transmission conditions to ensure that the local solution is the restriction to $\Omega_k \times (0, T]$ of the global solution. For the elastic problem (1.1) the transmission conditions read: (**TC1**) $[\![\mathbf{u}]\!] = 0$ and (**TC2**) $[\![\underline{\sigma}]\!] = \mathbf{0}$, where $[\![\cdot\,]\!]$ denotes the jump of a quantity across a given interface.

Next, in each Ω_k we introduce a partition $\mathcal{T}_{h_k}$, made by quadrilaterals elements Ω_k^j, with typical linear size h_k, say $h_k = \max_j h_k^j$ with $h_k^j = diam(\Omega_k^j)$, and $\overline{\Omega}_k = \bigcup_{j=1}^{J_k} \overline{\Omega}_k^j$ (see Figure 2.1). We remark that the global partition $\mathcal{T} = \bigcup_{k=1}^{K} \mathcal{T}_{h_k}$ must preserve the boundary decomposition introduced in (1.1).

Let us set $\widehat{\Omega} = (-1, 1)^d$ and suppose that there exists a suitable invertible mapping $\mathbf{F}_k^j : \widehat{\Omega} \to \Omega_k^j$ with (positive) Jacobian $J_{\Omega_k^j}$. This (meso) partition is instead geomet-

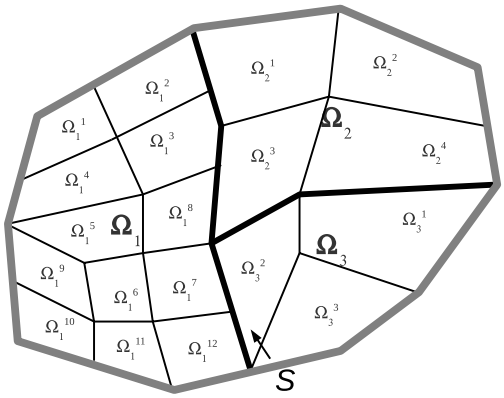

Figure 2.1: Example of a two dimensional subdomain partition. In this case $K = 3$ and $\overline{\Omega} = \overline{\Omega}_1 \cup \overline{\Omega}_2 \cup \overline{\Omega}_3$, with $\overline{\Omega}_1 = \bigcup_{j=1}^{12} \overline{\Omega}_1^j$, $\overline{\Omega}_2 = \bigcup_{j=1}^{4} \overline{\Omega}_2^j$ and $\overline{\Omega}_3 = \bigcup_{j=1}^{3} \overline{\Omega}_3^j$.

rically conforming in each Ω_k, thus the intersection of two elements Ω_k^j, Ω_k^ℓ, $\ell \neq j$, is either empty, or a vertex, or an edge of both Ω_k^j and Ω_k^ℓ (see Figure 2.1).
We thus have that

$$\int_{\Omega_k} f = \sum_{\Omega_k^j \in \mathcal{T}_{h_k}} \int_{\Omega_k^j} f = \sum_{\Omega_k^j \in \mathcal{T}_{h_k}} \int_{\hat{\Omega}} (f \circ \mathbf{F}_k^j) J_{\Omega_k^j}.$$

The third (micro) level will be represented by the so-called Gauss-Lobatto-Legendre (GLL) points in each mesh element Ω_k^j. Let $\mathbf{Q}_{N_k}(\widehat{\Omega})$ be the space of functions defined on $\widehat{\Omega}$ that are algebraic polynomials of degree less than or equal to $N_k \geq 2$ in each coordinate direction, and let

$$\mathbf{Q}_{N_k}(\Omega_k^j) = \{v = \widehat{v} \circ {\mathbf{F}_k^j}^{-1} : \widehat{v} \in \mathbf{Q}_{N_k}(\widehat{\Omega})\}.$$

We define the finite dimensional space $X_\delta(\Omega_k)$ as

$$X_\delta(\Omega_k) = \{v_\delta \in \mathcal{C}^0(\overline{\Omega}_k) : v_{\delta|\Omega_k^j} \in \mathbf{Q}_{N_k}(\Omega_k^j)\ \forall \Omega_k^j \in \mathcal{T}_{h_k}\},$$

and finally

$$V_\delta = \{\mathbf{v}_\delta \in \mathbf{L}^2(\Omega) : \mathbf{v}_{\delta|\Omega_k} \in \mathbf{X}_\delta(\Omega_k)\ \forall k = 1, ..., K : \mathbf{v}_{\delta|\Gamma_D} = \mathbf{0}\},$$

where $\delta = \{\mathbf{H}, \mathbf{h}, \mathbf{N}\}$ with $\mathbf{H} = (H_1, ..., H_K)$, $\mathbf{h} = (h_1, ..., h_K)$ and $\mathbf{N} = (N_1, ..., N_K)$ K-uplets of discretization parameters. Each component h_k and N_k represents the mesh

size and the degree of the polynomial interpolation in the subdomain Ω_k, respectively. In order to construct a nodal basis for V_δ, we introduce on each element Ω_k^j a set of interpolation points $\{\mathbf{p}_i\}$ and corresponding degrees of freedom which allow to identify uniquely a piecewise polynomial function in V_δ. We remark that, by the definition of the space V_δ, the basis functions will not be globally continuous on the whole domain Ω.

In the spectral element approximation, the interpolation points $\{\mathbf{p}_i\}$ are chosen to be the GLL points. On the reference element $\widehat{\Omega}$, these points are tensor product of points defined in the reference interval $[-1,1]$ as the zeros of $(1-x^2)L'_{N_k}$ where L'_{N_k} is the derivative of the Legendre polynomial L_{N_k}. This means that there exist N_k+1 points $\mathbf{p}_i$ for the interpolation of a polynomial of degree N_k in $[-1,1]$, see [27] for details. As previously observed, in higher dimensions, the spectral nodes $\{\mathbf{p}_i\}$ are defined on the reference element $\widehat{\Omega}=[-1,1]^d$, via tensor product of the one dimensional distribution, and are then mapped onto the generic element Ω_k^j in the physical space through $\mathbf{F}_k^j$. In the spectral element (SE) method, such interpolation points are also used as quadrature points. Thus, we have

$$\int_{\widehat{\Omega}}(f\circ\mathbf{F}_k^j)J_{\Omega_k^j}\approx\sum_{i=1}^{(N_k+1)^d}(f\circ\mathbf{F}_k^j)(\mathbf{p}_i)J_{\Omega_k^j}(\mathbf{p}_i)w_i,$$

where w_i are the weights of the GLL quadrature formula which is exact for all $(f\circ\mathbf{F}_k^j)J_{\Omega_k^j}\in\mathbf{Q}_{2N_k-1}(\widehat{\Omega})$. The spectral shape functions $\mathbf{\Psi}_i\in V_\delta$ are defined as $\mathbf{\Psi}_i(\mathbf{p}_j)=\delta_{ij}$, $i,j=1,...,(N_k+1)^d$, where δ_{ij} is the Kronecker symbol. It is straightforward to see that the restriction of any spectral function to Ω_k^j either coincides with a Lagrange polynomial or vanishes. Moreover the support of any shape function is limited to the neighbouring elements if the spectral node lies on the interface between two or more elements, while it is confined to only one element for internal nodes.

To introduce the non-conforming Discontinuous Galerkin (DG) and Mortar variational formulation, we write the equilibrium equations for a generic Ω_k, integrate it by parts and sum over $\Omega_k^j\in\mathcal{T}_{h_k}$. What we obtain is an equivalent form of the equation (1.9). For each $t\in(0,T]$, we now seek for a K-uplet $(\mathbf{u}_{\delta,1},\ldots,\mathbf{u}_{\delta,K})$ of functions, one for each subdomain Ω_k. Problem (1.10) is then equivalent to: $\forall t\in(0,T]$ *find* $(\mathbf{u}_{\delta,1}(t),\ldots,\mathbf{u}_{\delta,K}(t))\in V_\delta$ *such that*

$$\sum_{k=1}^{K}\left(\mathrm{d}_{tt}(\rho\mathbf{u}_{\delta,k},\mathbf{v}_k)_{\Omega_k}+\mathcal{A}(\mathbf{u}_{\delta,k},\mathbf{v}_k)_{\Omega_k}+\mathcal{B}(\mathbf{u}_{\delta,k},\mathbf{v}_k)_{\partial\Omega_k\setminus\partial\Omega}\right)=\sum_{k=1}^{K}\mathcal{L}(\mathbf{v}_k)_{\Omega_k},\qquad(2.1)$$

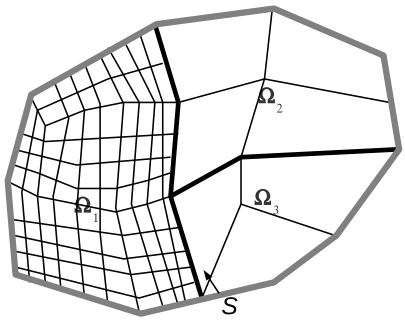

Figure 2.2: Example of non-conforming decomposition.

for all $(\mathbf{v}_1, \ldots, \mathbf{v}_K) \in V_\delta$, where

$$\mathcal{A}(\mathbf{u}, \mathbf{v})_{\Omega_k} = (\underline{\sigma}(\mathbf{u}), \underline{\varepsilon}(\mathbf{v}))_{\Omega_k}, \quad \text{and} \quad \mathcal{B}(\mathbf{u}, \mathbf{v})_{\partial\Omega_k \setminus \partial\Omega} = (\underline{\sigma}(\mathbf{u}) \cdot \mathbf{n}, \mathbf{v})_{\partial\Omega_k \setminus \partial\Omega}. \tag{2.2}$$

Depending on the chosen non-conforming approach, the functional space V_δ is completed by additional conditions on $\mathbf{u}_{\delta,k}$, $k = 1, \ldots, K$, on $\mathcal{S}$ which ensure that $\mathbf{u}_{\delta,k}$ is the restriction to Ω_k of $\mathbf{u}_\delta \in \mathbf{H}^1(\Omega)$. The bilinear form $\mathcal{B}(\cdot, \cdot)$ may either be zero or gather all the contributions $(\sigma(\mathbf{u}_{\delta,k}) \cdot \mathbf{n}_k, \mathbf{v}_k)_{\partial\Omega_k \setminus \partial\Omega}$, $k = 1, \ldots, K$, depending on the chosen approach. In fact, **TC1** is imposed by introducing a weak continuity condition on the skeleton $\mathcal{S}$ compatible with the considered formulations while **TC2** is enforced strongly. In both situations this lead to a strongly consistent numerical method. This means that the exact solution satisfies the numerical scheme for each choice of $\mathbf{h}$ and $\mathbf{N}$, [91].

Equation (2.1) represents the starting point to introduce the Discontinuous Galerkin and the Mortar variational formulation. With both formulations we will be able to treat more general situations like (i) geometric non-conformity and (ii) functional non-conformity (i.e. variable polynomial approximation degrees).

In (i) the partitions $\mathcal{T}_k$ and $\mathcal{T}_\ell$, of different subdomains Ω_k and Ω_ℓ can have different mesh sizes h_k and h_ℓ: in fact, the practical importance of the proposed methods for elastodynamics problems lies on the possibility of using computational grids with different local mesh sizes to take into account sharp variations in the physical parameters of the media.

Furthermore, the vertices of elements Ω_k^j and Ω_ℓ^i lying on the skeleton $\mathcal{S}$ do not necessarily have to match, not even in the case $h_k \approx h_\ell$ (Figure 2.2).

In (ii) we use different polynomial approximation degrees in each subdomain to get

higher precision without refining too much the grid only in the subdomain of interest. Moreover, as we show in Chapter 4, it is evident that high order methods do not significantly suffer from numerical dispersion. The combination of (i) and (ii) yields approximate solutions that are both numerically accurate and computationally cheap.
Obviously, interface conditions other than those we consider are possible as well: an intuitive alternative is offered by pointwise matching conditions which require different spectral solutions to match on a particular set of points lying on $\mathcal{S}$. The Mortar or Discontinuous Galerkin approach is preferred to the pointwise matching since it brings optimal convergence rate, which is not the case for methods based on pointwise conditions (see [18] for the elliptic case), without affecting significantly the computational effort.
In the sequel, we describe in detail the DG and Mortar non-conforming methods. To ease the presentation, we suppose that each partition $\mathcal{T}_{h_k}$ of Ω_k consists in only one element, this means that each subdomain is in fact a spectral element (*i.e.*, $h_k = H_k$). The more general case follows from similar arguments.

2.1 The Discontinuous Galerkin spectral element method

Before going into the detail of the DG spectral formulation let us introduce some notation that will be useful in the sequel. Let us subdivide the skeleton $\mathcal{S}$ in elementary components as follows:

$$\overline{\mathcal{S}} = \bigcup_{j=1}^{M} \overline{\gamma}_j, \quad \text{with } \gamma_i \cap \gamma_j = \emptyset, \quad \text{if } i \neq j, \tag{2.3}$$

where each element $\overline{\gamma}_j = (\partial\overline{\Omega}_{k(j)} \cap \partial\overline{\Omega}_{\ell(j)}) \setminus \partial\Omega$, for some different positive integers k and ℓ: this decomposition is unique (see Figure 2.3). Next we collect all the edges in the set $\mathcal{F}_I$.
For any pair of neighbouring subdomains Ω_i and Ω_j that share a non trivial edge $\gamma \in \mathcal{F}_I$, we denote by $\mathbf{v}_i, \underline{\sigma}_i$ (resp. $\mathbf{v}_j, \underline{\sigma}_j$) the restriction to Ω_i (resp. Ω_j) of regular enough functions $\mathbf{v}, \underline{\sigma}$. We also denote by $\mathbf{n}_i$ (resp. $\mathbf{n}_j$) the exterior unit normal to Ω_i (resp. Ω_j).
On each $\gamma \in \mathcal{F}_I$ we define the average and jump operators for $\mathbf{v}$ and $\underline{\sigma}$ as follows:

$$\{\mathbf{v}\} = \frac{1}{2}(\mathbf{v}_i + \mathbf{v}_j), \qquad [\![\mathbf{v}]\!] = \mathbf{v}_i \otimes \mathbf{n}_i + \mathbf{v}_j \otimes \mathbf{n}_j, \tag{2.4}$$

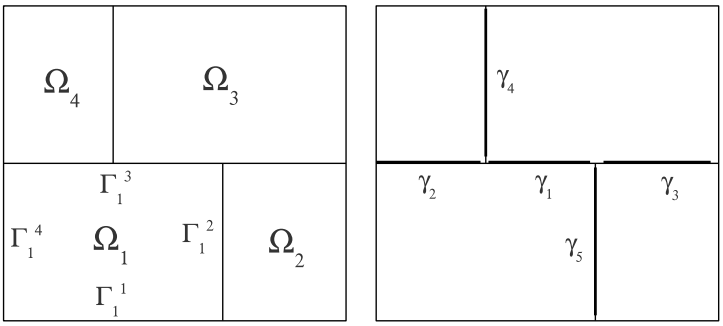

Figure 2.3: Non-conforming domain decomposition (left) and skeleton structure (right) showing the elementary components (dark continuous lines).

and

$$\{\underline{\sigma}\} = \frac{1}{2}(\underline{\sigma}_i + \underline{\sigma}_j), \qquad [\![\underline{\sigma}]\!] = \underline{\sigma}_i \cdot \mathbf{n}_i + \underline{\sigma}_j \cdot \mathbf{n}_j, \tag{2.5}$$

where $\mathbf{a} \otimes \mathbf{b} \in \mathbb{R}^{d\times d}$ is the tensor with entries $(\mathbf{a} \otimes \mathbf{b})_{ij} = a_i b_j, 1 \leq i, j \leq d$, for all $\mathbf{a}, \mathbf{b} \in \mathbb{R}^d$.

Starting from (2.1), the application of jump and average operators defined in (2.4)-(2.5) and the imposition of condition **TC2**, i.e., continuity of tractions across $\mathcal{S}$, we deduce that

$$\sum_{k=1}^{K} (\underline{\sigma}(\mathbf{u}) \cdot \mathbf{n}, \mathbf{v})_{\partial\Omega_k \setminus \partial\Omega} = \sum_{j=1}^{M} (\{\underline{\sigma}(\mathbf{u})\}, [\![\mathbf{v}]\!])_{\gamma_j} . \tag{2.6}$$

Since also **TC1** holds, i.e., $[\![\mathbf{u}]\!] = \underline{0}$ is zero across $\mathcal{S}$, we can further add other terms in (2.6) that penalize and control the jumps of the numerical solution,

$$\theta \sum_{j=1}^{M} ([\![\mathbf{u}_\delta]\!], \{\underline{\sigma}(\mathbf{v})\})_{\gamma_j} + \sum_{j=1}^{M} \eta_{\gamma_j} ([\![\mathbf{u}_\delta]\!], [\![\mathbf{v}]\!])_{\gamma_j} ,$$

with $\theta = \{-1, 0, 1\}$ and η_{γ_j} positive constants depending on the discretization parameters $\mathbf{h}$ and $\mathbf{N}$ and on the Lamé coefficients. The terms do not affect consistency of the method and are added with the purpose of providing more generality and better stability properties to the scheme (see [95, 96]).

In this context we choose $\eta_{\gamma_j} = \alpha\{\lambda + 2\mu\}_A \mathtt{N}_j^2/\mathtt{h}_j$, where $\{q\}_A$ represents the harmonic average of the quantity q, defined by $\{q\}_A = 2q_{k(j)}q_{\ell(j)}/(q_{k(j)} + q_{\ell(j)})$, $\mathtt{N_j} =$

$\max(N_{k(j)}, N_{\ell(j)})$, $\mathtt{h_j} = \min(h_{k(j)}^{d-1}, h_{\ell(j)}^{d-1})$ and α is a positive constant at disposal. The semi-discrete DG formulation reads:
$\forall t \in (0,T]$ *find* $\mathbf{u}_\delta = (\mathbf{u}_{\delta,1}(t), ..., \mathbf{u}_{\delta,K}(t)) \in V_\delta^{DG} \equiv V_\delta$ *such that*

$$\sum_{k=1}^{K} \left(\mathrm{d}_{tt} \left(\rho \mathbf{u}_\delta, \mathbf{v} \right)_{\Omega_k} + \mathcal{A}(\mathbf{u}_\delta, \mathbf{v})_{\Omega_k} \right) + \sum_{j=1}^{M} \mathcal{B}(\mathbf{u}_\delta, \mathbf{v})_{\gamma_j} = \sum_{k=1}^{K} \mathcal{L}(\mathbf{v}_k), \tag{2.7}$$

for all $\mathbf{v} = (\mathbf{v}_1, ..., \mathbf{v}_K) \in V_\delta^{DG}$, with

$$\mathcal{B}(\mathbf{u}, \mathbf{v})_{\gamma_j} = -\left(\{\underline{\sigma}(\mathbf{u})\}, [\![\mathbf{v}]\!] \right)_{\gamma_j} + \theta \left([\![\mathbf{u}]\!], \{\underline{\sigma}(\mathbf{v})\} \right)_{\gamma_j} + \eta_{\gamma_j} \left([\![\mathbf{u}]\!], [\![\mathbf{v}]\!] \right)_{\gamma_j}. \tag{2.8}$$

Corresponding to different choices of θ we obtain different DG schemes, namely: $\theta = -1$ (resp. $\theta = 1$) leads to the symmetric (resp. non-symmetric) interior penalty method SIPG (resp. NIPG), while $\theta = 0$ corresponds to the so-called incomplete interior penalty method IIPG (see [9, 95, 96, 98] for more details).

2.2 The Mortar spectral element method

In this section we introduce the Mortar spectral element (MSE) method for the solution of (2.1). The emphasis is on the numerical formulation, implementation and on the illustration of its flexibility and accuracy. To illustrate the key points, we consider the *free-vertex* variant of the MSE method [42, 16]. The *constrained-vertex* strategy can be implemented in a similar framework. For this latter technique the theoretical analysis is given in [19, 18, 73].
The MSE method relaxes the $\mathbf{H}^1$-continuity requirements of the conforming spectral-element method by considering each element (or in the general case each subdomain) separately and achieving matching or patching conditions through a variational process. The *mortars* play the role of gluing the bricks of the spectral construction. Through the use of *mortars*, one can also couple domains where spectral elements are employed with others treated by finite elements [18].
To begin, we denote by Γ_k^ℓ, $\ell = 1, \ldots, 2d$, the edges of each subdomain Ω_k, $k = 1, \ldots, K$, so that

$$\partial\Omega_k = \bigcup_{\ell=1}^{2d} \overline{\Gamma}_k^\ell.$$

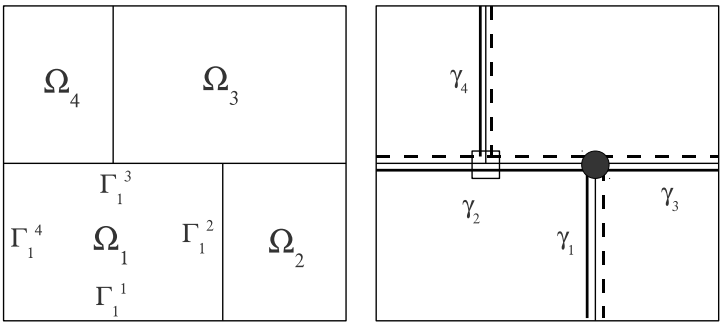

Figure 2.4: Non-conforming domain decomposition (left) and skeleton structure (right) showing a cross-point (•), a virtual vertex (□), the *mortars* (dark continuous lines) and the *non-mortars* (dark dashed lines).

We then represent the skeleton $\mathcal{S}$ as the union of elementary non-empty components called *mortars* (or *masters*), more precisely

$$\mathcal{S} = \bigcup_{k=1}^{K} (\partial\Omega_k \setminus \partial\Omega) = \bigcup_{m=1}^{M} \overline{\gamma}_m, \quad \text{with } \gamma_m \cap \gamma_n = \emptyset, \quad \text{if } m \neq n, \tag{2.9}$$

where each *mortar* is a whole edge $\Gamma_{k(m)}^{\ell(m)}$ of a specific element $\Omega_{k(m)}$ and m is an arbitrary numbering $m = 1, \ldots, M$, with M a positive integer. Those edges Γ_k^{ℓ} that do not coincide with a *mortar* are called *non-mortars* (or *slaves*) and provide a dual description of the skeleton, as

$$\mathcal{S} = \bigcup_{m\, mortar} \gamma_m^+ = \bigcup_{n\, non-mortar} \gamma_n^-.$$

The intersection of the closures of the *mortars* defines a set of vertices or *cross-points*

$$\mathcal{V} = \{\mathbf{x}_q = (\overline{\gamma}_r^+ \cap \overline{\gamma}_s^+),\ \mathbf{x}_q \notin \overline{\gamma}_m^+,\ m = 1, \ldots, M\},$$

where q is an arbitrary numbering $q = 1, \ldots, \mathtt{V}$. We define as well the set $\widetilde{\mathcal{V}}$ of *virtual* vertices (that are not cross-points) as

$$\widetilde{\mathcal{V}} = \{\widetilde{\mathbf{x}}_q = (\overline{\gamma}_r^+ \cap \gamma_s^+)\},$$

where q is an arbitrary numbering $q = 1, \ldots, \widetilde{\mathtt{V}}$ (see Figure 2.4).

We define $\Lambda_\delta(\Gamma_k^\ell) = \mathbf{Q}_{N_k}(\Gamma_k^\ell)$, the space of the traces of functions of $X_\delta(\Omega_k)$ over Γ_k^ℓ and we also introduce $\widehat{\Lambda}_\delta(\Gamma_k^\ell) = \mathbf{Q}_{N_k-2}(\Gamma_k^\ell)$.
We can now define the non-conforming spectral element discretization space $\widetilde{V}_\delta$ as the space of functions $\mathbf{v}_\delta \in V_\delta$ that satisfy the following additional *mortar matching condition*:

(**MC**) let Φ be the *mortar function* associated with $\mathbf{v}_\delta$, i.e., a function that is continuous on $\mathcal{S}$, zero on $\partial\Omega$ and such that on each *mortar* $\gamma_m = \Gamma_{k(m)}^{\ell(m)}$ it coincides with the restriction of $\mathbf{v}_{\delta,k} = \mathbf{v}_{\delta|\Omega_k}$ to γ_m; then, for all indices (k,ℓ) such that Γ_k^ℓ is contained in $\mathcal{S}$ but $(k,\ell) \neq (k(m),\ell(m))$ for all $m = 1,\ldots,M$ (that is for all indices (k,ℓ) such that Γ_k^ℓ is a *non-mortar*) we require that:

$$\int_{\Gamma_k^\ell} (\mathbf{v}_{\delta,k} - \Phi)\cdot\widehat{\Phi} = 0 \quad \forall \widehat{\Phi} \in [\widehat{\Lambda}_\delta(\Gamma_k^\ell)]^d \tag{2.10}$$

and that

$$\mathbf{v}_{\delta|\Omega_k}(\mathbf{x}_q) = \Phi(\mathbf{x}_q), \quad \forall\, \mathbf{x}_q \in \mathcal{V} \cup \widetilde{\mathcal{V}}. \tag{2.11}$$

The integral matching condition (2.10) represents a minimization of the jump of the functions at internal boundaries with respect to the L^2-norm and is the counterpart in the Mortar framework of condition **TC1**. The vertex condition (2.11) ensures exact continuity at cross-points. The Mortar spectral formulation is obtained by solving in each subdomain Ω_k the elastodynamics variational problem (2.1) with homogeneous Neumann boundary conditions on $\mathcal{S}$ ($\underline{\sigma}(\mathbf{u})\cdot\mathbf{n} = \mathbf{0}$ so that $\sum_k \mathcal{B}(\mathbf{u},\mathbf{v})_{\partial\Omega_k\setminus\partial\Omega}$ is identically zero, i.e., **TC2** is satisfied), and enforcing weak continuity of the displacement on $\mathcal{S}$ with *mortar condition* (2.10). Thus, the semi-discrete Mortar spectral formulation reads: $\forall t \in (0,T]$ *find* $(\mathbf{u}_{\delta,1}(t),\ldots,\mathbf{u}_{\delta,K}(t)) \in V_\delta^{mortar}$ *such that*

$$\sum_{k=1}^{K} d_{tt}\left(\rho\mathbf{u}_{\delta,k},\mathbf{v}_k\right)_{\Omega_k} + \mathcal{A}(\mathbf{u}_{\delta,k},\mathbf{v}_k)_{\Omega_k} = \sum_{k=1}^{K}\mathcal{L}(\mathbf{v}_k), \tag{2.12}$$

for all $(\mathbf{v}_1,\ldots,\mathbf{v}_K) \in V_\delta^{mortar}$ where

$$V_\delta^{mortar} = \{(\mathbf{v}_1,\ldots,\mathbf{v}_K) \in V_\delta : \textit{mortar condition } \mathbf{MC} \text{ is satisifed}\}.$$

The Mortar Element method was originally proposed as a non-overlapping domain decomposition approach, however recently it has been generalized to the case of overlapping subdomains [47, 75, 93]. The overlapping version may be quite useful in elastodynamics modelling to treat subdomains with complex shaped boundaries (see an application in Section 7.2). Let us consider the two cases presented in Figure 2.5.

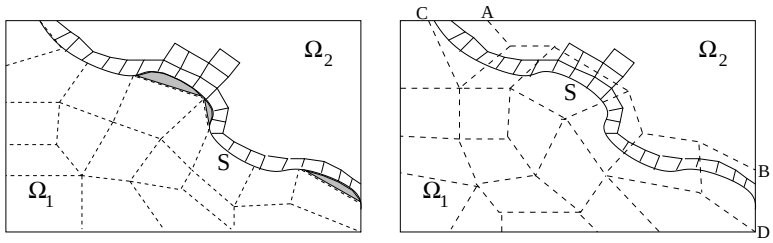

Figure 2.5: Example of rectangular domain Ω where the surface $\mathcal{S}$ separates two different physical materials. Non overlapping subdomains and meshes (left), holes as non meshed subdomains (shadowed areas) and overlapping subdomains and meshes (right).

On the one hand, the rectangular domain Ω is partitioned into two non-overlapping subdomains Ω_1, Ω_2 and the skeleton $\mathcal{S}$ of the decomposition coincides with the separation surface between two different materials such that elastic waves propagate faster in Ω_2 than in Ω_1. By adapting the mesh size h_k in each subdomain Ω_k according to the propagation velocity of the elastic waves in the subdomain, one reasonably selects $h_1 > h_2$. However, h_2 has to be small enough to follow the shape of $\mathcal{S}$ and h_1 cannot be too large otherwise some holes appear close to the surface $\mathcal{S}$. As a consequence, $h_1 \sim h_2$ in a neighbourhood of $\mathcal{S}$ resulting in a large number of unknowns to consider in both subdomains. The *mortar matching condition* allows to transfer the displacement from the set of *master* interpolation points to the set of *slave* ones and both sets of points are located on the $(d-1)$-dimensional surface $\mathcal{S}$. Note that numerical results are independent of the choice of the *master* and of the *slave* subdomains.

On the other hand, the rectangular domain Ω is partitioned into two overlapping subdomains, namely, Ω_1 which is the bottom left-handed subdomain under the dashed polyhedral surface AB and Ω_2 the top right-handed subdomain over the solid line $\mathcal{S}$. These two subdomains overlap in the region between $\mathcal{S}$ and the surface AB. In this case, we can have $h_1 > h_2$ everywhere in Ω_1 and the *mortar matching condition* allows to transfer the displacement from the set of interpolation points of Ω_1 which are contained in the d-dimensional region bounded by the polyhedral surfaces AB and CD to the set of interpolation points of Ω_2 which are on the $(d-1)$-dimensional surface $\mathcal{S}$. Indeed, in the overlapping case, the *slave* subdomain always covers the *master* one. Moreover, the *slave* subdomain is chosen as the one where the mesh best describes the surface $\mathcal{S}$ and the *master* subdomain contains the source of elastic waves. In the overlapping case, the matching condition reads:

(**MCO**) let Φ be a function that is equal to $\mathbf{v}_{\delta,k}$ in the d-dimensional elements of *master* subdomain Ω_k containing a part of $\mathcal{S}$, and zero elsewhere. Then, for each *slave* subdomain Ω_i such that $\partial\Omega_i \cap \mathcal{S} \neq \emptyset$, we require that:

$$\int_{\mathcal{S}} (\mathbf{v}_{\delta,i} - \Phi) \cdot \widehat{\Phi} = 0 \quad \forall \widehat{\Phi} \in [\Lambda_{\delta,i}(\mathcal{S})]^d \tag{2.13}$$

where $\Lambda_{\delta,i}(\mathcal{S})$ is the space of the traces over $\mathcal{S}$ of functions belonging to $X_\delta(\Omega_i)$.

2.3 Error analysis

In this section we introduce some notation and present *a priori* error estimates for the semi-discrete formulations (2.7) and (2.12) respectively. For the DG formulation (2.7), we show, in a suitable mesh-dependent energy norm, error estimates that are optimal with respect to the mesh size **h** and suboptimal with respect to the polynomial approximation degree **N**. Such results are in agreement with those proved in [98, 96, 97] for a slightly different DG method.

For the MSE formulation (2.12), in agreement with [19, 17], we prove an optimal error bound in both **h** and **N**, using the $\mathbf{H}^1$-broken norm.

For the error analysis we consider the problem (1.9) defined in $\Omega \subset \mathbb{R}^2$ with $\partial\Omega = \Gamma_N \cup \Gamma_D$. We suppose that its unique solution $\mathbf{u}$ is regular enough so that all the norms we introduce are well defined. Moreover, in the following, C will denote a positive constant that varies at each occurrence but is independent of the discretization parameters **h** and **N**. We also assume Ω to be partitioned into K non overlapping quadrilaterals $\Omega_1, ..., \Omega_K$ (i.e., $H_1 = h_1, ..., H_K = h_K$) and that $\mathcal{S}$ is subdivided in M elementary components $\gamma_1, ..., \gamma_M$ (resp. *non-mortar* edges $\gamma_1^-, ..., \gamma_M^-$) for the DGSE case (resp. for the MSE case). The more general situation can be obtained using similar arguments.

For $\Omega_k \subset \bar{\Omega}$ we denote by $\|\cdot\|_{p,\Omega_k}$ (resp. $|\cdot|_{p,\Omega_k}$) the $\mathbf{H}^p(\Omega_k)$ norm (resp. seminorm). When $\Omega_k = \Omega$ we simply write $\|\cdot\|_p = \|\cdot\|_{p,\Omega}$ (resp. $|\cdot|_p = |\cdot|_{p,\Omega}$). Since we are dealing with time dependent functions, we take the standard approach of treating these as maps from time into a Banach space X and set

$$||\mathbf{u}||_{L^p(0,t;X)} = \left(\int_0^t ||\mathbf{u}||_X^p \right)^{1/p}, \quad 0 \leq t \leq T,\ 1 \leq p < \infty,$$

with the obvious modifications when $p = \infty$.

2.3.1 Semi-discrete error estimates - DGSE method

To analyze the DG formulation (2.7) we introduce the enriched space $V(\delta) = V_\delta \oplus (\mathbf{H}^2(\Omega) \cap \mathbf{H}^1_{\Gamma_D}(\Omega))$ and define the following mesh-dependent norms on V_δ and $V(\delta)$:

$$||\mathbf{v}_\delta||_{DG} = \left(\sum_{k=1}^{K} ||\underline{\underline{\mathbf{D}}}^{1/2}\, \underline{\varepsilon}(\mathbf{v}_\delta)||^2_{0,\Omega_k} + \sum_{j=1}^{M} \eta_{\gamma_j} ||[\![\mathbf{v}_\delta]\!]||^2_{0,\gamma_j} \right)^{1/2} \quad \forall \mathbf{v}_\delta \in V_\delta, \tag{2.14}$$

and

$$|||\mathbf{v}|||_{DG} \;=\; \left(||\mathbf{v}||^2_{DG} + \sum_{k=1}^{K} \left(\frac{h_k}{N_k^2} \right)^2 |\mathbf{v}|^2_{2,\Omega_k} \right)^{1/2} \quad \forall \mathbf{v} \in V(\delta). \tag{2.15}$$

Notice that, when restricted to V_δ, these two norms are uniformly equivalent, thanks to a local inverse inequality [9]. We also set

$$\mathcal{A}_{DG}(\mathbf{u}, \mathbf{v}) \;=\; \sum_{k=1}^{K} \mathcal{A}(\mathbf{u}, \mathbf{v})_{\Omega_k} + \sum_{j=1}^{M} \mathcal{B}(\mathbf{u}, \mathbf{v})_{\gamma_j} \quad \forall \mathbf{u}, \mathbf{v} \in V(\delta). \tag{2.16}$$

Lemma 1. *There exist two positive constants M and κ such that:*

$$\mathcal{A}_{DG}(\mathbf{u}, \mathbf{v}) \;\leq\; M\, |||\mathbf{u}|||^2_{DG} |||\mathbf{v}|||^2_{DG} \quad \forall\, \mathbf{u}, \mathbf{v} \in V(\delta), \tag{2.17}$$

$$\mathcal{A}_{DG}(\mathbf{u}_\delta, \mathbf{u}_\delta) \;\geq\; \kappa \;\; ||\mathbf{u}_\delta||^2_{DG} \qquad \forall\, \mathbf{u}_\delta \in V_\delta. \tag{2.18}$$

For $\theta = 0, -1$ the last inequality holds provided that η_{γ_j} is chosen sufficiently large $\forall \gamma_j \in \mathcal{F}_I$.

Proof.

Inequality (2.17) follows from the definition of the $|||\cdot|||_{DG}$-norm (2.14) by applying the Cauchy-Schwarz and trace inequality [9]. Concerning estimate (2.18), if $\theta = -1$ (2.18) holds with $\kappa = 1$ (and is indeed an equality). If $\theta = -1$ or 0 we observe that by the trace and inverse inequalities, supposing that $N_k/N_j \approx 1$ and $h_k/h_j \approx 1$, we get $\forall \gamma_j \in \mathcal{F}_I : \gamma_j \subset \partial\overline{\Omega}_k$

$$||\{\underline{\sigma}(\mathbf{u})\}||^2_{0,\gamma_j} \leq C \frac{N_j^2}{h_j} (||\mathbf{u}||^2_{DG} + \frac{h_k^2}{N_k^4} |\mathbf{u}|^2_{2,\Omega_k}) \leq C \frac{N_j^2}{h_j} ||\mathbf{u}||^2_{DG} \quad \forall \mathbf{u} \in V_\delta,$$

see [9]. Setting $\delta^* = \min_j \{\lambda + 2\mu\}_{A,\gamma_j}$ we deduce

$$\sum_{j=1}^{M} |\, (\{\underline{\sigma}(\mathbf{u})\}, [\![\mathbf{u}]\!])_{\gamma_j}\, | \leq \frac{C}{\alpha\delta^*} ||\mathbf{u}||^2_{DG} \sum_{j=1}^{M} \eta_{\gamma_j} ||[\![\mathbf{u}]\!]||^2_{0,\gamma_j} \leq \frac{C}{\alpha\delta^*} ||\mathbf{u}||^2_{DG}.$$

Then, it holds

$$\begin{aligned}\mathcal{A}_{DG}(\mathbf{u},\mathbf{u}) &\geq ||\mathbf{u}||^2_{DG} - 2 \mid \sum_{j=1}^{M} \left(\{\underline{\sigma}(\mathbf{u})\}, [\![\mathbf{u}]\!]\right)_{\gamma_j} \mid \\ &\geq (1 - 2C/\alpha\delta^*)||\mathbf{u}||^2_{DG}.\end{aligned}$$

Choosing α sufficiently large so that $1 - 2C/\alpha\delta^*$ is bounded away from zero we have (2.18).

□

We recall from [10] the following approximation result. For any $\Omega_k \subset \Omega, \gamma_j \in \mathcal{F}_I$ and $\mathbf{u} \in \mathbf{H}^{s_k}(\Omega_k)$ there exists a sequence $\mathbf{u}_\mathcal{I} \in \mathbf{Q}_{N_k}(\Omega_k)$, for $N_k = 1, 2, ...$, such that

$$||\mathbf{u} - \mathbf{u}_\mathcal{I}||_{q,\Omega_k} \leq C\frac{h_k^{m_k-q}}{N_k^{s_k-q}}||\mathbf{u}||_{s_k,\Omega_k}, \quad 0 \leq q \leq s_k, \tag{2.19}$$

$$||\mathbf{u} - \mathbf{u}_\mathcal{I}||_{0,\gamma_j} \leq C\frac{h_k^{m_k-1/2}}{N_k^{s_k-1/2}}||\mathbf{u}||_{s_k,\Omega_k}, \quad s_k > 1/2, \tag{2.20}$$

where $m_k = \min(N_k + 1, s_k)$ and C is a positive constant independent of h_k and N_k. For further use we also introduce the projection operator $\Pi : V \longrightarrow V_\delta$ such that

$$\mathcal{A}_{DG}(\Pi\mathbf{u}, \mathbf{v}) = \mathcal{A}_{DG}(\mathbf{u}, \mathbf{v}) \quad \forall\, \mathbf{v} \in V_\delta. \tag{2.21}$$

Notice that $\Pi\mathbf{u}$ is well defined thanks to Lemma 1. Moreover, since $\Pi\mathbf{u}$ is a projection, we clearly have

$$\begin{aligned}|||\mathbf{u} - \Pi\mathbf{u}|||^2_{DG} &\leq 2|||\mathbf{u} - \mathbf{u}_\mathcal{I}|||^2_{DG} + 2|||\mathbf{u}_\mathcal{I} - \Pi\mathbf{u}|||^2_{DG} \\ &\leq 2|||\mathbf{u} - \mathbf{u}_\mathcal{I}|||^2_{DG} + \frac{2M}{\kappa}|||\mathbf{u}_\mathcal{I} - \mathbf{u}|||^2_{DG}|||\mathbf{u} - \Pi\mathbf{u}|||^2_{DG} \\ &\leq 2|||\mathbf{u} - \mathbf{u}_\mathcal{I}|||^2_{DG} + \frac{M}{\kappa\epsilon}|||\mathbf{u} - \mathbf{u}_\mathcal{I}|||^2_{DG} + \frac{M\epsilon}{\kappa}|||\mathbf{u} - \Pi\mathbf{u}|||^2_{DG},\end{aligned}$$

for any positive constant ϵ. Therefore for $\epsilon = \kappa/2M$ we have

$$|||\mathbf{u} - \Pi\mathbf{u}|||^2_{DG} \leq C|||\mathbf{u} - \mathbf{u}_\mathcal{I}|||^2_{DG}.$$

Finally, by using (2.19)-(2.20), it is easy to see that $\Pi\mathbf{u}$ satisfies the following approximation property.

Lemma 2. *There exists a positive constant C such that*

$$|||\mathbf{u}-\Pi\mathbf{u}|||_{DG} \leq C\left(\sum_{k=1}^{K}\frac{h_k^{2m_k-2}}{N_k^{2s_k-3}}||\mathbf{u}||^2_{s_k,\Omega_k}\right)^{1/2}. \tag{2.22}$$

Moreover, it holds

$$||\mathbf{u}-\Pi\mathbf{u}||_0 \leq C\left(\sum_{k=1}^{K}\frac{h_k^{2m_k}}{N_k^{2s_k-2}}||\mathbf{u}||^2_{s_k,\Omega_k}\right)^{1/2}. \tag{2.23}$$

where $N_k \geq 1$ and $m_k = \min(N_k+1, s_k)$.

Proof. We start showing inequality (2.22). Let $\boldsymbol{\chi} = \mathbf{u} - \mathbf{u}_{\mathcal{I}}$. By using the trace and inverse inequalities and the interpolation estimates (2.19)-(2.20) it follows

$$\begin{aligned}
|||\boldsymbol{\chi}|||^2_{DG} &= ||\boldsymbol{\chi}||^2_{DG} + \sum_{k=1}^{K}\left(\frac{h_k}{N_k^2}\right)^2|\boldsymbol{\chi}|^2_{2,\Omega_k} \\
&\leq C\sum_{k=1}^{K}||\nabla\boldsymbol{\chi}||^2_{0,\Omega_k} + \sum_{j=1}^{M}\eta_{\gamma_j}||[\![\boldsymbol{\chi}]\!]||^2_{0,\gamma_j} + \sum_{k=1}^{K}\left(\frac{h_k}{N_k^2}\right)^2|\boldsymbol{\chi}|^2_{2,\Omega_k} \\
&\leq C\left[\sum_{k=1}^{K}\frac{h_k^{m_k-2}}{N_k^{s_k-2}}||\mathbf{u}||^2_{s_k,\Omega_k} + \sum_{k=1}^{K}\frac{h_k^{2m_k-2}}{N_k^{2s_k-3}}||\mathbf{u}||^2_{s_k,\Omega_k}\sum_{k=1}^{K}\frac{h_k^{2m_k-2}}{N_k^{2s_k}}||\mathbf{u}||^2_{s_k,\Omega_k}\right] \\
&\leq C\sum_{k=1}^{K}\frac{h_k^{2m_k-2}}{N_k^{2s_k-3}}||\mathbf{u}||^2_{s_k,\Omega_k},
\end{aligned}$$

where $N_k \geq 1$, $m_k = \min(N_k+1, s_k)$. Next, we show (2.23). We set $\boldsymbol{\chi} = \Pi\mathbf{u} - \mathbf{u}$. We assume that Ω is sufficiently smooth so that the solution of the dual problem

$$\begin{cases} -\nabla\cdot\underline{\sigma}(\boldsymbol{\Phi}) = \boldsymbol{\chi}, & \text{in } \Omega, \\ \boldsymbol{\Phi} = \mathbf{0}, & \text{on } \partial\Omega, \end{cases}$$

belongs to $\mathbf{H}^2(\Omega)$, with continuous dependence on $\boldsymbol{\chi}$, i.e., $\exists C > 0$:

$$||\boldsymbol{\Phi}||_2 \leq C||\boldsymbol{\chi}||_0. \tag{2.24}$$

Integrating by parts element-wise yields:

$$||\boldsymbol{\chi}||^2_0 = (-\nabla\cdot\underline{\sigma}(\boldsymbol{\Phi}), \boldsymbol{\chi})_\Omega = \sum_{k=1}^{K}\left[(\underline{\sigma}(\boldsymbol{\Phi}), \nabla\boldsymbol{\chi})_{\Omega_k} - (\underline{\sigma}(\boldsymbol{\Phi})\cdot\mathbf{n}, \boldsymbol{\chi})_{\partial\Omega_k\setminus\partial\Omega}\right].$$

Thanks to the symmetry of $\underline{\sigma}$ and (2.6) we obtain

$$||\boldsymbol{\chi}||_0^2 = \sum_{k=1}^{K} (\underline{\sigma}(\boldsymbol{\Phi}) : \underline{\varepsilon}(\boldsymbol{\chi}))_{\Omega_k} - \sum_{j=1}^{M} (\{\underline{\sigma}(\boldsymbol{\Phi})\}, [\![\boldsymbol{\chi}]\!])_{\gamma_j},$$

since thanks to the regularity of $\boldsymbol{\Phi}$, $[\![\underline{\sigma}(\boldsymbol{\Phi})]\!] = \mathbf{0}$ on each γ_j. By subtracting the orthogonality equation for any $\boldsymbol{\Phi}^* \in V_\delta : \mathcal{A}_{DG}(\boldsymbol{\chi}, \boldsymbol{\Phi}^*) = \mathbf{0}$, using the symmetry of $\underline{\sigma}$ and the regularity of $\boldsymbol{\Phi}$ we have

$$\begin{aligned} ||\boldsymbol{\chi}||_0^2 &= \sum_{k=1}^{K} (\underline{\sigma}(\boldsymbol{\Phi} - \boldsymbol{\Phi}^*) : \underline{\varepsilon}(\boldsymbol{\chi}))_{\Omega_k} - (1+\theta) \sum_{j=1}^{M} (\{\underline{\sigma}(\boldsymbol{\Phi})\}, [\![\boldsymbol{\chi}]\!])_{\gamma_j} \\ &+\theta \sum_{j=1}^{M} (\{\underline{\sigma}(\boldsymbol{\Phi} - \boldsymbol{\Phi}^*)\}, [\![\boldsymbol{\chi}]\!])_{\gamma_j} + \sum_{j=1}^{M} (\{\underline{\sigma}(\boldsymbol{\chi})\}, [\![\boldsymbol{\Phi} - \boldsymbol{\Phi}^*]\!])_{\gamma_j} \\ &- \sum_{j=1}^{M} \eta_{\gamma_j} ([\![\underline{\sigma}(\boldsymbol{\chi})]\!], [\![\boldsymbol{\Phi} - \boldsymbol{\Phi}^*]\!])_{\gamma_j}. \end{aligned}$$

By using the trace and inverse inequalities, the estimate (2.24) and the approximation property (2.22) we have

$$||\boldsymbol{\chi}||_{0,\Omega_k}^2 \leq C \frac{h_k}{N_k^{1/2}} ||\boldsymbol{\Phi}||_{2,\Omega_k} |||\boldsymbol{\chi}|||_{DG} \leq C \frac{h_k}{N_k^{1/2}} ||\boldsymbol{\chi}||_{0,\Omega_k} |||\boldsymbol{\chi}|||_{DG}.$$

The inequality (2.23) follows now using (2.22).

□

Let now introduce the bilinear form

$$\mathcal{A}_{DG}^*(\mathbf{u}, \mathbf{v}) = \mathcal{A}_{DG}(\mathbf{u}, \mathbf{v}) + \sum_{j=1}^{M} \eta_{\gamma_j} ([\![\partial_t \mathbf{u}]\!], [\![\mathbf{v}]\!])_{\gamma_j} \quad \forall \mathbf{u}, \mathbf{v} \in V(\delta). \tag{2.25}$$

Notice that in the formulation (2.25) introduced in [98, 97], the presence of the (consistent) penalty term $([\![\partial_t \mathbf{u}]\!], [\![\mathbf{v}]\!])_{\gamma_j}$ has not a clear physical meaning, but it provides an auxiliary aid to to prove optimal error estimate in $\mathbf{h}$ and suboptimal in $\mathbf{N}$ for the DG scheme. In the sequel we will use the results in [98, 97] to complete the analysis. Now, for all $0 \leq t \leq T$ we set $\mathbf{u}_{DG} = \mathbf{u}_{DG}(t)$ and $\mathbf{u}_{DG}^* = \mathbf{u}_{DG}^*(t)$ the unique solutions in V_δ of the problems

$$\mathrm{d}_{tt} (\rho \mathbf{u}_{DG}, \mathbf{v}) + \mathcal{A}_{DG}(\mathbf{u}_{DG}, \mathbf{v}) = \mathcal{L}(\mathbf{v}), \quad \forall \mathbf{v} \in V_\delta, \tag{2.26}$$

$$\mathrm{d}_{tt} (\rho \mathbf{u}_{DG}^*, \mathbf{v}) + \mathcal{A}_{DG}^*(\mathbf{u}_{DG}^*, \mathbf{v}) = \mathcal{L}(\mathbf{v}), \quad \forall \mathbf{v} \in V_\delta, \tag{2.27}$$

respectively. From Lemma 1 and standard techniques, follows that the variational problem in (2.26) is well posed. The same is true for (2.27). From the results given in [98, 97], the estimates (2.22) and (2.23), we have

Lemma 3. *There exists a positive constant C such that for all $t \in [0,T]$*

$$|||(\mathbf{u}-\mathbf{u}^*_{DG})(t)|||_{DG} \leq C\left\{\sum_{k=1}^{K}\frac{h_k^{2m_k-2}}{N_k^{2s_k-3}}||\mathbf{u}||^2_{H^2(0,t;\mathbf{H}^{s_k}(\Omega_k))}\right\}^{1/2}, \tag{2.28}$$

where $N_k \geq 1$ and $m_k = \min(N_k+1, s_k)$.

The proof of Lemma 3 in given in [98, 97]. We report it for the sake of clarity. **Proof.** Let $\Pi\mathbf{u}$ be defined as in (2.21). By the triangle inequality we have

$$|||\mathbf{u}-\mathbf{u}^*_{DG}|||_{DG} \leq |||\mathbf{u}-\Pi\mathbf{u}|||_{DG} + |||\Pi\mathbf{u}-\mathbf{u}^*_{DG}|||_{DG} = T_1 + T_2.$$

Estimate (2.22) yields

$$|T_1| \leq C\left(\sum_{k=1}^{K}\frac{h_k^{2m_k-2}}{N_k^{2s_k-3}}||\mathbf{u}||^2_{s_k,\Omega_k}\right)^{1/2}. \tag{2.29}$$

For the term T_2 we set $\boldsymbol{\chi} = \mathbf{u}^*_{DG} - \Pi\mathbf{u}$ and $\boldsymbol{\xi} = \mathbf{u} - \Pi\mathbf{u}$. We have for $t > 0$

$$(\rho\boldsymbol{\chi}_{tt}, \mathbf{v}) + \mathcal{A}^*_{DG}(\boldsymbol{\chi}, \mathbf{v}) = (\rho\boldsymbol{\xi}_{tt}, \mathbf{v}) + \mathcal{A}^*_{DG}(\boldsymbol{\xi}, \mathbf{v}) \quad \forall\, \mathbf{v} \in L^2(0,T;V_\delta).$$

Denoting by $J(\mathbf{u},\mathbf{v}) = \sum_{j=1}^{M}\eta_{\gamma_j}\left([\![\mathbf{u}]\!],[\![\mathbf{v}]\!]\right)_{\gamma_j}$ and recalling (2.21), the above equation reduces to

$$(\rho\boldsymbol{\chi}_{tt}, \mathbf{v}) + \mathcal{A}^*_{DG}(\boldsymbol{\chi}, \mathbf{v}) = (\rho\boldsymbol{\xi}_{tt}, \mathbf{v}) + J(\boldsymbol{\xi}_t, \mathbf{v}) \quad \forall\, \mathbf{v} \in L^2(0,T;V_\delta). \tag{2.30}$$

By choosing $\mathbf{v} = \boldsymbol{\chi}_t$, the error equation (2.30) becomes

$$(\rho\boldsymbol{\chi}_{tt}, \boldsymbol{\chi}_t) + \mathcal{A}_{DG}(\boldsymbol{\chi}, \boldsymbol{\chi}_t) + J(\boldsymbol{\chi}_t, \boldsymbol{\chi}_t) = (\rho\boldsymbol{\xi}_{tt}, \boldsymbol{\chi}_t) + J(\boldsymbol{\xi}_t, \boldsymbol{\chi}_t).$$

We can rewrite the above equation as follows

$$\begin{aligned}\frac{1}{2}d_t||\rho^{1/2}\boldsymbol{\chi}_t||_0^2 + \sum_{k=1}^{K}(\underline{\sigma}(\boldsymbol{\chi}), \underline{\varepsilon}(\boldsymbol{\chi}_t))_{\Omega_k} + J(\boldsymbol{\chi},\boldsymbol{\chi}_t) + J(\boldsymbol{\chi}_t,\boldsymbol{\chi}_t) &= (\rho\boldsymbol{\xi}_{tt},\boldsymbol{\chi}_t)\\ + J(\boldsymbol{\xi}_t,\boldsymbol{\chi}_t) + \sum_{j=1}^{M}(\{\underline{\sigma}(\boldsymbol{\chi})\}, [\![\boldsymbol{\chi}_t]\!])_{\gamma_j} - \theta\sum_{j=1}^{M}([\![\boldsymbol{\chi}]\!], \{\underline{\sigma}(\boldsymbol{\chi}_t)\})_{\gamma_j}&\end{aligned}$$

which is equivalent to

$$\frac{1}{2}d_t||\rho^{1/2}\boldsymbol{\chi}_t||_0^2+\frac{1}{2}d_t||\boldsymbol{\chi}||_{DG}^2+J(\boldsymbol{\chi}_t,\boldsymbol{\chi}_t)=(\rho\boldsymbol{\xi}_{tt},\boldsymbol{\chi}_t)+J(\boldsymbol{\xi}_t,\boldsymbol{\chi}_t)$$
$$+\sum_{j=1}^{M}(\{\underline{\sigma}(\boldsymbol{\chi})\},[\![\boldsymbol{\chi}_t]\!])_{\gamma_j}-\theta\sum_{j=1}^{M}([\![\boldsymbol{\chi}]\!],\{\underline{\sigma}(\boldsymbol{\chi}_t)\})_{\gamma_j}\,. \tag{2.31}$$

Therefore, integrating (2.31) in time between 0 and t and noting that by definition $\boldsymbol{\chi}(0)=\mathbf{0}$, we obtain:

$$\frac{1}{2}||\rho^{1/2}\boldsymbol{\chi}_t(t)||_0^2+\frac{1}{2}||\boldsymbol{\chi}(t)||_{DG}^2+\int_0^t J(\boldsymbol{\chi}_t,\boldsymbol{\chi}_t)=\int_0^t(\rho\boldsymbol{\xi}_{tt},\boldsymbol{\chi}_t)+\int_0^t J(\boldsymbol{\xi}_t,\boldsymbol{\chi}_t)$$
$$-\theta\sum_{j=1}^{M}([\![\boldsymbol{\chi}]\!],\{\underline{\sigma}(\boldsymbol{\chi})\})_{\gamma_j}(t)+(1+\theta)\int_0^t\sum_{j=1}^{M}(\{\underline{\sigma}(\boldsymbol{\chi})\},[\![\boldsymbol{\chi}_t]\!])_{\gamma_j}$$
$$+\frac{1}{2}||\rho^{1/2}\boldsymbol{\chi}_t(0)||_0^2. \tag{2.32}$$

We now bound each of the terms on the right-hand side of (2.32) that involves integrals on γ_j, using the trace inequality:

$$\begin{aligned}|(1+\theta)\int_0^t\sum_{j=1}^{M}(\{\underline{\sigma}(\boldsymbol{\chi})\},[\![\boldsymbol{\chi}_t]\!])_{\gamma_j}| &\leq \frac{C}{2\epsilon}\int_0^t||\boldsymbol{\chi}||_{DG}^2+\frac{\epsilon}{2}\int_0^t J(\boldsymbol{\chi}_t,\boldsymbol{\chi}_t),\\ |\theta\sum_{j=1}^{M}([\![\boldsymbol{\chi}]\!],\{\underline{\sigma}(\boldsymbol{\chi})\})_{\gamma_j}| &\leq \frac{\hat{\epsilon}}{2}||\boldsymbol{\chi}||_{DG}^2+\frac{C}{2\hat{\epsilon}\alpha}J(\boldsymbol{\chi},\boldsymbol{\chi}),\end{aligned}$$

$\forall\epsilon,\hat{\epsilon}>0$. We also have

$$\int_0^t(\rho\boldsymbol{\xi}_{tt},\boldsymbol{\chi}_t) \leq \int_0^t\frac{1}{2}||\rho^{1/2}\boldsymbol{\chi}_t||_0^2+\int_0^t\frac{1}{2}||\rho^{1/2}\boldsymbol{\xi}_{tt}||_0^2,$$

and

$$\int_0^t J(\boldsymbol{\xi}_t,\boldsymbol{\chi}_t)\leq\frac{C}{2\epsilon}\int_0^t J(\boldsymbol{\xi}_t,\boldsymbol{\xi}_t)+\frac{\epsilon}{2}\int_0^t J(\boldsymbol{\chi}_t,\boldsymbol{\chi}_t).$$

Then, equation (2.32) reduces to

$$\frac{1}{2}||\rho^{1/2}\boldsymbol{\chi}_t(t)||_0^2+(\frac{1}{2}-\frac{\hat{\epsilon}}{2})||\boldsymbol{\chi}(t)||_{DG}^2+(1-\epsilon)\int_0^t J(\boldsymbol{\chi}_t,\boldsymbol{\chi}_t)-\frac{C}{2\hat{\epsilon}\alpha}J(\boldsymbol{\chi},\boldsymbol{\chi})$$
$$\leq\frac{1}{2}||\rho^{1/2}\boldsymbol{\chi}_t(0)||_0^2+\frac{C}{2\epsilon}\int_0^t||\boldsymbol{\chi}||_{DG}^2+\int_0^t\frac{1}{2}||\rho^{1/2}\boldsymbol{\chi}_t||_0^2$$
$$+\int_0^t\frac{1}{2}||\rho^{1/2}\boldsymbol{\xi}_{tt}||_0^2+\frac{C}{2\epsilon}\int_0^t J(\boldsymbol{\xi}_t,\boldsymbol{\xi}_t). \tag{2.33}$$

Taking $\epsilon = 1/4$, $\hat{\epsilon} = 1/2$ and $\alpha \geq 4C$ we have

$$||\rho^{1/2}\boldsymbol{\chi}_t(t)||_0^2 + ||\boldsymbol{\chi}(t)||_{DG}^2 \leq C\left[\int_0^t \left(||\rho^{1/2}\boldsymbol{\chi}_t||_0^2 + ||\boldsymbol{\chi}||_{DG}^2\right) + ||\rho^{1/2}\boldsymbol{\chi}_t(0)||_0^2 + \int_0^t ||\rho^{1/2}\boldsymbol{\xi}_{tt}||_0^2 + \int_0^t J(\boldsymbol{\xi}_t, \boldsymbol{\xi}_t)\right].$$

By applying the Gronwall's lemma [92] we obtain

$$\begin{aligned} ||\rho^{1/2}\boldsymbol{\chi}_t(t)||_0^2 + ||\boldsymbol{\chi}(t)||_{DG}^2 &\leq C\left[||\rho^{1/2}\boldsymbol{\chi}_t(0)||_0^2 \right. \\ &\left. + \int_0^t ||\rho^{1/2}\boldsymbol{\xi}_{tt}||_0^2 + \int_0^t J(\boldsymbol{\xi}_t, \boldsymbol{\xi}_t)\right]. \end{aligned}$$

By the approximation property (2.22) it holds:

$$\begin{aligned} ||\rho^{1/2}\boldsymbol{\chi}_t(0)||_0^2 &\leq C\sum_{k=1}^{K} \frac{h_k^{2m_k}}{N_k^{2s_k}} ||\mathbf{u}_t||^2_{L^2(0,t;\mathbf{H}^{s_k}(\Omega_k))} \\ \int_0^t ||\rho^{1/2}\boldsymbol{\xi}_{tt}||_0^2 &\leq C\sum_{k=1}^{K} \frac{h_k^{2m_k-2}}{N_k^{2s_k-3}} ||\mathbf{u}_{tt}||^2_{L^2(0,t;\mathbf{H}^{s_k}(\Omega_k))} \\ \int_0^t J(\boldsymbol{\xi}_t, \boldsymbol{\xi}_t) &\leq C\sum_{k=1}^{K} \frac{h_k^{2m_k-2}}{N_k^{2s_k-3}} ||\mathbf{u}_t||^2_{L^2(0,t;\mathbf{H}^{s_k}(\Omega_k))} \end{aligned}$$

Therefore

$$|T_2| \leq C\left(\sum_{k=1}^{K} \frac{h_k^{2m_k-2}}{N_k^{2s_k-3}} \left[||\mathbf{u}_t||^2_{L^2(0,t;\mathbf{H}^{s_k}(\Omega_k))} + ||\mathbf{u}_{tt}||^2_{L^2(0,t;\mathbf{H}^{s_k}(\Omega_k))}\right]\right)^{1/2}. \tag{2.34}$$

Then, (2.28) follows by combining the estimate (2.29) and (2.34) and taking the supremum over all $t \in [0, T]$.

□

For $\mathbf{u}_{DG}$ we have the following convergence result.

Theorem 1. *Suppose that $\mathbf{u}_{DG} \in H^2(0,T;\mathbf{H}^{s_k}(\Omega_k))$ for any $\Omega_k \subset \Omega$. There exists a positive constant C such that*

$$\sup_{t\in[0,T]} |||(\mathbf{u} - \mathbf{u}_{DG})(t)|||_{DG} \leq C\left\{\sum_{k=1}^{K} \frac{h_k^{2m_k-2}}{N_k^{2s_k-3}} ||\mathbf{u}||^2_{H^2(0,T;\mathbf{H}^{s_k}(\Omega_k))}\right\}^{1/2}, \tag{2.35}$$

where $N_k \geq 1$ and $m_k = \min(N_k + 1, s_k)$.

Proof. Let $\mathbf{u}^*_{DG} \in V_\delta$ be the solution of (2.27). From Lemma 1 we can show that

$$|||(\mathbf{u}_{DG} - \mathbf{u}^*_{DG})(t)|||_{DG} \leq C|||(\mathbf{u} - \mathbf{u}^*_{DG})(t)|||_{DG} \quad \forall\, t \in [0,T]. \tag{2.36}$$

In fact, it holds

$$\begin{aligned} |||\mathbf{u}_{DG} - \mathbf{u}^*_{DG}|||^2_{DG} &\leq C||\mathbf{u}_{DG} - \mathbf{u}^*_{DG}||^2_{DG} \\ &\leq \frac{C}{\kappa}\mathcal{A}_{DG}(\mathbf{u}_{DG} - \mathbf{u}^*_{DG}, \mathbf{u}_{DG} - \mathbf{u}^*_{DG}) \\ &= \frac{C}{\kappa}\mathcal{A}_{DG}(\mathbf{u} - \mathbf{u}^*_{DG}, \mathbf{u}_{DG} - \mathbf{u}^*_{DG}) \\ &\leq \frac{CM}{\kappa}|||\mathbf{u} - \mathbf{u}^*_{DG}|||_{DG}|||\mathbf{u}_{DG} - \mathbf{u}^*_{DG}|||_{DG}. \end{aligned}$$

Now, by the triangle inequality,

$$|||(\mathbf{u} - \mathbf{u}_{DG})(t)|||_{DG} \leq |||(\mathbf{u} - \mathbf{u}^*_{DG})(t)|||_{DG} + |||(\mathbf{u}_{DG} - \mathbf{u}^*_{DG})(t)|||_{DG},$$

then, the desired result is obtained using (2.28)-(2.36) and taking the supremum over all $t \in [0,T]$.

□

2.3.2 Semi-discrete error estimates - MSE method

We now move to the error analysis for the MSE method semi-discretization (2.12). Let $\mathbf{H}^{1/2}(\partial\Omega_k)$ be the trace space of $\mathbf{H}^1(\Omega_k)$ on $\partial\Omega_k$, endowed with the norm

$$||\mathbf{u}||_{1/2,\partial\Omega_k} = \left(||\mathbf{u}||^2_{0,\Omega_k} + |\mathbf{u}|^2_{1/2,\partial\Omega_k}\right)^{1/2},$$

with $|\mathbf{u}|_{1/2,\partial\Omega_k} = \min_{\mathbf{v}_{|\partial\Omega_k}=\mathbf{u}} |\mathbf{v}|_{1,\Omega_k}$, and for any $\gamma \subset \partial\Omega_k$, define the space $\mathbf{H}^{1/2}_{00}(\gamma)$ as

$$\mathbf{H}^{1/2}_{00}(\gamma) = \{\mathbf{u} \in \mathbf{H}^{1/2}(\gamma) : \widehat{\mathbf{u}} \in \mathbf{H}^{1/2}(\partial\Omega_k)\},$$

where $\widehat{\mathbf{u}}$ is the extension by zero of $\mathbf{u}$ to $\partial\Omega_k$, see [1]. Moreover we introduce the mesh-dependent norm

$$||\mathbf{u}||_* = \left(\sum_{k=1}^{K} ||\mathbf{u}||^2_{1,\Omega_k}\right)^{1/2} \qquad \forall \mathbf{u} \in V(\delta),$$

and we define the bilinear form $\mathcal{A}_M(\cdot,\cdot)$ by

$$\mathcal{A}_M(\mathbf{u},\mathbf{v}) = \sum_{k=1}^{K} \mathcal{A}(\mathbf{u},\mathbf{v})_{\Omega_k} \quad \forall \mathbf{u},\mathbf{v} \in V(\delta).$$

We have the following properties for $\mathcal{A}_M(\cdot,\cdot)$.

Lemma 4. *There exists two positive constants M and κ, independent of $\boldsymbol{h}$ and $\boldsymbol{N}$, such that*

$$\mathcal{A}_M(\mathbf{u},\mathbf{v}) \leq M||\mathbf{u}||_*||\mathbf{v}||_* \quad \forall \mathbf{u},\mathbf{v} \in V(\delta), \tag{2.37}$$

$$\mathcal{A}_M(\mathbf{u}_\delta,\mathbf{u}_\delta) \geq \kappa||\mathbf{u}_\delta||_*^2 \quad \forall \mathbf{u}_\delta \in V_\delta^{mortar}. \tag{2.38}$$

Proof.
Inequality (2.37) is a direct consequence of the Cauchy-Schwarz inequality, while (2.38) is easily obtained using the generalized Korn's first inequality and the Poincaré inequality for $\mathbf{u}_\delta \in V_\delta^{mortar}$, see [23].

□

The crucial point of the MSE method error analysis relies on the construction of a modified elliptic projection operator Π from V to V_δ^{mortar} satisfying optimal error estimate with respect to both $\mathbf{h}$ and $\mathbf{N}$. In order to define it we need some preliminary approximation results that we recall from [19, 21, 17].
For any *non-mortar* side γ_n^- of $\mathcal{S}$ such that $\gamma_n^- = \gamma_{n(k)}^- \subset \partial\overline{\Omega}_k$, we define the projection operator

$$\boldsymbol{\pi}_n : [L^2(\gamma_n^-)]^2 \longrightarrow [\Lambda_\delta(\gamma_n^-)]^2 \cap \mathbf{H}_0^1(\gamma_n^-),$$

by

$$\int_{\gamma_n^-} (\mathbf{v} - \boldsymbol{\pi}_n\mathbf{v}) \cdot \widehat{\Phi} = 0 \quad \forall \widehat{\Phi} \in [\widehat{\Lambda}_\delta(\gamma_n^-)]^2. \tag{2.39}$$

Then, see [21], for any non-negative real numbers s and q it holds

$$||\mathbf{v} - \boldsymbol{\pi}_n\mathbf{v}||_{-q,\gamma_n^-} \leq C\left(\frac{h_k}{N_k}\right)^{q+s} ||\mathbf{v}||_{s,\gamma_n^-} \quad \forall\, \mathbf{v} \in \mathbf{H}^s(\gamma_n^-).$$

We now define a lifting operator $\mathcal{R}_n : [\Lambda_\delta(\gamma_n^-)]^2 \cap \mathbf{H}_0^1(\gamma_n^-) \longrightarrow [X_\delta(\Omega_k)]^2$ such that $\mathcal{R}_n\mathbf{v} = \mathbf{v}$ on γ_n^-, $\mathcal{R}_n$ vanishes on each side of Ω_k except on γ_n^- and satisfies (see [22])

$$||\mathcal{R}_n\mathbf{v}||_{1,\Omega_k} \leq C||\mathbf{v}||_{1/2,\gamma_n^-} \quad \forall \mathbf{v} \in [\Lambda_\delta(\gamma_n^-)]^2 \cap \mathbf{H}_0^1(\gamma_n^-).$$

Moreover we introduce the operator $\mathcal{P} : V \longrightarrow V_\delta^{mortar}$ defined by

$$\mathcal{P}\mathbf{u} = \sum_{k=1}^{K} \left(\mathbf{u}_{\mathcal{I}_{|\Omega_k}} + \sum_{\Gamma_k^\ell \subset \partial\overline{\Omega}_k} \boldsymbol{\varrho}_k^\ell \right), \tag{2.40}$$

where $\mathbf{u}_{\mathcal{I}}$ satisfies (2.19)-(2.20) and

$$\boldsymbol{\varrho}_k^l = \begin{cases} \mathbf{0}, & \text{if } \Gamma_k^\ell \text{ is a } \textit{mortar} \text{ edge,} \\ \mathcal{R}_n[\boldsymbol{\pi}_n(\mathbf{u}-\mathbf{u}_{\mathcal{I}})_{|_{\gamma_n^-}}], & \text{if } \gamma_n^- = \Gamma_{k(n)}^{\ell(n)} \text{ is a } \textit{non-mortar} \text{ edge.} \end{cases}$$

Finally we state the following approximation result (see [19] for the proof).

Lemma 5. *There exists a positive constant C, independent of $\boldsymbol{h}$ and $\boldsymbol{N}$ such that for any $\mathbf{v} \in \mathbf{H}^{s_k}(\Omega_k)$ it holds*

$$||\mathbf{v}-\mathcal{P}\mathbf{v}||_{1,\Omega_k} \leq C\frac{h_k^{m_k-1}}{N_k^{s_k-1}}||\mathbf{v}||_{s_k,\Omega_k}, \quad s_k > 3/2, \tag{2.41}$$

with $N_k \geq 1$ and $m_k = \min(N_k+1, s_k)$.

We now define the modified elliptic projection $\Pi : V \to V_\delta^{mortar}$ as:

$$\mathcal{A}_M(\mathbf{u}-\Pi\mathbf{u}, \mathbf{v}) - \sum_{n=1}^{M} (\underline{\sigma}(\mathbf{u}), [\![\mathbf{v}]\!])_{\gamma_n^-} = \mathbf{0} \quad \forall\, \mathbf{v} \in V_\delta^{mortar}. \tag{2.42}$$

Note that $\Pi\mathbf{u} \in V_\delta^{mortar}$ is well defined since the bilinear form $\mathcal{A}_M(\cdot,\cdot)$ satisfies the coercive property (2.38).

Lemma 6. *There exists a positive constant C such that*

$$||\mathbf{u}-\Pi\mathbf{u}||_* \leq C\left(\sum_{k=1}^{K}\frac{h_k^{2m_k-2}}{N_k^{2s_k-2}}||\mathbf{u}||_{s_k,\Omega_k}^2\right)^{1/2} \qquad s_k > 3/2. \tag{2.43}$$

with $N_k \geq 1$ and $m_k = \min(N_k+1, s_k)$. Moreover it holds

$$||\mathbf{u}-\Pi\mathbf{u}||_0 \leq C\left(\sum_{k=1}^{K}\frac{h_k^{2m_k}}{N_k^{2s_k}}||\mathbf{u}||_{s_k,\Omega_k}^2\right)^{1/2}. \tag{2.44}$$

Proof. Using the projection operator introduced in (2.40) we rewrite the equation (2.42) obtaining

$$\mathcal{A}_M(\mathcal{P}\mathbf{u}-\Pi\mathbf{u}, \boldsymbol{\chi}) = -\mathcal{A}_M(\mathbf{u}-\mathcal{P}\mathbf{u}, \chi) + \sum_{n=1}^{M} (\underline{\sigma}(\mathbf{u}), [\![\boldsymbol{\chi}]\!])_{\gamma_n^-} = \mathbf{0} \quad \forall\, \boldsymbol{\chi} \in V_\delta^{mortar}.$$

Choosing $\boldsymbol{\chi} = \mathcal{P}\mathbf{u}-\Pi\mathbf{u}$ and using the boundedness and coercive property (2.37) and (2.38) respectively, we have

$$\kappa||\boldsymbol{\chi}||_*^2 \leq M||\mathbf{u}-\mathcal{P}\mathbf{u}||_*||\boldsymbol{\chi}||_* + \sum_{n=1}^{M} |\,(\underline{\sigma}(\mathbf{u}), [\![\boldsymbol{\chi}]\!])_{\gamma_n^-}\,|.$$

Now, from [21, Proposition 3.1] we have

$$\sum_n |\,(\underline{\sigma}(\mathbf{u}) : [\![\boldsymbol{\chi}]\!])_{\gamma_n^-}\,| \leq C \sum_{k=1}^{K} \frac{h_k^{m_k-1}}{N_k^{s_k-1}} ||\mathbf{u}||_{s_k,\Omega_k} ||\boldsymbol{\chi}||_*. \tag{2.45}$$

Therefore,

$$||\boldsymbol{\chi}||_* \leq C \left[||\mathbf{u} - \mathcal{P}\mathbf{u}||_* + \sum_{k=1}^{K} \frac{h_k^{m_k-1}}{N_k^{s_k-1}} ||\mathbf{u}||_{s_k,\Omega_k} \right].$$

(2.43) is obtained combining the above inequality with the estimate (2.41) and using the triangle inequality

$$||\mathbf{u} - \Pi\mathbf{u}||_* \leq ||\mathbf{u} - \mathcal{P}\mathbf{u}||_* + ||\mathcal{P}\mathbf{u} - \Pi\mathbf{u}||_*.$$

To prove (2.44) we set $\boldsymbol{\chi} = \Pi\mathbf{u} - \mathbf{u}$. By duality arguments (see proof of Lemma 2) and integrating by parts on each element yields:

$$||\boldsymbol{\chi}||_0^2 = (-\nabla \cdot \underline{\sigma}(\boldsymbol{\Phi}), \boldsymbol{\chi})_\Omega = \mathcal{A}_M(\Phi, \boldsymbol{\chi}) - \sum_{n=1}^{M} (\underline{\sigma}(\boldsymbol{\Phi}), [\![\boldsymbol{\chi}]\!])_{\gamma_n^-},$$

or equivalently,

$$||\boldsymbol{\chi}||_0^2 = \mathcal{A}_M(\boldsymbol{\Phi} - \mathcal{P}\boldsymbol{\Phi}, \boldsymbol{\chi}) + \mathcal{A}_M(\mathcal{P}\boldsymbol{\Phi}, \boldsymbol{\chi}) - \sum_{n=1}^{M} (\underline{\sigma}(\boldsymbol{\Phi}), [\![\boldsymbol{\chi}]\!])_{\gamma_n^-}.$$

Using the symmetry of $\underline{\sigma}$ and the properties (2.42) and (2.39) we have

$$\begin{aligned} ||\boldsymbol{\chi}||_0^2 = \mathcal{A}_M(\boldsymbol{\Phi} - \mathcal{P}\boldsymbol{\Phi}, \boldsymbol{\chi}) &+ \sum_n (\underline{\sigma}(\mathbf{u}), [\![\mathcal{P}\boldsymbol{\Phi}]\!])_{\gamma_n^-} \\ &- \sum_{n=1}^{M} ((\underline{\sigma}(\boldsymbol{\Phi}) - \boldsymbol{\pi}_n \underline{\sigma}(\boldsymbol{\Phi})), [\![\boldsymbol{\chi}]\!])_{\gamma_n^-}. \end{aligned}$$

We now bound the three terms on the right-hand side of the above equation. Using (2.37) we have

$$|\mathcal{A}_M(\boldsymbol{\Phi} - \mathcal{P}\boldsymbol{\Phi}, \boldsymbol{\chi})_{\Omega_k}| \leq C \frac{h_k}{N_k} ||\boldsymbol{\chi}||_0 ||\boldsymbol{\chi}||_{1,\Omega_k}$$

for any Ω_k, $k = 1, ..., K$. By trace inequality we obtain

$$\begin{aligned} |\,(\underline{\sigma}(\mathbf{u}) : [\![\mathcal{P}\boldsymbol{\Phi}]\!])_{\gamma_n^-}\,| &\leq C \frac{h_k^{m_k}}{N_k^{s_k}} ||\boldsymbol{\chi}||_0 ||\mathbf{u}||_{s_k,\Omega_k}, \\ |\,((\underline{\sigma}(\boldsymbol{\Phi}) - \boldsymbol{\pi}_n \underline{\sigma}(\boldsymbol{\Phi})), [\![\boldsymbol{\chi}]\!])_{\gamma_n^-}\,| &\leq C \frac{h_k}{N_k} ||\boldsymbol{\chi}||_0 ||\boldsymbol{\chi}||_{1,\Omega_k}, \end{aligned}$$

for any $\gamma_n^- \subset \partial\overline{\Omega}_k$. Therefore we conclude combining the above estimates with (2.43).

□

Let $\mathbf{u}_M = \mathbf{u}_M(t)$ be the solution of the variational problem (2.12) in V_δ^{mortar} or equivalently of

$$(\rho\partial_{tt}\mathbf{u}_M, \mathbf{v}) + \mathcal{A}_M(\mathbf{u}_M, \mathbf{v}) = \mathcal{L}(\mathbf{v}) \quad \forall \mathbf{v} \in V_\delta^{mortar}. \tag{2.46}$$

From the results given in [19, 17], the estimate (2.43) and (2.44) we have the following

Lemma 7. *There exists a positive constant C such that for all $t \in [0,T]$ it holds*

$$||(\Pi\mathbf{u} - \mathbf{u}_M)(t)||_* \leq C \left\{ \sum_{k=1}^{K} \frac{h_k^{2m_k-2}}{N_k^{2s_k-2}} ||\mathbf{u}||^2_{H^2(0,T;\mathbf{H}^{s_k}(\Omega_k))} \right\}^{1/2}, \tag{2.47}$$

where $N_k \geq 1$ and $m_k = \min(N_k + 1, s_k)$.

Proof. We introduce the modified elliptic projection $\Pi\mathbf{u}$ as in (2.42) and we set $\boldsymbol{\xi} = \mathbf{u} - \Pi\mathbf{u}$ and $\boldsymbol{\chi} = \mathbf{u}_M - \Pi\mathbf{u}$. When multiplying the first line in (1.1) by a function $\mathbf{v} = \mathbf{v}(t) \in L^2(0,T;V_\delta^{mortar})$ and integrating by parts on each Ω_k, we observe that

$$(\rho\partial_{tt}\mathbf{u}, \mathbf{v}) + \mathcal{A}_M(\mathbf{u}, \mathbf{v}) + \sum_{n=1}^{M} (\underline{\sigma}(\mathbf{u}), [\![\mathbf{v}]\!])_{\gamma_n^-} = \mathcal{L}(\mathbf{v}).$$

Now subtracting (2.46) from the above equation we have, for any $\mathbf{v} \in L^2(0,T;V_\delta^{mortar})$,

$$(\rho\partial_{tt}(\mathbf{u} - \mathbf{u}_M), \mathbf{v}) + \mathcal{A}_M(\mathbf{u} - \mathbf{u}_M, \mathbf{v}) + \sum_{n=1}^{M} (\underline{\sigma}(\mathbf{u}), [\![\mathbf{v}]\!])_{\gamma_n^-} = 0,$$

or equivalently,

$$(\rho\boldsymbol{\chi}_{tt}, \mathbf{v}) + \mathcal{A}_M(\boldsymbol{\chi}, \mathbf{v}) = (\rho\boldsymbol{\xi}_{tt}, \mathbf{v}) + \mathcal{A}_M(\boldsymbol{\xi}, \mathbf{v}) + \sum_{n=1}^{M} (\underline{\sigma}(\mathbf{u}), [\![\mathbf{v}]\!])_{\gamma_n^-}.$$

Choosing $\mathbf{v} = \boldsymbol{\chi}_t$ and using the property (2.42) we obtain

$$(\rho\boldsymbol{\chi}_{tt}, \boldsymbol{\chi}_t) + \mathcal{A}_M(\boldsymbol{\chi}, \boldsymbol{\chi}_t) = (\rho\boldsymbol{\xi}_{tt}, \boldsymbol{\chi}_t) + 2\sum_{n=1}^{M} (\underline{\sigma}(\mathbf{u}), [\![\mathbf{v}]\!])_{\gamma_n^-}.$$

We rewrite it as follows

$$\frac{1}{2} d_t ||\rho^{1/2}\boldsymbol{\chi}_t||_0^2 + \frac{1}{2} d_t \mathcal{A}_M(\boldsymbol{\chi}, \boldsymbol{\chi}) = (\rho\boldsymbol{\xi}_{tt}, \boldsymbol{\chi}_t) + 2\sum_{n=1}^{M} (d_t(\underline{\sigma}(\mathbf{u}), [\![\boldsymbol{\chi}]\!])_{\gamma_n^-}$$
$$-2\sum_{n=1}^{M} (\underline{\sigma}(\mathbf{u}_t), [\![\boldsymbol{\chi}_t]\!])_{\gamma_n^-}. \tag{2.48}$$

Therefore, integrating (2.48) in time between 0 and t, noting that by definition $\boldsymbol{\chi}(0) = 0$ and using (2.38) we obtain

$$\frac{1}{2}||\rho^{1/2}\boldsymbol{\chi}_t(t)||_0^2 + \frac{\kappa}{2}||\boldsymbol{\chi}(t)||_*^2 \leq \int_0^t (\rho\boldsymbol{\xi}_{tt}, \boldsymbol{\chi}_t) + 2\sum_{n=1}^{M} (\underline{\sigma}(\mathbf{u}), [\![\boldsymbol{\chi}]\!])_{\gamma_n^-}(t)$$
$$-2\int_0^t \sum_{n=1}^{M} (\underline{\sigma}(\mathbf{u}_t), [\![\boldsymbol{\chi}_t]\!])_{\gamma_n^-} + \frac{1}{2}||\rho^{1/2}\boldsymbol{\chi}_t(0)||_0^2. \tag{2.49}$$

We now bound each of the terms in the right-hand side of (2.49) that involves integrals on γ_n^-, using the trace inequality:

$$\begin{aligned} |2\int_0^t \sum_{n=1}^{M} (\underline{\sigma}(\mathbf{u}_t), [\![\boldsymbol{\chi}]\!])_{\gamma_n^-}| &\leq C\sum_{k=1}^{K} \frac{h_k^{2m_k-2}}{N_k^{2s_k-2}} \int_0^t ||\mathbf{u}_t||_{s_k,\Omega_k}^2 + \frac{1}{2}\int_0^t ||\boldsymbol{\chi}||_*^2, \\ |2\sum_{n=1}^{M} (\underline{\sigma}(\mathbf{u}), [\![\boldsymbol{\chi}]\!])_{\gamma_n^-}| &\leq \frac{C}{2\epsilon}\sum_{k=1}^{K} \frac{h_k^{2m_k-2}}{N_k^{2s_k-2}} ||\mathbf{u}||_{s_k,\Omega_k}^2 + \frac{\epsilon}{2}||\boldsymbol{\chi}||_*^2, \end{aligned}$$

$\forall \epsilon > 0$. We also have

$$\int_0^t (\rho\boldsymbol{\xi}_{tt}, \boldsymbol{\chi}_t) \leq \int_0^t \frac{1}{2}||\rho^{1/2}\boldsymbol{\chi}_t||_0^2 + \int_0^t \frac{1}{2}||\rho^{1/2}\boldsymbol{\xi}_{tt}||_0^2.$$

Then, inequality (2.49) yields

$$\frac{1}{2}||\rho^{1/2}\boldsymbol{\chi}_t(t)||_0^2 + (\frac{\kappa}{2} - \frac{\epsilon}{2})||\boldsymbol{\chi}(t)||_*^2 \leq \frac{1}{2}\int_0^t \left(||\rho^{1/2}\boldsymbol{\chi}_t||_0^2 + ||\boldsymbol{\chi}||_*^2\right)$$
$$+\frac{1}{2}\int_0^t ||\rho^{1/2}\boldsymbol{\xi}_{tt}||_0^2 + \frac{C}{2\epsilon}\sum_{k=1}^{K} \frac{h_k^{2m_k-2}}{N_k^{2s_k-2}} ||\mathbf{u}||_{s_k,\Omega_k}^2 + \frac{1}{2}||\rho^{1/2}\boldsymbol{\chi}_t(0)||_0^2$$
$$+C\sum_{k=1}^{K} \frac{h_k^{2m_k-2}}{N_k^{2s_k-2}} \int_0^t ||\mathbf{u}_t||_{s_k,\Omega_k}^2. \tag{2.50}$$

Choosing ϵ such that $\kappa - \epsilon$ is bounded away from 0 we obtain

$$||\rho^{1/2}\boldsymbol{\chi}_t(t)||_0^2 + ||\boldsymbol{\chi}(t)||_*^2 \leq C\left[\int_0^t \left(||\rho^{1/2}\boldsymbol{\chi}_t||_0^2 + ||\boldsymbol{\chi}||_*^2\right) + \int_0^t ||\rho^{1/2}\boldsymbol{\xi}_{tt}||_0^2\right.$$
$$\left.+\sum_{k=1}^{K} \frac{h_k^{2m_k-2}}{N_k^{2s_k-2}} ||\mathbf{u}||_{s_k,\Omega_k}^2 + ||\rho^{1/2}\boldsymbol{\chi}_t(0)||_0^2 + \sum_{k=1}^{K} \frac{h_k^{2m_k-2}}{N_k^{2s_k-2}} \int_0^t ||\mathbf{u}_t||_{s_k,\Omega_k}^2\right].$$

By applying the Gronwall's lemma [92] it holds

$$||\rho^{1/2}\boldsymbol{\chi}_t(t)||_0^2 + ||\boldsymbol{\chi}(t)||_*^2 \leq C\left[\int_0^t ||\rho^{1/2}\boldsymbol{\xi}_{tt}||_0^2 + \sum_{k=1}^{K} \frac{h_k^{2m_k-2}}{N_k^{2s_k-2}} ||\mathbf{u}||_{s_k,\Omega_k}^2\right.$$
$$\left.+||\rho^{1/2}\boldsymbol{\chi}_t(0)||_0^2 + \sum_{k=1}^{K} \frac{h_k^{2m_k-2}}{N_k^{2s_k-2}} \int_0^t ||\mathbf{u}_t||_{s_k,\Omega_k}^2\right].$$

Using the approximation properties (2.43)-(2.44) it follows that:

$$
\begin{aligned}
||\rho^{1/2}\boldsymbol{\chi}_t(0)||_0^2 &\leq C\sum_{k=1}^{K}\frac{h_k^{2m_k}}{N_k^{2s_k}}||\mathbf{u}_t||^2_{L^2(0,t;\mathbf{H}^{s_k}(\Omega_k))},\\
\int_0^t ||\rho^{1/2}\boldsymbol{\xi}_{tt}||_0^2 &\leq C\sum_{k=1}^{K}\frac{h_k^{2m_k-2}}{N_k^{2s_k-2}}||\mathbf{u}_{tt}||^2_{L^2(0,t;\mathbf{H}^{s_k}(\Omega_k))}.
\end{aligned}
$$

Therefore we have

$$
||\boldsymbol{\chi}(t)||_*^2 \leq C\sum_{k=1}^{K}\frac{h_k^{2m_k-2}}{N_k^{2s_k-2}}||\mathbf{u}||^2_{H^2(0,t;\mathbf{H}^{s_k}(\Omega_k))}.
$$

□

For $\mathbf{u}_M$ it holds the following convergence result.

Theorem 2. *Suppose that* $\mathbf{u}_M \in H^2(0,T;\mathbf{H}^{s_k}(\Omega_k))$ *for any* $\Omega_k \subset \Omega$. *There exists a positive constant* C *such that*

$$
\sup_{t\in[0,T]}||(\mathbf{u}-\mathbf{u}_M)(t)||_* \leq C\left\{\sum_{k=1}^{K}\frac{h_k^{2m_k-2}}{N_k^{2s_k-2}}||\mathbf{u}||^2_{H^2(0,T;\mathbf{H}^{s_k}(\Omega_k))}\right\}^{1/2}, \tag{2.51}
$$

where $N_k \geq 1$ *and* $m_k = \min(N_k+1, s_k)$.

The proof of Theorem 2 is obtained using the triangle inequality, estimates (2.43)-(2.44) and (2.47) and taking the supremum over all $t \in [0,T]$.

2.3.3 Semi-discrete L^2-error estimates - DGSE/MSE methods

Starting from the estimates in Theorems 1 and 2 and using standard duality arguments it is possible to prove the following L^2-error estimates for the $\mathbf{u}_{DG}$ and $\mathbf{u}_M$ semi-discrete solutions, respectively. Here, for the sake of brevity we report only the final result.

Theorem 3. *There exists two positive constant* C_1 *and* C_2 *such that*

$$
\sup_{t\in[0,T]}||(\mathbf{u}-\mathbf{u}_{DG})(t)||_0 \leq C_1\left\{\sum_{k=1}^{K}\frac{h_k^{2m_k}}{N_k^{2s_k-1}}||\mathbf{u}||^2_{H^2(0,T;\mathbf{H}^{s_k}(\Omega_k))}\right\}^{1/2},
$$

and

$$
\sup_{t\in[0,T]}||(\mathbf{u}-\mathbf{u}_M)(t)||_0 \leq C_2\left\{\sum_{k=1}^{K}\frac{h_k^{2m_k}}{N_k^{2s_k}}||\mathbf{u}||^2_{H^2(0,T;\mathbf{H}^{s_k}(\Omega_k))}\right\}^{1/2},
$$

where $N_k \geq 1$ *and* $m_k = \min(N_k+1, s_k)$.

We remark that in the family of DGSE approximations the above result holds for the SIPG method but is no longer true when the NIPG method is applied [9]. In this case the NIPG solution satisfies a L^2-error estimate similar to (2.35).

2.4 Algebraic formulation of the semi-discrete formulations

For simplicity we consider the elastodynamics equation (1.1) in a bounded domain $\Omega \subset \mathbb{R}^2$ with mixed Dirichlet Neumann boundary condition, thus $\Gamma_D \cup \Gamma_N \equiv \Gamma$, $\Gamma_{NR} = \emptyset$. To ease the presentation let also suppose that Ω is partitioned into K non-overlapping spectral elements $\Omega_1, ..., \Omega_K$ so that $\overline{\mathcal{S}} = \bigcap_{k=1}^{K} \partial\overline{\Omega}_k \setminus \Gamma$. The more general case can be obtained with similar arguments. The extension of this theory to viscoelastic external forces and absorbing boundary conditions is addressed in Sections 2.4.1 and 2.4.2 respectively, while the algorithmic aspects and implementation issues are discussed in Chapter 5.
We denote by $D = \sum_{k=1}^{K}(N_k+1)^2$ the dimension of each component of V_δ and we introduce a basis $\{\boldsymbol{\Psi}_i^1, \boldsymbol{\Psi}_i^2\}_{i=1}^{D}$ for the finite dimensional space V_δ, where $\boldsymbol{\Psi}_i^1 = \left(\Psi_i^1, 0\right)^\top$ and $\boldsymbol{\Psi}_i^2 = \left(0, \Psi_i^2\right)^\top$. Dropping the subscript δ, we write the trial functions $\mathbf{u} \in V_\delta$ as linear combination of the basis functions, i.e.,

$$\mathbf{u}(\mathbf{x},t) = \sum_{j=1}^{D} \begin{bmatrix} \Psi_j^1(\mathbf{x}) \\ 0 \end{bmatrix} U_j^1(t) + \sum_{j=1}^{D} \begin{bmatrix} 0 \\ \Psi_j^2(\mathbf{x}) \end{bmatrix} U_j^2(t), \tag{2.52}$$

Next, we define

$$a_k = 1 + \sum_{j=1}^{k-1}(N_j+1)^2 \quad \text{and} \quad b_k = \sum_{j=1}^{k}(N_j+1)^2$$

and we order the basis functions such that

$$\mathbf{u}_{|\Omega_k} = (u_1, u_2)_{|\Omega_k}^\top = \left(\sum_{j=a_k}^{b_k} \Psi_j^1 U_{j,k}^1 \,, \sum_{j=a_k}^{b_k} \Psi_j^2 U_{j,k}^2 \right)^\top, \tag{2.53}$$

for $k = 1, ..., K$. With the notation just introduced, we write the equation (2.1) for any test function $\boldsymbol{\Psi}_j^\ell(\mathbf{x})$, for $\ell = 1, 2$, in the space V_δ and we obtain the following set of ordinary differential equations:

$$\underline{\mathrm{M}}\ddot{\mathbf{U}} + \underline{\mathrm{A}}\mathbf{U} + \underline{\mathrm{B}}\mathbf{U} = \mathbf{F}^{ext}, \tag{2.54}$$

or equivalently

$$\begin{bmatrix} \underline{\mathrm{M}}^1 & \underline{0} \\ \underline{0} & \underline{\mathrm{M}}^2 \end{bmatrix} \begin{bmatrix} \ddot{\mathbf{U}}^1 \\ \ddot{\mathbf{U}}^2 \end{bmatrix} + \begin{bmatrix} \underline{\mathrm{A}}^1 + \underline{\mathrm{B}}^1 & \underline{\mathrm{A}}^2 + \underline{\mathrm{B}}^2 \\ \underline{\mathrm{A}}^3 + \underline{\mathrm{B}}^3 & \underline{\mathrm{A}}^4 + \underline{\mathrm{B}}^4 \end{bmatrix} \begin{bmatrix} \mathbf{U}^1 \\ \mathbf{U}^2 \end{bmatrix} = \begin{bmatrix} \mathbf{F}^{ext,1} \\ \mathbf{F}^{ext,2} \end{bmatrix}, \tag{2.55}$$

where $\ddot{\mathbf{U}}$ represents the vector of nodal acceleration and $\mathbf{F}^{ext}$ the vector of externally applied loads defined as

$$F_i^{ext,\ell} = (\mathbf{t}, \mathbf{\Psi}_i^\ell)_{\Gamma_N} + (\mathbf{f}, \mathbf{\Psi}_i^\ell)_\Omega, \quad \text{for } \ell = 1, 2.$$

As a consequence of assumptions on the basis functions, the mass matrices $\underline{\mathrm{M}}^1$ and $\underline{\mathrm{M}}^2$ have a block diagonal structure $\underline{\mathrm{M}}^\ell = \mathtt{diag}(\underline{\mathrm{M}}_1^\ell, \underline{\mathrm{M}}_2^\ell, ..., \underline{\mathrm{M}}_K^\ell)$, $\ell = 1, 2$, where each block $\underline{\mathrm{M}}_k^\ell$ is associated to the spectral element Ω_k and

$$\mathrm{M}_k^\ell(i,j) = (\rho \Psi_j^\ell, \Psi_i^\ell)_{\Omega_k}, \quad \text{for } i, j = a_k, ..., b_k. \tag{2.56}$$

The matrix $\underline{\mathrm{A}}$ associated to the bilinear form $\mathcal{A}(\cdot,\cdot)$ defined in (2.2) takes the form

$$\underline{\mathrm{A}} = \begin{bmatrix} \underline{\mathrm{A}}^1 & \underline{\mathrm{A}}^2 \\ \underline{\mathrm{A}}^3 & \underline{\mathrm{A}}^4 \end{bmatrix},$$

where the block diagonal matrices $\underline{\mathrm{A}}^\ell$, $\ell = 1, .., 4$, are equal to $\underline{\mathrm{A}}^\ell = \mathtt{diag}(\underline{\mathrm{A}}_1^\ell, \underline{\mathrm{A}}_2^\ell, ..., \underline{\mathrm{A}}_K^\ell)$. The elements of the matrices $\underline{\mathrm{A}}_k^\ell$, for $\ell = 1, ..., 4$ and $k = 1, .., K$ are defined by

$$\begin{aligned} &\mathrm{A}_k^1(i,j) = \mathcal{A}(\underline{\sigma}(\mathbf{\Psi}_j^1), \underline{\varepsilon}(\mathbf{\Psi}_i^1))_{\Omega_k}, \quad \mathrm{A}_k^2(i,j) = \mathcal{A}(\underline{\sigma}(\mathbf{\Psi}_j^2), \underline{\varepsilon}(\mathbf{\Psi}_i^1))_{\Omega_k}, \\ &\mathrm{A}_k^3(i,j) = \mathcal{A}(\underline{\sigma}(\mathbf{\Psi}_j^1), \underline{\varepsilon}(\mathbf{\Psi}_i^2))_{\Omega_k}, \quad \mathrm{A}_k^4(i,j) = \mathcal{A}(\underline{\sigma}(\mathbf{\Psi}_j^2), \underline{\varepsilon}(\mathbf{\Psi}_i^2))_{\Omega_k}, \end{aligned} \tag{2.57}$$

for $i, j = a_k, ..., b_k$, or equivalently by

$$\begin{aligned} \mathrm{A}_k^1(i,j) &= ([\lambda + 2\mu] \frac{\partial \Psi_j^1}{\partial x_1}, \frac{\partial \Psi_i^1}{\partial x_1})_{\Omega_k} + (\mu \frac{\partial \Psi_j^1}{\partial x_2}, \frac{\partial \Psi_i^1}{\partial x_2})_{\Omega_k}, \\ \mathrm{A}_k^2(i,j) &= (\lambda \frac{\partial \Psi_j^2}{\partial x_2}, \frac{\partial \Psi_i^1}{\partial x_1})_{\Omega_k} + (\mu \frac{\partial \Psi_j^2}{\partial x_1}, \frac{\partial \Psi_i^1}{\partial x_2})_{\Omega_k}, \\ \mathrm{A}_k^3(i,j) &= (\mu \frac{\partial \Psi_j^1}{\partial x_2}, \frac{\partial \Psi_i^2}{\partial x_1})_{\Omega_k} + (\lambda \frac{\partial \Psi_j^1}{\partial x_1}, \frac{\partial \Psi_i^2}{\partial x_2})_{\Omega_k}, \\ \mathrm{A}_k^4(i,j) &= ([\lambda + 2\mu] \frac{\partial \Psi_j^2}{\partial x_2}, \frac{\partial \Psi_i^2}{\partial x_2})_{\Omega_k} + (\mu \frac{\partial \Psi_j^2}{\partial x_1}, \frac{\partial \Psi_i^2}{\partial x_1})_{\Omega_k}. \end{aligned}$$

by definitions of the stress and strain tensors $\underline{\sigma}$ and $\underline{\varepsilon}$, respectively. We remark that the matrices $\underline{\mathrm{M}}$ and $\underline{\mathrm{A}}$ are very similar to those resulting from the discretization of the elastodynamics equation (1.9) with conforming spectral element method (see [26, 27]). The matrix $\underline{\mathrm{B}}$, associated to the bilinear form $\mathcal{B}(\cdot,\cdot)$ defined in (2.2), is the one that takes into account the discontinuity of the numerical solution across the skeleton $\mathcal{S}$. In the DG approach it is given by

$$\underline{\mathrm{B}} = \begin{bmatrix} \underline{\mathrm{B}}^1 & \underline{\mathrm{B}}^2 \\ \underline{\mathrm{B}}^3 & \underline{\mathrm{B}}^4 \end{bmatrix},$$

where

$$\underline{\mathrm{B}}^\ell = \begin{bmatrix} \underline{\mathrm{B}}^\ell_{1,1} & \cdots & \underline{\mathrm{B}}^\ell_{1,K} \\ \vdots & \ddots & \vdots \\ \underline{\mathrm{B}}^\ell_{K,1} & \cdots & \underline{\mathrm{B}}^\ell_{K,K} \end{bmatrix}, \quad \text{for } \ell = 1, ..., 4.$$

In particular the elements of each matrix $\underline{\mathrm{B}}^1_{k,n}$ are defined by:

$$\begin{aligned} \mathrm{B}^1_{k,n}(i,j) &= \sum_{\gamma\in\mathcal{F}_I} \mathcal{B}(\boldsymbol{\Psi}^1_j, \boldsymbol{\Psi}^1_i)_\gamma \\ &= \sum_{\gamma\in\mathcal{F}_I} -\int_\gamma \{\underline{\sigma}(\boldsymbol{\Psi}^1_j)\} : [\![\boldsymbol{\Psi}^1_i]\!] + \theta \int_\gamma [\![\boldsymbol{\Psi}^1_j]\!] : \{\underline{\sigma}(\boldsymbol{\Psi}^1_i)\} \\ &\qquad +\eta_\gamma \int_\gamma [\![\boldsymbol{\Psi}^1_j]\!] : [\![\boldsymbol{\Psi}^1_i]\!], \end{aligned} \tag{2.58}$$

for $i = a_k, ..., b_k$ and $j = a_n, ..., b_n$. The elements of the matrices $\underline{\mathrm{B}}^\ell_{k,n}$, for $\ell = 2, 3, 4$, are defined in a similar way.

The situation is a little bit more complicated in the Mortar approach, since the weak continuity condition across the skeleton $\mathcal{S}$ does not appear explicitly in the variational equation but it is a constraint in the functional space V^{mortar}_δ: in fact, in the Mortar Variational Formulation, $\mathcal{B}(\cdot,\cdot) = 0$ implies that $\underline{\mathrm{B}}$ is a null matrix.

To account for **MC** we need to modify (2.55) as follows. Without loss of generality let us suppose that γ^-_n is a *non-mortar* edge contained in $\mathcal{S}$ and moreover that it is shared by two subdomains Ω_m and Ω_n. We call *master* the side of γ^-_n belonging to $\overline{\Omega}_m$ and *slave* the other side. Thus, the *mortar conditions* **MC** can be recast as:

(i) $\boldsymbol{\Phi} = \mathbf{u}_m$ on γ^-_n,

(ii) $\int_{\gamma^-_n} (\mathbf{u}_n - \mathbf{u}_m) \cdot \widehat{\Phi} = 0 \quad \forall \widehat{\Phi} \in [\widehat{\Lambda}_\delta(\gamma^-_n)]^2$.

We remark that when interfaces do not match geometrically, i.e. γ_n^- is shared by M^*+1 subdomains $\Omega_n, \Omega_{m(1)}, ..., \Omega_{m(M^*)}$, condition **(ii)** reads as

$$\sum_{\ell=1}^{M^*} \int_{\gamma_n^- \cap \partial\overline{\Omega}_{m(\ell)}} (\mathbf{u}_n - \mathbf{u}_{m(\ell)}) \cdot \widehat{\Phi} = 0 \quad \forall \widehat{\Phi} \in [\widehat{\Lambda}_\delta(\gamma_n^-)]^d.$$

Then the following arguments have to be intended for each integral in the above expression. Now, for the spectral element Ω_n (resp. Ω_m) we order first the N_n+1 (resp. N_m+1) degrees of freedom (d.o.f.) associated to the spectral nodes $\mathbf{p}_i$ that live in γ_n^- and next the d.o.f. associated to the remaining spectral nodes $\mathbf{p}_i$. With this assumptions the restriction of the function $\mathbf{u}_n$ on γ_n^- is rewritten as

$$\mathbf{u}_{n|_{\gamma_n^-}} = (\sum_{j=1}^{N_n+1} \Psi_j^1 U_{j,n}^1, \sum_{j=1}^{N_n+1} \Psi_j^2 U_{j,n}^2)^\top,$$

and the same for the function $\mathbf{u}_{m|_{\gamma_n^-}}$. Hence, by definition of scalar product, the *mortar condition* **(ii)** becomes

$$\int_{\gamma_n^-} (u_{1,n} - u_{1,m})\widehat{\Phi}^1 + \int_{\gamma_n^-} (u_{2,n} - u_{2,m})\widehat{\Phi}^2 = 0 \quad \forall\, \widehat{\Phi}^1, \widehat{\Phi}^2 \in \widehat{\Lambda}_\delta(\gamma_n^-). \tag{2.59}$$

Since the integrals in (2.59) concern separately the two components of the displacement, we focus the attention onto one of them, dropping the subscripts 1 and 2 to ease the notation. The other one is treated in the same manner. For the *slave* side of the *mortar* we obtain

$$\int_{\gamma_n^-} u_n \widehat{\Phi}_i = \sum_{j=1}^{N_n+1} U_{j,n} \int_{\gamma_n^-} \Psi_j \widehat{\Phi}_i = \sum_{j=1}^{N_n+1} R_{i,j} U_{j,n}, \quad \text{for } i = 1, .., N_n - 1, \tag{2.60}$$

where $R_{i,j} = \int_{\gamma_n^-} \Psi_j \widehat{\Phi}_i$. For the *master* side, using the *mortar condition* **(i)**, we have that

$$\int_{\gamma_n^-} u_m \widehat{\Phi}_i = \sum_{j=1}^{N_m+1} U_{j,m} \int_{\gamma_n^-} \Phi_j \widehat{\Phi}_i = \sum_{j=1}^{N_m+1} P_{i,j} U_{j,m}, \quad \text{for } i = 1, .., N_n - 1, \tag{2.61}$$

with $P_{i,j} = \int_{\gamma_n^-} \Phi_j \widehat{\Phi}_i$. One may use (2.60)-(2.61) to recast the *mortar constraint* **MC** in matrix notation

$$\underline{R} \begin{bmatrix} U_{1,n} \\ \vdots \\ U_{N_n+1,n} \end{bmatrix} = \underline{P} \begin{bmatrix} U_{1,m} \\ \vdots \\ U_{N_m+1,m} \end{bmatrix}. \tag{2.62}$$

Now, to compute numerically the matrices $\underline{R}$ and $\underline{P}$ we use suitable quadrature formulas depending if we are on the *slave* or in the *master* side of the *mortar*. We choose N_n+1 GLL nodes to evaluate the integrals $\int_{\gamma_n^-} \Psi_j \widehat{\Phi}_i ds$ such that the matrix $\underline{R}$ takes a special structure. In fact, because of this choice the interior part $\underline{R}_{int}$ is diagonal. The first and the last columns are full but they are concerned only with d.o.f. (namely, $U_{1,n}$ and $U_{N_n+1,n}$) but do not depend on the matching conditions. We observe also that the matrix $\underline{P}$ is full. Then the local projection operator can be written in a matrix form as

$$\begin{bmatrix} U_{2,n} \\ \vdots \\ U_{N_n,n} \end{bmatrix} = \underbrace{\underline{R}_{int}^{-1} \begin{bmatrix} P_{1,1} & \cdots & P_{1,N_m+1} & -R_{1,1} & -R_{1,N_n+1} \\ \vdots & \ddots & \vdots & \vdots & \vdots \\ P_{N_n-1,1} & \cdots & P_{N_n-1,N_m+1} & -R_{N_n-1,1} & -R_{N_n-1,N_n+1} \end{bmatrix}}_{\underline{Q}_n} \begin{bmatrix} U_{1,m} \\ \vdots \\ U_{N_m+1,m} \\ U_{1,n} \\ U_{N_n+1,n} \end{bmatrix}.$$

Thanks to the projection operator $\underline{Q}_n$, we are then able to recover the *slave* unknowns in γ_n^- once we know the *master* ones. To obtain a global projection operator $\widetilde{\underline{Q}}$ we proceed as follows. For each component of $\mathbf{u}$ we denote by $\mathbf{U}_{slave}$ the vector of unknowns associated to d.o.f. that lay on the *slave* side of $\mathcal{S}$ and by $\mathbf{U}_{master}$ the vector of unknowns associated to all the remaining d.o.f. Then, for each γ_n^- belonging to the skeleton $\mathcal{S}$ we build the local projection operator $\underline{Q}_n$ and we store it into the matrix $\widetilde{\underline{Q}}$. In this way $\widetilde{\underline{Q}}$ has a block structure of the form

$$\widetilde{\underline{Q}} = \begin{bmatrix} \widehat{\underline{Q}} & \underline{0} \\ \underline{0} & \widehat{\underline{Q}} \end{bmatrix}, \tag{2.63}$$

where $\widehat{\underline{Q}}$ is a block diagonal matrix with a block equal to the identity and the other equal to the rectangular matrix $\underline{Q}$ containing all the local matrices $\underline{Q}_n$. Thus, we have that the global linear system can be expressed as

$$\widetilde{\underline{\mathrm{Q}}}^{\top} \widetilde{\underline{\mathrm{M}}} \widetilde{\underline{\mathrm{Q}}} \ddot{\mathbf{U}}_{master} + \widetilde{\underline{\mathrm{Q}}}^{\top} \widetilde{\underline{\mathrm{A}}} \widetilde{\underline{\mathrm{Q}}} \mathbf{U}_{master} = \widetilde{\underline{\mathrm{Q}}}^{\top} \mathbf{F}^{ext}, \tag{2.64}$$

where the matrices $\widetilde{\underline{\mathrm{M}}}$ and $\widetilde{\underline{\mathrm{A}}}$ have columns and rows modified with respect to the ones of $\underline{\mathrm{M}}$ and $\underline{\mathrm{A}}$ according to latter assumptions on the unknowns reordering. All the terms appearing in the matrices of the two algebraic formulation are computed using Gauss-Lobatto quadrature rule in which the quadrature points coincide with the GLL points. We remark that since the term $\Psi_j^\ell \Psi_i^\ell \in Q_{N_k}$, for some k, while the Gauss-Lobatto rule with N_k points is exact for polynomials up to degree $2N_k - 1$ in each variable, the spectral mass matrix $\underline{\mathrm{M}}$ is slightly under integrated. However, the final accuracy of spectral methods is maintained [26].

2.4.1 Structural damping

When using equation (1.3) to model viscoelastic materials, very useful for seismic applications, we must compute additional external forces:

$$\mathbf{F}^{visc} = -\underline{\mathrm{C}}\dot{\mathbf{U}} - \underline{\mathrm{D}}\mathbf{U}, \tag{2.65}$$

or equivalently

$$\begin{bmatrix} \mathbf{F}^{visc,1} \\ \mathbf{F}^{visc,2} \end{bmatrix} = - \begin{bmatrix} \underline{\mathrm{C}}^1 & \underline{0} \\ \underline{0} & \underline{\mathrm{C}}^2 \end{bmatrix} \begin{bmatrix} \dot{\mathbf{U}}^1 \\ \dot{\mathbf{U}}^2 \end{bmatrix} - \begin{bmatrix} \underline{\mathrm{D}}^1 & \underline{0} \\ \underline{0} & \underline{\mathrm{D}}^2 \end{bmatrix} \begin{bmatrix} \mathbf{U}^1 \\ \mathbf{U}^2 \end{bmatrix},$$

where the matrices $\underline{\mathrm{C}}^\ell$ and $\underline{\mathrm{D}}^\ell$, for $\ell = 1, 2$, are block diagonal. Each block $\underline{\mathrm{C}}^\ell_k$ and $\underline{\mathrm{D}}^\ell_k$ is associated to a spectral element Ω_k and

$$\mathrm{C}^\ell_k(i,j) = (\rho\zeta\Psi^\ell_j, \Psi^\ell_i)_{\Omega_k}, \quad \mathrm{D}^\ell_k(i,j) = (\rho\zeta^2\Psi^\ell_j, \Psi^\ell_i)_{\Omega_k}, \quad \text{for } i,j = a_k, ..., b_k, \tag{2.66}$$

respectively. Then, the DGSE system becomes:

$$\underline{\mathrm{M}}\ddot{\mathbf{U}} + \underline{\mathrm{C}}\dot{\mathbf{U}} + (\underline{\mathrm{A}} + \underline{\mathrm{B}} + \underline{\mathrm{D}})\mathbf{U} = \mathbf{F}^{ext}, \tag{2.67}$$

where $\dot{\mathbf{U}}$ represents the nodal velocity vector.
Obviously when MSE method is considered, the above system is modified as explained in the previous section (see 2.64). This leads to the final system

$$\widetilde{\underline{\mathrm{Q}}}^\top \underline{\widetilde{\mathrm{M}}}\widetilde{\underline{\mathrm{Q}}}\ddot{\mathbf{U}}_{master} + \widetilde{\underline{\mathrm{Q}}}^\top \underline{\widetilde{\mathrm{C}}}\widetilde{\underline{\mathrm{Q}}}\dot{\mathbf{U}}_{master} + \widetilde{\underline{\mathrm{Q}}}^\top (\underline{\widetilde{\mathrm{A}}} + \underline{\widetilde{\mathrm{D}}})\widetilde{\underline{\mathrm{Q}}}\mathbf{U}_{master} = \widetilde{\underline{\mathrm{Q}}}^\top \mathbf{F}^{ext}. \tag{2.68}$$

2.4.2 Absorbing boundary conditions

Special attention must be paid if absorbing boundary conditions (ABC) are considered in the model (1.1). As we described in Section 1.2, ABCs are prescribed on Γ_{NR} introducing fictitious tractions $\mathbf{t}^*$ depending on space and time derivatives of $\mathbf{u}$ as in (1.7). At the discrete level ABCs are in the form

$$\mathbf{F}^{abc} = \underline{\mathrm{S}}\dot{\mathbf{U}} + \underline{\mathrm{R}}\mathbf{U}, \tag{2.69}$$

or equivalently

$$\begin{bmatrix} \mathbf{F}^{abc,1} \\ \mathbf{F}^{abc,2} \end{bmatrix} = \begin{bmatrix} \underline{\mathrm{S}}^1 & \underline{0} \\ \underline{0} & \underline{\mathrm{S}}^2 \end{bmatrix} \begin{bmatrix} \dot{\mathbf{U}}^1 \\ \dot{\mathbf{U}}^2 \end{bmatrix} + \begin{bmatrix} \underline{\mathrm{R}}^1 & \underline{\mathrm{R}}^2 \\ \underline{\mathrm{R}}^3 & \underline{\mathrm{R}}^4 \end{bmatrix} \begin{bmatrix} \mathbf{U}^1 \\ \mathbf{U}^2 \end{bmatrix}.$$

On the one hand, the block matrices $\underline{\mathrm{S}}^{\ell}$, for $\ell = 1, 2$, are diagonal and each block $\underline{\mathrm{S}}_k^{\ell}$ associated to an Ω_k such that $\gamma_k^* = \partial\Omega_k \cap \Gamma_{NR} \neq \emptyset$, is defined by

$$\mathrm{S}_k^{\ell}(i,j) = (c_\ell \Psi_j^{\ell}, \Psi_i^{\ell})_{\gamma_k^*}, \quad i,j = a_k, ..., b_k, \tag{2.70}$$

with

$$c_1 = [-\frac{\lambda + 2\mu}{c_P}(n_1 n_2 + n_1^2) - \frac{\mu}{c_S}(n_1 n_2 + n_2^2)], \tag{2.71}$$

$$c_2 = [-\frac{\lambda + 2\mu}{c_P}(n_1 n_2 + n_2^2) + \frac{\mu}{c_S}(n_1 n_2 + n_1^2)]. \tag{2.72}$$

On the other hand, matrices $\underline{\mathrm{R}}^{\ell}$, for $\ell = 1, .., 4$, are still block diagonal, i.e.,

$$\underline{\mathrm{R}}^{\ell} = \mathrm{diag}\left(\underline{\mathrm{R}}_1^{\ell}, \cdots, \underline{\mathrm{R}}_K^{\ell}\right). \tag{2.73}$$

but each $\underline{\mathrm{R}}_k^{\ell}$, for $k = 1, ..., K$ is non diagonal. In fact, setting

$$c_3 = \frac{\mu(2c_S - c_P)}{c_S} \quad \text{and} \quad c_4 = \frac{\lambda c_S + 2\mu(c_S - c_P)}{c_P},$$

it is possible to write the blocks $\underline{\mathrm{R}}_k^{\ell}$ in the following form

$$\begin{aligned}
\underline{\mathrm{R}}_k^1(i,j) &= ([c_3 n_1 n_2^2 + c_4 n_1 n_2^2]\Psi_j^1, \frac{\partial \Psi_i^1}{\partial x_1})_{\gamma_k^*} + ([-c_3 n_1^2 n_2 - c_4 n_1^2 n_2]\Psi_j^1, \frac{\partial \Psi_i^1}{\partial x_2})_{\gamma_k^*} \\
\underline{\mathrm{R}}_k^2(i,j) &= ([c_3 n_2^3 - c_4 n_1^2 n_2]\Psi_j^1, \frac{\partial \Psi_i^2}{\partial x_1})_{\gamma_k^*} + ([-c_3 n_1 n_2^2 + c_4 n_1^3]\Psi_j^1, \frac{\partial \Psi_i^2}{\partial x_2})_{\gamma_k^*} \\
\underline{\mathrm{R}}_k^3(i,j) &= ([-c_3 n_1^2 n_2 + c_4 n_2^3]\Psi_j^2, \frac{\partial \Psi_i^1}{\partial x_1})_{\gamma_k^*} + ([c_3 n_1^3 - c_4 n_1 n_2^2]\Psi_j^2, \frac{\partial \Psi_i^1}{\partial x_2})_{\gamma_k^*} \\
\underline{\mathrm{R}}_k^4(i,j) &= ([c_3 n_1 n_2^2 - c_4 n_1 n_2^2]\Psi_j^2, \frac{\partial \Psi_i^2}{\partial x_1})_{\gamma_k^*} + ([c_3 n_1^2 n_2 + c_4 n_1^2 n_2]\Psi_j^2, \frac{\partial \Psi_i^2}{\partial x_2})_{\gamma_k^*}
\end{aligned}$$

for $i, j = a_k, ..., b_k$. Finally, taking into account of both viscoelastic and absorbing terms, i.e., (2.65) and (2.69) respectively, the global discretized system reads

$$\underline{\mathrm{M}}\ddot{\mathbf{U}} + (\underline{\mathrm{C}} - \underline{\mathrm{S}})\dot{\mathbf{U}} + (\underline{\mathrm{A}} + \underline{\mathrm{B}} + \underline{\mathrm{D}} - \underline{\mathrm{R}})\mathbf{U} = \mathbf{F}^{ext}, \tag{2.74}$$

for the DGSE method and

$$\underline{\widetilde{\mathrm{Q}}}^{\top}\underline{\widetilde{\mathrm{M}}}\underline{\widetilde{\mathrm{Q}}}\ddot{\mathbf{U}}_{master} + \underline{\widetilde{\mathrm{Q}}}^{\top}(\underline{\widetilde{\mathrm{C}}} - \underline{\widetilde{\mathrm{S}}})\underline{\widetilde{\mathrm{Q}}}\dot{\mathbf{U}}_{master} + \underline{\widetilde{\mathrm{Q}}}^{\top}(\underline{\widetilde{\mathrm{A}}} + \underline{\widetilde{\mathrm{D}}} - \underline{\widetilde{\mathrm{R}}})\underline{\widetilde{\mathrm{Q}}}\mathbf{U}_{master} = \underline{\widetilde{\mathrm{Q}}}^{\top}\mathbf{F}^{ext}, \tag{2.75}$$

for the MSE method, respectively. In the next chapter we describe three time integration schemes that we adopted for solving (2.74) and (2.75). In particular we focused on the leap-frog scheme, the fourth order explicit Runge-Kutta method and the Implicit Midpoint method.

2.5 Extension to three dimensional problems

Non-conforming discretizations can be used as well for the approximation of three dimensional problems and the general theory (such as the formulation, the discretization and the error analysis) follows easily from the results presented in the previous sections. However, for three dimensional wave propagations we decide to implement and study only the DGSE method. In fact, as we will see in Chapter 7, to simulate realistic earthquake scenarios, an efficient numerical algorithm well suited for parallel computations is mandatory. Form an algorithmic point of view, the interface integrals introduced with the bilinear form $\mathcal{B}(\cdot,\cdot)$ in (2.8) are easier to compute than the mortar condition **MC** defined in the MSE formulation.

Indeed, as we will see in Chapter 5 the definition of the space of multipliers $\widehat{\Lambda}_\delta$ is quite elaborate in two dimension and it is almost prohibitive in three dimension. For this reason, it is preferable to use in a three dimensional framework, a different Mortar approach in which the *mortar* constraint is directly imposed into the weak formulation, e.g. [69, 15]. At the algebraic level this technique leads to a saddle-point problem and special solvers are needed for the solution of the resulting algebraic system.

On the contrary, using the DGSE method, no modifications occur to the algebraic system (2.55) and this yields enormous advantages from the computational point of view. Since we allow the possibility of dealing with meshes independently defined with respect to the neighbouring ones, the algorithmic key point resides on the computation of interface integrals having support on the elementary components (now intersection of quadrilateral surfaces). The procedure we follow is very similar to that described for the general two dimensional configurations, so we refer to Chapter 5 for a detailed description.

Chapter 3

Time discretization

In this chapter we describe three different approaches for solving the ordinary differential system of equations (2.74) and (2.75), resulting from the DGSE or MSE semi-discretization, respectively. Since DGSE and MSE methods are high-order techniques (see Chapter 2.3), we are looking for time integration schemes that preserve also in time their good approximations properties. In particular, these methods must be stable (with a not too restrictive CFL condition) and must produce low dispersion and dissipation errors during the propagation of the wavefield. Moreover they must be computationally cheap in terms of both memory storage and computational time.
In the following we describe three different time integration schemes, namely the leap-frog (LF) finite difference method, the implicit midpoint (IM) method and the fourth order explicit Runge-Kutta (RK4) method, see [91]. The development of much general high order semi implicit and implicit integration schemes and the related preconditioners is under investigation.
The LF scheme, which is the most popular time-stepping scheme for wave propagation [35, 62, 61, 63, 50, 39, 34, 36, 79, 12], belongs to the family of the Newmark methods [91, 92]. It is second order accurate, explicit and conditionally stable.
The IM scheme comes from the family of the Runge-Kutta methods [68] and it is still second order accurate but implicit and unconditionally stable.
At the best of our knowledge, implicit time integration schemes have been applied coupled only with finite differences or collocation methods to solve acoustic [54] and elastic wave propagation problems [118]. The main advantage of this approach relies on their unconditioned stability, that allows to choose a time integration step ten times larger

than in the explicit case [118].
For higher order accurate time integration schemes we consider the Runge-Kutta approach [25]. Other high order methods proposed for the discretization in time are Taylor-Galerkin method [39], the ADER-DG method [57, 41], the rapid expansion method [112, 64] and the symplectic method [105, 85, 112]. A comparison of these methods is beyond of the scope of this present work and will be the subject of future research.
High order Runge-Kutta schemes are one step methods that increase their accuracy at the price of increasing the number of functional evaluations at each time level, thus sacrifying linearity. These methods are studied and applied in wave propagation [54, 71] because they are highly accurate and low dispersive. Moreover, in the explicit case their absolute stability region is not more restrictive than the LF one (cf. Chapter 4). Here and in the following we analyze in detail the four stage Runge-Kutta method RK4, that is explicit, fourth order accurate and conditionally stable.
In this chapter the attention is focused on the analysis of LF, IM and RK4 time discretizations when coupled to DGSE and MSE semi-discretizations and on the corresponding fully discrete formulations.

3.1 Fully-discrete formulations

To ease the notation we present the analysis in absence of viscoelastic materials and absorbing forces, i.e, starting from the algebraic systems (2.54) and (2.64) coming from the DG and Mortar formulations. Moreover we suppose that $\Omega \subset \mathbb{R}^2$ is partitioned into K non-overlapping spectral elements $\Omega_1, ..., \Omega_K$. The more general situation and the extension to three dimensional problems can be obtained straightforwardly with similar arguments.

3.1.1 Leap-frog finite difference method

Here and in the following we call $\mathbf{V} = \dot{\mathbf{U}}$ the vector of nodal velocities and we prescribe initial conditions $\mathbf{U}(0) = \mathbf{u}_0$ and $\mathbf{V}(0) = \mathbf{u}_1$.Consider the system (2.54). Let now subdivide the interval $(0, T]$ into N subinterval of amplitude $\Delta t = T/N$ and set $t_n = n\Delta t$, for $n = 1, ..., N$.

Time integration for the DGSE method

The Newmark method [94] applied to (2.54) consists in finding the approximations $\{\mathbf{U}(t_n)\}_n$ to $\mathbf{u}(t_n)$ such that

$$[\underline{\mathrm{M}} + \Delta t^2\beta(\underline{\mathrm{A}} + \underline{\mathrm{B}})]\mathbf{U}(t_{n+1}) = \left[2\underline{\mathrm{M}} - \Delta t^2(\frac{1}{2} - 2\beta + \vartheta)(\underline{\mathrm{A}} + \underline{\mathrm{B}})\right]\mathbf{U}(t_n)$$
$$-[\underline{\mathrm{M}} + \Delta t^2(\frac{1}{2} + \beta - \vartheta)]\mathbf{U}(t_{n-1})$$
$$+\Delta t^2[\beta\mathbf{F}^{ext}(t_{n+1}) + (\frac{1}{2} - 2\beta + \vartheta)\mathbf{F}^{ext}(t_n) + (\frac{1}{2} + \beta - \vartheta)\mathbf{F}^{ext}(t_{n-1})], \quad n \geq 2, \quad (3.1)$$

with

$$[\underline{\mathrm{M}} + \Delta t^2\beta(\underline{\mathrm{A}} + \underline{\mathrm{B}})]\mathbf{U}(t_1) = \left[\underline{\mathrm{M}} - \Delta t^2(\frac{1}{2} - \beta)(\underline{\mathrm{A}} + \underline{\mathrm{B}})\right]\mathbf{U}(t_0) - \Delta t\underline{\mathrm{M}}\mathbf{V}(t_0)$$
$$+\Delta t^2[\beta\mathbf{F}^{ext}(t_1) + (\frac{1}{2} - \beta)\mathbf{F}^{ext}(t_0)]. \quad (3.2)$$

Notice that, at each time step t_{n+1} the solution of (3.3) can be obtained provided $\mathbf{U}(t_n)$ and $\mathbf{U}(t_{n-1})$ are known.

Here, $\beta \geq 0$ and $\vartheta \geq \frac{1}{2}$ are parameters to be chosen. We recall that for $\vartheta = \frac{1}{2}$ the Newmark scheme is second order accurate in time, whereas it is only first order accurate for $\vartheta > \frac{1}{2}$. For $\beta = 0$ the Newmark scheme (3.2)-(3.1) requires at each time step the solution of a linear system with the mass matrix $\underline{\mathrm{M}}$. However, because elements are decoupled, $\underline{\mathrm{M}}$ is block-diagonal with each block of size equal to the number of degrees of freedom in the element. Therefore, it can be inverted at very low computational cost and the scheme is essentially fully explicit. Indeed, due to the choice of the basis functions, $\underline{\mathrm{M}}$ reduces to a diagonal matrix, cf. Section (2.4). With $\vartheta = \frac{1}{2}$, the explicit Newmark method corresponds to the standard leap-frog scheme. For $\beta > 0$, the resulting scheme is implicit and involves the solution of a linear system of equations with a positive definite matrix $\underline{\mathrm{M}} + \Delta t^2\beta(\underline{\mathrm{A}} + \underline{\mathrm{B}})$ at each time step. We finally note that the second-order Newmark scheme with $\vartheta = \frac{1}{2}$ is unconditionally stable for $\beta \geq \frac{1}{4}$, whereas for $0 \leq \beta < \frac{1}{4}$ the time step Δt has to be restricted by a CFL condition, [94]. In the case $\beta = 0$, this restriction depends on the maximum eigenvalue of the matrix $\underline{\mathrm{A}} + \underline{\mathrm{B}}$, see Chapter 4 for more details. For $\vartheta = 1/2$ and $\beta = 0$, the explicit Newmark method (3.1) corresponds to the standard leap-frog scheme

$$\underline{\mathrm{M}}\mathbf{U}(t_{n+1}) = \left[2\underline{\mathrm{M}} - \Delta t^2(\underline{\mathrm{A}} + \underline{\mathrm{B}})\right]\mathbf{U}(t_n) - \underline{\mathrm{M}}\mathbf{U}(t_{n-1}) + \Delta t^2\mathbf{F}^{ext}(t_n), \quad (3.3)$$

for $n = 1, ..., N$, with

$$\underline{\mathrm{M}}\mathbf{U}(t_1) = \left[\underline{\mathrm{M}} - \frac{\Delta t^2}{2}(\underline{\mathrm{A}} + \underline{\mathrm{B}})\right]\mathbf{U}(t_0) - \Delta t\underline{\mathrm{M}}\mathbf{V}(t_0) + \frac{\Delta t^2}{2}\mathbf{F}^{ext}(t_0).$$

Time integration for the MSE method

Consider now the system (2.64) coming from the Mortar semi-discretization. Setting $\vartheta = 1/2$ and $\beta = 0$ in (3.2)-(3.1), the leap-frog scheme is given by

$$\widetilde{\underline{\mathrm{Q}}}^{\top}\widetilde{\underline{\mathrm{M}}}\widetilde{\underline{\mathrm{Q}}}\mathbf{U}_{ms}(t_{n+1}) = \widetilde{\underline{\mathrm{Q}}}^{\top}[(2\widetilde{\underline{\mathrm{M}}} - \Delta t^2\widetilde{\underline{\mathrm{A}}})\widetilde{\underline{\mathrm{Q}}}\mathbf{U}_{ms}(t_n) - \widetilde{\underline{\mathrm{M}}}\widetilde{\underline{\mathrm{Q}}}\mathbf{U}_{ms}(t_{n-1}) + \Delta t^2\mathbf{F}^{ext}(t_n)], \quad n \geq 2, \tag{3.4}$$

with

$$\widetilde{\underline{\mathrm{Q}}}^{\top}\widetilde{\underline{\mathrm{M}}}\widetilde{\underline{\mathrm{Q}}}\mathbf{U}_{ms}(t_1) = \widetilde{\underline{\mathrm{Q}}}^{\top}[(\widetilde{\underline{\mathrm{M}}} - \frac{\Delta t^2}{2}\widetilde{\underline{\mathrm{A}}})\widetilde{\underline{\mathrm{Q}}}\mathbf{U}_{ms}(t_0) - \Delta t\widetilde{\underline{\mathrm{M}}}\widetilde{\underline{\mathrm{Q}}}\mathbf{V}_{ms}(t_0) + \frac{\Delta t^2}{2}\mathbf{F}^{ext}(t_n)].$$

Here and in the following the abbreviations *ms* and *sl* stand for *master* and *slave*, respectively. In the MSE method the matrix $\widetilde{\underline{\mathrm{Q}}}^{\top}\widetilde{\underline{\mathrm{M}}}\widetilde{\underline{\mathrm{Q}}}$ is non-diagonal, but taking advantage of the structure of $\widetilde{\underline{\mathrm{Q}}}$ it is possible to split the linear system (3.4) as follows

$$\begin{bmatrix} \underline{\mathrm{M}}^{\mathcal{I}}_{ms} & 0 \\ 0 & \widetilde{\underline{\mathrm{M}}}^{\mathcal{S}}_{ms} \end{bmatrix} \begin{bmatrix} \mathbf{U}^{\mathcal{I}}_{ms}(t_{n+1}) \\ \mathbf{U}^{\mathcal{S}}_{ms}(t_{n+1}) \end{bmatrix} = \begin{bmatrix} \mathbf{b}^{\mathcal{I}}_{ms} \\ \widetilde{\mathbf{b}}^{\mathcal{S}}_{ms} \end{bmatrix}, \quad n \geq 2, \tag{3.5}$$

with

$$\mathbf{b} = [(2\widetilde{\underline{\mathrm{M}}} - \Delta t^2\widetilde{\underline{\mathrm{A}}})\widetilde{\underline{\mathrm{Q}}}\mathbf{U}(t_n) - \widetilde{\underline{\mathrm{M}}}\widetilde{\underline{\mathrm{Q}}}\mathbf{U}(t_{n-1}) + \Delta t^2\mathbf{F}^{ext}(t_n)], \quad n \geq 2,$$

and where

$$\widetilde{\underline{\mathrm{M}}}^{\mathcal{S}}_{ms} = \begin{bmatrix} \underline{\mathrm{M}}^{\mathcal{S},1}_{ms} + \underline{Q}^{\top}\underline{\mathrm{M}}^{\mathcal{S},1}_{sl}\underline{Q} & \underline{0} \\ \underline{0} & \underline{\mathrm{M}}^{\mathcal{S},2}_{ms} + \underline{Q}^{\top}\underline{\mathrm{M}}^{\mathcal{S},2}_{sl}\underline{Q} \end{bmatrix} \quad \text{and} \quad \widetilde{\mathbf{b}}^{\mathcal{S}}_{ms} = \begin{bmatrix} \mathbf{b}^{\mathcal{S},1}_{ms} + \underline{Q}^{\top}\mathbf{b}^{\mathcal{S},1}_{sl} \\ \mathbf{b}^{\mathcal{S},2}_{ms} + \underline{Q}^{\top}\mathbf{b}^{\mathcal{S},2}_{sl} \end{bmatrix}. \tag{3.6}$$

The superscripts $\mathcal{I}$ and $\mathcal{S}$ identify those unknowns belonging to the interior or to the skeleton of the domain respectively.

At each time step, it is possible to solve separately the two blocks of the linear system (3.5). The first block is diagonal and then easily solvable. The second one is a block matrix with identical blocks on the diagonal. Then, we perform the LU-factorization (see [91]) of one of the two blocks and then we solve separately for the two components. This technique does not increase too much the computational cost because of the very low dimension of this system with respect to the full one (3.5).

3.1.2 Runge-Kutta 4

We now move on the description of Runge-Kutta time integration scheme, starting from the four-stage Runge-Kutta method.

Time integration for the DGSE method

Using the notation introduced in Section 3.1.1, we rewrite (2.54) as the following first order system of equations

$$\begin{bmatrix} \underline{\mathrm{I}} & \underline{0} \\ \underline{0} & \underline{\mathrm{M}} \end{bmatrix} \begin{bmatrix} \dot{\mathbf{U}}(t) \\ \dot{\mathbf{V}}(t) \end{bmatrix} = \begin{bmatrix} \underline{0} & \underline{\mathrm{I}} \\ -(\underline{A}+\underline{\mathrm{B}}) & \underline{0} \end{bmatrix} \begin{bmatrix} \mathbf{U}(t) \\ \mathbf{V}(t) \end{bmatrix} + \begin{bmatrix} \mathbf{0} \\ \mathbf{F}^{ext}(t) \end{bmatrix}, \tag{3.7}$$

where $\underline{\mathrm{I}}$ is the identity matrix. Now, setting $\mathbf{W}(t) = [\mathbf{U}(t)\ \ \mathbf{V}(t)]^\top$, (3.7) becomes

$$\dot{\mathbf{W}}(t) = \mathbf{g}(t, \mathbf{W}(t)), \tag{3.8}$$

with

$$\mathbf{g}(t, \mathbf{W}(t)) = \begin{bmatrix} \underline{0} & \underline{\mathrm{I}} \\ -\underline{\mathrm{M}}^{-1}(\underline{A}+\underline{\mathrm{B}}) & \underline{0} \end{bmatrix} \mathbf{W}(t) + \begin{bmatrix} \mathbf{0} \\ \underline{\mathrm{M}}^{-1}\mathbf{F}^{ext}(t) \end{bmatrix}. \tag{3.9}$$

The Runge-Kutta method can be written as

$$\mathbf{W}(t_{n+1}) = \mathbf{W}(t_n) + \Delta t \mathbf{G}(t_n, \mathbf{W}(t_n)), \tag{3.10}$$

where $\mathbf{G}$ is the incremental function defined as

$$\begin{aligned} \mathbf{G}(t_n, \mathbf{W}(t_n)) &= \sum_{i=1}^{s} b_i \mathbf{K}_i, \\ \mathbf{K}_i &= \mathbf{g}(t_n + c_i \Delta t, \mathbf{W}(t_n) + \Delta t \sum_{j=1}^{s} a_{ij} \mathbf{K}_j), \quad i = 1, 2, ..., 4. \end{aligned}$$

The coefficients $\{a_{ij}\}, \{c_i\}$ and $\{b_i\}$ fully characterize the RK methods and they are collected in the following Butcher array, [91]

$$\begin{array}{c|cccc} c_1 & a_{11} & a_{12} & \cdots & a_{14} \\ c_2 & a_{21} & a_{22} & & a_{24} \\ c_3 & \vdots & & \ddots & \vdots \\ c_4 & a_{41} & a_{42} & \cdots & a_{44} \\ \hline & b_1 & b_2 & \cdots & b_4 \end{array}$$

where the following condition holds

$$c_i = \sum_{j=1}^{4} a_{ij}, \quad i = 1, ..., 4.$$

If the coefficients a_{ij} are equal to zero for $j \geq i$, with $i = 1, 2, ..., 4$, then each $\mathbf{K}_i$ can be explicitly computed in term of $i-1$ coefficients $\mathbf{K}_1, ..., \mathbf{K}_{i-1}$ that have already been determined. In such a case the RK method is explicit. Otherwise, it is implicit and solving a non-linear system of size 4 is necessary for computing the coefficients of $\mathbf{K}_i$. In the case we are interested in, i.e. the fourth order explicit RK4, the Butcher array takes the form

$$\begin{array}{c|cccc} 0 & & & & \\ \frac{1}{2} & \frac{1}{2} & & & \\ \frac{1}{2} & 0 & \frac{1}{2} & & \\ 1 & 0 & 0 & 1 & \\ \hline & \frac{1}{6} & \frac{1}{3} & \frac{1}{3} & \frac{1}{6} \end{array}$$

and consequently (3.10) becomes

$$\mathbf{W}(t_{n+1}) = \mathbf{W}(t_n) + \frac{\Delta t}{6} \left(\mathbf{K}_1 + 2\mathbf{K}_2 + 2\mathbf{K}_3 + \mathbf{K}_4 \right), \tag{3.11}$$

where

$$\begin{aligned} \mathbf{K}_1 &= \mathbf{g}(t_n, \mathbf{W}(t_n)), \\ \mathbf{K}_2 &= \mathbf{g}(t_{n+\frac{1}{2}}, \mathbf{W}(t_n) + \frac{\Delta t}{2}\mathbf{K}_1), \\ \mathbf{K}_3 &= \mathbf{g}(t_{n+\frac{1}{2}}, \mathbf{W}(t_n) + \frac{\Delta t}{2}\mathbf{K}_2), \\ \mathbf{K}_4 &= \mathbf{g}(t_{n+1}, \mathbf{W}(t_n) + \Delta t \mathbf{K}_3). \end{aligned}$$

Notice that, since $\sum_{i=1}^{4} b_i = 1$, the RK4 method is consistent [25]. Moreover 4 is the maximum number of stages for which the order of the method is not less than the number of stages itself, see [68, 91] for details. Notice that the number of unknowns in (3.11) is twice with respect to the LF scheme and five different vectors $\mathbf{K}_1, ..., \mathbf{K}_4$ and $\mathbf{W}(t_n)$ must be stored at each time step to compute the solution at the next time step.

Time integration for the MSE method

As in the previous case we rewrite (2.64) as the following first order system of equations

$$\begin{bmatrix} \widetilde{\underline{\mathrm{Q}}}^{\top}\widetilde{\underline{\mathrm{I}}}\widetilde{\underline{\mathrm{Q}}} & \underline{0} \\ \underline{0} & \widetilde{\underline{\mathrm{Q}}}^{\top}\widetilde{\underline{\mathrm{M}}}\widetilde{\underline{\mathrm{Q}}} \end{bmatrix} \begin{bmatrix} \dot{\mathbf{U}}(t) \\ \dot{\mathbf{V}}(t) \end{bmatrix} = \begin{bmatrix} \underline{0} & \widetilde{\underline{\mathrm{Q}}}^{\top}\widetilde{\underline{\mathrm{I}}}\widetilde{\underline{\mathrm{Q}}} \\ -\widetilde{\underline{\mathrm{Q}}}^{\top}\widetilde{\underline{\mathrm{A}}}\widetilde{\underline{\mathrm{Q}}} & \underline{0} \end{bmatrix} \begin{bmatrix} \mathbf{U}(t) \\ \mathbf{V}(t) \end{bmatrix} + \begin{bmatrix} \mathbf{0} \\ \widetilde{\underline{\mathrm{Q}}}^{\top}\mathbf{F}^{ext}(t) \end{bmatrix}. \tag{3.12}$$

Setting $\widetilde{\underline{\mathrm{H}}}_{ms} = \mathrm{diag}(\underline{\mathrm{H}}^1_{ms} + \underline{Q}^{\top}\underline{\mathrm{H}}^1_{sl}\underline{Q},\ \underline{\mathrm{H}}^2_{ms} + \underline{Q}^{\top}\underline{\mathrm{H}}^2_{sl}\underline{Q})$, for $\underline{\mathrm{H}} = \underline{\mathrm{I}}, \underline{\mathrm{A}}, \underline{\mathrm{M}}$ and $\widetilde{\mathbf{F}}^{ext}_{ms}$ and taking advantage of the structure of $\widetilde{\underline{\mathrm{Q}}}$ it is possible to rewrite the above system in the form

$$\begin{bmatrix} \underline{\mathrm{I}}^{\mathcal{I}}_{ms} & \underline{0} & \underline{0} & \underline{0} \\ \underline{0} & \widetilde{\underline{\mathrm{I}}}^{\mathcal{S}}_{ms} & \underline{0} & \underline{0} \\ \underline{0} & \underline{0} & \underline{\mathrm{M}}^{\mathcal{I}}_{ms} & \underline{0} \\ \underline{0} & \underline{0} & \underline{0} & \widetilde{\underline{\mathrm{M}}}^{\mathcal{S}}_{ms} \end{bmatrix} \begin{bmatrix} \dot{\mathbf{U}}^{\mathcal{I}}_{ms}(t) \\ \dot{\mathbf{U}}^{\mathcal{S}}_{ms}(t) \\ \dot{\mathbf{V}}^{\mathcal{I}}_{ms}(t) \\ \dot{\mathbf{V}}^{\mathcal{S}}_{ms}(t) \end{bmatrix} = \begin{bmatrix} \underline{0} & \underline{0} & \underline{\mathrm{I}}^{\mathcal{I}}_{ms} & \underline{0} \\ \underline{0} & \underline{0} & \underline{0} & \widetilde{\underline{\mathrm{I}}}^{\mathcal{S}}_{ms} \\ -\underline{\mathrm{A}}^{\mathcal{I}}_{ms} & \underline{0} & \underline{0} & \underline{0} \\ \underline{0} & -\widetilde{\underline{\mathrm{A}}}^{\mathcal{S}}_{ms} & \underline{0} & \underline{0} \end{bmatrix} \begin{bmatrix} \mathbf{U}^{\mathcal{I}}_{ms}(t) \\ \mathbf{U}^{\mathcal{S}}_{ms}(t) \\ \mathbf{V}^{\mathcal{I}}_{ms}(t) \\ \mathbf{V}^{\mathcal{S}}_{ms}(t) \end{bmatrix} + \begin{bmatrix} \mathbf{0} \\ \mathbf{0} \\ \mathbf{F}^{ext,\mathcal{I}}_{ms}(t) \\ \widetilde{\mathbf{F}}^{ext,\mathcal{S}}_{ms}(t) \end{bmatrix}, \tag{3.13}$$

Let $\mathbf{W}^{\mathcal{I}}_{ms}(t) = [\mathbf{U}^{\mathcal{I}}_{ms}(t)\ \ \mathbf{V}^{\mathcal{I}}_{ms}(t)]^{\top}$ (resp. $\mathbf{W}^{\mathcal{S}}_{ms}(t) = [\mathbf{U}^{\mathcal{S}}_{ms}(t)\ \ \mathbf{V}^{\mathcal{S}}_{ms}(t)]^{\top}$) be the vector containing the *master* nodal displacements and velocities, belonging to the interior (resp. skeleton) of the domain.

Then, we decouple (3.13) in two linear systems of the following form

$$\dot{\mathbf{W}}^{\mathcal{I}}_{ms}(t) = \mathbf{g}_1(t, \mathbf{W}^{\mathcal{I}}_{ms}(t)), \tag{3.14}$$

where

$$\mathbf{g}_1(t, \mathbf{W}(t)) = \begin{bmatrix} \underline{0} & \underline{\mathrm{I}}^{\mathcal{I}}_{ms} \\ -(\underline{\mathrm{M}}^{\mathcal{I}}_{ms})^{-1}\underline{\mathrm{A}}^{\mathcal{I}}_{ms} & \underline{0} \end{bmatrix} \mathbf{W}(t) + \begin{bmatrix} \mathbf{0} \\ \mathbf{F}^{ext,\mathcal{I}}_{ms}(t) \end{bmatrix}, \tag{3.15}$$

and

$$\underline{\mathrm{N}}^{\mathcal{S}}_{ms}\dot{\mathbf{W}}^{\mathcal{S}}_{ms}(t) = \mathbf{g}_2(t, \mathbf{W}^{\mathcal{S}}_{ms}(t)), \tag{3.16}$$

where

$$\underline{\mathrm{N}}^{\mathcal{S}}_{ms} = \begin{bmatrix} \widetilde{\underline{\mathrm{I}}}^{\mathcal{S}}_{ms} & \underline{0} \\ \underline{0} & \widetilde{\underline{\mathrm{M}}}^{\mathcal{S}}_{ms} \end{bmatrix} \quad \text{and} \quad \mathbf{g}_2(t, \mathbf{W}) = \begin{bmatrix} \underline{0} & \widetilde{\underline{\mathrm{I}}}^{\mathcal{S}}_{ms} \\ -\widetilde{\underline{\mathrm{A}}}^{\mathcal{S}}_{ms} & \underline{0} \end{bmatrix} \mathbf{W}(t) + \begin{bmatrix} \mathbf{0} \\ \widetilde{\mathbf{F}}^{ext,\mathcal{S}}_{ms}(t) \end{bmatrix}. \tag{3.17}$$

On the one hand the RK4 method applied to (3.14) produces a time integration scheme similar to that described in Section 3.1.2. On the other hand when RK4 is derived for (3.16), at each intermediate step between t_n and t_{n+1} we need to solve four linear systems. In fact, in this last case RK4 method reads

$$\underline{\mathrm{N}}^{\mathcal{S}}_{ms}\dot{\mathbf{W}}^{\mathcal{S}}_{ms}(t_{n+1}) = \underline{\mathrm{N}}^{\mathcal{S}}_{ms}\dot{\mathbf{W}}^{\mathcal{S}}_{ms}(t_n) + \frac{\Delta t}{6}\left(\mathbf{K}^{\mathcal{S}}_{ms,1} + 2\mathbf{K}^{\mathcal{S}}_{ms,2} + 2\mathbf{K}^{\mathcal{S}}_{ms,3} + \mathbf{K}^{\mathcal{S}}_{ms,4}\right),$$

with

$$\begin{aligned}
\underline{\mathrm{N}}^{\mathcal{S}}_{ms}\mathbf{K}^{\mathcal{S}}_{ms,1} &= \mathbf{g}_2(t_n, \mathbf{W}(t_n)), \\
\underline{\mathrm{N}}^{\mathcal{S}}_{ms}\mathbf{K}^{\mathcal{S}}_{ms,2} &= \mathbf{g}_2(t_{n+\frac{1}{2}}, \mathbf{W}(t_n) + \frac{\Delta t}{2}\mathbf{K}^{\mathcal{S}}_{ms,1}), \\
\underline{\mathrm{N}}^{\mathcal{S}}_{ms}\mathbf{K}^{\mathcal{S}}_{ms,3} &= \mathbf{g}_2(t_{n+\frac{1}{2}}, \mathbf{W}(t_n) + \frac{\Delta t}{2}\mathbf{K}^{\mathcal{S}}_{ms,2}), \\
\underline{\mathrm{N}}^{\mathcal{S}}_{ms}\mathbf{K}^{\mathcal{S}}_{ms,4} &= \mathbf{g}_2(t_{n+1}, \mathbf{W}(t_n) + \Delta t\mathbf{K}^{\mathcal{S}}_{ms,3}).
\end{aligned} \tag{3.18}$$

Fortunately, as described in Section 3.1.2 each system in (3.18) has the same structure as (3.6) and involves only *master* unknowns on the skeleton. For this reason, even in this case it is possible to solve each linear system in (3.18) in a low computational cost, for example with an LU-factorization, [91]. We also remark that, as usual, *slave* unknowns on the interfaces are recovered using the *master* ones. In particular, we have that

$$\mathbf{W}^{\mathcal{S}}_{sl}(t) = \begin{bmatrix} \mathbf{U}^{\mathcal{S}}_{sl}(t) \\ \mathbf{V}^{\mathcal{S}}_{sl}(t) \end{bmatrix} = \begin{bmatrix} \underline{Q} & \underline{0} \\ \underline{0} & \underline{Q} \end{bmatrix} \begin{bmatrix} \mathbf{U}^{\mathcal{S}}_{ms}(t) \\ \mathbf{V}^{\mathcal{S}}_{ms}(t) \end{bmatrix} = \begin{bmatrix} \underline{Q} & \underline{0} \\ \underline{0} & \underline{Q} \end{bmatrix} \mathbf{W}^{\mathcal{S}}_{ms}(t), \tag{3.19}$$

and then

$$\mathbf{K}^{\mathcal{S}}_{sl,i} = \begin{bmatrix} \underline{Q} & \underline{0} \\ \underline{0} & \underline{Q} \end{bmatrix} \mathbf{K}^{\mathcal{S}}_{ms,i}, \quad i = 1, ..., 4.$$

To ensure stability, the explicit LF and RK4 schemes must satisfy the usual Courant-Friedrichs-Levy (CFL) condition (see [92]) that imposes a restriction on Δt. We see in Chapter 4 that this limitation is proportional to the minimal distance between two neighbouring spectral nodes of the numerical grid. Since this distance scales as $h_k N_k^{-2}$ (h_k size of the spectral element Ω_k), the stability requirement on Δt may become too restrictive for very large polynomial degrees N_k. For these cases an implicit time scheme is recommended.

3.1.3 Implicit midpoint method

To derive the expression of the implicit midpoint (IM) method for the time integration of the DGSE and Mortar semi-discrete formulations we proceed as follows.

Time integration for the DGSE method

Let us start considering the following system of ordinary differential equations

$$\begin{cases} \dot{\mathbf{W}}(t) = \mathbf{g}(t, \mathbf{W}(t)), \quad t \in [0, T], \\ \mathbf{W}(0) = \mathbf{W}_0, \end{cases} \tag{3.20}$$

where $\mathbf{g}(t, \mathbf{W}(t))$ is the real vector-valued function defined in (3.9). Since $\mathbf{g}$ is linear and continuous with respect to t, then the solution of (3.20) satisfies

$$\mathbf{W}(t) - \mathbf{W}_0 = \int_0^t \mathbf{g}(\tau, \mathbf{W}(\tau)). \tag{3.21}$$

Now, if a quadrature formula with s nodes in (t_n, t_{n+1}) is employed to approximate the integral of $\mathbf{g}$, which we assume for simplicity to depend only on t, we get

$$\int_{t_n}^{t_{n+1}} \mathbf{g}(\tau) \approx \Delta t \sum_{i=1}^{s} b_i \mathbf{g}(t_n + c_j \Delta t),$$

having denoted by b_j the weights and by $t_n + c_j \Delta t$ the quadrature nodes. It can be proved (see [25]) that for any RK formula (3.10), there exists a correspondence between the coefficients b_j, c_j of the formula and the weights and nodes of a Gauss quadrature rule (see, [68], Section 5.11). Once the s coefficients c_j have been found, we can construct RK methods of order $2s$, by determining the coefficients a_{ij} and b_j as being the solutions of the linear systems

$$\begin{aligned} \sum_{j=1}^{s} c_j^{k-1} a_{ij} &= \frac{1}{k} c_i^k, \quad k = 1, 2, ..., s, \quad i = 1, ..., s, \\ \sum_{j=1}^{s} c_j^{k-1} b_j &= 1/k, \quad k = 1, ..., s. \end{aligned}$$

In particular, if Gauss-Legendre quadrature rule is employed, it is possible to attain the maximum possible order $2s$ for a fixed number of stages s. The IM is a special one step method of order two of the form

$$\mathbf{W}(t_{n+1}) = \mathbf{W}(t_n) + \Delta t \mathbf{g}\left(t_n + \frac{\Delta t}{2}, \frac{\mathbf{W}(t_n) + \mathbf{W}(t_{n+1})}{2}\right), \quad n = 0, ..., N, \qquad \begin{array}{c|c} \frac{1}{2} & \frac{1}{2} \\ \hline 0 & 1 \end{array}. \tag{3.22}$$

The IM method applied to DGSE discretization becomes

$$\begin{bmatrix} \underline{\mathrm{I}} & -\frac{\Delta t}{2}\underline{\mathrm{I}} \\ \frac{\Delta t}{2}(\underline{\mathrm{A}} + \underline{\mathrm{B}}) & \underline{\mathrm{M}} \end{bmatrix} \begin{bmatrix} \mathbf{U}(t_{n+1}) \\ \mathbf{V}(t_{n+1}) \end{bmatrix} = \begin{bmatrix} \underline{\mathrm{I}} & \frac{\Delta t}{2}\underline{\mathrm{I}} \\ -\frac{\Delta t}{2}(\underline{\mathrm{A}} + \underline{\mathrm{B}}) & \underline{\mathrm{M}} \end{bmatrix} \begin{bmatrix} \mathbf{U}(t_n) \\ \mathbf{V}(t_n) \end{bmatrix} + \begin{bmatrix} \mathbf{0} \\ \Delta t \mathbf{F}^{ext}(t_{n+\frac{1}{2}}) \end{bmatrix}, \tag{3.23}$$

The solution of (3.23) is obtained as follows. From the first equation of (3.23) we deduce that

$$\mathbf{U}(t_{n+1}) = \mathbf{U}(t_n) + \frac{\Delta t}{2}(\mathbf{V}(t_n) + \mathbf{V}(t_{n+1})). \tag{3.24}$$

Then, by substituting (3.24) in the second equation of (3.23) we obtain

$$\left[\frac{\Delta t}{4}(\underline{\mathrm{A}} + \underline{\mathrm{B}}) + \underline{\mathrm{M}}\right] \mathbf{V}(t_{n+1}) = \mathbf{b} \tag{3.25}$$

with

$$\mathbf{b} = \mathbf{F}^{ext}(t_{n+\frac{1}{2}}) - (\underline{\mathrm{A}} + \underline{\mathrm{B}})\mathbf{U}(t_n) - \left[\frac{\Delta t}{4}(\underline{\mathrm{A}} + \underline{\mathrm{B}}) - \underline{\mathrm{M}}\right] \mathbf{V}(t_n).$$

Due to (2.18) we have that the matrix in (3.25) is positive definite (thus invertible). Moreover it is symmetric if the SIPG method (2.7) is considered. So, at least in this case, the Conjugate Gradient method can be used to solve the linear systems (3.25).
If absorbing boundary conditions are taken into account equation (3.25) becomes

$$\left[\frac{\Delta t}{4}(\underline{\mathrm{A}} + \underline{\mathrm{B}} - \underline{\mathrm{R}}) + \underline{\mathrm{M}} - \frac{\Delta t}{2}\underline{\mathrm{S}}\right] \mathbf{V}(t_{n+1}) = \mathbf{b}$$

where the matrices $\underline{\mathrm{R}}$ and $\underline{\mathrm{S}}$ are defined in (2.70) and (2.73), respectively,

$$\mathbf{b} = \mathbf{F}^{ext}(t_{n+\frac{1}{2}}) - (\underline{\mathrm{A}} + \underline{\mathrm{B}} - \underline{\mathrm{R}})\mathbf{U}(t_n) - \left[\frac{\Delta t}{4}(\underline{\mathrm{A}} + \underline{\mathrm{B}} - \underline{\mathrm{R}}) + \underline{\mathrm{M}} - \frac{\Delta t}{2}\underline{\mathrm{S}}\right] \mathbf{V}(t_n).$$

In this case the resulting matrix is non-symmetric, even if the SIPG method is considered. Then, a preconditioned iterative method is mandatory. For example one can use the ILUT factorization and then the GMRES method, see [91].

Time integration for the MSE method

In order to write the final linear systems coming from the IM time discretization we subdivide the unknowns in *master* and *slave* ones using the notation introduced in Section 3.1.2. For interior unknowns $\mathbf{W}^{\mathcal{I}}_{ms}(t) = [\mathbf{U}^{\mathcal{I}}_{ms}(t)\ \mathbf{V}^{\mathcal{I}}_{ms}(t)]^\top$ the IM method reduces to

$$\mathbf{W}^{\mathcal{I}}_{ms}(t_{n+1}) = \mathbf{W}^{\mathcal{I}}_{ms}(t_n) + \Delta t \mathbf{g}_1\left(t_n + \frac{\Delta t}{2}, \frac{\mathbf{W}(t_n) + \mathbf{W}(t_{n+1})}{2}\right), \quad n = 0, ..., N-1,$$

where $\mathbf{g}_1$ is defined as in (3.15). In matrix notation the above equation becomes

$$\begin{bmatrix} \underline{\mathrm{I}}^{\mathcal{I}}_{ms} & -\frac{\Delta t}{2}\underline{\mathrm{I}}^{\mathcal{I}}_{ms} \\ \frac{\Delta t}{2}\underline{\mathrm{A}}^{\mathcal{I}}_{ms} & \underline{\mathrm{M}}^{\mathcal{I}}_{ms} \end{bmatrix} \begin{bmatrix} \mathbf{U}^{\mathcal{I}}_{ms}(t_{n+1}) \\ \mathbf{V}^{\mathcal{I}}_{ms}(t_{n+1}) \end{bmatrix} = \begin{bmatrix} \underline{\mathrm{I}}^{\mathcal{I}}_{ms} & \frac{\Delta t}{2}\underline{\mathrm{I}}^{\mathcal{I}} \\ -\frac{\Delta t}{2}\underline{\mathrm{A}}^{\mathcal{I}}_{ms} & \underline{\mathrm{M}}^{\mathcal{I}}_{ms} \end{bmatrix} \begin{bmatrix} \mathbf{U}^{\mathcal{I}}_{ms}(t_n) \\ \mathbf{V}^{\mathcal{I}}_{ms}(t_n) \end{bmatrix} + \begin{bmatrix} \mathbf{0} \\ \Delta t \mathbf{F}^{ext,\mathcal{I}}_{ms}(t_{n+\frac{1}{2}}) \end{bmatrix}, \tag{3.26}$$

for $n = 0, ..., N-1$, which is similar to (3.23).
For *master* skeleton unknowns $\mathbf{W}^{\mathcal{S}}_{ms}(t) = [\mathbf{U}^{\mathcal{S}}_{ms}(t)\ \mathbf{V}^{\mathcal{S}}_{ms}(t)]^{\top}$, at each time level we have

$$\mathbf{W}^{\mathcal{S}}_{ms}(t_{n+1}) = \mathbf{W}^{\mathcal{S}}_{ms}(t_n) + \Delta t \mathbf{g}_2\left(t_n + \frac{\Delta t}{2}, \frac{\mathbf{W}(t_n) + \mathbf{W}(t_{n+1})}{2}\right), \quad n = 0, ..., N-1,$$

where $\mathbf{g}_2$ is defined in (3.17), or equivalently

$$\begin{bmatrix} \widetilde{\underline{\mathrm{I}}}^{\mathcal{S}}_{ms} & -\frac{\Delta t}{2}\widetilde{\underline{\mathrm{I}}}^{\mathcal{S}}_{ms} \\ \frac{\Delta t}{2}\widetilde{\underline{\mathrm{A}}}^{\mathcal{S}}_{ms} & \widetilde{\underline{\mathrm{M}}}^{\mathcal{S}}_{ms} \end{bmatrix} \begin{bmatrix} \mathbf{U}^{\mathcal{S}}_{ms}(t_{n+1}) \\ \mathbf{V}^{\mathcal{S}}_{ms}(t_{n+1}) \end{bmatrix} = \begin{bmatrix} \widetilde{\underline{\mathrm{I}}}^{\mathcal{S}}_{ms} & \frac{\Delta t}{2}\widetilde{\underline{\mathrm{I}}}^{\mathcal{S}} \\ -\frac{\Delta t}{2}\widetilde{\underline{\mathrm{A}}}^{\mathcal{S}}_{ms} & \widetilde{\underline{\mathrm{M}}}^{\mathcal{S}}_{ms} \end{bmatrix} \begin{bmatrix} \mathbf{U}^{\mathcal{S}}_{ms}(t_n) \\ \mathbf{V}^{\mathcal{S}}_{ms}(t_n) \end{bmatrix} + \begin{bmatrix} \mathbf{0} \\ \Delta t \widetilde{\mathbf{F}}^{ext,\mathcal{S}}_{ms}(t_{n+\frac{1}{2}}) \end{bmatrix}. \tag{3.27}$$

Then, we project the solution of (3.27) to recover the *slave* unknowns $\mathbf{W}^{\mathcal{S}}_{sl}(t_{n+1})$ at the interfaces. As for DGSE discretization to solve both systems (3.26)-(3.27) we the GMRES iterative method preconditioned by the ILUT factorization.

3.2 Fully-discrete error estimates

As mentioned at the beginning of this chapter, we sketch the proof of the fully discrete error estimates form the DG and Mortar formulations. We recall that the discrete formulation of problems (2.7) and (2.12) is obtained by approximating time derivatives with either LF, RK4 or IM methods as described in Section 3.1. For the LF scheme, at each time step $t_n = n\Delta t$, $n \geq 2$, the problem reads: find $\mathbf{u}_\delta(t_n) \in V_\delta$ such that

$$\sum_{k=1}^{K} \frac{1}{\Delta t^2}\left(\rho(\mathbf{u}_\delta(t_n) - 2\mathbf{u}_\delta(t_{n-1}) + \mathbf{u}_\delta(t_{n-2})), \mathbf{v}\right)_{\Omega_k} + \sum_{k=1}^{K} \mathcal{A}(\mathbf{u}_\delta(t_{n-1}), \mathbf{v})_{\Omega_k} + \sum_{j=1}^{M} \mathcal{B}(\mathbf{u}_\delta(t_{n-1}), \mathbf{v})_{\gamma_j} = \sum_{k=1}^{K} \mathcal{L}(\mathbf{v}_k) \quad \forall \mathbf{v} \in V_\delta \tag{3.28}$$

for the DGSE case, and: find $\mathbf{u}_\delta(t_n) \in V_\delta^{mortar}$ such that

$$\sum_{k=1}^{K} \frac{1}{\Delta t^2}\left(\rho(\mathbf{u}_\delta(t_n) - 2\mathbf{u}_\delta(t_{n-1}) + \mathbf{u}_\delta(t_{n-2})), \mathbf{v}\right)_{\Omega_k} + \sum_{k=1}^{K} \mathcal{A}(\mathbf{u}_\delta(t_{n-1}), \mathbf{v})_{\Omega_k} = \sum_{k=1}^{K} \mathcal{L}(\mathbf{v}_k) \quad \forall \mathbf{v} \in V_\delta^{mortar} \tag{3.29}$$

for the MSE case, respectively. Comparing the fully discrete solution (3.28) (resp. (3.29)) with the semi-discrete solution (2.7) (resp. (2.12)) using estimate (2.35) (resp. (2.51)) and standard techniques it is possible to prove the following result.

Theorem 4. *Suppose that* $\mathbf{u}_0, \mathbf{u}_1, \mathbf{f}, \mathbf{t}$ *and the solution* $\mathbf{u}$ *of (1.1) are sufficiently smooth. Then, there exists a constant* $C = C(\mathbf{u}_0, \mathbf{u}_1, \mathbf{f}, \mathbf{t}, \mathbf{u})$ *such that it holds*

$$||\mathbf{u}(t_n) - \mathbf{u}_{DG}(t_n)||_{DG} \leq C \left(\Delta t^2 + \sum_{k=1}^{K} \frac{h_k^{m_k-1}}{N_k^{s_k-3/2}} \right) \quad \forall n \geq 2,$$

for the DGSE method, and

$$||\mathbf{u}(t_n) - \mathbf{u}_M(t_n)||_* \leq C \left(\Delta t^2 + \sum_{k=1}^{K} \frac{h_k^{m_k-1}}{N_k^{s_k-1}} \right) \quad \forall n \geq 2,$$

for the MSE method, where $N_k \geq 1$ *and* $m_k = \min(N_k + 1, s_k)$.

See [97] for the proof. Since Runge-Kutta methods are non-linear with respect to $\mathbf{u}$ the proof of fully discrete estimates is more involved than that for the leap-frog scheme. We recall that the local truncation error $\boldsymbol{\tau}_{n+1}(\Delta t)$ at the observation time t_{n+1} of the RK method (3.10) is defined by the relation

$$\Delta t \boldsymbol{\tau}_{n+1}(\Delta t) = \mathbf{Y}(t_{n+1}) - \mathbf{Y}(t_n) - \Delta t \mathbf{G}(t_n, \mathbf{Y}(t_n)),$$

where $\mathbf{Y}(t)$ is the exact solution of the Cauchy problem (3.8) for the DGSE method or (3.14)-(3.16) for the MSE method. Moreover we have the following

Definition 1. *The method (3.10) is consistent if*

$$\boldsymbol{\tau}(\Delta t) = \max_n |\boldsymbol{\tau}_n(\Delta t)| \to 0 \quad as \quad \Delta t \to 0,$$

and it is of order $p \geq 1$ *with respect to* Δt *if*

$$\boldsymbol{\tau}(\Delta t) = \mathcal{O}(\Delta t^p) \quad as \quad \Delta t \to 0.$$

Since RK methods are one-step methods, consistency implies stability and, in turn, convergence. Since RK4 and IM methods are both consistent, estimates on the local truncation error can be derived [68]; however, these estimates are often too involved to be profitably used. We only recall that if a RK scheme has a local truncation error of order Δt^p, for any t_n, then also the convergence order will be equal to p, see [91]. For RK4 and IM methods it is possible to show that $p = 4$ and $p = 2$ respectively, as it is stated in the following

Proposition 1. *The order of an* $s-$*stage explicit RK method cannot be greater than* s. *Moreover, there do not exist* $s-$*stage explicit RK methods with order* s *if* $s \geq 5$. *As far as implicit schemes are concerned, the maximum achievable order using* s *stages is equal to* $2s$.

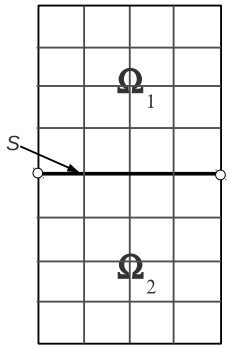

Figure 3.1: Domain decomposition where $\Omega = \Omega_1 \cup \Omega_2$. The skeleton $\mathcal{S} = \partial\Omega_1 \cap \partial\Omega_2$.

For the proof see [25].

Now, we consider the following test which has the aim of validating the convergence order for the LF, RK4 and IM coupled with DGSE and MSE discretizations. In particular we want to estimate the exponent p such that

$$||(\mathbf{u} - \mathbf{u}_\delta)(t)||_0 \leq C(\Delta t^p + o(\Delta t^p)), \quad \text{for } t \in [0, T], \tag{3.30}$$

where $\mathbf{u}_\delta$ can be either the discrete solution obtained with the DGSE ($\mathbf{u}_{DG}$) or the MSE ($\mathbf{u}_M$) methods. To validate the above result let us consider an elastic medium occupying the finite region $\Omega = (-\frac{1}{2}, \frac{1}{2}) \times (-1, 1)$ with $\Omega = \Omega_1 \cup \Omega_2$ and $h_1 = h_2 = \frac{1}{4}$, see Figure 3.1. We assume also that homogeneous Neumann boundary conditions are imposed on $\partial\Omega$, $\rho = 1$ and that the Lamé elastic coefficients are set equal to $\lambda = 0$ and $\mu = \frac{1}{2}$. Moreover, we impose initial conditions such that the exact solution for the problem (1.1) in Ω is

$$\mathbf{u}(x_1, x_2, t) = \sin(t) \begin{bmatrix} \sin(\pi x_1)\sin(\pi x_2) \\ \cos(\pi x_1)\cos(\pi x_2) \end{bmatrix}, \quad \text{for } t \in [0, T]. \tag{3.31}$$

Then we fix the polynomial order of approximation $N_1 = N_2 = 8$.

Since $\mathbf{u} \in \mathcal{C}^\infty([0, T], \boldsymbol{\mathcal{C}}^\infty(\Omega))$, we expect that the spatial-discretization error in Theroem 4 is negligible with respect to the time-discretization error. In Figure 3.2 we show the behaviour of the time-discretization error (3.30) for the LF, RK4 and IM schemes

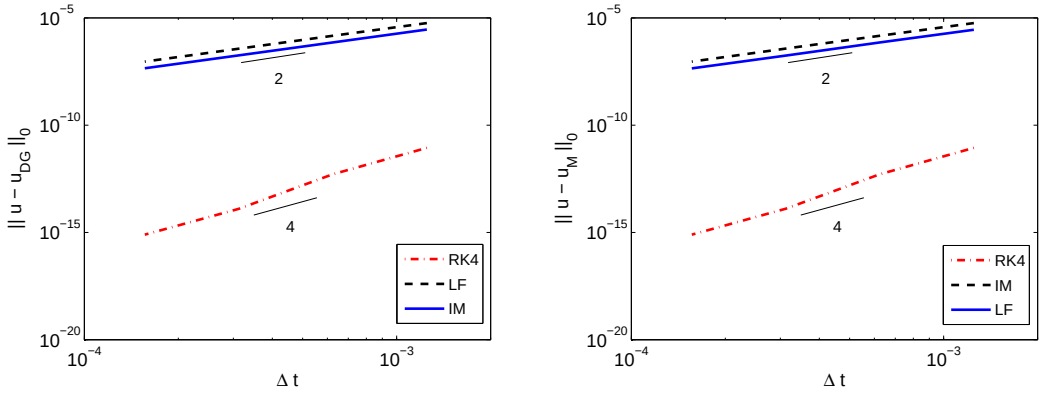

Figure 3.2: Computed error $||\mathbf{u}_\delta(T) - \mathbf{u}(T)||_{0,\Omega}$, $T = 20$, with respect to the time step Δt for the LF, RK4 and IM methods coupled with DGSE (left) and MSE (right) methods respectively.

coupled with DGSE and MSE space-discretization, respectively. As expected we obtain $p = 4$ for the RK4 and $p = 2$ for the LF and the IM methods.

Chapter 4

Analysis of grid dispersion, dissipation and stability

For wave propagation problems, the accuracy of the approximate solution relies on the dispersion and the dissipation properties of the numerical scheme employed. The dispersion and dissipation errors are the numerical noises related to grid spacing, which have a negative effect on accuracy. They occur because the computed velocity of high-frequency waves in the grid is different from the real velocity. This is called grid dispersion/dissipation because it is originated by the grid and it can occur even when the physical problem is not dispersive/dissipative. For instance, consider a displacement profile $\mathbf{u} = \mathbf{f}(x - \alpha t)$ that represents a travelling perturbation with velocity α in an unbounded homogeneous mono dimensional domain, see Figure 4.1. In this case, once the wave profile $\mathbf{f}(x)$ has been defined at the time $t = 0$, for $t = t^* > 0$ the profile will move undistorted in the direction of the x axis of the amount αt^*. When introducing a numerical scheme, the wave velocity in the computational grid is an approximation α_h of the real velocity α. The less α_h differs from α (low dispersion/dissipation) and the more the computed profile $\mathbf{u}_\delta$ will be similar to the exact displacement $\mathbf{u}$. On the other hand, the more the numerical velocity α_h differs from α the more $\mathbf{u}_\delta$ provides a rough approximation of $\mathbf{u}$, see Figure 4.1.

The grid dispersion error is defined as the relative error between the computed velocity α_h and real one α, i.e., $e = 1 - \alpha_h/\alpha$. In particular, since each elastic bi-dimensional wave can be written as a superposition of shear (S) and compressional (P) waves, we

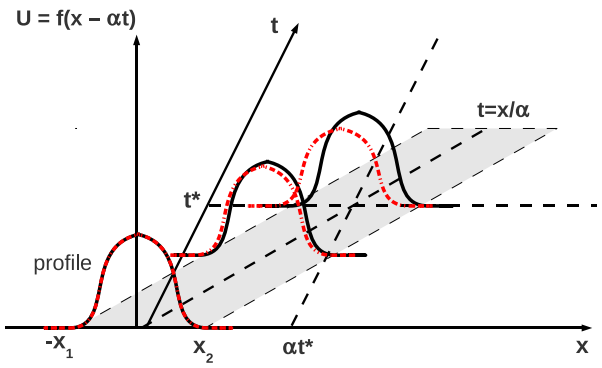

Figure 4.1: Displacement profile $\mathbf{u} = \mathbf{f}(x - \alpha t)$ (solid line) and computed profile $\mathbf{u}_\delta$ affected by dispersion and dissipation (dashed line).

analyze separately S and P grid dispersion errors, i.e.,

$$e_S = c_{S,h}/c_S - 1 \quad \text{and} \quad e_P = c_{P,h}/c_P - 1,$$

being $c_{S,h}$ ($c_{P,h}$) and c_S (c_P) the approximated shear (resp. compressional) and exact shear (resp. compressional) velocities. We define dissipation error as the maximum ratio between the amplitudes $||\mathbf{f}(x - \alpha_h t)||_\infty / ||\mathbf{f}(x - \alpha t)||_\infty$. As described for the dispersion error, we consider separately the P and the S dissipation errors.

We remark that the error introduced by the grid dispersion/dissipation depends on the combined effect of space and time discretizations. For such a reason, in the first part of this chapter we address the grid dispersion/dissipation properties of the non-conforming techniques introduced in Chapter 2, deriving dispersion/dissipation relations for the semi-discrete problems (2.54) and (2.64). Moreover, we compare the results with those obtained using standard SE techniques, [103]. In the second part, we extend this analysis to the corresponding fully-discrete problems presented in Chapter 3, addressing the combined effect of the LF, RK4, IM time discretizations with DGSE and MSE approximations. Finally, the technical stability analysis is carried out for LF and RK4 methods. Indeed, explicit time integration schemes, as the LF and RK4 methods, are conditionally stable and, in order to be stable, they must satisfy the Courant-Friedrichs-Levy (CFL) condition [91], that imposes a restrictions on the time step employed in the

numerical scheme.
Before going into the detail of the grid dispersion analysis we introduce some notation useful in the sequel. A generalized framework to describe a plane wave travelling in an arbitrary direction is the following

$$\mathbf{a}(\mathbf{x},t) = \mathbf{a}_0 \cos(\boldsymbol{\kappa}\cdot\mathbf{x} - \omega t + \varphi), \tag{4.1}$$

where $\boldsymbol{\kappa} = (\kappa_x, \kappa_y)$ is the wave vector which components κ_x, κ_y and magnitude $|\boldsymbol{\kappa}| = 2\pi/L$. The direction of the wave vector $\boldsymbol{\kappa}$ is the direction the plane wave is travelling. Here, L is the wave length, ω the angular frequency, φ the phase shift and $\mathbf{x}$ the position vector which defines a point in the two-dimensional space. In the following, we choose a more general formulation that employs the following representation in the complex plane

$$\mathbf{U}(\mathbf{x},t) = \mathbf{a}_0 e^{i(\boldsymbol{\kappa}\cdot\mathbf{x}-\omega t+\varphi)}. \tag{4.2}$$

We observe that the first term on the right hand side equals the real form of the plane wave (4.1). The complex form of the plane wave (4.2) can be simplified by using the complex valued amplitude $\mathbf{c} = \mathbf{a}_0 e^{i\varphi}$, in place of the real valued amplitude $\mathbf{a}_0$. More precisely, (4.2) can be written as

$$\mathbf{U}(\mathbf{x},t) = \mathbf{c} e^{i(\boldsymbol{\kappa}\cdot\mathbf{x}-\omega t)},$$

where the real part of the above equation represents the physical plane wave. Without loss of generality, in the following analysis we consider plane waves with unitary amplitude $\mathbf{c} = \mathbf{1}$.

4.1 Grid dispersion and dissipation errors for semi-discrete approximations

In this section we present the Von Neumann analysis [91], which provides the lowest sampling ratio, i.e., the minimum number of discretization points per wavelength such that the numerical solution has a prescribed accuracy.
Let us consider the wave equation (1.1) in an isotropic, elastic, unbounded domain $\Omega \subset \mathbb{R}^2$, with $\mathbf{u}(\mathbf{x},t) \to 0$ as $|\mathbf{x}| \to \infty$ for all t. We also assume $\mathbf{f} \equiv 0$: this is not a limitation. We point out that the above assumptions are standard when dealing with the Von Neumann's method (plane wave analysis), see [2, 3, 4, 40, 36, 108, 84, 76]. At

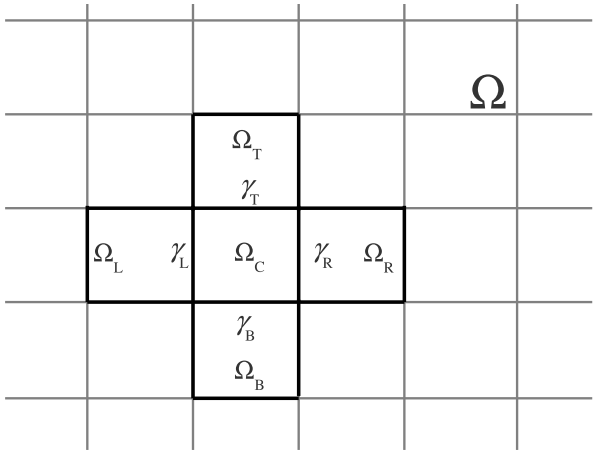

Figure 4.2: Periodic grid made by square elements with sides parallel to the coordinate axis. The reference element Ω_C with sides γ_f and neighbouring elements Ω_f, for $f = \{R, L, T, B\}$.

the discrete level we assume that Ω is partitioned into non-overlapping spectral elements Ω_k having uniform size h. This partition is supposed to be periodic and made by square elements with sides parallel to the coordinate axes (cf. Figure 4.2). We also suppose that the polynomial approximation degree is equal to N in each Ω_k.

Semi-discrete grid dispersion error: DGSE method

We present the analysis of grid dispersion for the DGSE method, see also [40] for the scalar case. Let $\mathbf{\Psi}^{\ell,\Omega_f}$, $\ell = 1, 2$ be the basis functions with support in Ω_f with $f \in \{C, T, B, L, R\}$ (cf. Figure 4.2). Without loss of generality, we suppose that the test and trial functions can be written as

$$\mathbf{\Psi}_i^\ell = \begin{cases} \mathbf{\Psi}_i^{\ell,\Omega_C} & \text{in } \Omega_C, \\ \mathbf{0} & \text{otherwise,} \end{cases} \quad \text{and } \mathbf{\Psi}_j^\ell = \begin{cases} \mathbf{\Psi}_j^{\ell,\Omega_C} & \text{in } \Omega_C, \\ \mathbf{\Psi}_j^{\ell,\Omega_f} & \text{in } \Omega_f,\ f \in \{T, B, L, R\}, \\ \mathbf{0} & \text{otherwise,} \end{cases} \tag{4.3}$$

respectively. By rewriting equation (2.55), we obtain a rectangular linear system, in the unknowns

$$\mathbf{U}^\ell = [\mathbf{U}^{\ell,\Omega_C}, \mathbf{U}^{\ell,\Omega_T}, \mathbf{U}^{\ell,\Omega_B}, \mathbf{U}^{\ell,\Omega_L}, \mathbf{U}^{\ell,\Omega_R}], \quad \ell = 1, 2, \tag{4.4}$$

that is underdetermined because the number of columns, $10(N+1)^2$, exceeds the number of rows, $2(N+1)^2$. To reduce it into a square linear system, we make use of the following

plane wave hypotheses. Let us assume that the displacement is a plane wave, i.e., in Ω_C we have

$$U_j^{\ell,\Omega_C} = e^{i(\boldsymbol{\kappa}\cdot\mathbf{p}_j - \omega t)},\ \ell = 1,2, \tag{4.5}$$

where $\boldsymbol{\kappa} = (k_x, k_y)$ is the wave vector and $\mathbf{p}_j$ contains the j^{th} node in Cartesian coordinates. The above assumption implies that

$$U_j^{\ell,\Omega_f} = e^{\beta_f} U_j^{\ell,\Omega_C},\ \ell = 1,2, \tag{4.6}$$

with $\beta_f = \{-ik_yh, ik_yh, -ik_xh, ik_xh\}$ and $f = \{T, B, R, L\}$, respectively. Substituting (4.6) in (4.4) lead to the following modified linear system of equations of dimension $2(N+1)^2$:

$$\begin{bmatrix} \underline{\mathrm{M}}^1 & \underline{0} \\ \underline{0} & \underline{\mathrm{M}}^2 \end{bmatrix} \begin{bmatrix} \ddot{\mathbf{U}}^{1,\Omega_C} \\ \ddot{\mathbf{U}}^{2,\Omega_C} \end{bmatrix} + \begin{bmatrix} \underline{\mathrm{A}}^1 + \widetilde{\underline{\mathrm{B}}}^1 & \underline{\mathrm{A}}^2 + \widetilde{\underline{\mathrm{B}}}^2 \\ \underline{\mathrm{A}}^3 + \widetilde{\underline{\mathrm{B}}}^3 & \underline{\mathrm{A}}^4 + \widetilde{\underline{\mathrm{B}}}^4 \end{bmatrix} \begin{bmatrix} \mathbf{U}^{1,\Omega_C} \\ \mathbf{U}^{2,\Omega_C} \end{bmatrix} = \begin{bmatrix} \mathbf{0} \\ \mathbf{0} \end{bmatrix}, \tag{4.7}$$

where $\underline{\mathrm{M}}^i$, $i = 1, 2$, and $\underline{\mathrm{A}}^i$, $i = 1, ..., 4$, are defined in (2.56) and (2.57), respectively. The matrices $\widetilde{\underline{\mathrm{B}}}^\ell$, for $\ell = 1, ...4$, are defined taking into account the hypothesis of periodicity and the plane wave assumption (4.5). For example, $\widetilde{\underline{\mathrm{B}}}^1$ is given by

$$\widetilde{\underline{\mathrm{B}}}^1(i,j) = \underline{\mathrm{B}}^1(i,j) + \sum_{f=\{T,B,R,L\}} e^{\beta_f} \underline{\mathrm{B}}^{1,f}(i,j), \quad i,j = 1, ..., (N+1)^2,$$

where

$$\begin{aligned} \underline{\mathrm{B}}^1(i,j) &= \sum_{f=\{T,B,R,L\}} -\int_{\gamma_f} \{\underline{\sigma}(\boldsymbol{\Psi}_j^{1,\Omega_C})\} : [\![\boldsymbol{\Psi}_i^{1,\Omega_C}]\!] \\ &+ \theta \int_{\gamma_f} [\![\boldsymbol{\Psi}_j^{1,\Omega_C}]\!] : \{\underline{\sigma}(\boldsymbol{\Psi}_i^{1,\Omega_C})\} + \eta_f \int_{\gamma_f} [\![\boldsymbol{\Psi}_j^{1,\Omega_C}]\!] : [\![\boldsymbol{\Psi}_i^{1,\Omega_C}]\!], \end{aligned}$$

and

$$\begin{aligned} \underline{\mathrm{B}}^{1,f}(i,j) &= -\int_{\gamma_f} \{\underline{\sigma}(\boldsymbol{\Psi}_j^{1,\Omega_f})\} : [\![\boldsymbol{\Psi}_i^{1,\Omega_C}]\!] + \theta \int_{\gamma_f} [\![\boldsymbol{\Psi}_j^{1,\Omega_f}]\!] : \{\underline{\sigma}(\boldsymbol{\Psi}_i^{1,\Omega_C})\} \\ &+ \eta_f \int_{\gamma_f} [\![\boldsymbol{\Psi}_j^{1,\Omega_f}]\!] : [\![\boldsymbol{\Psi}_i^{1,\Omega_C}]\!]. \end{aligned}$$

The matrices $\widetilde{\underline{\mathrm{B}}}^\ell$ for $\ell = 2, 3, 4$ are defined analogously. Now, taking the second derivative of $\mathbf{U}^{\ell,\Omega_C}$ with respect to time, and setting $\widetilde{\underline{\mathrm{K}}} = \underline{\mathrm{A}} + \widetilde{\underline{\mathrm{B}}}$ we obtain the following generalized eigenvalue problem

$$\widetilde{\underline{\mathrm{K}}} \mathbf{U}^{\Omega_C} = \Lambda\, \underline{\mathrm{M}} \mathbf{U}^{\Omega_C}, \tag{4.8}$$

where $\Lambda = \omega_h^2$, with ω_h the angular frequency at which the wave is travelling. As observed in [39, 40] and in [102], the number of eigenvalues of problem (4.8) naturally exceeds the number of admissible physical modes. Then, we need a strategy to select which eigenvalues correspond to the compressional (c_P) and the shear (c_S) wave velocities. This can be done by computing all the velocities associated to the eigenvalues of (4.8) and then comparing them to the real c_P and c_S velocities defined in (1.5). We denote by Λ_P and Λ_S the eigenvalues that realize the best approximations $c_{P,h}$ and $c_{S,h}$ of c_P and c_S, respectively.

Note that whenever IIPG and NIPG discretizations are employed, system (4.8) is no longer symmetric, thus complex eigenvalues might arise. However, in [40] it has been pointed out that Λ_P and Λ_S are, in fact, always real numbers. Next, we define the grid dispersion of pressure and shear waves as the ratio between the numerical velocity at which the wave travels in the grid and the physical velocity. By definition, the numerical shear velocity $c_{S,h}$ is given by

$$c_{S,h} = h\omega_h/(2\pi\delta),$$

where $\delta = h/(NL)$ is the sampling ratio (or equivalently δ^{-1} is the number of GLL points per wavelength), and L is the wavelength of the plane wave. We have that

$$c_{S,h} = h\sqrt{\Lambda_S}/(2\pi\delta),$$

and therefore the grid dispersion is the relative error in the velocity, given by

$$e_S = c_{S,h}/c_S - 1.$$

Analogously we set

$$c_{P,h} = h\sqrt{\Lambda_P}/(2\pi\delta) \quad \text{and} \quad e_P = c_{P,h}/c_P - 1.$$

We remark that in the definition of e_S and e_P the sign of the error indicates if the numerical approximation causes a delay (negative sign) or an acceleration (positive sign) of the travelling wave. The grid dispersion error will depend on the sampling ratio δ, the wave vector $\boldsymbol{\kappa}$, the degree of the basis function N and on the velocities c_P and c_S. For the DGSE method the grid dispersion errors will depend also on the stability parameter η.

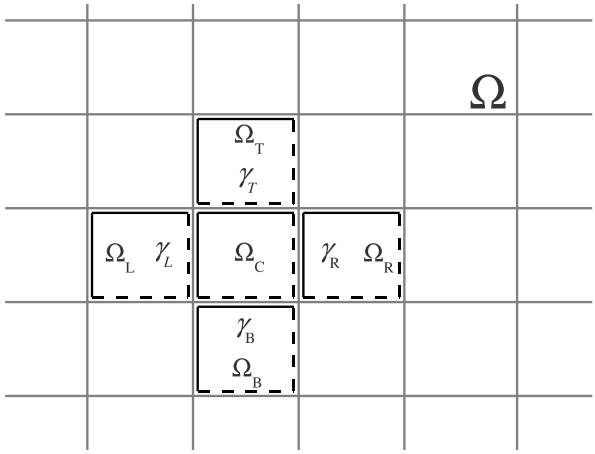

Figure 4.3: Periodic grid made by square elements with sides parallel to the coordinate axis. The reference element Ω_C with sides γ_f and neighbouring elements Ω_f, for $f = \{R, L, T, B\}$. The solid lines (-) are the *master* edges and the dashed lines (- -) are the *slave* edges.

Semi-discrete grid dispersion error: MSE method

In order to carry out the dispersion analysis for the MSE method, we adopt a strategy similar to the one described for the DGSE method. The goal is to obtain a generalized eigenvalue problem associated only to the degrees of freedom belonging to Ω_C. Under the same hypothesis of regularity and periodicity of the mesh, we observe that the skeleton of the partition is uniquely defined once the *master* and *slave* edges for the reference element Ω_C are selected. Consider the configuration shown in Figure 4.3: this is the unique, up to a rotation, possible combination of *master* and *slave* edges for Ω_C that does not violate the hypothesis of grid periodicity. We next rewrite the ODE system (2.54) in the MSE framework. Using (4.3) we obtain

$$\underline{\mathrm{M}}\ddot{\mathbf{U}}^{\Omega_C} + \underline{\mathrm{A}}\mathbf{U}^{\Omega_C} = \mathbf{0}, \tag{4.9}$$

where $\underline{\mathrm{M}}$ and $\underline{\mathrm{A}}$ are defined in (2.56) and (2.57), respectively. Next, we impose the *mortar conditions* **MC1** on the *slave* unknowns at the interfaces γ_B and γ_R. In particular, for $\ell = 1, 2$ and $f = \{R, B\}$, we have that

$$\sum_{j:\mathbf{p}_j \in \gamma_f} U_j^{\ell,\Omega_C} \int_{\gamma_f} \Psi_j^{\ell,\Omega_C} \widehat{\Phi}_i^{\ell} = \sum_{j:\mathbf{p}_j \in \gamma_f} U_j^{\ell,\Omega_f} \int_{\gamma_f} \Psi_j^{\ell,\Omega_f} \widehat{\Phi}_i^{\ell} \quad \forall\, \widehat{\Phi}_i^{\ell} \in \widehat{\Lambda}_\delta(\gamma_f). \tag{4.10}$$

To recast these conditions in terms of unknowns and basis functions defined only on Ω_C we simply notice that, by periodicity,

$$\Psi_j^{\ell,\Omega_R}{}_{|\gamma_R} = \Psi_j^{\ell,\Omega_C}{}_{|\gamma_L} \text{ and } \Psi_j^{\ell,\Omega_B}{}_{|\gamma_B} = \Psi_j^{\ell,\Omega_C}{}_{|\gamma_T}, \quad \ell = 1,2, \tag{4.11}$$

and by the plane wave assumption, equation (4.6) holds. By substituting (4.11) in (4.10) we obtain

$$\sum_{j:\mathbf{p}_j\in\gamma_f} U_j^{\ell,\Omega_C} \int_{\gamma_f} \Psi_j^{\ell,\Omega_C} \widehat{\Phi}_i^{\ell} = \sum_{j:\mathbf{p}_j\in\gamma_f} e^{\beta_f} U_j^{\ell,\Omega_C} \int_{\gamma_f} \Psi_j^{\ell,\Omega_f} \widehat{\Phi}_i^{\ell} \quad \forall \widehat{\Phi}_i^{\ell} \in \widehat{\Lambda}_\delta(\gamma_f), \tag{4.12}$$

for $\ell = 1,2$ and $f = \{B, R\}$. We remark that equation (4.12) links *slave* unknowns in Ω_C to *master* unknowns still in Ω_C: this means that the matrix projection $\underline{\widetilde{\mathrm{Q}}}$ refers only to the element Ω_C. We use then $\underline{\widetilde{\mathrm{Q}}}$ to reduce the linear system (4.9) to a linear system in the *master* unknowns only

$$\underline{\widetilde{\mathrm{Q}}}^{\top} \underline{\widetilde{\mathrm{M}}} \underline{\widetilde{\mathrm{Q}}} \ddot{\mathbf{U}}_{master}^{\Omega_C} + \underline{\widetilde{\mathrm{Q}}}^{\top} \underline{\widetilde{\mathrm{A}}} \underline{\widetilde{\mathrm{Q}}} \mathbf{U}_{master}^{\Omega_C} = \mathbf{0}. \tag{4.13}$$

We notice that $\underline{\widetilde{\mathrm{Q}}}$ has always a block diagonal structure like (2.63) where each block $\underline{\widehat{\mathrm{Q}}}$ is modified according to (4.12). Taking the second derivative of the displacement with respect to time and defining $\underline{\widetilde{\mathrm{K}}} = \underline{\widetilde{\mathrm{Q}}}^{\top} \underline{\widetilde{\mathrm{A}}} \underline{\widetilde{\mathrm{Q}}}$, we finally obtain the following generalized eigenvalue problem of size $2(N^2+3)$

$$\underline{\widetilde{\mathrm{K}}} \mathbf{U}_{master}^{\Omega_C} = \Lambda \, \underline{\widetilde{\mathrm{Q}}}^{\top} \underline{\widetilde{\mathrm{M}}} \underline{\widetilde{\mathrm{Q}}} \mathbf{U}_{master}^{\Omega_C}, \tag{4.14}$$

where $\Lambda = \omega_h^2$ as before.

Numerical Results

Now, we analyze the semi-discrete grid dispersion errors for both the MSE and the DGSE formulations from three different points of view: (i) the convergence with respect to the polynomial degree N, (ii) the convergence with respect to the sampling ratio δ, and (iii) the numerical anisotropy introduced by the grid dispersion. Finally, we compare the obtained results with the analogous ones obtained with the conforming SE method. The grid dispersion analysis for the semi-discrete SE formulation has been obtained with technique similar to the one described in the MSE case, and the results obtained are in agreement with [40, 103].

In the first set of experiments, we fix the ratio between the velocities $r = c_P/c_S = 2$ (notice that is a very common choice in geophysical applications), the incidence angle

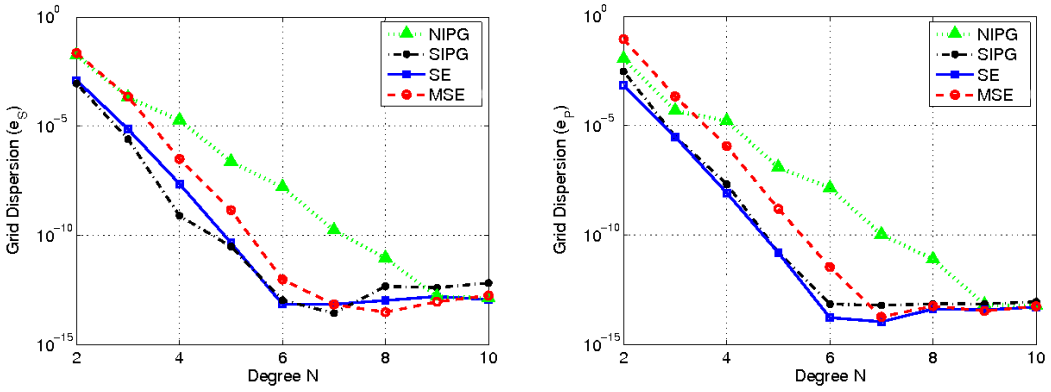

Figure 4.4: Grid dispersion versus the polynomial degree N: sampling ratio $\delta = 0.2$ and incident angle $\theta = \pi/4$.

$\theta = \pi/4$ and, for the DGSE method, we set $\eta = 2N^2/h$. In Figure 4.4 we show the grid dispersion errors versus the polynomial approximation degree N, fixing $\delta = 0.2$ (i.e., 5 grid points per wavelength). All the non-conforming approaches, except the NIPG, feature the same spectral convergence of the SE method. Indeed, the SIPG and the MSE methods reach the threshold value $\approx 10^{-13}$ for $N = 6$ while the NIPG for $N = 9$. The grid dispersion error as a function of sampling ratio δ is shown in Figure 4.5 for $N = 2, .., 5$, respectively. The aim of this set of experiments is to establish a relation between the absolute value $|e_S|$, resp. $|e_P|$, and the mesh size h (i.e., determine q, resp. q', such that $|e_S| = \mathcal{O}(h^q)$, resp. $|e_P| = \mathcal{O}(h^{q'})$). The computed order of convergence is then given by the slope of the lines in Figure 4.5. From the results reported in Figure 4.5 it seems that both the SIPG and SE methods converge with optimal order $q = q' = \mathcal{O}(2N)$; whereas a suboptimal order $q = q' = \mathcal{O}(N + 1)$ is observed for both NIPG and MSE methods. These results are in agreement with [6], where it is shown that the symmetric DG methods approximate with an optimal rate the spectrum of compact operators, whereas the non-symmetric DG methods are suboptimal in the approximation of the spectrum.

Finally, in Figure 4.6, we show the anisotropy (that is the ratio $c_{S,h}/c_S$ and the ratio $c_{P,h}/c_P$) introduced by the numerical schemes. We consider $N = 2, 3, 4$ and five points per wavelength. For $N > 4$ the anisotropy is less than 10^{-6}. We notice that, for $N = 2$, in the SIPG and in the MSE methods the waves are slightly delayed for all possible incident angles while in the NIPG method the waves are accelerated. In Table 4.1 we

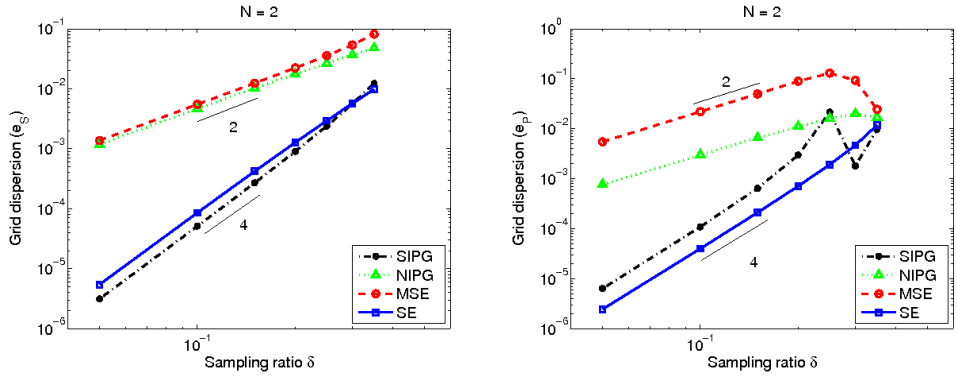

(a)

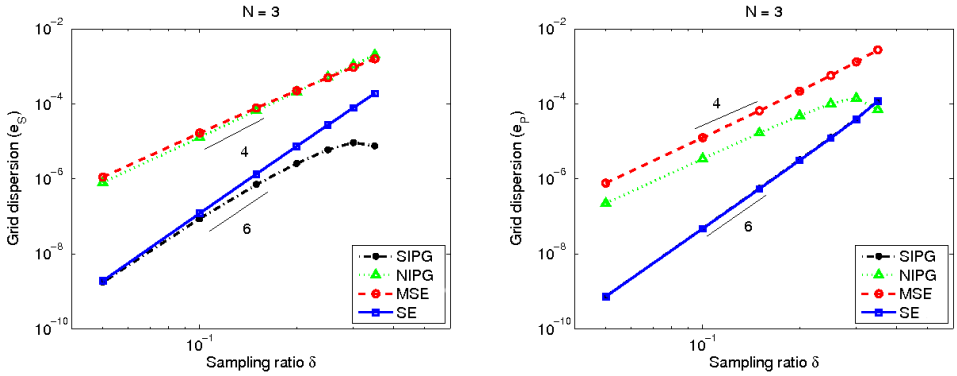

(b)

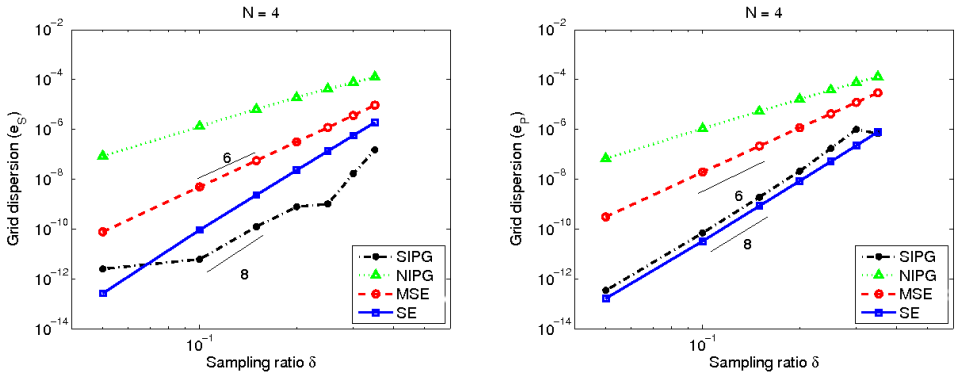

(c)

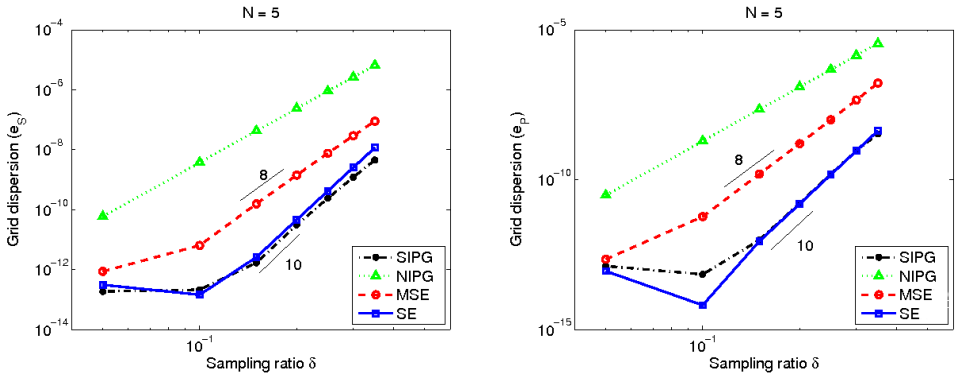

(d)

Figure 4.5: Grid dispersion versus the sampling ratio δ for $N = 2, 3, 4, 5$.

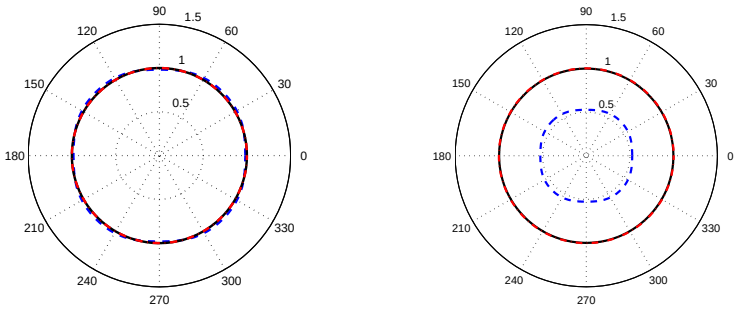

(a) Anisotropy curves $c_{S,h}/c_S$ of the SE (left) and MSE (right).

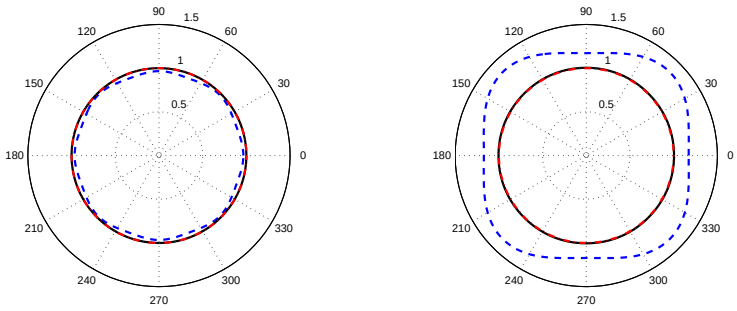

(b) Anisotropy curves $c_{S,h}/c_S$ of the SIPG (left) and NIPG (right).

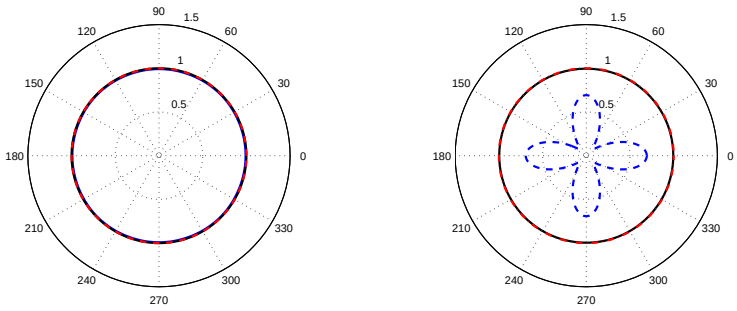

(c) Anisotropy curves $c_{P,h}/c_P$ of the SE (left) and MSE (right).

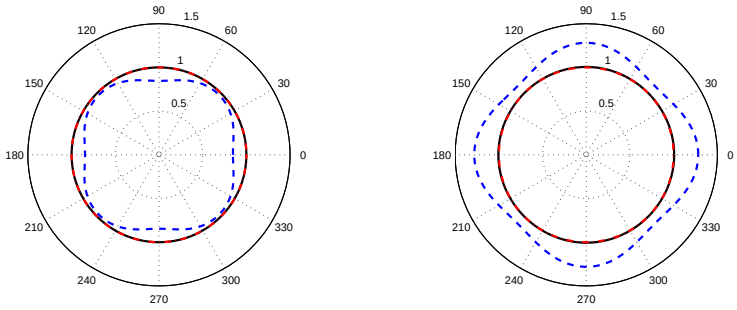

(d) Anisotropy curves $c_{P,h}/c_P$ of the SIPG (left) and NIPG (right).

Figure 4.6: Anisotropy curves. Sampling ratio $\delta = 0.2$ for polynomial degrees $N = 2$ (- -), $N = 3$ (-) and $N = 4$ (.-). For visualization purposes, the grid dispersion has been magnified by a factor 10.

(a) S-anisotropy

N	SE	SIPG	NIPG	MSE
2	1.2684e-03	2.7156e-03	1.7540e-02	2.3728e-02
3	8.7429e-06	7.5949e-06	2.7196e-04	2.2247e-04
4	4.2894e-08	5.2818e-08	2.4372e-05	1.3029e-06

(b) P-anisotropy

N	SE	SIPG	NIPG	MSE
2	9.8805e-04	1.5402e-02	2.8146e-02	8.8991e-02
3	6.8628e-06	1.8732e-05	5.6250e-04	2.4218e-04
4	3.1687e-08	3.3492e-07	6.8619e-05	1.5325e-06

Table 4.1: Maximum value $\max_{0\leq\theta\leq 2\pi}|e_S|$ (top) and $\max_{0\leq\theta\leq 2\pi}|e_P|$ (bottom) for $N = 2, 3, 4$.

also report the maximum value $\max_{0\leq\theta\leq 2\pi}|e_S|$ and $\max_{0\leq\theta\leq 2\pi}|e_P|$, respectively. From these results it can be inferred that all the methods perform in a very similar way and the dispersion errors are negligible.

Dissipation error for semi-discrete approximations

To quantify the semi-discrete dissipation error, we still assume that the displacement $\mathbf{u}$ is a plane wave of the form (4.5). Since $\boldsymbol{\kappa}$ has real components, it follows that the wave has amplitude

$$|e^{i(\boldsymbol{\kappa}\cdot\mathbf{x}_j-\omega t)}| = e^{t\mathrm{Im}(\omega)} \qquad \forall\,\mathbf{x}_j, \quad \forall\, t > 0. \tag{4.15}$$

Thus it decays exponentially if $\mathrm{Im}(\omega) < 0$. If $\mathrm{Im}(\omega) = 0$ the plane wave amplitude is equal to 1 for all $t > 0$. Therefore, a discrete scheme is:

- *non dissipative* if $\mathrm{Im}(\omega_h) = 0$ for all $\boldsymbol{\kappa}$,
- *dissipative* if $\mathrm{Im}(\omega_h) < 0$ for all $\boldsymbol{\kappa} \neq \mathbf{0}$,

where ω_h is related to solutions of the associated generalized eigenvalue problems (4.8) or (4.14) in the DG or Mortar case, respectively. Note that ω_h can be either $\omega_{S,h}$ or $\omega_{P,h}$, depending if we are considering S- or P-waves.
For the semi-discrete dissipation error, in Table 4.2 (resp. Table 4.3) we report the values of $\mathrm{Im}(\omega_h)$ for the semi-discrete problems (4.8) and (4.14) respectively, varying the polynomial approximation degree N (resp. the sampling ratio δ). We fix the incident

	SE		SIPG		MSE	
N	$\mathrm{Im}(\omega_{S,h})$	$\mathrm{Im}(\omega_{P,h})$	$\mathrm{Im}(\omega_{S,h})$	$\mathrm{Im}(\omega_{P,h})$	$\mathrm{Im}(\omega_{S,h})$	$\mathrm{Im}(\omega_{P,h})$
2	-1.8687e-16	-1.6884e-16	-6.9782e-16	-9.6888e-16	-5.5165e-16	-2.5680e-16
3	-1.2386e-15	-1.1085e-15	8.8005e-16	3.2135e-16	8.0515e-16	-2.5558e-16
4	-1.1744e-16	3.1257e-16	-4.2113e-15	-5.0858e-16	3.1670e-15	6.1221e-16
5	1.4644e-15	8.9666e-16	-1.9977e-15	-6.5793e-15	-2.1894e-15	-4.6190e-15
6	-6.0645e-16	8.0892e-17	-3.4844e-15	4.8253e-15	-4.1583e-15	5.8972e-15
7	-1.5149e-14	-7.2159e-15	3.7452e-15	-8.5995e-15	1.1333e-14	-4.3412e-15
8	-7.2058e-15	-6.2394e-15	-1.4276e-14	-1.4739e-14	9.7548e-15	1.0194e-14
9	7.5118e-16	-2.6108e-15	2.3753e-14	-6.2472e-15	-7.6537e-15	-9.0125e-15
10	4.2337e-15	2.5439e-15	-5.1072e-14	2.3077e-14	-1.5956e-14	1.0328e-14

Table 4.2: Computed values of $\mathrm{Im}(\omega_{S,h})$ and $\mathrm{Im}(\omega_{P,h})$. $N = 2, .., 9$, $\delta = 0.2$ and $\theta = \pi/4$.

	SE		SIPG		MSE	
$1/\delta$	$\mathrm{Im}(\omega_{S,h})$	$\mathrm{Im}(\omega_{P,h})$	$\mathrm{Im}(\omega_{S,h})$	$\mathrm{Im}(\omega_{P,h})$	$\mathrm{Im}(\omega_{S,h})$	$\mathrm{Im}(\omega_{P,h})$
2	-4.6681e-17	-1.7229e-16	-1.7660e-15	-5.4334e-16	7.9602e-16	-3.9736e-16
4	-1.1896e-15	-1.8173e-15	-3.2565e-15	2.0011e-15	1.6631e-15	-1.8589e-15
6	-8.5509e-16	1.9686e-15	-3.8813e-15	7.3660e-16	3.9770e-16	-1.4470e-16
8	1.7380e-15	-3.8377e-16	1.3998e-15	1.8561e-15	-2.4063e-15	2.2529e-15
10	-4.8637e-16	-1.1671e-15	8.1446e-16	4.6269e-16	-3.8415e-15	-2.9109e-16

Table 4.3: Computed values of $\mathrm{Im}(\omega_{S,h})$ and $\mathrm{Im}(\omega_{P,h})$ varying the sampling ratio δ. $N = 4$ and $\theta = \pi/4$.

angle $\theta = \pi/4$ and we compare the results with those obtained with SE discretizations. From the results reported in Table 4.2 and 4.3 we can conclude that all the methods considered are non dissipative. Similar conclusions can be inferred using different values of the incident angle θ. These results are not reported for the sake of brevity.

4.2 Grid dispersion and dissipation errors for fully-discrete approximations

In this section we investigate the dissipation and dispersion properties of the DGSE and MSE methods when coupled with the LF, RK4 and IM time integration schemes. With

this perspective we start considering the following problem

$$\underline{\widehat{\mathrm{M}}}\ddot{\mathbf{U}} + \underline{\widehat{\mathrm{K}}}\mathbf{U} = \mathbf{0}, \tag{4.16}$$

where all the terms appearing in the above equation are defined on the reference element Ω_C (we omit the superscripts to ease the notation). In the DG framework $\underline{\widehat{\mathrm{K}}} = \underline{\mathrm{A}} + \underline{\widetilde{\mathrm{B}}}$ and $\underline{\widehat{\mathrm{M}}} = \underline{\mathrm{M}}$ (cf. (4.8)), whereas in the Mortar approach $\underline{\widehat{\mathrm{K}}} = \underline{\widetilde{\mathrm{Q}}}^{\top}\underline{\widetilde{\mathrm{A}}}\underline{\widetilde{\mathrm{Q}}}$ and $\underline{\widehat{\mathrm{M}}} = \underline{\widetilde{\mathrm{Q}}}^{\top}\underline{\widetilde{\mathrm{M}}}\underline{\widetilde{\mathrm{Q}}}$ (cf. (4.14). Now, approximating the second order derivative in (4.16) with one of the numerical schemes introduced in Chapter 3 we obtain different generalized eigenvalue problems, from which we can infer the dispersion relation we are interested in. Among all the DG methods considered so far, in the following we will address only the performance of the SIPG scheme since, as shown in the previous section, it has better grid dispersion properties than the NIPG.

Leap-frog time integration scheme

Assuming that the solution is the plane wave given in (4.5), substituting this expression in (4.16) and employing the leap-frog scheme for the discretization of the time derivative we obtain

$$\underline{\widehat{\mathrm{M}}}\frac{1}{\Delta t^2}(e^{-i\omega_h t_{n+1}} - 2e^{-i\omega_h t_n} + e^{-i\omega_h t_{n-1}})\mathbf{u}_0 + \underline{\widehat{\mathrm{K}}}e^{-i\omega_h t_n}\mathbf{u}_0 = \mathbf{0}, \tag{4.17}$$

for $n = 1, ..., N-1$, where $\mathbf{u}_0$ is the initial condition related to the amplitude of the plane wave. System (4.17) can be rewritten in an equivalent form as follows

$$\underline{\widehat{\mathrm{M}}}\frac{1}{\Delta t^2}(2 - e^{-i\omega_h \Delta t} - e^{i\omega_h \Delta t})\mathbf{u}_0 = \underline{\widehat{\mathrm{K}}}e^{-i\omega_h t_n}\mathbf{u}_0.$$

Now, notice that

$$2 - e^{-i\omega_h \Delta t} - e^{i\omega_h \Delta t} = 2(\cos(\omega_h \Delta t) - 1) = 4\sin^2\left(\frac{\omega_h \Delta t}{2}\right).$$

We thus obtain the following fully-discrete eigenvalue problem

$$\underline{\widehat{\mathrm{K}}}\mathbf{u}_0 = \Lambda\,\underline{\widehat{\mathrm{M}}}\mathbf{u}_0, \tag{4.18}$$

for (3.3) or (3.4) respectively, depending on the degrees of freedom inside the reference element Ω_C and where

$$\Lambda = \frac{4}{\Delta t^2}\sin^2\left(\frac{\omega_h \Delta t}{2}\right),$$

or equivalently

$$\omega_h = \frac{2}{\Delta t}\arcsin\left(\frac{\Delta t}{2}\sqrt{\Lambda}\right).$$

Then, the grid dispersion can be obtained as described in Section 4.1. More precisely, the grid dispersion for the leap-frog scheme can be obtained by computing the velocities $c_{S,h}$ and $c_{P,h}$ associated to the eigenvalues of (4.18) and comparing them to the c_P and c_S velocities defined in (1.5). We remark that the grid dispersion errors for the angular frequencies

$$e_S = \frac{\omega_{S,h}}{\omega_S} - 1 \quad \text{and} \quad e_P = \frac{\omega_{P,h}}{\omega_P} - 1,$$

are equivalent to those introduced in Section 4.1 for the velocities $c_{S,h}$ and $c_{P,h}$.

Runge-Kutta 4 time integration scheme

To determine the grid dispersion relation for the RK4 method we rewrite system (4.16) in the form

$$\begin{bmatrix} \dot{\mathbf{U}}(t) \\ \dot{\mathbf{V}}(t) \end{bmatrix} = \begin{bmatrix} \underline{0} & \widehat{\underline{\mathrm{I}}} \\ -\widehat{\underline{\mathrm{M}}}^{-1}\widehat{\underline{\mathrm{K}}} & \underline{0} \end{bmatrix} \begin{bmatrix} \mathbf{U}(t) \\ \mathbf{V}(t) \end{bmatrix},$$

or in a compact form

$$\dot{\mathbf{W}}(t) = \widehat{\underline{\mathrm{T}}}\mathbf{W}(t). \tag{4.19}$$

where all the terms appearing in the above equation refer to Ω_C. Now, applying the Runge-Kutta 4 scheme defined in (3.10) to the above system of ODE we can express the coefficients $\mathbf{K}_1, \mathbf{K}_2, \mathbf{K}_3$ and $\mathbf{K}_4$ as

$$\begin{aligned}
\mathbf{K}_1 &= \widehat{\underline{\mathrm{T}}}\mathbf{W}(t_n), \\
\mathbf{K}_2 &= (\widehat{\underline{\mathrm{T}}} + \frac{\Delta t}{2}\widehat{\underline{\mathrm{T}}}^2)\mathbf{W}(t_n), \\
\mathbf{K}_3 &= (\widehat{\underline{\mathrm{T}}} + \frac{\Delta t}{2}\widehat{\underline{\mathrm{T}}}^2 + \frac{\Delta t^2}{4}\widehat{\underline{\mathrm{T}}}^3)\mathbf{W}(t_n), \\
\mathbf{K}_4 &= (\widehat{\underline{\mathrm{T}}} + \Delta t\widehat{\underline{\mathrm{T}}}^2 + \frac{\Delta t^2}{2}\widehat{\underline{\mathrm{T}}}^3 + \frac{\Delta t^3}{4}\widehat{\underline{\mathrm{T}}}^4)\mathbf{W}(t_n).
\end{aligned}$$

Therefore we have

$$\mathbf{W}(t_{n+1}) = \sum_{k=0}^{4} \frac{(\Delta t\widehat{\underline{\mathrm{T}}})^k}{k!}\mathbf{W}(t_n). \tag{4.20}$$

Since both the velocity and the displacement are plane waves, it holds

$$\mathbf{W}(t) = \begin{bmatrix} \mathbf{1} \\ \mathbf{1} \end{bmatrix} e^{i(\boldsymbol{\kappa}\cdot\mathbf{p}_j - \omega t)},$$

with **1** identity vector. Substituting the above expression in (4.20) leads to the following eigenvalue problem

$$\sum_{k=0}^{4} \frac{(\Delta t \widehat{\underline{\mathrm{T}}})^k}{k!} \mathbf{W}(0) = \Lambda \mathbf{W}(0), \tag{4.21}$$

where $\Lambda = e^{-i\omega_h \Delta t}$. We therefore have the following fully-discrete dispersion relations

$$\omega_{h,S} = \Re e \left[\frac{i}{\Delta t} \log(\Lambda_S) \right] \quad \text{and} \quad \omega_{h,P} = \Re e \left[\frac{i}{\Delta t} \log(\Lambda_P) \right]. \tag{4.22}$$

Implicit midpoint time integration scheme

We apply the IM method described in Section 3.1.3 to the system (4.16) to obtain

$$\begin{bmatrix} \widehat{\underline{\mathrm{I}}} & -\frac{\Delta t}{2}\widehat{\underline{\mathrm{I}}} \\ \frac{\Delta t}{2}\widehat{\underline{\mathrm{K}}} & \widehat{\underline{\mathrm{M}}} \end{bmatrix} \mathbf{W}(t_{n+1}) = \begin{bmatrix} \widehat{\underline{\mathrm{I}}} & \frac{\Delta t}{2}\widehat{\underline{\mathrm{I}}} \\ -\frac{\Delta t}{2}\widehat{\underline{\mathrm{K}}} & \widehat{\underline{\mathrm{M}}} \end{bmatrix} \mathbf{W}(t_n),$$

where all the matrices are modified according to the plane wave assumptions (4.5). Now, proceeding as before we obtain the following generalized eigenvalue problem

$$\begin{bmatrix} \widehat{\underline{\mathrm{I}}} & -\frac{\Delta t}{2}\widehat{\underline{\mathrm{I}}} \\ \frac{\Delta t}{2}\widehat{\underline{\mathrm{K}}} & \widehat{\underline{\mathrm{M}}} \end{bmatrix} \Lambda \mathbf{W}(0) = \begin{bmatrix} \widehat{\underline{\mathrm{I}}} & \frac{\Delta t}{2}\widehat{\underline{\mathrm{I}}} \\ -\frac{\Delta t}{2}\widehat{\underline{\mathrm{K}}} & \widehat{\underline{\mathrm{M}}} \end{bmatrix} \mathbf{W}(0), \tag{4.23}$$

with dispersion relations given by

$$\omega_{h,S} = \Re e \left[\frac{i}{\Delta t} \log(\Lambda_S) \right] \quad \text{and} \quad \omega_{h,P} = \Re e \left[\frac{i}{\Delta t} \log(\Lambda_P) \right].$$

Notice that the above relations have the same form of (4.22) but they are different because they refer to different eigenvalue problems.

Numerical Results

In this section we address the different time integration schemes LF, RK and IM coupled with the DGSE and the MSE formulations. In this case the fully-discrete grid dispersion error will depend not only N, δ and $\boldsymbol{\kappa}$ but also on the time step Δt. In particular, we expect that the fully-discrete dispersion errors tend to the semi-discrete dispersion errors as Δt goes to zero.

First, we analyze the convergence with respect to the polynomial degree N, then the convergence with respect to the sampling ratio δ and finally the numerical anisotropy

introduced by the fully-discrete grid dispersion. All the results are compared with the ones obtained by the semi-discrete formulation. Throughout the section when needed we have chosen Δt in such a way that the resulting scheme is stable.

In the first test case we set the shear and compressional wave velocities such that $r = c_P/c_S = 2$ and the incidence angle $\theta = \pi/4$. As usual, for the SIPG method, we fix the parameter $\eta = 2N^2/h$. For all the considered time integration methods, in Figure 4.7 we show the computed shear grid dispersion error e_S versus the polynomial approximation degree N for different choices of discretization steps Δt. The analogous results obtained for the compressional grid dispersion error e_P are shown in Figure 4.8. All the results are compared with the analogous one obtained in the semi-discrete case. It is clear that as Δt goes to zero, the fully-discrete error tends to the semi-discrete one. In particular when $\Delta t \leq 10^{-3}$ both e_S and e_P turn out to be negligible, indeed e_S and e_P are less than 10^{-6}.
We also notice that the LF scheme outperforms the IM scheme. Indeed, when LF scheme is coupled with SIPG or MSE methods the error is of order 10^{-6} when $N \geq 3$ and $\Delta t \leq 10^{-2}$. On the other hand, to obtain the same accuracy with the IM scheme we need $N \geq 5$ and $\Delta t \leq 10^{-3}$. The explicit RK4 method has better dispersion properties than LF and IM methods, since the threshold value 10^{-6} is reached with $N \geq 4$ and $\Delta t \leq 10^{-1}$.
Now, let us consider the same set of parameters r, δ and θ as before and fix $\Delta t = 10^{-3}$. In Figure 4.9 we compare the fully-discrete grid dispersion errors for different polynomial degrees N. The results are in agreement with analogous ones obtained for the corresponding semi-discrete formulations (cf. Figure 4.4). We observe that for $N \geq 6$ the SE, SIPG and MSE methods are equivalent in terms of grid dispersion.
Next, we fix $N = 4$, $\theta = \pi/4$ and $r = 2$ and we address the behaviour of the fully discrete dispersion error as a function of the sampling ratio δ. The results obtained in Figures 4.10-4.11 show that at least 5 points per wavelength (vertical dashed line) and $\Delta t \leq 10^{-2}$ are enough to have a grid dispersion error less than 10^{-6}. These results are in agreement with the analogous ones reported in Figures 4.7-4.8 and 4.9 for the semi-discrete case. In Figure 4.12 we compare the grid dispersion errors obtained with $\Delta t = 10^{-3}$ for SE, SIPG and MSE discretizations. From the graphics it is evident that all methods considered are low-dispersive and have the same behaviour for $\delta \leq 0.1$ (number of points per wavelength greater than 10). If $\delta \leq 0.1$ the SIPG method is

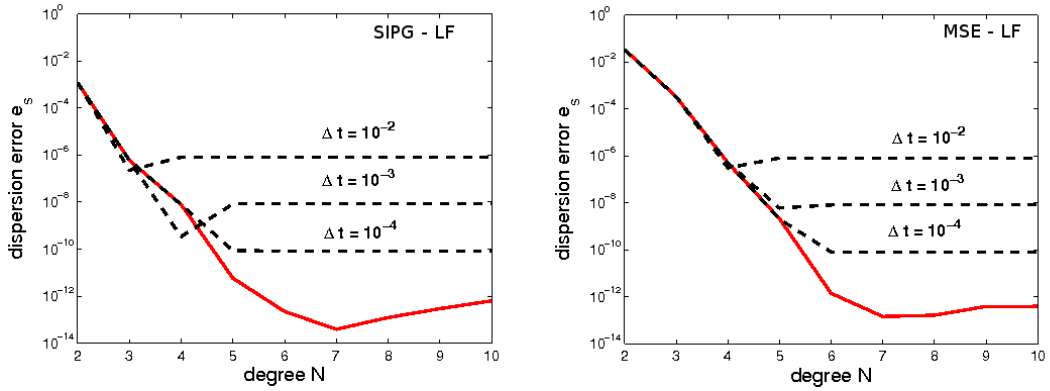

(a) SIPG - leap-frog (left) and MSE - leap-frog (right).

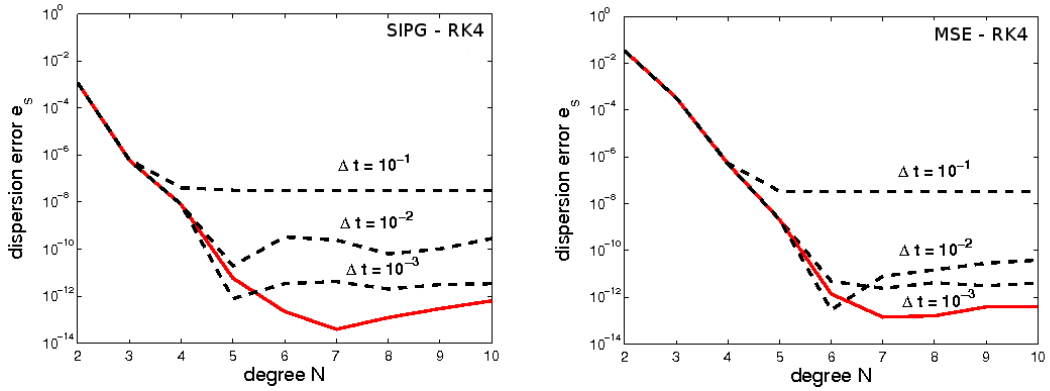

(b) SIPG - Runge-Kutta 4 (left) and MSE - Runge-Kutta 4 (right).

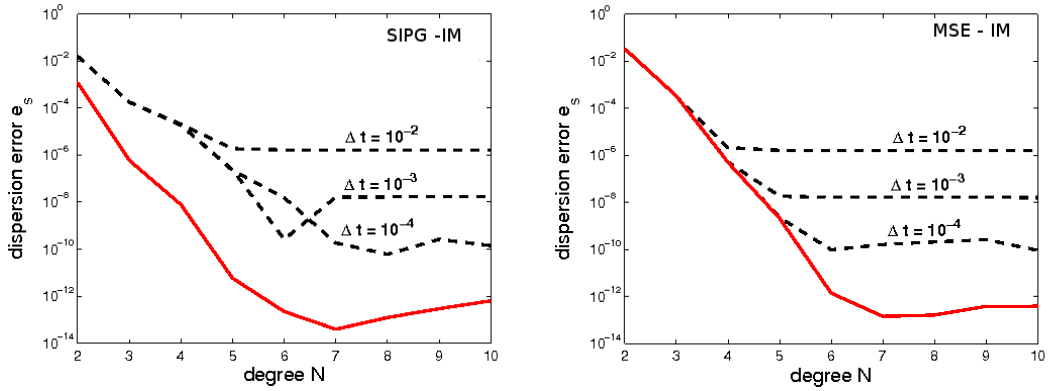

(c) SIPG - implicit midpoint method (left) and MSE - implicit midpoint method (right).

Figure 4.7: Shear grid dispersion error e_S versus the polynomial degree N: $\delta = 0.2$ and incident angle $\theta = \pi/4$. Comparison between fully-discretization (dashed lines) and semi-discretization (solid lines) for SIPG (left column) and MSE (right column) methods.

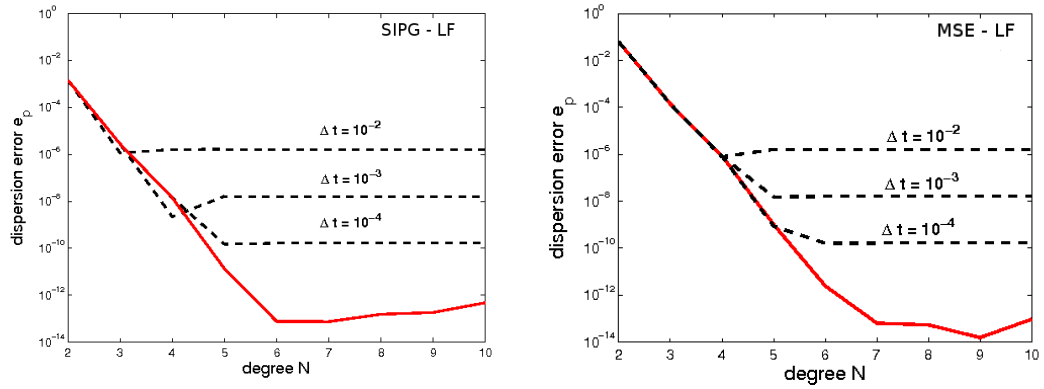

(a) SIPG - leap-frog (left) and MSE - leap-frog (right).

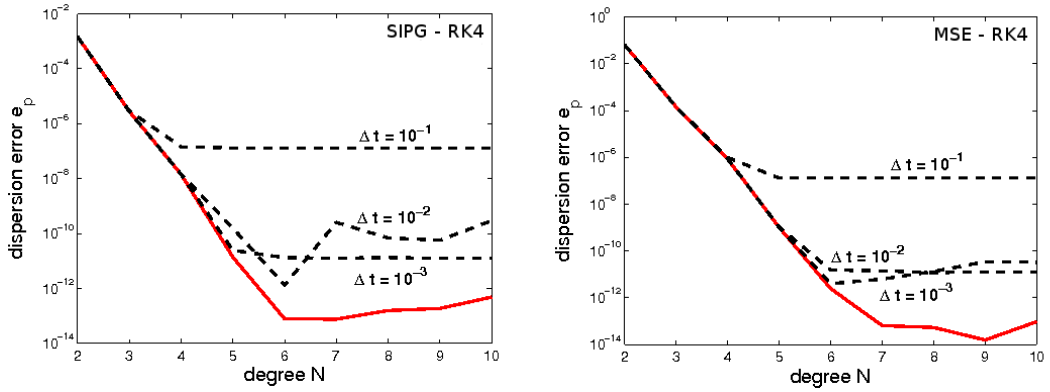

(b) SIPG - Runge-Kutta 4 (left) and MSE - Runge-Kutta 4 (right).

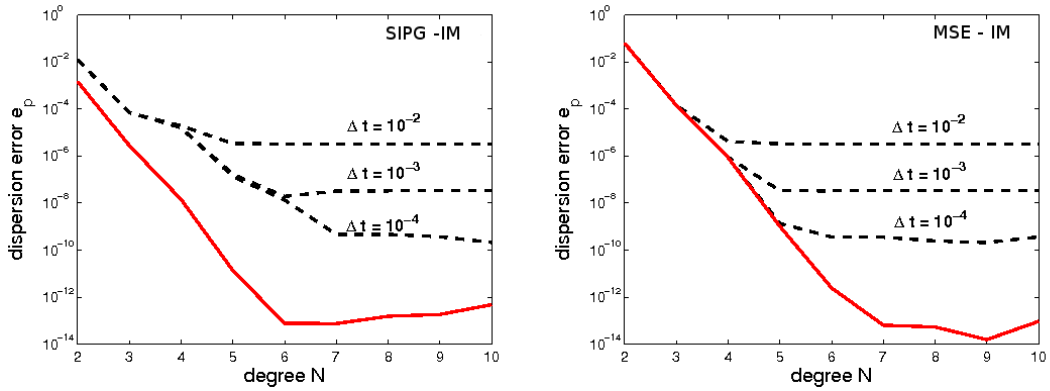

(c) SIPG - implicit midpoint method (left) and MSE - implicit midpoint method (right).

Figure 4.8: Shear grid dispersion error e_P versus the polynomial degree N: $\delta = 0.2$ and incident angle $\theta = \pi/4$. Comparison between fully-discretization (dashed lines) and semi-discretization (solid lines) for SIPG (left column) and MSE (right column) methods.

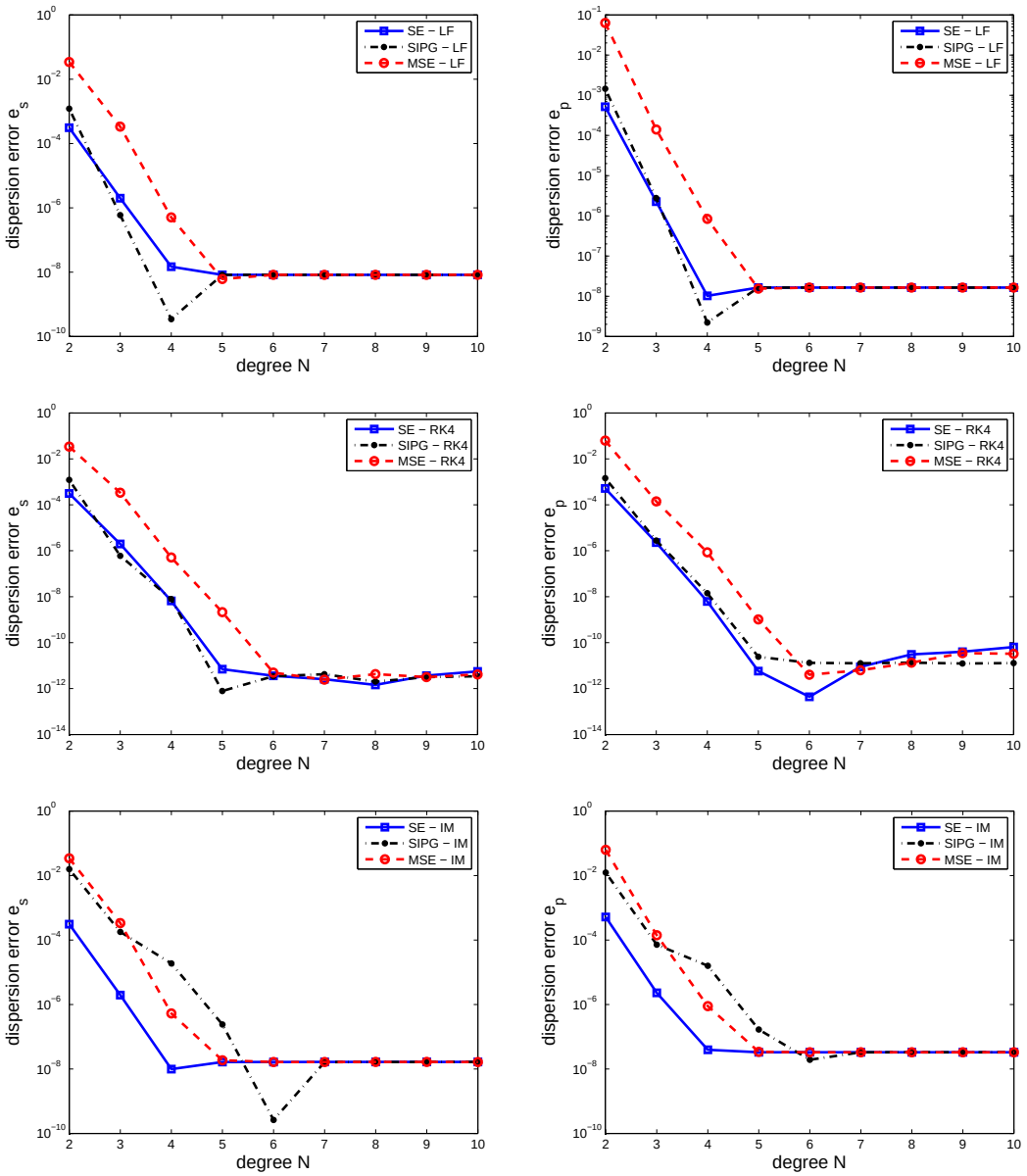

Figure 4.9: Fully-discrete dispersion errors e_S (left) and e_P (right) obtained with $\Delta t = 10^{-3}$, $r = 2, \delta = 0.2$ and $\theta = \pi/4$. Comparison between SE, SIPG and MSE discretizations coupled with the LF (top), RK (middle) and IM (bottom) time integration schemes.

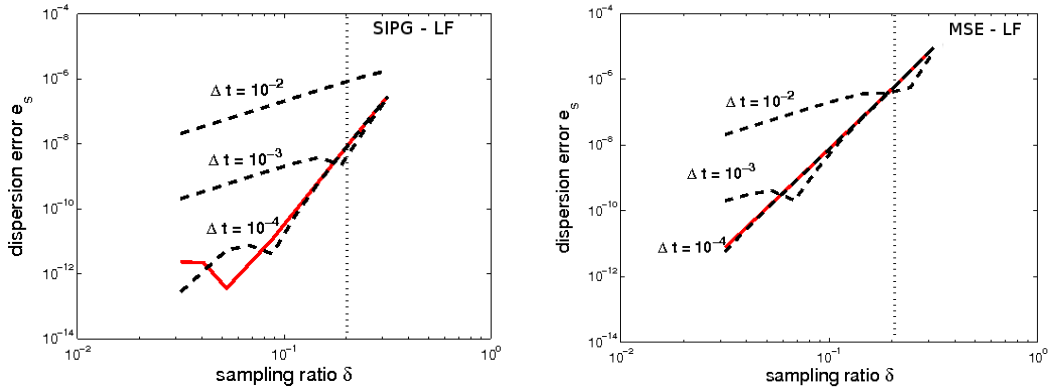

(a) SIPG - leap-frog (left) and MSE - leap-frog (right).

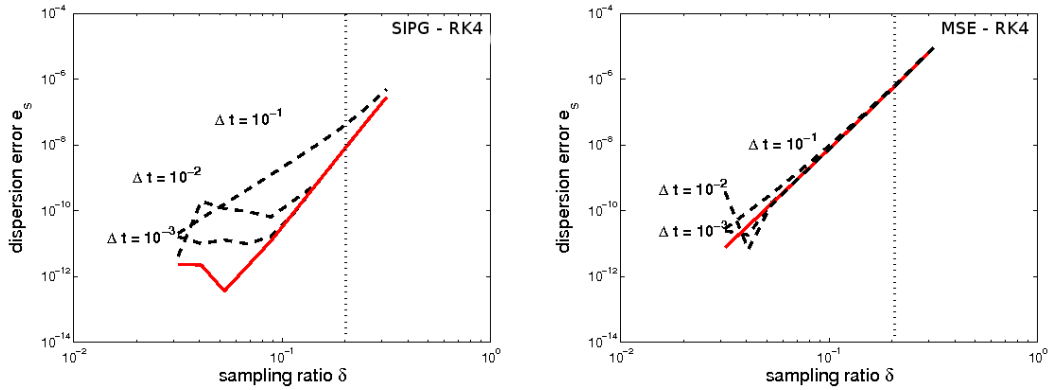

(b) SIPG - Runge-Kutta 4 (left) and MSE - Runge-Kutta 4 (right).

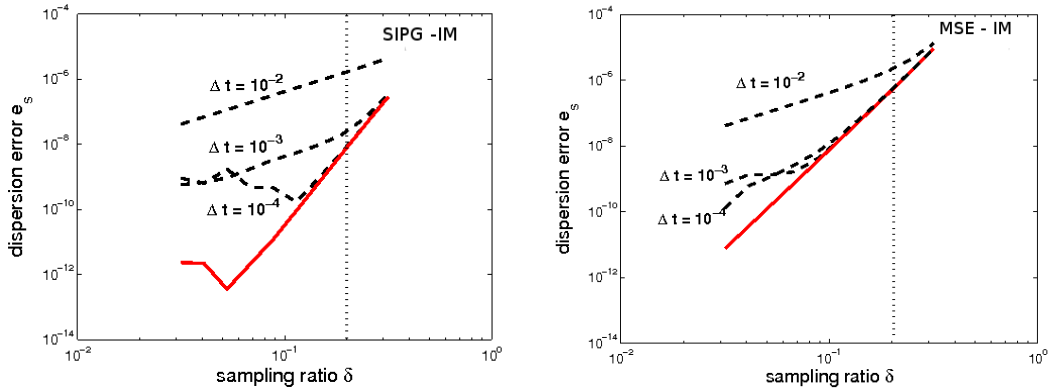

(c) SIPG - implicit midpoint method (left) and MSE - implicit midpoint method (right).

Figure 4.10: Fully-discrete shear grid dispersion versus the sampling ratio δ: $N = 4$. Comparison with the SIPG (left) and the MSE (right) fully-discrete formulations (dashed lines) and the corresponding semi-discrete formulations (solid line.) The threshold $\delta = 0.2$ is shown with a dashed vertical line.

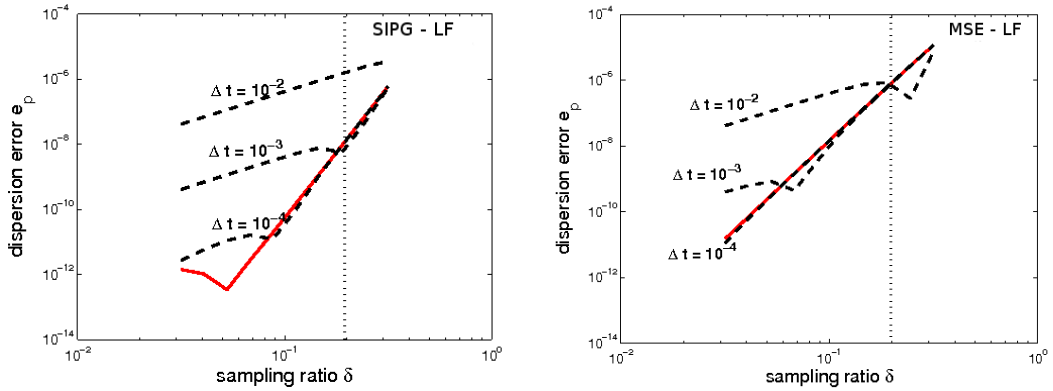

(a) SIPG - leap-frog (left) and MSE - leap-frog (right).

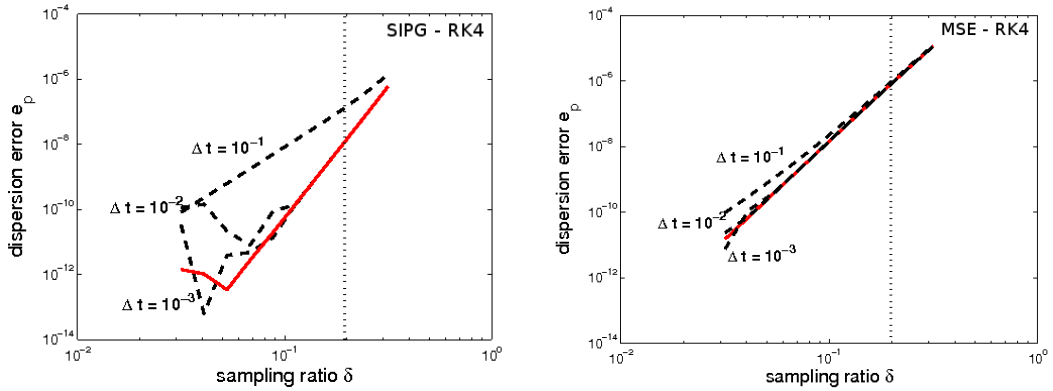

(b) SIPG - Runge-Kutta 4 (left) and MSE - Runge-Kutta 4 (right).

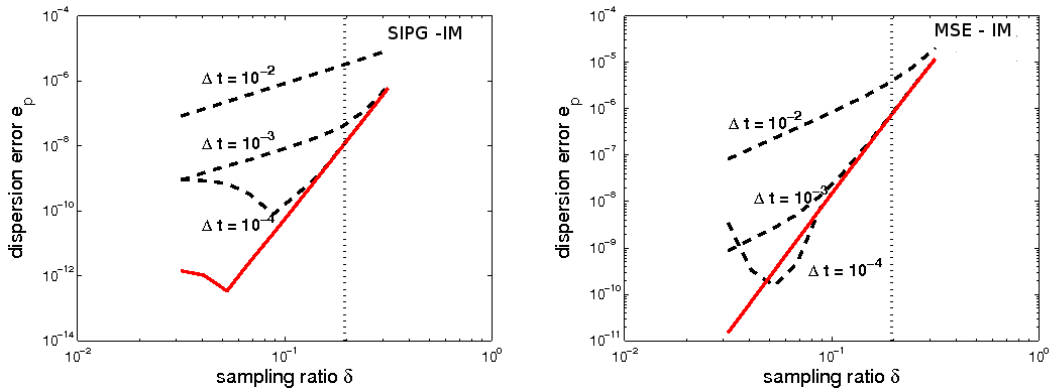

(c) SIPG - implicit midpoint method (left) and MSE - implicit midpoint method (right).

Figure 4.11: Fully-discrete compressional grid dispersion versus the sampling ratio δ: $N = 4$. Comparison with the SIPG (left) and the MSE (right) fully-discrete formulations (dashed lines) and the corresponding semi-discrete formulations (solid line.) The threshold $\delta = 0.2$ is shown with a dashed vertical line.

N	method	LF		RK		IM	
		e_S	e_P	e_S	e_P	e_S	e_P
2	SE	9.1325e-4	9.1324e-4	9.1326e-4	9.1326e-4	9.1327e-4	9.1329e-4
	SIPG	3.1768e-3	8.4215e-3	3.1768e-3	8.4215e-3	3.1768e-3	8.4215e-3
	MSE	3.5424e-2	6.2759e-2	3.5424e-2	6.2759e-2	3.5424e-2	6.2759e-2
3	SE	6.5154e-6	6.5072e-6	6.5237e-6	6.5237e-6	6.5401e-6	6.5565e-6
	SIPG	9.5991e-6	2.43323e-5	9.6073e-6	2.3340e-5	9.6238e-6	2.3372e-5
	MSE	3.3503e-4	1.4030e-4	3.3503e-4	1.4031e-4	3.3505e-4	1.4034e-4
4	SE	2.2038e-8	1.3813e-8	3.0263e-8	3.0263e-8	4.6714e-8	6.3161e-8
	SIPG	7.9786e-8	2.3355e-7	8.8012e-8	2.5000e-7	1.0446e-7	2.8290e-7
	MSE	1.9357e-6	6.2759e-7	1.9439e-6	8.5602e-7	1.9603e-6	8.8892e-7

Table 4.4: Maximum value $\max_{0\leq\theta\leq 2\pi}|e_S|$ and $\max_{0\leq\theta\leq 2\pi}|e_P|$, fixing $\delta = 0.2$, $r = 2$ and $\Delta t = 10^{-3}$, computed with the SE, SIPG and MSE discretizations and all the time integration schemes.

preferable to MSE method.

To analyze the anisotropy introduced by time integration schemes, we fix $N = 3, \delta = 0.2$, $r = 2$ and $\Delta t = 10^{-3}$. We compare the results with the semi-discrete ones reported in Figure 4.6. In Figure 4.13 we plot the ratios $c_{S,h}/c_S$ and $c_{P,h}/c_P$ varying the incident angle θ. To catch the small nuances between LF, RK4 and IM coupled wit SE, SIPG, MSE discretizations we report in Table 4.4 the maximum value $\max_{0<\theta<2\pi}|e_S|$ and $\max_{0<\theta<2\pi}|e_P|$ respectively.

We consider polynomial degree $N = 2, 3, 4$. For higher degrees the anisotropy is very small for all the practical purposes. Table 4.4 confirms that SIPG is lower dispersive with respect to the MSE method.

Dissipation error for fully-discrete approximations

In this section we address the dissipation error introduced by the DGSE and MSE discretization coupled with LF, RK4 and IM time integration schemes. As in the semi-discrete analysis the amplitude of the plane wave is given by

$$|e^{i(\kappa\cdot\mathbf{x}_j-\omega t_n)}| = e^{t_n \mathrm{Im}(\omega)} \qquad \forall\,\mathbf{x}_j, \qquad \forall\, t_n \in [0,T],$$

with ω replaced by the numerical values $\omega_{S,h}$, $\omega_{P,h}$, for S- or P-waves respectively. Clearly $\omega_{S,h}$ and $\omega_{P,h}$ depend on the chosen time integration scheme considered. Table 4.5 shows the computed values of $\mathrm{Im}(\omega_{S,h})$ and $\mathrm{Im}(\omega_{P,h})$ for the fully-discrete methods obtained with the LF, RK4 and IM time integration schemes for different choices of the

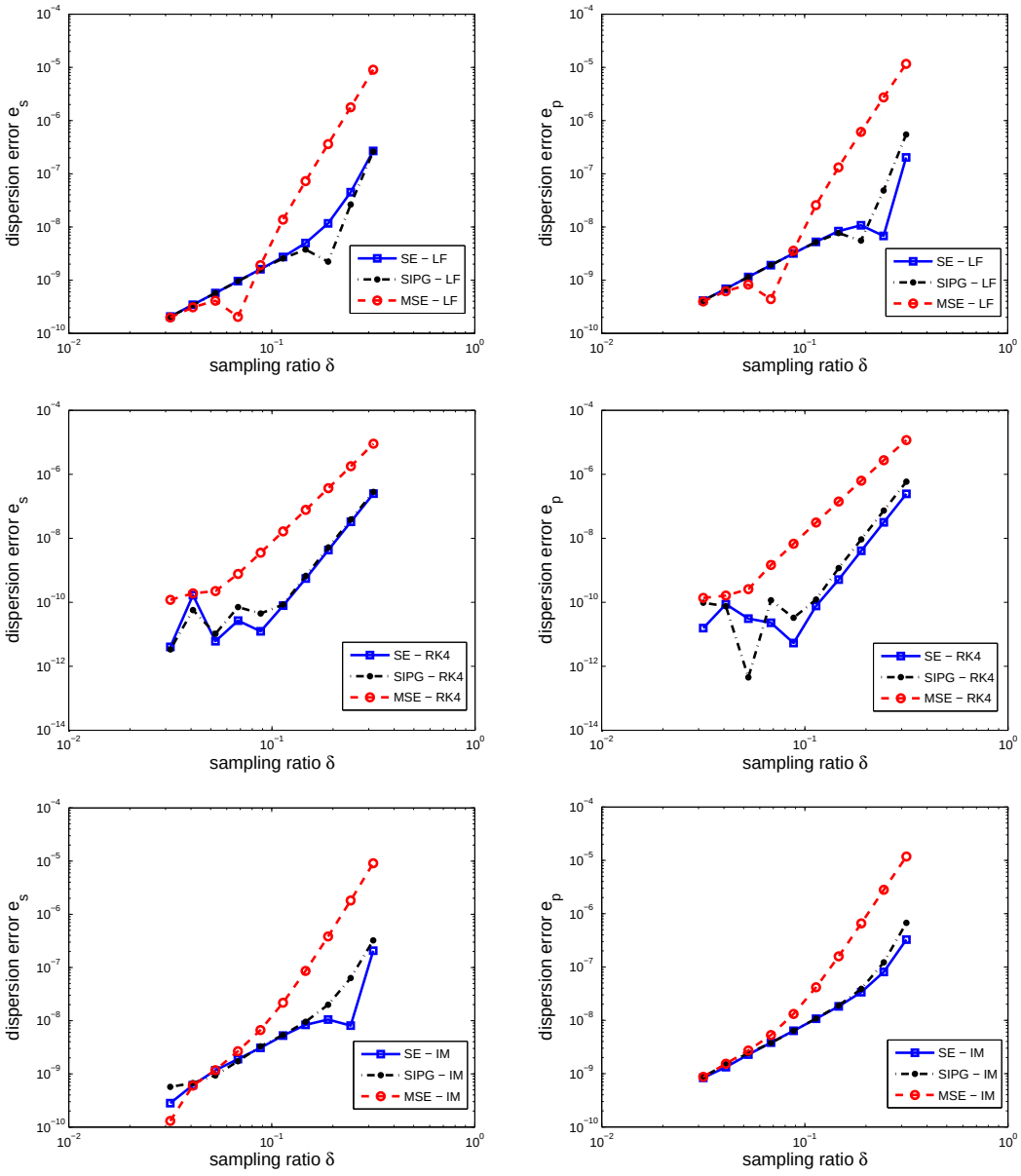

Figure 4.12: Shear (left) and compressional (right) fully-discrete dispersion errors versus the sampling ratio δ: $N = 4, r = 2$ and $\theta = \pi/4$. Comparison between SE, SIPG, MSE formulations coupled with the LF (top), RK (middle) and IM (bottom) time integration schemes.

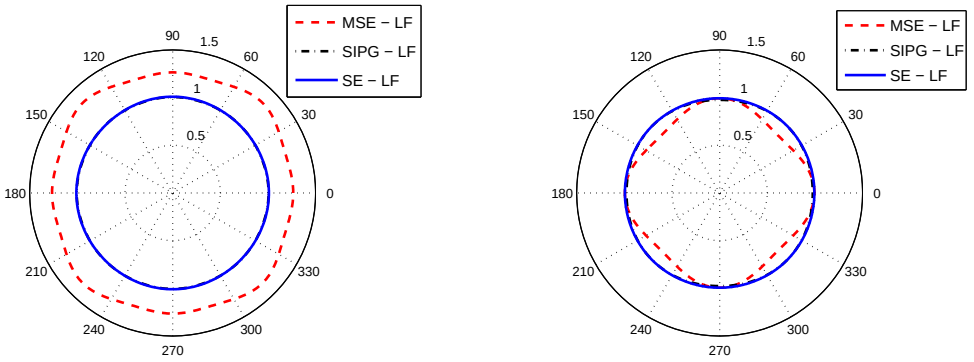

(a) Leap-frog time integration scheme.

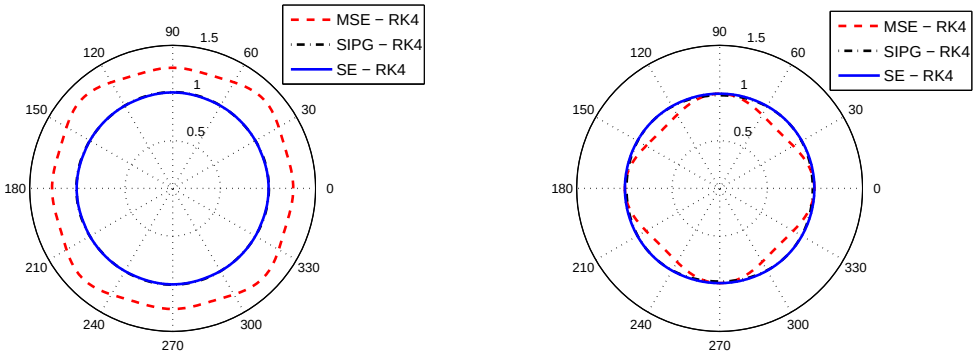

(b) Runge-Kutta 4 time integration scheme.

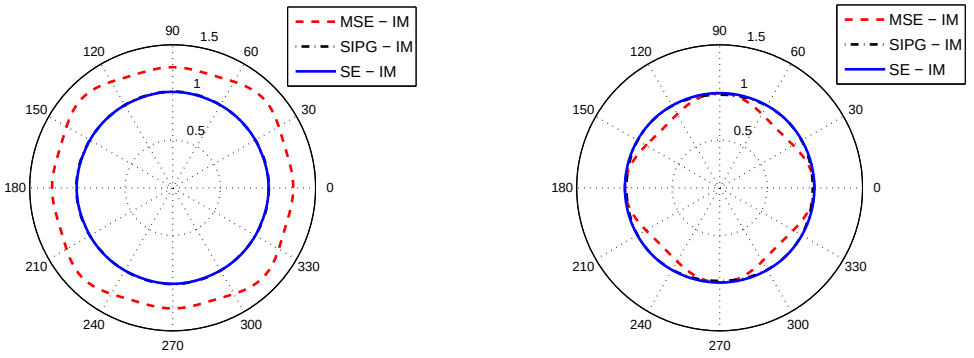

(c) Implicit midpoint method time integration scheme.

Figure 4.13: Fully-discrete numerical anisotropy for S- (left) and P- (right) waves: $N = 3$ and $\delta = 0.2$. All results are magnified by a factor 10^3.

polynomial approximation degree N, fixing $\Delta t = 10^{-3}$. The analogous results obtained with $N = 4$ and varying the sampling ration δ are shown in Table 4.6. We remark that all the considered methods do not suffer from global dissipation error. In particular with the SIPG-LF and MSE-LF methods we obtain the lowest dissipation errors.

4.3 Stability analysis

In this section we examine the stability properties for the explicit time integration schemes LF and RK4. The aim of this analysis is to establish a criterion that determines the largest time step Δt that we are allowed to use such that the discrete solution remains bounded with respect to the problem's data. In the literature this is known as the Courant, Friedrichs and Lewy (CFL) condition and imposes a restriction on the time step of the form

$$\Delta t \leq C_{\mathrm{CFL}} \frac{\Delta x}{c_P},$$

where Δx is the minimum distance between two neighbouring discretization nodes, c_P is the P wave velocity. We recall that the Courant number C_{CFL} depends on the dimension, the order of the scheme and the mesh geometry. In the applications is empirically chosen to be between $0.3 - 0.6$, see for example [61, 60, 85, 30]. In the following solving a generalized eigenvalue problem, we derive instead precise bounds for the C_{CFL} constant, both for the SIPG and MSE discretizations coupled with LF and the RK4 method. All the results will be compared with the analogous ones obtained with the SE methods.

Leap-frog time integration scheme

Let us start considering the eigenvalue problem (4.18). In order to make explicit the dependence of Λ on either the mesh size h and the polynomial approximation degree N, we rewrite (4.18) as

$$\widehat{\underline{\mathrm{K}}}\mathbf{U} = \Lambda' \widehat{\underline{\mathrm{M}}}\mathbf{U}, \tag{4.24}$$

with $\Lambda' = (h/\Delta t)^2 \sin^2(\omega_h \Delta t/2)$. Defining the *stability parameter* $q = c_P \Delta t/h$, we deduce the relation

$$q^2 \Lambda' = c_P^2 \sin^2\left(\frac{\omega_h \Delta t}{2}\right) \leq c_P^2,$$

or equivalently

$$q \leq c_P \frac{1}{\sqrt{\Lambda'}} = C_{\mathrm{CFL}}(\Lambda'), \tag{4.25}$$

(a) LF time integration scheme.

	SE-LF		SIPG-LF		MSE-LF	
N	$\mathrm{Im}(\omega_{S,h})$	$\mathrm{Im}(\omega_{P,h})$	$\mathrm{Im}(\omega_{S,h})$	$\mathrm{Im}(\omega_{P,h})$	$\mathrm{Im}(\omega_{S,h})$	$\mathrm{Im}(\omega_{P,h})$
2	-1.8687e-16	-1.6884e-16	-6.9782e-16	-9.6888e-16	-5.5165e-16	-2.5680e-16
3	-1.2386e-15	-1.1085e-15	8.8005e-16	3.2135e-16	8.0515e-16	-2.5558e-16
4	-1.1744e-16	3.1257e-16	-4.2113e-15	-5.0858e-16	3.1670e-15	6.1221e-16
5	1.4644e-15	8.9666e-16	-1.9977e-15	-6.5793e-15	-2.1894e-15	-4.6190e-15
6	-6.0645e-16	8.0892e-17	-3.4844e-15	4.8253e-15	-4.1583e-15	5.8972e-15
7	-1.5149e-14	-7.2159e-15	3.7452e-15	-8.5995e-15	1.1333e-14	-4.3412e-15
8	-7.2058e-15	-6.2394e-15	-1.4276e-14	-1.4739e-14	9.7548e-15	1.0194e-14
9	7.5118e-16	-2.6108e-15	2.3753e-14	-6.2472e-15	-7.6537e-15	-9.0125e-15
10	4.2337e-15	2.5439e-15	-5.1072e-14	2.3077e-14	-1.5956e-14	1.0328e-14

(b) RK4 time integration scheme.

	SE-RK		SIPG-RK		MSE-RK	
N	$\mathrm{Im}(\omega_{S,h})$	$\mathrm{Im}(\omega_{P,h})$	$\mathrm{Im}(\omega_{S,h})$	$\mathrm{Im}(\omega_{P,h})$	$\mathrm{Im}(\omega_{S,h})$	$\mathrm{Im}(\omega_{P,h})$
2	8.8818e-13	-9.9920e-13	4.4409e-13	-1.1102e-12	4.4409e-13	-1.1102e-12
3	-9.9920e-13	-9.9920e-13	-5.5511e-13	6.6613e-13	-5.5511e-13	6.6613e-13
4	-9.9920e-13	-1.8874e-12	3.1086e-12	3.7748e-12	3.1086e-12	3.7748e-12
5	1.3323e-12	4.6629e-12	2.4425e-12	4.4409e-13	2.4425e-12	4.4409e-13
6	1.1546e-11	-6.4393e-12	1.3323e-12	3.3307e-12	1.3323e-12	3.3307e-12
7	-1.9984e-12	2.6645e-12	1.3323e-12	-6.4393e-12	1.3323e-12	-6.4393e-12
8	-1.9651e-11	3.9080e-11	-1.2212e-12	-6.5503e-12	-1.2212e-12	-6.5503e-12
9	1.5543e-12	-5.5511e-13	1.6653e-11	-9.8810e-12	1.6653e-11	-9.8810e-12
10	-7.9936e-12	1.1324e-11	-2.8866e-12	-1.1102e-13	-2.8866e-12	-1.1102e-13

(c) IM time integration scheme.

	SE-IM		SIPG-IM		MSE-IM	
N	$\mathrm{Im}(\omega_{S,h})$	$\mathrm{Im}(\omega_{P,h})$	$\mathrm{Im}(\omega_{S,h})$	$\mathrm{Im}(\omega_{P,h})$	$\mathrm{Im}(\omega_{S,h})$	$\mathrm{Im}(\omega_{P,h})$
2	-3.3307e-13	1.5543e-12	-6.6613e-13	1.5543e-12	-6.6613e-13	1.5543e-12
3	-8.8818e-13	6.6613e-13	-4.4409e-13	3.5527e-12	-4.4409e-13	3.5527e-12
4	1.5543e-12	-4.6629e-12	2.4425e-12	1.3323e-12	2.4425e-12	1.3323e-12
5	-1.1102e-13	4.6629e-12	-2.2204e-12	-3.1086e-12	-2.2204e-12	-3.1086e-12
6	4.4409e-13	2.2204e-13	1.1768e-11	6.6613e-13	1.1768e-11	6.6613e-13
7	4.6629e-12	-6.3283e-12	7.1054e-12	-1.0325e-11	7.1054e-12	-1.0325e-11
8	3.3974e-12	-6.8834e-12	1.3323e-12	-3.3307e-13	1.3323e-12	-3.3307e-13
9	1.1990e-11	-2.9976e-11	1.1102e-11	-2.0317e-11	1.1102e-11	-2.0317e-11
10	4.5532e-12	-9.6589e-12	-8.7708e-12	-1.1102e-13	-8.7708e-12	-1.1102e-13

Table 4.5: Computed values of $\mathrm{Im}(\omega_{S,h})$ and $\mathrm{Im}(\omega_{P,h})$ for $N = 2,..,9$: $\delta = 0.2$, $\theta = \pi/4$ and $\Delta t = 10^{-3}$.

(a) LF time integration scheme.

	SE-LF		SIPG-LF		MSE-LF	
$1/\delta$	$\mathrm{Im}(\omega_{S,h})$	$\mathrm{Im}(\omega_{P,h})$	$\mathrm{Im}(\omega_{S,h})$	$\mathrm{Im}(\omega_{P,h})$	$\mathrm{Im}(\omega_{S,h})$	$\mathrm{Im}(\omega_{P,h})$
2	-4.6681e-17	-1.7229e-16	-1.7660e-15	-5.4334e-16	7.9602e-16	-3.9736e-16
4	-1.1896e-15	-1.8173e-15	-3.2565e-15	2.0011e-15	1.6631e-15	-1.8589e-15
6	-8.5509e-16	1.9686e-15	-3.8813e-15	7.3660e-16	3.9770e-16	-1.4470e-16
8	1.7380e-15	-3.8377e-16	1.3998e-15	1.8561e-15	-2.4063e-15	2.2529e-15
10	-4.8637e-16	-1.1671e-15	8.1446e-16	4.6269e-16	-3.8415e-15	-2.9109e-16

(b) RK4 time integration scheme.

	SE-RK		SIPG-RK		MSE-RK	
$1/\delta$	$\mathrm{Im}(\omega_{S,h})$	$\mathrm{Im}(\omega_{P,h})$	$\mathrm{Im}(\omega_{S,h})$	$\mathrm{Im}(\omega_{P,h})$	$\mathrm{Im}(\omega_{S,h})$	$\mathrm{Im}(\omega_{P,h})$
2	-3.3307e-13	-1.7764e-12	1.9984e-12	-6.6613e-13	2.4425e-12	-2.5535e-12
4	-2.3315e-12	3.5527e-12	-5.5511e-13	-9.9920e-13	-1.8874e-12	2.8866e-12
6	1.9984e-12	-4.9960e-12	1.9984e-12	-5.7732e-12	-4.9960e-12	1.7764e-12
8	-2.2204e-13	4.4409e-13	1.7764e-12	-1.2768e-11	3.7748e-12	3.9968e-12
10	-4.2188e-12	2.8866e-12	1.4655e-11	5.9952e-12	7.3275e-12	2.2204e-12

(c) IM time integration scheme.

	SE-IM		SIPG-IM		MSE-IM	
$1/\delta$	$\mathrm{Im}(\omega_{S,h})$	$\mathrm{Im}(\omega_{P,h})$	$\mathrm{Im}(\omega_{S,h})$	$\mathrm{Im}(\omega_{P,h})$	$\mathrm{Im}(\omega_{S,h})$	$\mathrm{Im}(\omega_{P,h})$
2	-2.3315e-12	2.2204e-13	4.4409e-13	-4.3299e-12	1.7764e-12	1.1102e-12
4	1.3323e-12	-2.8866e-12	-5.5511e-13	-3.6637e-12	-4.4409e-13	-2.9976e-12
6	2.4425e-12	3.7748e-12	-6.6613e-13	-7.8826e-12	6.6613e-13	2.2204e-12
8	-3.1086e-12	4.2188e-12	-1.3545e-11	-2.3315e-12	-4.6629e-12	-3.3307e-12
10	5.5511e-12	-1.0991e-11	9.5479e-12	-2.2204e-12	2.6645e-12	-1.7764e-12

Table 4.6: Values of $\mathrm{Im}(\omega_{S,h})$ and $\mathrm{Im}(\omega_{P,h})$ varying the sampling ratio δ: $N = 4$, $\theta = \pi/4$ and $\Delta t = 10^{-3}$.

As noted in [39], C_{CFL} is a function of Λ' and therefore depends implicitly on the wave vector $\boldsymbol{\kappa}$ through the matrices $\widehat{\underline{\mathrm{K}}}$ and $\widehat{\underline{\mathrm{M}}}$. Moreover, inequality (4.25) must be fulfilled for all the eigenvalues and all the wave vectors $\boldsymbol{\kappa} = 2\pi\delta/h(\cos(\theta), \sin(\theta))$.
Thus, the stability condition is given by

$$q = \min_{1\leq j\leq \nu} \min_{0\leq\theta\leq 2\pi} C_{\mathrm{CFL}}({\Lambda'}_j(\theta)), \tag{4.26}$$

where θ is the incident angle of the plane wave and ν is the number of the eigenvalues of problem (4.24). We remark that condition (4.26) is equivalent to require that

$$q \leq \frac{c(\lambda,\mu)}{\sqrt{\Lambda_{\max}}},$$

where $\Lambda_{\max}$ is the largest eigenvalue of problem (4.24) and $c(\lambda,\mu)$ is a positive constant that depends on the Lamé coefficients λ and μ. Thus, by estimating $\Lambda_{\max}$ in terms of h and N, it is possible to determine a bound for q.
In the DG approach, the bilinear form $\widehat{\mathcal{K}}(\cdot,\cdot)$ associated to the matrix $\widehat{\underline{\mathrm{K}}}$ in (4.18) takes the form

$$\begin{aligned}\widehat{\mathcal{K}}(\mathbf{u},\mathbf{v}) = &\int_{\Omega_C} \underline{\sigma}(\mathbf{u}) : \underline{\varepsilon}(\mathbf{v}) - \sum_{f=\{T,B,R,L\}} \int_{\gamma_f} \underline{\sigma}(\mathbf{u}) : \mathbf{v}\otimes\mathbf{n} \\ &+\theta\int_{\gamma_f} (\mathbf{u}-\mathbf{g}_f)\otimes\mathbf{n} : \underline{\sigma}(\mathbf{v}) + \eta_f \int_{\gamma_f} (\mathbf{u}-\mathbf{g}_f)\otimes\mathbf{n} : \mathbf{v}\otimes\mathbf{n},\end{aligned}$$

where the functions $\mathbf{u},\mathbf{v} \in V_\delta^{DG}$ are zero outside Ω_C, and $\mathbf{n}$ is the normal unit vector pointing outside Ω_C. According to the plane wave hypothesis (4.5), we take

$$\mathbf{g}_f = e^{\beta_f}\mathbf{u}, \quad \text{for} \quad f = \{T,B,L,R\}.$$

Following [7] we obtain

$$\widehat{\mathcal{K}}(\mathbf{u},\mathbf{u}) \leq c(\lambda,\mu,\alpha)\frac{N^4}{h^2}||\mathbf{u}||^2_{0,\Omega_C}.$$

Thus, for the generalized eigenvalue problem (4.24), we can derive the estimate

$$\Lambda_{\max} \leq c(\lambda,\mu,\alpha)\frac{N^4}{h^2},$$

and, consequently,

$$\Lambda'_{\max} \leq c(\lambda,\mu,\alpha)N^4. \tag{4.27}$$

For the MSE method we observe that writing $\Lambda'_{\max}$ through the generalized Rayleigh quotient yields

$$\begin{aligned}
\Lambda'_{\max} &= \sup_{\mathbf{v}\in\mathbb{R}^{2m}\setminus\{\mathbf{0}\}} \frac{(\widehat{\underline{\mathrm{K}}}\mathbf{v},\mathbf{v})_{\Omega_C}}{(\widehat{\underline{\mathrm{M}}}\mathbf{v},\mathbf{v})_{\Omega_C}} = \sup_{\mathbf{v}\in\mathbb{R}^{2m}\setminus\{\mathbf{0}\}} \frac{(\widetilde{\underline{\mathrm{Q}}}^{\top}\widetilde{\underline{\mathrm{A}}}\widetilde{\underline{\mathrm{Q}}}\mathbf{v},\mathbf{v})_{\Omega_C}}{(\widetilde{\underline{\mathrm{Q}}}^{\top}\widetilde{\underline{\mathrm{M}}}\widetilde{\underline{\mathrm{Q}}}\mathbf{v},\mathbf{v})_{\Omega_C}} \\
&= \sup_{\mathbf{v}\in\mathbb{R}^{2m}\setminus\{\mathbf{0}\}} \frac{(\widetilde{\underline{\mathrm{A}}}\widetilde{\underline{\mathrm{Q}}}\mathbf{v},\widetilde{\underline{\mathrm{Q}}}\mathbf{v})_{\Omega_C}}{(\widetilde{\underline{\mathrm{M}}}\widetilde{\underline{\mathrm{Q}}}\mathbf{v},\widetilde{\underline{\mathrm{Q}}}\mathbf{v})_{\Omega_C}} = \sup_{\substack{\mathbf{w}=\widetilde{\underline{\mathrm{Q}}}\mathbf{v}\in\mathbb{R}^{2n}\setminus\{\mathbf{0}\} \\ \exists\, i=1,\dots,2m:\ \mathbf{v}\cdot\mathbf{e}_i\neq\mathbf{0}}} \frac{(\widetilde{\underline{\mathrm{A}}}\mathbf{w},\mathbf{w})_{\Omega_C}}{(\widetilde{\underline{\mathrm{M}}}\mathbf{w},\mathbf{w})_{\Omega_C}} \\
&\leq \sup_{\mathbf{v}\in\mathbb{R}^{2n}\setminus\{\mathbf{0}\}} \frac{(\widetilde{\underline{\mathrm{A}}}\mathbf{v},\mathbf{v})_{\Omega_C}}{(\widetilde{\underline{\mathrm{M}}}\mathbf{v},\mathbf{v})_{\Omega_C}} = \sup_{\mathbf{v}\in\mathbb{R}^{2n}\setminus\{\mathbf{0}\}} \frac{(\underline{\mathrm{A}}\mathbf{v},\mathbf{v})_{\Omega_C}}{(\underline{\mathrm{M}}\mathbf{v},\mathbf{v})_{\Omega_C}},
\end{aligned} \tag{4.28}$$

where $m = (N^2+3)$ and $n = (N+1)^2$. In this way, we obtain an upper bound for the maximum eigenvalue of (4.24) when using MSE approximation. Indeed, the last term in (4.28) is exactly the maximum eigenvalue of the SE discretization for which the following estimate holds (cf. [20])

$$c_1 N^4 \leq \Lambda'_{\max} \leq c_2 N^4, \tag{4.29}$$

for c_1 and c_2 positive constants. Finally, we can resume the stability analysis in the following statement.

Proposition 2. *For every $\mu > 0, \lambda \geq 0$ and $\alpha \geq \alpha_{\min} > 0$, the CFL condition (4.25) is satisfied for both the MSE and SIPG methods if there exists a positive constant $c^*(\lambda,\mu,\alpha)$ such that*

$$q \leq \frac{c^*(\lambda,\mu,\alpha)}{N^2}. \tag{4.30}$$

Moreover, for the MSE and the NIPG methods it holds $\alpha_{\min} = 0$ and $c^*(\lambda,\mu,\alpha) = c^*(\lambda,\mu)$.

We remark that for the SIPG, the constant $c^*(\lambda,\mu,\alpha)$ is proportional to $\alpha^{-1/2}$ (cf. [7]). Then a less restrictive bound for q in (4.30) is achieved when $\alpha = \alpha_{\min}$. Moreover, it is possible to determine exactly the threshold value $\alpha_{\min}$ (cf. [45] for the elliptic case), but this is beyond the objective of this study. For the numerical simulations in Section 4.3 we choose $\alpha = 1$.

Runge-Kutta 4 time integration scheme

To derive the CFL condition for the fully-discrete scheme resulting from the RK4 integration, let us consider the ordinary differential system of equations (4.19). Suppose

that the matrix $\underline{\widehat{\mathrm{T}}}$ is diagonalizable in $\mathbb{C}$, that means that there exists a complete set of m linearly independent eigenvectors $\mathbf{Y}_k$ satisfying

$$\underline{\widehat{\mathrm{T}}}\mathbf{Y}_k = \xi_k \mathbf{Y}_k, \quad k = 1, ..., m, \tag{4.31}$$

where $m = 4(N+1)^2$ (resp. $m = 4(N^2+3)$) for SIPG (resp. MSE) discretizations. Let $\underline{\mathrm{Y}} = [\mathbf{Y}_1, \mathbf{Y}_2, ..., \mathbf{Y}_m]$ and $\underline{\Sigma} = [\xi_1, ..., \xi_m]$ be the matrices containing the eigenvectors and the eigenvalues of (4.31) . Then, we obtain

$$\underline{\widehat{\mathrm{T}}} = \underline{\mathrm{Y}}\,\underline{\Sigma}\,\underline{\mathrm{Y}}^{-1} \quad \text{and} \quad \underline{\Sigma} = \underline{\mathrm{Y}}^{-1}\underline{\widehat{\mathrm{T}}}\,\underline{\mathrm{Y}}.$$

Multiplying equation (4.19) by $\underline{\mathrm{Y}}^{-1}$ on both sides and introducing $\underline{\mathrm{I}} = \underline{\mathrm{Y}}\underline{\mathrm{Y}}^{-1}$ we have the following equivalent system of ordinary differential equations

$$\underline{\mathrm{Y}}^{-1}\dot{\mathbf{W}}(t) = (\underline{\mathrm{Y}}^{-1}\underline{\widehat{\mathrm{T}}}\underline{\mathrm{Y}})\underline{\mathrm{Y}}^{-1}\mathbf{W}(t),$$

that by setting $\mathbf{Z}(t) = \underline{\mathrm{Y}}^{-1}\mathbf{W}(t)$, can be rewritten as

$$\dot{\mathbf{Z}}(t) = \underline{\Sigma}\mathbf{Z}(t).$$

This is a diagonal system of ordinary differential equations, i.e., m independent scalar equations, one for each component of $\mathbf{Z}$. The k-th such equation reads

$$\dot{Z}_k(t) = \xi_k Z_k(t), \quad k = 1, ..., m. \tag{4.32}$$

When applying the RK4 method to the above system we obtain m independent scalar equations of the form

$$Z_k(t_{n+1}) = \mathcal{R}(\Delta t \xi_k) Z_k(t_n), \quad k = 1, ..., m,$$

where

$$\mathcal{R}(z) = \sum_{j=0}^{4} \frac{z^j}{j!}.$$

For the method to be stable, each of the resulting scalar problems must be stable, and this clearly imply that $\Delta t \xi_k$ must be in the stability region of the RK4 method for all k. The region of stability (more properly called region of absolute stability) of a one step method, is simply given by $S = \{z \in \mathbb{C} : |\mathcal{R}(z)| \leq 1\}$, see [91]. We notice that it is possible to obtain an equivalent estimate starting from

$$\mathbf{W}(t_{n+1}) = \sum_{k=0}^{4} \frac{(\Delta t \underline{\widehat{\mathrm{T}}})^k}{k!} \mathbf{W}(t_n),$$

and noticing that the region of absolute stability

$$S' = \{z \in \mathbb{C} : \; z = \texttt{eig}\left(\sum_{k=0}^{4} \frac{(\Delta t \widehat{\underline{\mathrm{T}}})^k}{k!}\right) \quad \text{and} \quad |z| \leq 1\},$$

is such that $S' = S$. Moreover, we remark that, if we are able to estimate the region of absolute stability S or S' automatically this provide a limitation for Δt. As we will see in the next section, C_{CFL} behaves as $C_{\mathrm{CFL}} \lesssim N^{-2}$, as for the leap-frog scheme.

Numerical Results

To estimate the stability parameter q for the LF scheme we fix $\delta = 0.2$ and the ratio $r = 1.414$. This choice gives a restrictive stability condition: higher values of $r = c_P/c_S$ lead milder stability conditions [39]. As for the grid dispersion analysis we have fixed $\eta = 2N^2/h$ for the SIPG and the NIPG methods. In Table 4.7-(a) are shown the estimated threshold values for q, for $N = 2, ..., 10$. The constants for the SIPG method are around 70 percent with respect to the ones of the SE method, while for the MSE method are around 95 percent. The NIPG method has constants always more restrictive than those of the SIPG method.

In Table 4.7-(a) it is also shown the asymptotic behaviour of the q constant with respect to N (N-rate), computed as the average of the rates obtained for $N = 2, ..., 20$: as expected the decay rate of q is approximately proportional to N^{-2}. In Figure 4.14 we show the computed value of $\Lambda'_{\max}$ versus the polynomial degree N. In agreement with the theoretical estimate $\Lambda'_{\max} \approx N^{-4}$. In practice, the time step is often bounded, not by the size of the spectral elements h, but by the smaller space increment Δx between to neighbouring spectral nodes. In Table 4.7-(b) we compute the upper bounds for the modified stability parameter $q' = c_P \Delta t/\Delta x$. It is evident that the CFL condition (4.26) is less restrictive for the MSE method than for the SIPG scheme. We have repeated the same set of experiments employing the RK4 integration scheme. In order to compare the RK4 method with the LF scheme, we fix the same set of parameters, i.e., $r = 1.414$, $\delta = 0.2$ and $\eta = 2N^2/h$ for the SIPG scheme.

As described in the previous section to compute the stability constant for the RK4 method we consider a large set of combinations $(\Delta t, \theta)$ for polynomial degrees $N = 2, ...10$. In Table 4.8-(a) we report the computed values obtained with the SE, SIPG and MSE discretizations together with the asymptotic rate (N-rate). As for the LF scheme, the trend for the RK4 method is approximately proportional to N^{-2} and the

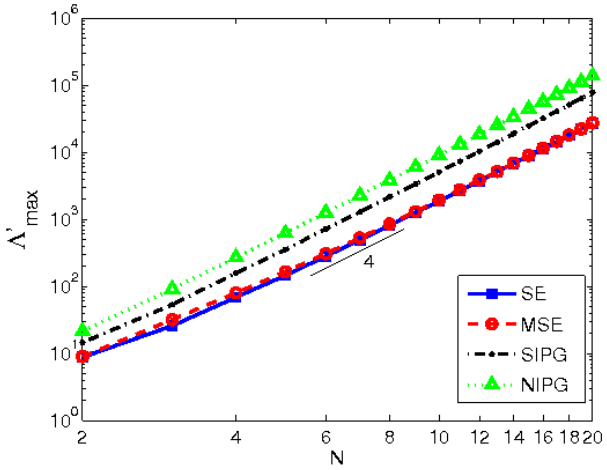

Figure 4.14: $\Lambda'_{\max}$ (cf. (4.27) and (4.29))versus the polynomial degree N for the generalized eigenvalue problem (4.24).

(a)

N	SE	MSE	SIPG	NIPG
2	0.3376	0.3333	0.2621	0.2163
3	0.1967	0.1770	0.1368	0.1045
4	0.1206	0.1118	0.0795	0.0607
5	0.0827	0.0776	0.0530	0.0400
6	0.0596	0.0570	0.0374	0.0281
7	0.0449	0.0434	0.0280	0.0210
8	0.0351	0.0342	0.0216	0.0162
9	0.0281	0.0277	0.0172	0.0129
10	0.0231	0.0227	0.0140	0.0105
N-rate	-1.8463	-1.8253	-1.9247	-1.9360

(b)

N	SE	MSE	SIPG	NIPG
2	0.6752	0.6667	0.5241	0.4326
3	0.7115	0.6403	0.4951	0.3782
4	0.6983	0.6474	0.4607	0.3516
5	0.7039	0.6608	0.4515	0.3409
6	0.7017	0.6712	0.4400	0.3315
7	0.7009	0.6769	0.4360	0.3273
8	0.7005	0.6819	0.4303	0.3228
9	0.6994	0.6878	0.4282	0.3206
10	0.6995	0.6871	0.4247	0.3180
average	0.6990	0.6689	0.4545	0.3471

Table 4.7: LF method. Computed upper bound for the stability parameter $q = c_P \Delta t/h$ (a) and $q' = c_P \Delta t/\Delta x$ (b) for $r = 1.414$. Rate of decay of q with respect to N (a). Stability parameter q' proportional to qN^2 thus constant for different choices of Δx (b).

(a)

N	SE	MSE	SIPG
2	0.4815	0.4175	0.3739
3	0.2835	0.2505	0.1972
4	0.1715	0.1585	0.1165
5	0.1175	0.1100	0.0762
6	0.0845	0.0810	0.0560
7	0.0640	0.0586	0.0408
8	0.0500	0.0450	0.0307
9	0.0400	0.0360	0.0257
10	0.0330	0.0295	0.0200
N-rate	-1.8348	-1.8513	-1.9597

(b)

N	SE	MSE	SIPG
2	0.9630	0.8350	0.7478
3	1.0257	0.9063	0.7135
4	0.9932	0.9179	0.6747
5	1.0002	0.9364	0.6487
6	0.9954	0.9542	0.6597
7	0.9980	0.9138	0.6362
8	0.9976	0.8978	0.6125
9	0.9942	0.8948	0.6388
10	1.0000	0.8940	0.6061
average	0.9964	0.9056	0.6598

Table 4.8: RK4 method. Computed upper bound for the stability parameter $q = c_P\Delta t/h$ (a) and $q' = c_P\Delta t/\Delta x$ (b) for $r = 1.414$. Rate of decay of q with respect to N (a). Stability parameter q' proportional to qN^2 thus constant for different choices of Δx (b).

N-rate is computed using polynomial degree up to 20. In the family of DG strategies NIPG and IIPG approaches have C_{CFL} bounds always lower than SIPG. The results confirm that stability bounds are less restrictive for the MSE method with respect to the SIPG. In particular the former are around 90 percent of the SE ones while the latter around 65 percent.

In Table 4.8-(b) we also report the estimated bound for the modified stability parameter $q' = c_P\Delta t/\Delta x$, i.e., q scaled by the minimum distance Δx between two consecutive GLL-nodes. Comparing Tables 4.7-(b) and 4.8-(b) we notice that in this case the RK4 stability bounds are less restrictive of the LF ones, so from this point of view RK4 is preferable to LF.

Chapter 5

Implementation issues

In this chapter we detail the algorithmic aspects of the DGSE and MSE formulations, describing their implementation in a spectral element based code.
In Section 5.1 we describe the strategy employed to compute the integrals appearing in the algebraic formulations (2.54) and (2.64), respectively. We give special attention to the non-conforming part of the semi-discretizations (2.7) and (2.12) describing in detail the procedure adopted to compute the interface terms and the *mortar condition* **MC**.
In Section 5.2 we compare the DG and Mortar semi-discretizations from the efficiency view point. We remark that in this context the word "efficiency" means both low memory storage and computational time.

5.1 Numerical integration

As described in Chapter 2 we supposed Ω subdivided into K non overlapping subdomains Ω_k, $k = 1, ..., K$, such that $\overline{\Omega} = \bigcup_{k=1}^{K} \overline{\Omega}_k$ with $\Omega_k \cap \Omega_\ell = \emptyset$ if $k \neq \ell$. Moreover, in each Ω_k we introduce a partitioning $\mathcal{T}_{h_k}$, made by quadrilaterals elements Ω_k^j, with granularity h_k. We denote by $\Gamma_{j(k)}^{\ell}$, $\ell = 1, ..., 4$, the boundary edges of each Ω_k^j (see Figure 5.1 (left)).

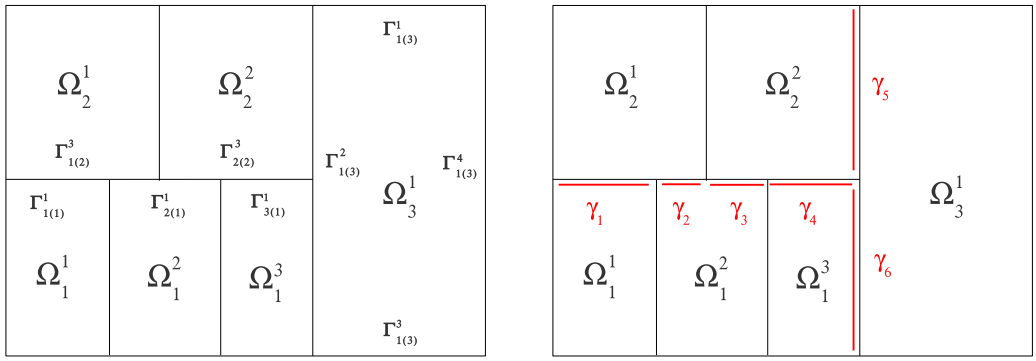

Figure 5.1: Left: example of subdomain partitio into $K = 3$ subdomains ($\overline{\Omega} = \overline{\Omega}_1 \cup \overline{\Omega}_2 \cup \overline{\Omega}_3$) with $\overline{\Omega}_1 = \bigcup_{j=1}^3 \overline{\Omega}_1^j$, $\overline{\Omega}_2 = \bigcup_{j=1}^2 \overline{\Omega}_2^j$ and $\overline{\Omega}_3 = \overline{\Omega}_3^1$. Right: edges $\gamma_1, ..., \gamma_6$.

Interface integrals for the DGSE method

In the DGSE approach the skeleton of the decomposition is defined as the union of elementary components, i.e.,

$$\mathcal{S} = \bigcup_{k=1}^{K} \partial\Omega_k \setminus \partial\Omega = \bigcup_{i=1}^{M} \gamma_i$$

where $\gamma_i = \Gamma^{\ell}_{j(k)} \cap \Gamma^{\ell'}_{j'(k')}$ for some triples (j,k,ℓ) and (j',k',ℓ') with $k \neq k'$. To easy the notation we let Ω^+ and Ω^- be two elements that shear the edge γ_i, see Figure 5.2. We recall that the bilinear form $\mathcal{B}(\cdot,\cdot)$ is given by

$$\mathcal{B}(\mathbf{u},\mathbf{v})_{\gamma_i} = -\left(\{\underline{\sigma}(\mathbf{u})\}, [\![\mathbf{v}]\!]\right)_{\gamma_i} + \theta\left([\![\mathbf{u}]\!], \{\underline{\sigma}(\mathbf{v})\}\right)_{\gamma_i} + \eta_{\gamma_i}\left([\![\mathbf{u}]\!], [\![\mathbf{v}]\!]\right)_{\gamma_i},$$

cf. (2.8). Using the definition of $\{\cdot\}$ and $[\![\cdot]\!]$ introduced in (2.4) and (2.5), respectively we have

$$\begin{aligned}\mathcal{B}(\mathbf{u},\mathbf{v})_{\gamma_i} \;=\; & -\frac{1}{2}\left(\underline{\sigma}(\mathbf{u}^+) + \underline{\sigma}(\mathbf{u}^-), \mathbf{v}^+ \otimes \mathbf{n}^+ + \mathbf{v}^- \otimes \mathbf{n}^-\right)_{\gamma_i} \\ & + \frac{\theta}{2}\left(\mathbf{u}^+ \otimes \mathbf{n}^+ + \mathbf{u}^- \otimes \mathbf{n}^-, \underline{\sigma}(\mathbf{v}^+) + \underline{\sigma}(\mathbf{v}^-)\right)_{\gamma_i} \\ & + \eta_{\gamma_i}\left(\mathbf{u}^+ \otimes \mathbf{n}^+ + \mathbf{u}^- \otimes \mathbf{n}^-, \mathbf{v}^+ \otimes \mathbf{n}^+ + \mathbf{v}^- \otimes \mathbf{n}^-\right)_{\gamma_i}.\end{aligned}$$

The above integrals are computed for each element Ω^+ of the meso decomposition that has an edge $\gamma_i \in \mathcal{S}$. So when we look to γ_i from Ω^+ we consider only the contributions

$$\begin{aligned}\mathcal{B}(\mathbf{u},\mathbf{v})_{\gamma_i} &= -\frac{1}{2}\left(\underline{\sigma}(\mathbf{u}^+)+\underline{\sigma}(\mathbf{u}^-),\mathbf{v}^+\otimes\mathbf{n}^+\right)_{\gamma_i}\\ &\quad+\frac{\theta}{2}\left(\mathbf{u}^+\otimes\mathbf{n}^++\mathbf{u}^-\otimes\mathbf{n}^-,\underline{\sigma}(\mathbf{v}^+)\right)_{\gamma_i}\\ &\quad+\eta_{\gamma_i}\left(\mathbf{u}^+\otimes\mathbf{n}^++\mathbf{u}^-\otimes\mathbf{n}^-,\mathbf{v}^+\otimes\mathbf{n}^+\right)_{\gamma_i},\end{aligned} \tag{5.1}$$

while when we look to γ_i from Ω^- we compute

$$\begin{aligned}\mathcal{B}(\mathbf{u},\mathbf{v})_{\gamma_i} &= -\frac{1}{2}\left(\underline{\sigma}(\mathbf{u}^+)+\underline{\sigma}(\mathbf{u}^-),\mathbf{v}^-\otimes\mathbf{n}^-\right)_{\gamma_i}\\ &\quad+\frac{\theta}{2}\left(\mathbf{u}^+\otimes\mathbf{n}^++\mathbf{u}^-\otimes\mathbf{n}^-,\underline{\sigma}(\mathbf{v}^-)\right)_{\gamma_i}\\ &\quad+\eta_{\gamma_i}\left(\mathbf{u}^+\otimes\mathbf{n}^++\mathbf{u}^-\otimes\mathbf{n}^-,\mathbf{v}^-\otimes\mathbf{n}^-\right)_{\gamma_i}.\end{aligned} \tag{5.2}$$

Now, as a reference example, we consider the integral $(\underline{\sigma}(\mathbf{u}^+)+\underline{\sigma}(\mathbf{u}^-),\mathbf{v}^+\otimes\mathbf{n}^+)_{\gamma_i}$. All the other terms in (5.1) and (5.2) can be treated similarly. By choosing as a test function $\mathbf{v}=(\Psi_i^1,\Psi_i^2)^\top$ we have

$$\begin{aligned}\left(\underline{\sigma}(\mathbf{u}^+)+\underline{\sigma}(\mathbf{u}^-),\mathbf{v}^+\otimes\mathbf{n}^+\right)_{\gamma_i} &= \left(\sigma_{11}(\mathbf{u}^+),\Psi_i^{1,+}n^{1,+}\right)_{\gamma_i}+\left(\sigma_{12}(\mathbf{u}^+),\Psi_i^{1,+}n^{2,+}\right)_{\gamma_i}\\ &+ \left(\sigma_{21}(\mathbf{u}^+),\Psi_i^{2,+}n^{1,+}\right)_{\gamma_i}+\left(\sigma_{22}(\mathbf{u}^+),\Psi_i^{2,+}n^{2,+}\right)_{\gamma_i},\\ &= \left(\sigma_{11}(\mathbf{u}^-),\Psi_i^{1,+}n^{1,+}\right)_{\gamma_i}+\left(\sigma_{12}(\mathbf{u}^-),\Psi_i^{1,+}n^{2,+}\right)_{\gamma_i}\\ &+ \left(\sigma_{21}(\mathbf{u}^-),\Psi_i^{2,+}n^{1,+}\right)_{\gamma_i}+\left(\sigma_{22}(\mathbf{u}^-),\Psi_i^{2,+}n^{2,+}\right)_{\gamma_i},\end{aligned}$$

for $i=a^+,...,b^+$, with a^+,b^+ positive integers (depending on the unknowns numeration). Then, noticing that

$$\begin{aligned}\sigma_{11}(\mathbf{u}^\pm) &= \{\lambda+2\mu\}_A\frac{\partial u_1^\pm}{\partial x_1}+\{\lambda\}_A\frac{\partial u_2^\pm}{\partial x_2},\\ \sigma_{12}(\mathbf{u}^\pm) &= \{\mu\}_A\left(\frac{\partial u_1^\pm}{\partial x_2}+\frac{\partial u_2^\pm}{\partial x_1}\right),\\ \sigma_{21}(\mathbf{u}^\pm) &= \{\mu\}_A\left(\frac{\partial u_2^\pm}{\partial x_1}+\frac{\partial u_1^\pm}{\partial x_2}\right),\\ \sigma_{22}(\mathbf{u}^\pm) &= \{\lambda+2\mu\}_A\frac{\partial u_2^\pm}{\partial x_2}+\{\lambda\}_A\frac{\partial u_1^\pm}{\partial x_1},\end{aligned}$$

we obtain

$$\begin{aligned}\left(\underline{\sigma}(\mathbf{u}^+),\mathbf{v}^+\otimes\mathbf{n}^+\right)_{\gamma_i} &= \sum_{j=a^+}^{b^+} U_j^{1,+}\left\{c_1\left(\frac{\partial\Psi_j^{1,+}}{\partial x_1},\Psi_i^{1,+}\right)_{\gamma_i}+c_2\left(\frac{\partial\Psi_j^{1,+}}{\partial x_1},\Psi_i^{2,+}\right)_{\gamma_i}\right.\\ &\quad \left.+c_3\left(\frac{\partial\Psi_j^{1,+}}{\partial x_2},\Psi_i^{1,+}\right)_{\gamma_i}+c_4\left(\frac{\partial\Psi_j^{1,+}}{\partial x_2},\Psi_i^{2,+}\right)_{\gamma_i}\right\}\\ &+ \sum_{j=a^+}^{b^+} U_j^{2,+}\left\{c_5\left(\frac{\partial\Psi_j^{2,+}}{\partial x_2},\Psi_i^{2,+}\right)_{\gamma_i}+c_2\left(\frac{\partial\Psi_j^{2,+}}{\partial x_2},\Psi_i^{1,+}\right)_{\gamma_i}\right.\\ &\quad \left.+c_3\left(\frac{\partial\Psi_j^{2,+}}{\partial x_1},\Psi_i^{1,+}\right)_{\gamma_i}+c_4\left(\frac{\partial\Psi_j^{2,+}}{\partial x_1},\Psi_i^{2,+}\right)_{\gamma_i}\right\}.\end{aligned}$$

and

$$\begin{aligned}\left(\underline{\sigma}(\mathbf{u}^-),\mathbf{v}^+\otimes\mathbf{n}^+\right)_{\gamma_i} &= \sum_{j=a^-}^{b^-} U_j^{1,-}\left\{c_1\left(\frac{\partial\Psi_j^{1,-}}{\partial x_1},\Psi_i^{1,+}\right)_{\gamma_i}+c_2\left(\frac{\partial\Psi_j^{1,-}}{\partial x_1},\Psi_i^{2,+}\right)_{\gamma_i}\right.\\ &\quad \left.+c_3\left(\frac{\partial\Psi_j^{1,-}}{\partial x_2},\Psi_i^{1,+}\right)_{\gamma_i}+c_4\left(\frac{\partial\Psi_j^{1,-}}{\partial x_2},\Psi_i^{2,+}\right)_{\gamma_i}\right\}\\ &+ \sum_{j=a^-}^{b^-} U_j^{2,-}\left\{c_5\left(\frac{\partial\Psi_j^{2,-}}{\partial x_2},\Psi_i^{2,+}\right)_{\gamma_i}+c_2\left(\frac{\partial\Psi_j^{2,-}}{\partial x_2},\Psi_i^{1,+}\right)_{\gamma_i}\right.\\ &\quad \left.+c_3\left(\frac{\partial\Psi_j^{2,-}}{\partial x_1},\Psi_i^{1,+}\right)_{\gamma_i}+c_4\left(\frac{\partial\Psi_j^{2,-}}{\partial x_1},\Psi_i^{2,+}\right)_{\gamma_i}\right\}.\end{aligned}$$

with a^-, b^+ positive integer (depending on the unknowns numeration) and

$$\begin{aligned}c_1 &= \{\lambda+2\mu\}_A\, n^{1,+},\\ c_2 &= \{\lambda\}_A\, n^{2,+},\\ c_3 &= \{\mu\}_A\, n^{2,+},\\ c_4 &= \{\mu\}_A\, n^{1,+},\\ c_5 &= \{\lambda+2\mu\}_A\, n^{2,+}.\end{aligned}$$

Now, the key point is how to compute the quantities

$$\left(\frac{\partial\Psi_j^{\pm}}{\partial x_1},\Psi_i^{+}\right)_{\gamma_i} \quad \text{and} \quad \left(\frac{\partial\Psi_j^{\pm}}{\partial x_2},\Psi_i^{+}\right)_{\gamma_i}. \tag{5.3}$$

In order to do that, we recall that the any element Ω is the image through a bilinear map $\mathbf{F}$ of the reference element $\widehat{\Omega} = (-1,1)^2$. This means that the physical variables $(x_1, x_2) \in \Omega$ depends on the local variables $(\xi, \eta) \in \widehat{\Omega}$ through $\mathbf{F}$, i.e. $\mathbf{F}(\xi,\eta) = (x_1(\xi,\eta), x_2(\xi,\eta))$. Therefore, it holds

$$\begin{aligned}\frac{\partial \Psi_i}{\partial \xi} &= \frac{\partial x_1}{\partial \xi}\frac{\partial \Psi_i}{\partial x_1} + \frac{\partial x_1}{\partial \xi}\frac{\partial \Psi_i}{\partial x_2},\\ \frac{\partial \Psi_i}{\partial \eta} &= \frac{\partial x_1}{\partial \eta}\frac{\partial \Psi_i}{\partial x_1} + \frac{\partial x_2}{\partial \eta}\frac{\partial \Psi_i}{\partial x_2},\end{aligned}$$

or, in matrix form,

$$\begin{bmatrix}\dfrac{\partial \Psi_i}{\partial \xi}\\[2ex] \dfrac{\partial \Psi_i}{\partial \eta}\end{bmatrix} = \begin{bmatrix}\dfrac{\partial x_1}{\partial \xi} & \dfrac{\partial x_2}{\partial \xi}\\[2ex] \dfrac{\partial x_1}{\partial \eta} & \dfrac{\partial x_2}{\partial \eta}\end{bmatrix}\begin{bmatrix}\dfrac{\partial \Psi_i}{\partial x_1}\\[2ex] \dfrac{\partial \Psi_i}{\partial x_2}\end{bmatrix} = J\begin{bmatrix}\dfrac{\partial \Psi_i}{\partial x_1}\\[2ex] \dfrac{\partial \Psi_i}{\partial x_2}\end{bmatrix}, \tag{5.4}$$

where

$$J = \frac{\partial x_1}{\partial \xi}\frac{\partial x_2}{\partial \eta} - \frac{\partial x_1}{\partial \eta}\frac{\partial x_2}{\partial \xi},$$

is the Jacobian of the map $\mathbf{F}$. From (5.4) we derive

$$\begin{aligned}\frac{\partial \Psi_i}{\partial x_1} &= (\frac{\partial x_2}{\partial \eta}\frac{\partial \Psi_i}{\partial \xi} - \frac{\partial x_2}{\partial \xi}\frac{\partial \Psi_i}{\partial \eta})/J,\\ \frac{\partial \Psi_i}{\partial x_2} &= (\frac{\partial x_1}{\partial \xi}\frac{\partial \Psi_i}{\partial \eta} - \frac{\partial x_1}{\partial \eta}\frac{\partial \Psi_i}{\partial \xi})/J.\end{aligned}$$

Then the integrals (5.3) becomes

$$\begin{aligned}\int_{\gamma_i} \frac{\partial \Psi_j^{\pm}}{\partial x_1}\Psi_i^{+} &= \int_{\widehat{\gamma}_i} (\frac{\partial x_2^{\pm}}{\partial \eta}\frac{\partial \Psi_j^{\pm}}{\partial \xi} - \frac{\partial x_2^{\pm}}{\partial \xi}\frac{\partial \Psi_j^{\pm}}{\partial \eta})\Psi_i^{+}\\ \int_{\gamma_i} \frac{\partial \Psi_j^{\pm}}{\partial x_2}\Psi_i^{+} &= \int_{\widehat{\gamma}_i} (\frac{\partial x_1^{\pm}}{\partial \xi}\frac{\partial \Psi_j^{\pm}}{\partial \eta} - \frac{\partial x_1^{\pm}}{\partial \eta}\frac{\partial \Psi_j^{\pm}}{\partial \xi})\Psi_i^{+}.\end{aligned}$$

where $\gamma_i = \mathbf{F}(\widehat{\gamma}_i)$. Now, to compute the above integrals we use a GLL quadrature rule with N^* nodes. Here N^* is chosen so that the resulting formula is exact for the integrand under consideration. Therefore we have

$$A = \int_{\widehat{\gamma}_i} (\frac{\partial x_2^{\pm}}{\partial \eta}\frac{\partial \Psi_j^{\pm}}{\partial \xi} - \frac{\partial x_2^{\pm}}{\partial \xi}\frac{\partial \Psi_j^{\pm}}{\partial \eta})\Psi_i^{+} = \frac{|\widehat{\gamma}_i|}{2}\sum_{k=1}^{N^*} (\frac{\partial x_2^{\pm}}{\partial \eta}\frac{\partial \Psi_j^{\pm}}{\partial \xi} - \frac{\partial x_2^{\pm}}{\partial \xi}\frac{\partial \Psi_j^{\pm}}{\partial \eta})(\mathbf{p}_k)\Psi_i^{+}(\mathbf{p}_k)w_k, \tag{5.5}$$

$$B = \int_{\widehat{\gamma}_i} (\frac{\partial x_1^{\pm}}{\partial \xi}\frac{\partial \Psi_j^{\pm}}{\partial \eta} - \frac{\partial x_1^{\pm}}{\partial \eta}\frac{\partial \Psi_j^{\pm}}{\partial \xi})\Psi_i^{+} = \frac{|\widehat{\gamma}_i|}{2}\sum_{k=1}^{N^*} (\frac{\partial x_1^{\pm}}{\partial \xi}\frac{\partial \Psi_j^{\pm}}{\partial \eta} - \frac{\partial x_1^{\pm}}{\partial \eta}\frac{\partial \Psi_j^{\pm}}{\partial \xi})(\mathbf{p}_k)\Psi_i^{+}(\mathbf{p}_k)w_k, \tag{5.6}$$

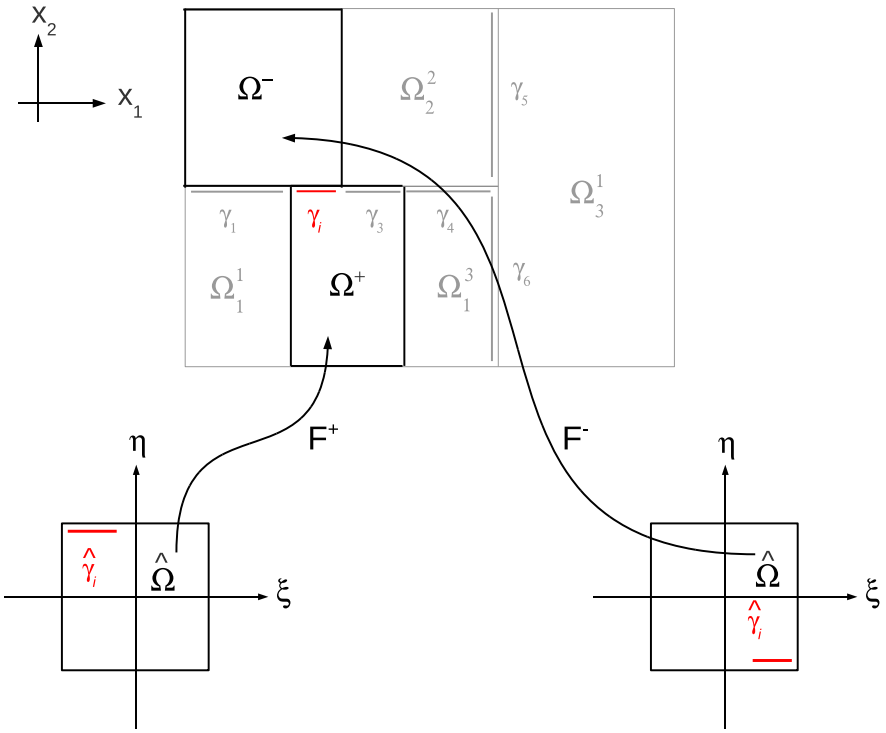

Figure 5.2: Domain decomposition for DGSE discretizations. In this case $\overline{\gamma}_i = \partial\overline{\Omega}^+ \cap \partial\overline{\Omega}^-$. Bilinear maps $\mathbf{F}^+, \mathbf{F}^-$ used to map Ω^+ and Ω^- to the reference element $\widehat{\Omega}$.

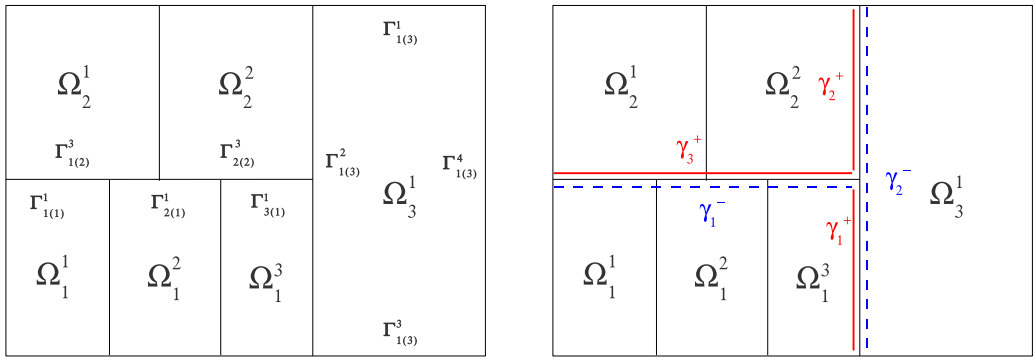

Figure 5.3: Example of domain decomposition with MSE method. In this case $\mathcal{S} = \gamma_1^- \cup \gamma_2^-$.

where $\{\mathbf{p}, w\}$ are the quadrature nodes and weights respectively. We remark that if N^+, resp. N^-, is the polynomial degree in Ω^+, resp. Ω^- each function $\Psi_j^\pm$, and Ψ_i^+, is obtained by tensor product of monodimensional polynomial functions of degree N^+, resp. N^-, i.e.,

$$\begin{aligned}\Psi_j^\pm(\xi,\eta) &= \phi_r^\pm(\xi)\phi_s^\pm(\eta), \quad \text{with } j = (s-1)N^\pm + r,\\ \Psi_i^+(\xi,\eta) &= \phi_m^+(\xi)\phi_n^+(\eta), \quad \text{with } i = (n-1)N^+ + m.\end{aligned}$$

Moreover, setting $\mathbf{p}_k = (p_k^\pm, q_k^\pm)$, (5.5)-(5.6) have to be intended as

$$A = \frac{|\widehat{\gamma}_i|}{2}\sum_{k=1}^{N^*}\left(\frac{\partial x_2^\pm}{\partial\eta}(p_k^\pm)\frac{\partial\phi_r^\pm}{\partial\xi}(p_k^\pm)\phi_s^\pm(q_k^\pm) - \frac{\partial x_2^\pm}{\partial\xi}(q_k^\pm)\phi_r^\pm(p_k^\pm)\frac{\partial\phi_s^\pm}{\partial\eta}(q_k^\pm)\right)\phi_m^+(p_k^+)\phi_n^+(q_k^+)w_k,$$

$$B = \frac{|\widehat{\gamma}_i|}{2}\sum_{k=1}^{N^*}\left(\frac{\partial x_1^\pm}{\partial\xi}(q_k^\pm)\phi_r^\pm(p_k^\pm)\frac{\partial\phi_s^\pm}{\partial\eta}(q_k^\pm) - \frac{\partial x_1^\pm}{\partial\eta}(p_k^\pm)\frac{\partial\phi_r^\pm}{\partial\xi}(p_k^\pm)\phi_s^\pm(q_k^\pm)\right)\phi_m^+(p_k^+)\phi_n^+(q_k^+)w_k,$$

Since $\mathbf{F}^\pm$ is not invertible, to define the GLL points $\mathbf{p}$ on the segment $\widehat{\gamma}_i$ we define the quadrature point on the edge γ_i and then we use the Newton-Raphson algorithm [91] to find their corresponding position on the reference element.

Mortar condition for the MSE method

In this section we describe how the mortar condition **MC**, introduced in Section 2.2, is implemented in practice. We recall that in the MSE approach the skeleton $\mathcal{S}$ of the

decomposition has a dual description made by *master* or *slave* edges, i.e.,

$$\mathcal{S} = \bigcup_{m\, master} \gamma_m^+ = \bigcup_{s\, slave} \gamma_s^-,$$

and that **MC** holds for the *slave* part of $\mathcal{S}$. Moreover, each γ_s^- is a complete edge of a subdomains Ω_k, for $k = 1, ..., K$.
In this context, the crucial point is the definition of a basis for the space of multipliers

$$\mathbf{\Lambda}_\delta(\mathcal{S}) = \bigoplus_{s\, slave} \mathbf{\Lambda}_\delta(\gamma_s^-).$$

Since **MC** applies separately for the components u^1, u^2 of the displacement $\mathbf{u}$, see Section 2.4, here and in the sequel we consider only the first component u^1 and drop the superscripts. According to the notation introduced in Section 5.1, in each element Ω_k^j the displacement u can be written as

$$u(x_1(\xi,\eta), x_2(\xi,\eta)) = \sum_{j=1}^{(N_k+1)^2} U_j \Psi_j(\xi,\eta) = \sum_{m,n=1}^{N_k+1} U_{m,n} \phi_m(\xi)\phi_n(\eta),$$

where ϕ_m and ϕ_n are the one dimensional Lagrangian interpolants of order N_k, defined by

$$\phi_m^{N_k}(\xi) = \frac{-L'_{N_k}(\xi)(1-\xi^2)}{N_k(N_k-1)L_{N_k}(p_m^{N_k})(\xi - p_m^{N_k})}, \quad m = 1, ..., N_k + 1. \tag{5.7}$$

$\phi_m^{N_k} \in Q^{N_k}([-1,1])$, $\phi_m^{N_k}(p_\ell) = \delta_{m\ell}$, $m, \ell = 1, ..., N_k + 1$, and L_{N_k} is the Legendre polynomial of order N_k. The points p_ℓ are the GLL points of order N_k.
For each element edge $\Gamma_{j(k)}^\ell$ such that $\partial\Omega_k^j = \bigcup_{\ell=1}^4 \Gamma_{j(k)}^\ell$, it is possible to expand u as:

$$u(x_1(\xi), x_2(\xi)) = \sum_{m=1}^{N_k+1} U_m \phi_m^{N_k}(\xi),$$

where $x_1(\xi), x_2(\xi)$ represents the coordinate transformation restricted to $\Gamma_{j(k)}^\ell$. To define a basis for the space $\Lambda_\delta(\gamma_s^-)$ we detect whether the end points of γ_s^- coincide with the end points of $\Gamma_{j(k)}^\ell$, since nodal values on the vertices of γ_s^- are *master* unknowns. Depending on that we have to choose projection polynomials of order one or two, less than the Legendre function (5.7) of order N_k. Moreover, to avoid loosing the diagonality in the left hand side of the projection (2.62), we have:

1. If $\gamma_s^- = \Gamma_{j(k)}^\ell$ a basis for $\Lambda_\delta(\gamma_s^-)$ is a set of $N_k - 1$ polynomials of order $N_k - 2$, which has the form

$$\widehat{\phi}_m^{N_k-2}(\xi) = \frac{-L'_{N_k}(\xi)(1-p_m^{N_k})(1+p_m^{N_k})}{N_k(N_k-1)L_{N_k}(p_m^{N_k})(\xi - p_m^{N_k})}, \quad m = 2, ..., N_k,$$

   where p_m, $m = 2, ..., N_k$ are the GLL points, cf. Section 2.2.

2. In the general case when $\gamma_s^- = \bigcup_{j=1}^J \Gamma_{j(k)}^\ell$, with $J > 1$ the basis for $\Lambda_\delta(\gamma_s^-)$ consist of the union of basis functions for all edges $\Gamma_{j(k)}^\ell$.
   For an edge that does not share any end points with the *mortar*, the basis is a set of $N_K + 1$ Lagrangian interpolants of order N_k:

$$\widehat{\phi}_m^{N_k} = \phi_m^{N_k}, \quad m = 1, ..., N_k + 1.$$

   In the last case when an edge $\Gamma_{j(k)}^\ell$ shares only one end point with a *mortar* γ_s^-, the basis functions are polynomials of order $N_k - 1$. If the end point corresponds to $p_1 = -1$, the polynomials are:

$$\widehat{\phi}_m^{N_k-1}(\xi) = \frac{-L'_{N_k}(\xi)(1-\xi)(1+p_m^{N_k})}{N_k(N_k-1)L_{N_k}(p_m^{N_k})(\xi - p_m^{N_k})}, \quad m = 2, ..., N_k + 1,$$

   Otherwise, if the end point corresponds to $p_{N_k+1} = 1$ the polynomials are:

$$\widehat{\phi}_m^{N_k-1}(\xi) = \frac{-L'_{N_k}(\xi)(1-p_m^{N_k})(1+\xi)}{N_k(N_k-1)L_{N_k}(p_m^{N_k})(\xi - p_m^{N_k})}, \quad m = 1, ..., N_k.$$

   Since, we use the Lagrangian interpolants through GLL points, the functions ϕ_m defined above, satisfy the relation $\phi_m(p_n) = \delta_{mn}$ for all nodal points p_n , except those that coincide with the end points of the *mortar*, see Figure 5.4.

In order to see how this definition reflects on the computation of **MC** let us consider as a reference case the one illustrated in Figure 5.3, where $\mathcal{S} = \gamma_1^- \cup \gamma_2^-$ with

$$\begin{aligned} \gamma_1^- &= \Gamma_{1(1)}^1 \cup \Gamma_{2(1)}^1 \cup \Gamma_{3(1)}^1, \\ \gamma_2^- &= \Gamma_{1(3)}^2. \end{aligned}$$

In this configuration, we obtain

1. $\int_{\gamma_1^-}(u_1 - u_2)\widehat{\phi} = 0 \quad \forall \widehat{\phi} \in \widehat{\Lambda}_\delta(\gamma_1^-)$,
2. $\int_{\gamma_2^-}(u_3 - u_1 - u_2)\widehat{\phi} = 0 \quad \forall \widehat{\phi} \in \widehat{\Lambda}_\delta(\gamma_2^-)$.

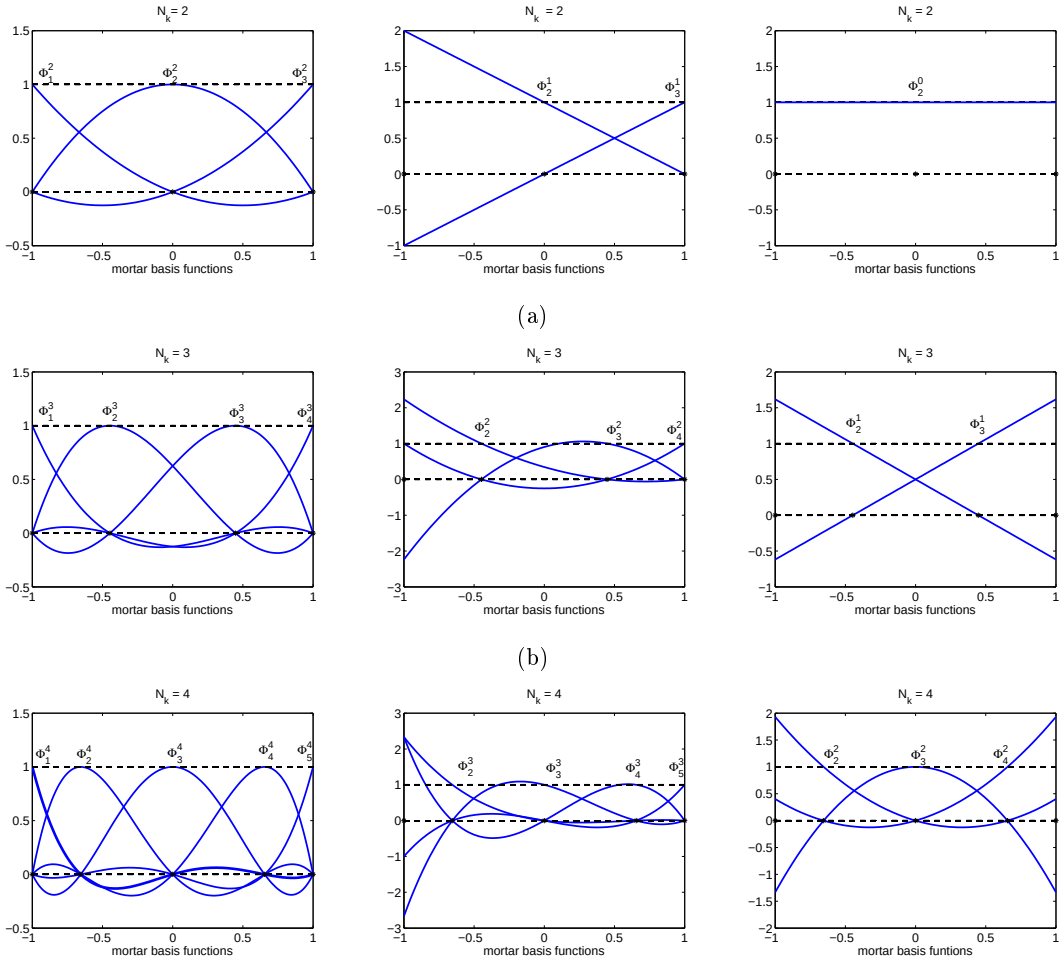

Figure 5.4: *Mortar* edge basis functions on the reference element $(-1, 1)$ for different configurations: (a) $N_k = 2$, (b) $N_k = 3$ and (c) $N_k = 4$. Edge γ_i^- sharing no end points with the *mortar* edge (left), the left end point with the *mortar* edge (middle) and both end points with the *mortar* edge (right).

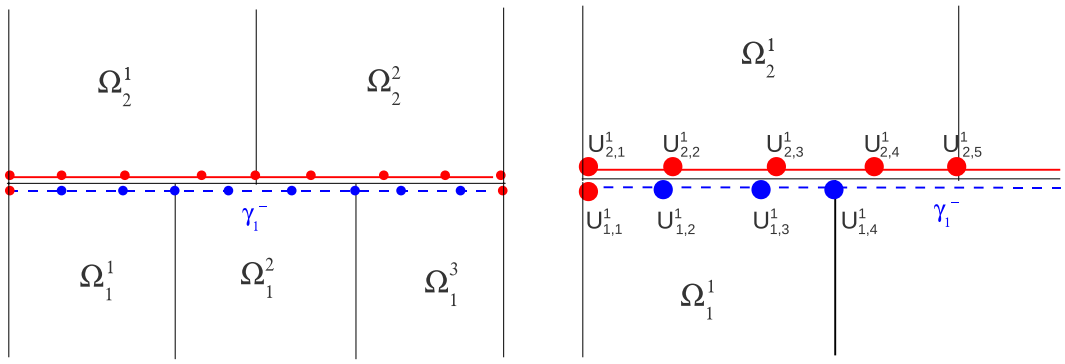

Figure 5.5: Unknowns reordering for Condition 1.

Since $\widehat{\Lambda}_\delta(\gamma_1^-) = \widehat{\Lambda}_\delta(\Gamma^1_{1(1)}) \oplus \widehat{\Lambda}_\delta(\Gamma^1_{2(1)}) \oplus \widehat{\Lambda}_\delta(\Gamma^1_{3(1)})$ each function $\widehat{\phi} \in \widehat{\Lambda}_\delta(\gamma_1^-)$ can be written as

$$\widehat{\phi} = \widehat{\phi}^1 + \widehat{\phi}^2 + \widehat{\phi}^3,$$

with $\widehat{\phi}^j \in \widehat{\Lambda}_\delta(\Gamma^1_{j(1)})$ and with $supp(\widehat{\phi}^j) \subset \Gamma^1_{j(1)}$ for $j = 1, 2, 3$. According to these definitions $\widehat{\phi}^1, \widehat{\phi}^2$ and $\widehat{\phi}^3$ are polynomials of degree $N_1 - 1, N_1$ and $N_1 - 1$, respectively. Setting $u_k^j = u_{|_{\Omega_k^j}}$ we can rewrite Condition 1., as

$$\int_{\Gamma^1_{1(1)}} (u_1^1 - u_2^1)\widehat{\phi}^1 + \int_{\Gamma^1_{2(1)} \cap \Gamma^3_{1(2)}} (u_1^2 - u_2^1)\widehat{\phi}^2 + \int_{\Gamma^1_{2(1)} \cap \Gamma^3_{2(2)}} (u_1^2 - u_2^2)\widehat{\phi}^2 + \int_{\Gamma^1_{3(1)}} (u_1^3 - u_2^2)\widehat{\phi}^3 = 0. \tag{5.8}$$

Substituting the expression of u_k^j in terms of the basis functions introduced before, and computing the integral as we are going to explain in a moment, we obtain the projection matrix $\underline{Q}_1$ related to the *mortar* γ_1^-. For simplicity let us consider the first term in (5.8) and let us suppose that the left end point of γ_1^- corresponds to $p_1 = -1$ in the reference interval $[-1, 1]$. For each $\widehat{\phi}_i^1 \in \widehat{\Lambda}_\delta(\Gamma^1_{1(1)})$ it holds

$$\int_{\Gamma^1_{1(1)}} (u_1^1 - u_2^1)\widehat{\phi}_i^1 = \sum_{j=1}^{N_1+1} U_{1,j}^1 \int_{\Gamma^1_{1(1)}} \phi_j^1 \widehat{\phi}_i^1 - \sum_{j=1}^{N_2+1} U_{1,j}^2 \int_{\Gamma^1_{1(1)}} \phi_j^2 \widehat{\phi}_i^1 = 0 \quad \text{for } i = 2, ..., N_1 + 1, \tag{5.9}$$

or equivalently

$$\sum_{j=2}^{N_1+1} U_{1,j}^1 \int_{\Gamma^1_{1(1)}} \phi_j^1 \widehat{\phi}_i^1 = \sum_{j=1}^{N_2+1} U_{1,j}^2 \int_{\Gamma^1_{1(1)}} \phi_j^2 \widehat{\phi}_i^1 - U_{1,1}^1 \int_{\Gamma^1_{1(1)}} \phi_1^1 \widehat{\phi}_i^1 \quad \text{for } i = 2, ..., N_1 + 1,$$

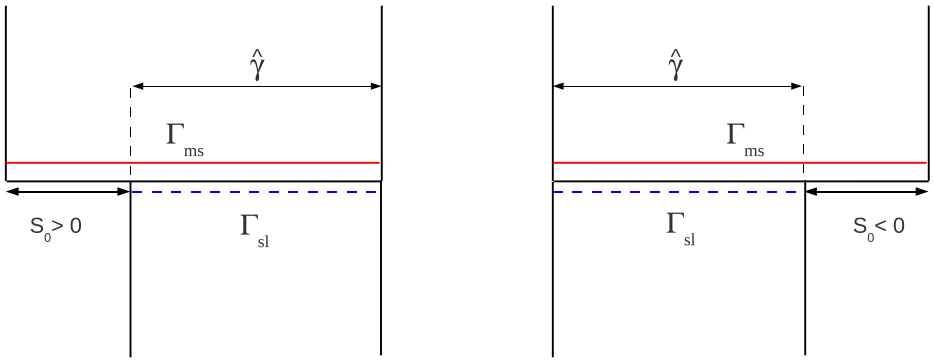

Figure 5.6: Definition of the *mortar* offset s_0 for different *master-slave* configurations. In the considered case $\Gamma_{sl} = \widehat{\gamma} = \Gamma^1_{1(1)}$, $\Gamma_{ms} = \Gamma^3_{1(2)}$ and $s_0 < 0$.

where we have ordered the unknowns as in Figure 5.5. To compute the integral on the left end side, we map the segment $\Gamma^1_{1(1)}$ onto $[-1, 1]$ and we introduce the set of $N_1 + 1$ GLL nodes and weights $\{p_k, \omega_k\}$. Since $\phi^1_j(p_k) = \delta_{jk}$, for $j, k = 1, ..., N_1 + 1$, we obtain

$$\int_{\Gamma^1_{1(1)}} \phi^1_j \widehat{\phi}^1_i = \frac{|\Gamma^1_{1(1)}|}{2} \sum_{k=1}^{N_1+1} \phi^1_j(p_k)\widehat{\phi}^1_i(p_k)\omega_k = \frac{|\Gamma^1_{1(1)}|}{2}\delta_{jk}\widehat{\phi}^1_i(p_k)\omega_k \quad \text{for } i = 2, ..., N_1 + 1.$$

The diagonal form of the matrix $\underline{\mathrm{R}}_{int}$ is thus preserved, see Section 2.4:

$$\underline{\mathrm{R}}_{int}(i, j) = \frac{|\Gamma^1_{1(1)}|}{2}\delta_{ij}\omega_j, \quad \text{for } i, j = 2, ..., N_1 + 1.$$

On the other hand to compute $\int_{\Gamma^1_{1(1)}} \phi^2_j \widehat{\phi}^1_i$ we need to introduce the notions of *mortar* offset s_0 [16, 19], see Figure 5.6. Then, the integral becomes

$$\int_{\Gamma^1_{1(1)}} \phi^2_j \widehat{\phi}^1_i = \frac{|\Gamma^1_{1(1)}|}{2} \sum_{k=1}^{N^*} \phi^2_j(r(p_k))\widehat{\phi}^1_i(s(p_k))\omega_k \quad \text{for } i = 2, ..., N_1 + 1, \tag{5.10}$$

where N^* is chosen such that the quadrature rule is exact for the set of polynomials under consideration. In (5.10) we introduce the coordinate transformations $r(\cdot)$ and $s(\cdot)$ for the *master* and the *slave* part of $\Gamma^1_{1(1)}$ respectively, i.e.,

$$r(p_k) = \begin{cases} \dfrac{2|s_0|}{|\Gamma_{ms}|} - 1 + (1 + p_k)\dfrac{|\Gamma_{sl}|}{|\Gamma_{ms}|} & \text{if } s_0 < 0, \\ -1 + (1 + p_k)\dfrac{|\widehat{\gamma}|}{|\Gamma_{ms}|} & \text{if } s_0 > 0, \end{cases}$$

and

$$s(p_k) = \begin{cases} -1 + (1+p_k)\dfrac{|\widehat{\gamma}|}{|\Gamma_{sl}|} & \text{if } s_0 < 0, \\ \dfrac{2s_0}{|\Gamma_{sl}|} - 1 + (1+p_k)\dfrac{|\widehat{\gamma}|}{|\Gamma_{sl}|} & \text{if } s_0 > 0. \end{cases}$$

To compute all the remaining integrals in (5.8) we proceed similarly, paying attention to the definition of the *mortar* spaces $\widehat{\Lambda}_\delta(\Gamma^1_{2(1)})$ and $\widehat{\Lambda}_\delta(\Gamma^1_{3(1)})$.
To impose Condition 2., we observe that since $\Gamma^2_{1(3)}$ shares both end point of γ_2^- the functional space $\widehat{\Lambda}_\delta(\gamma_2^-) = \text{span}\{\widehat{\phi}_i\}$, $i = 2, ..., N_3$, where $\widehat{\phi}_i \in \mathrm{Q}^{N_3-2}(\gamma_2^-)$. Then, it holds that

$$\int_{\gamma_2^-} (u_3 - u_1 - u_2)\widehat{\phi}_i = \int_{\gamma_2^-} (u_3^1 - u_1^3 - u_2^2)\widehat{\phi}_i,$$

and finally

$$\begin{aligned} \sum_{j=2}^{N_3} U^1_{3,j} \int_{\gamma_2^-} \phi_j^3 \widehat{\phi}_i \;=\; & \sum_{j=1}^{N_1+1} U^3_{1,j} \int_{\gamma_1^+} \phi_j^1 \widehat{\phi}_i + \sum_{j=1}^{N_2+1} U^2_{2,j} \int_{\gamma_2^+} \phi_j^2 \widehat{\phi}_i \\ & - U^1_{3,1} \int_{\gamma_2^-} \phi_1^3 \widehat{\phi}_i - U^1_{3,N_3+1} \int_{\gamma_2^-} \phi^3_{N_3+1} \widehat{\phi}_i \quad \text{for } i = 2, ..., N_3. \end{aligned}$$

Now, the above integrals are computed as before.

5.2 Implementation details

In this section we describe the flowchart of the developed numerical code. The guidelines can be followed also in three dimensional problems in conjunction with ad-hoc strategies for parallel computations.
We refer to the general problem (1.1) with viscous forcing terms and the corresponding algebraic linear systems introduced in Section 2.4. After setting the initial condition $\mathbf{U}(0) = \mathbf{u}_0$ and $\mathbf{V}(0) = \mathbf{u}_1$, we build the skeleton $\mathcal{S}$ as explained in (2.3)-(2.9) for the DGSE or the MSE approaches respectively.
Next,

- we compute all the matrix defined in (2.74)-(2.75),
- we stored them using a sparse format, since they show a highly sparse pattern,
- we solve the resulting ODE system using a time integration scheme choosing between LF, RK4 or IM, see Chapter 3.

In Algorithm 1 we summarize the DG solution scheme.
We recall that, when using explicit LF or RK4 methods at each discrete time t_n, the matrix of the system is diagonal. On the other hand, the CFL condition has to be respected and therefore a large number of time steps is required to compute the approximated solution. When considering the IM method, larger time steps are allowed and the final time T can be reached in few iteration. However at each discrete time t_n the solution of the resulting (ill-conditioned) linear system of equations is needed. In these cases, suitable preconditioners are mandatory (especially for three dimensional problems).
In the mortar solution scheme, see Algorithm 2, a further step is required in order to identify the *master* and the *slave* decomposition of $\mathcal{S}$. Moreover, we remark that the solution is computed firstly for the *master* unknowns and then projected to the *slave* ones. At each time level, to steps are then required. Finally, we remark that all the matrix-vector products of Algorithms 1-2 can performed subdomain per subdomain.

Algorithm 1: DG Solution Scheme

1. Set the initial conditions $\mathbf{u}_0$ and $\mathbf{u}_1$.
2. Build the skeleton $\mathcal{S}$.
3. Decompose $\mathcal{S}$ into elementary components (edges).
4. Build the matrices $\underline{\mathrm{M}}, \underline{\mathrm{A}}, \underline{\mathrm{B}}, \underline{\mathrm{C}}, \underline{\mathrm{D}}, \underline{\mathrm{R}}$ and $\underline{\mathrm{S}}$.
5. For each discrete time t_n:
   - Solve the ODE system $\underline{\mathrm{M}}\ddot{\mathbf{U}} + (\underline{\mathrm{C}} - \underline{\mathrm{S}})\dot{\mathbf{U}} + (\underline{\mathrm{A}} + \underline{\mathrm{B}} + \underline{\mathrm{D}} - \underline{\mathrm{R}})\mathbf{U} = \mathbf{F}^{ext}$ using a suitable time integration scheme.
   - If the final time T is not reached set $t_n \leftarrow t_{n+1}$ and go to step 5.

Algorithm 2: Mortar Solution Scheme

1. Set the initial conditions $\mathbf{u}_0$ and $\mathbf{u}_1$.
2. Build the skeleton $\mathcal{S}$.
3. Decompose $\mathcal{S}$ into the union of *master* and *slave* edges.
4. Build the matrices $\underline{\mathrm{M}}, \underline{\mathrm{A}}, \underline{\mathrm{C}}, \underline{\mathrm{D}}, \underline{\mathrm{R}}$ and $\underline{\mathrm{S}}$ and the projection operator $\underline{Q}$ for the interface unknowns $\mathbf{U}_{slave}$.
5. For each discrete time t_n:

- solve for the *master* unknowns $\mathbf{U}_{master}$ the systems

$$\underline{\widetilde{\mathrm{Q}}}^{\top}\underline{\widetilde{\mathrm{M}}}\underline{\widetilde{\mathrm{Q}}}\ddot{\mathbf{U}}_{master}+\underline{\widetilde{\mathrm{Q}}}^{\top}(\underline{\widetilde{\mathrm{C}}}-\underline{\widetilde{\mathrm{S}}})\underline{\widetilde{\mathrm{Q}}}\dot{\mathbf{U}}_{master}+\underline{\widetilde{\mathrm{Q}}}^{\top}(\underline{\widetilde{\mathrm{A}}}+\underline{\widetilde{\mathrm{D}}}-\underline{\widetilde{\mathrm{R}}})\underline{\widetilde{\mathrm{Q}}}\mathbf{U}_{master}=\underline{\widetilde{\mathrm{Q}}}^{\top}\mathbf{F}^{ext}$$

  using a suitable time integration scheme.

- perform the projection on the *slave* unknowns;

- if the final time T is not reached set $t_n \leftarrow t_{n+1}$ and go to step 5.

Chapter 6

Numerical results for test cases

The aim of this chapter is the validation of the non-conforming approaches on two and three dimensional benchmarks. We present first a two dimensional analytical test case in order to test the accuracy of the DGSE and MSE methods when a smooth solution is considered and to validate the theoretical estimates proved in Chapter 2. Then, we show the flexibility of DGSE and MSE discretizations considering an elastic wave propagation problem on a square domain with a circular cavity. We show that, exploiting the flexibility of non-conforming grids, it is possible to obtain reliable solutions saving computational time.

In the second part of Chapter 6 we test the DGSE approach on three dimensional test cases. We consider two benchmarks widely used in the literature to validate the performance of different numerical approximations of elastodynamics problems. The first problem we consider, known in literature with the acronym LOH (Layer Over a Half space), has become in the last years a reference benchmark for all the seismic oriented codes. The results obtained with the DGSE method are satisfactory and show once again the flexibility of the DGSE discretization. The second problem consists in the seismic response of a valley having a curved profile. In this case we consider a conforming grid but different polynomial approximation degrees for the valley and the underlying bedrock. The results are in agreement with those obtained with the SE method.

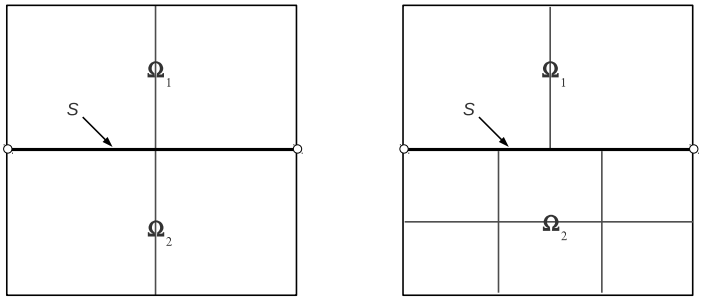

Figure 6.1: First level of refinement (L1) for the `grid A` (left) and `B` (right). The end points of the skeleton $\mathcal{S}$ are highlighted by two circles.

6.1 Accuracy and order of convergence

We solve a wave propagation problem in $\Omega = (0,1)^2$, setting the elastic parameters $\lambda = \mu = \rho = 1$, and choosing $\mathbf{f}$ such that the exact solution of (1.1) is

$$\mathbf{u}(t,x,y) = \sin(\sqrt{2}\pi t) \begin{bmatrix} -\sin^2(\pi x)\sin(2\pi y) \\ \sin(2\pi x)\sin^2(\pi y) \end{bmatrix}. \tag{6.1}$$

The Dirichlet boundary conditions on $\partial\Omega$, the initial displacement $\mathbf{u}_0$ and the initial velocity $\mathbf{u}_1$ are set accordingly.

We consider a subdomain partition made by subdomain Ω_1 and Ω_2 with corresponding refinements $\mathcal{T}_{h_1}$ and $\mathcal{T}_{h_2}$ (cf. Figure 6.1). We denote by N_1 and N_2 the degrees of the spectral expansion in each subdomain, respectively. The skeleton is defined as $\mathcal{S} = \partial\overline{\Omega}_1 \cap \partial\overline{\Omega}_2$ as it is shown in Figure 6.1. In order to investigate the convergence properties of MSE an DGSE methods with respect to $\mathbf{h} = (h_1, h_2)$ and $\mathbf{N} = (N_1, N_2)$ we address two different situations: the first corresponding to a Cartesian matching grid (Figure 6.1, left) while the second to a Cartesian non-matching grid (Figure 6.1, right), referred to as `grid A` and `grid B`, respectively. In Figure 6.1 is shown the first level (L1) of refinement for both grids, corresponding to the initial mesh sizes h_1 and h_2 for Ω_1 and Ω_2 respectively. At each further step of refinement (for a maximum number of four steps), we consider a uniform refinement of the grids at the previous level, in particular for `grid A`, L_i refers to $h_1 = h_2 = 2^{-i}$ whereas for `grid B`, L_i refers to $h_1 = 2^{-i}$ and

$h_2 \approx (2/3)h_1$. For the time integration we employ the second order explicit leap-frog scheme described in Chapter 3.

We have compared the results with the analogous ones obtain with the SE method. We recall that, for the SE approximations under suitable assumptions on the mesh size $\mathbf{h}$ and on the polynomial degree $\mathbf{N}$ the following *a priori* error bound holds (see [27])

$$\|\mathbf{u} - \mathbf{u}_\delta\|_0 \leq C \left[\Delta t^2 + \left\{ \sum_{k=1}^{K} \frac{h_k^{2m_k}}{N_k^{2s_k}} \|\mathbf{u}\|^2_{H^{s_k}(\Omega_k)} \right\}^{\frac{1}{2}} \right],$$

where C is a positive constant. Here s_k represents the Sobolev regularity of $\mathbf{u}$ in Ω_k, $m_k = \min(N_k + 1, s_k)$ and Δt the time step. Similar bounds can be proved for DGSE and MSE on the basis of the estimates in Theorem 3 in Section 2.3.3.

In particular, if the solution is analytic, we expect exponential convergence as $\mathbf{N} \to +\infty$, whereas algebraic convergence is expected whenever $\mathbf{N}$ is fixed and $\mathbf{h} \to 0$.

In the family of proposed DGSE methods, we analyze in detail the SIPG method (i.e., $\theta = -1$ in (2.8)) because it exhibits better performances in term of grid dispersion and stability (see Chapter 4).

In Figure 6.2-(a) (resp. Figure 6.2-(b)) we report (semilog scale) the computed L^2-error using the MSE and SIPG methods with `grid A` versus $\mathbf{N}$ (resp. degrees of freedom). The estimated error is computed at the observation time $t^* = 2$ using $\Delta t = 5 \cdot 10^{-4}$.

The results show that both discretizations exhibit the same rate of convergence as the SE method. We have repeated the same set of experiments with $\Delta t = 10^{-4}$. The computed errors are shown in Figure 6.3. The results confirm that SIPG and MSE methods exhibit exponential convergence in $\mathbf{N}$, until the threshold value given by $\approx \Delta t^2$ is reached.

Now, we fix $N_1 = N_2$ and we investigate the accuracy of the SIPG and MSE methods with respect to the mesh size h. For each level of refinement we compute the error in the L^2-norm obtained using `grid A` and `grid B`. The algebraic order of convergence $\mathcal{O}(h^{N+1})$ is clearly achieved in both cases for different choices of $\mathbf{N}$ and Δt (see Figure 6.4).

Finally in Figure 6.5-(a) and Figure 6.5-(b) we show a qualitative analysis of stability of SIPG and MSE methods applied to this test case. The results are in agreement with those obtained in Section 4.3 and confirm that the region of stability for the MSE method is larger than that for SIPG scheme.

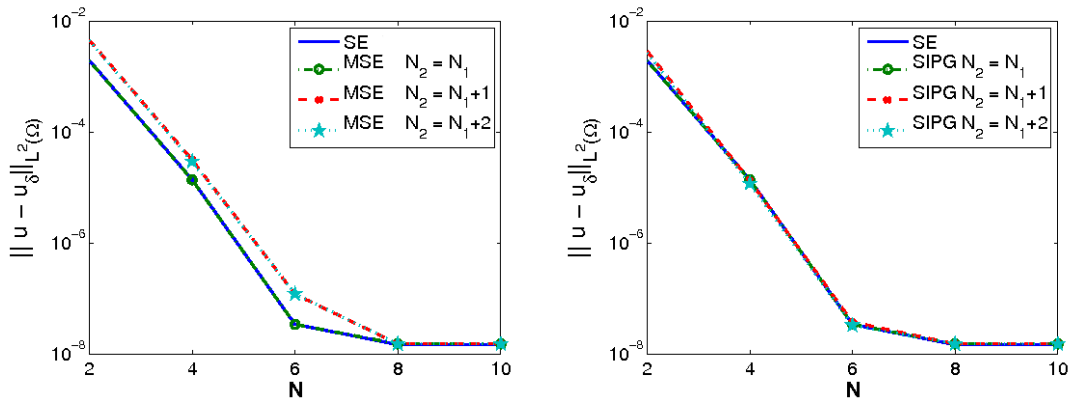

(a) Computed errors versus the polynomial degree **N**.

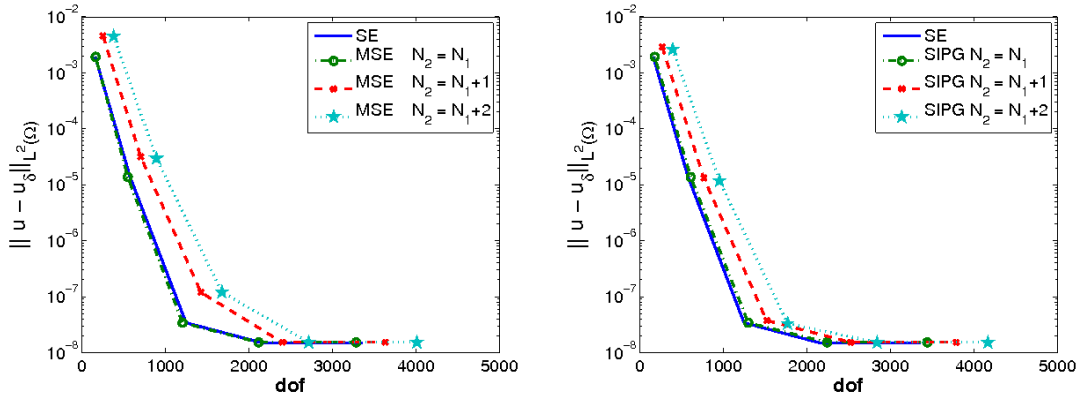

(b) Computed errors versus the number of degrees of freedom (d.o.f.).

Figure 6.2: Computed errors: MSE (left) and SIPG (right) methods at the observation time $t^* = 2$ ($\Delta t = 5 \cdot 10^{-4}$). The results are obtained with the `grid A` and the refinement level L2.

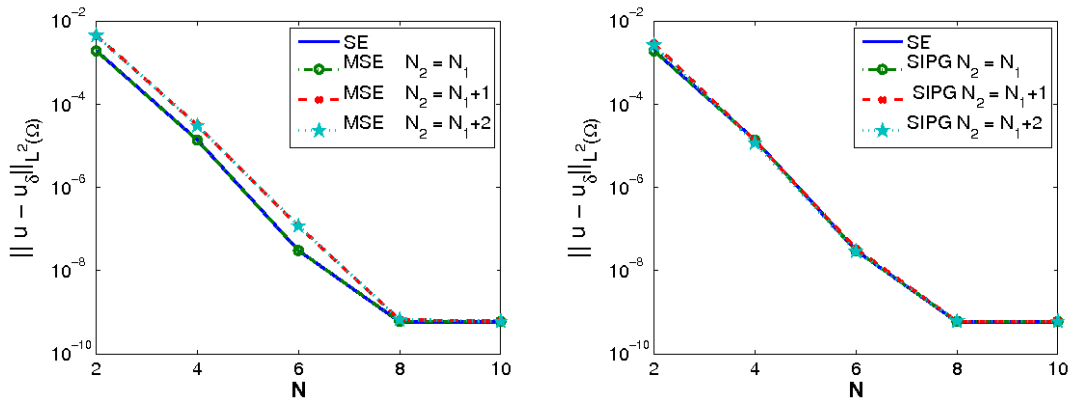

(a) Computed errors versus the polynomial degree N.

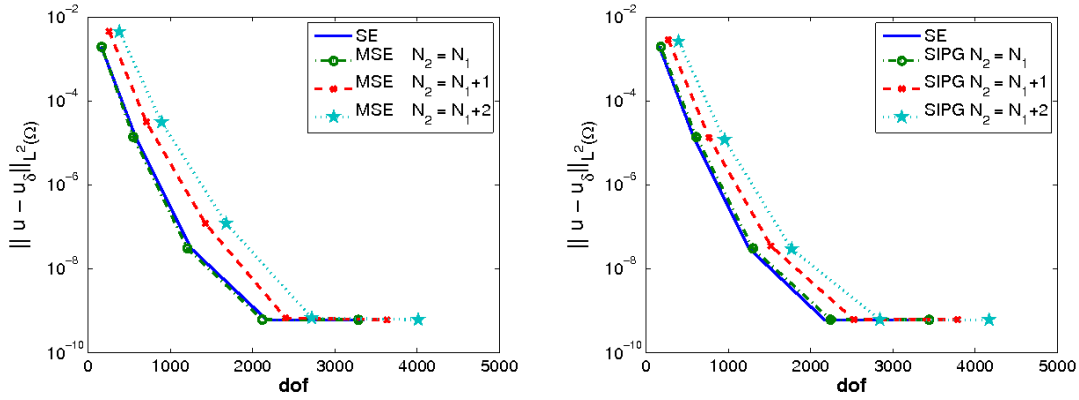

(b) Computed errors versus the number of degrees of freedom (d.o.f.).

Figure 6.3: Computed errors: MSE (left) and DGSE (right) methods at the observation time $t^* = 2$ ($\Delta t = 1 \cdot 10^{-4}$). The results are obtained with the `grid A` and the refinement level L2.

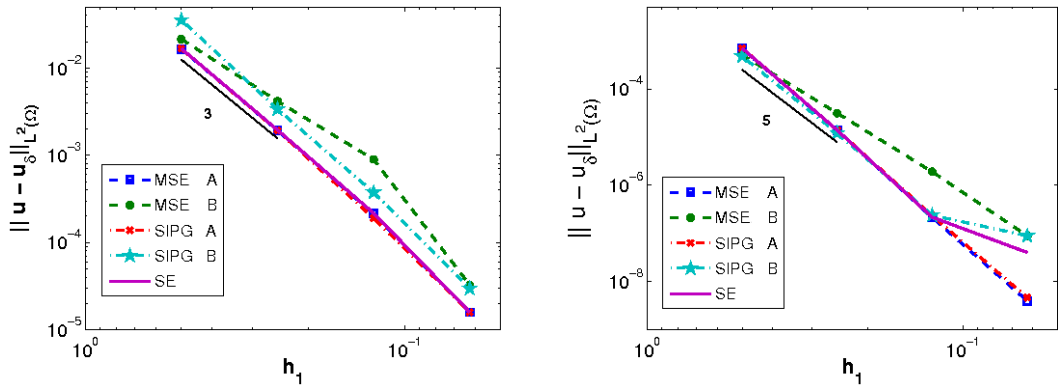

(a) Computed errors versus the mesh size **h**.

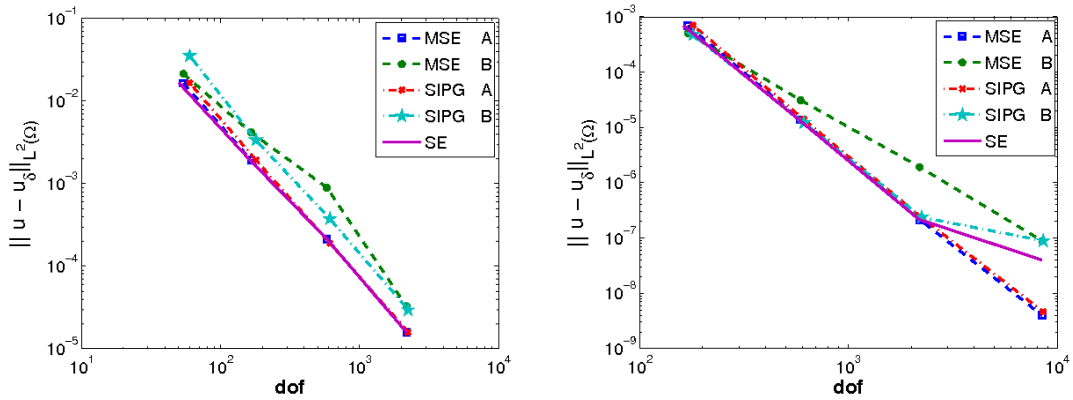

(b) Computed errors versus the number of degrees of freedom.

Figure 6.4: Computed errors: $N_1 = N_2 = 2$, $\Delta t = 10^{-3}$ (left) and $N_1 = N_2 = 4$ and $\Delta t = 10^{-4}$ (right). The error in the L^2-norm is computed at the observation time $t^* = 2$ for all the refinement levels L1-L4. The suffixes A,B in the legend refer to the grids employed in the computation.

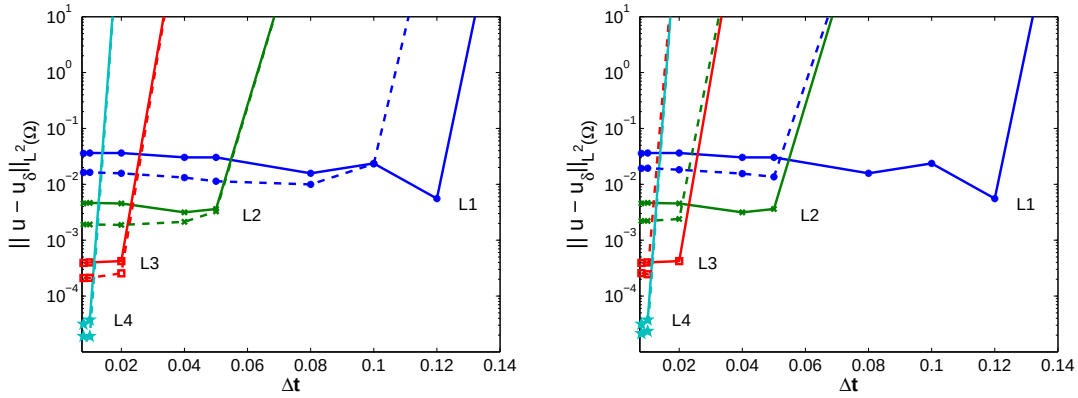

(a) Stability analysis with respect to the mesh size **h**.

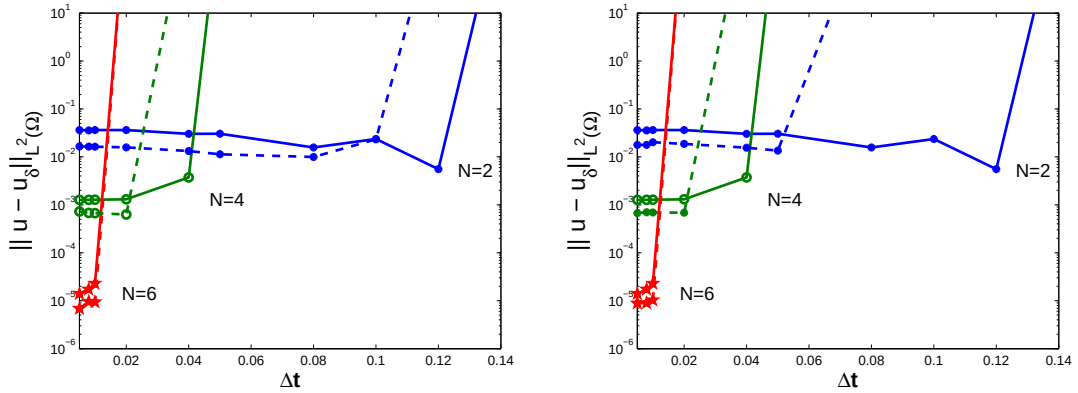

(b) Stability analysis with respect to the polynomial order **N**.

Figure 6.5: Stability analysis of the MSE (left) and SIPG (right) methods. The L^2-error is computed at the observation time $t^* = 20$ with $N_1 = N_2 = 2$. Solid lines (-) correspond to SE approximations, while dashed lines (- -) to non-conforming approximations.

6.2 Circular inclusion

This example illustrate the scattering of a plane wave by an elastic circle included in a homogeneous halfspace, see Figure 6.6. Such an example appears frequently in non-destructive testing and near surface seismic studies (cavity, gas inclusions). From the numerical point of view, the main difficulty lies on meshing the curved internal interface, specially in the case of two media with high velocity contrast where both an accurate approximation of the body and of the interface waves are mandatory.
In order to illustrate the flexibility of the proposed non-conforming approximations we consider three different cases (cf. Table 6.1):

(i) a stiff circular inclusion is included within a more compliant elastic space,

(ii) a compliant circular inclusion in a stiffer space,

(iii) a more compliant inclusion is included in a stiffer elastic space (in order to test the accuracy of DGSE and MSE methods for extremely high velocity contrast).

In all the cases the physical model is a circular inclusion of diameter 500 m embedded in the square elastic half space $(0, 2000)\ m \times (0, -2000)\ m$. In Table 6.1 we report the different material properties for the three different cases considered. These parameters were borrowed form [79] and were used firstly in [90] to study a two quarter space problem, that is two elastic half-spaces in contact along a vertical material discontinuity, with special emphasis in the simulation of the interface waves travelling along the vertical interface, a geometry well suited for classical SE methods based on quadrilateral meshes. Here, we consider the scattering by an elastic circle of a plane wave travelling upwards. In this example, an interface wave is expected to travel along the circular boundary of the buried circle.

Case	Layers	$\rho\,[Kg/m^3]$	$c_P\,[m/s]$	$c_S\,[m/s]$
(i)	C	2	3000	1732
	HS	1	2000	1155
(ii)	C	1	2000	1155
	HS	2	3000	1732
(iii)	C	1	600	1400
	HS	2	2310	4000

Table 6.1: Dynamic and mechanical parameters for the circle (C) and the halfspace (HS).

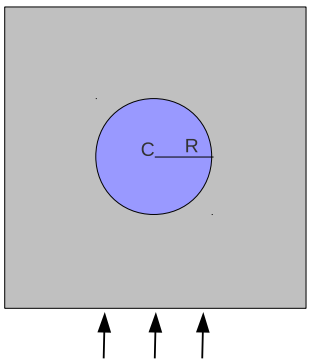

Figure 6.6: Circular inclusion with center $C = (0, -1000)\ m$ and radius $R = 500\ m$ in the halfspace $(0, 2000)\ m \times (0, -2000)\ m$.

The partition within the circle and the halfspace is designed in order to have $1/\delta \geq 5$ points per wavelength with polynomial degree $N = 4$, see Chapter 4. In particular, we have set

- test case (i): $h_C = 100\ m$ and $h_{HS} = 70\ m$,
- test case (ii): $h_C = 70\ m$ and $h_{HS} = 100\ m$,
- test case (iii): $h_C = 35\ m$ and $h_{HS} = 70\ m$,

for the circle (C) and the half-space respectively (HS). We apply free-surface boundary conditions, i.e. $\mathbf{t} = \mathbf{0}$, on the top of the domain, while non-reflecting boundary conditions are imposed on the remaining parts of the boundary. A Ricker plane wave with incident angle $\vartheta = 0$ and modulation of $5Hz$ central frequency is prescribed along the bottom boundary by an initial displacement $\mathbf{u}_0$ and velocity $\mathbf{u}_1$, see Figure 6.7. Along the curved interface, starting from the point $R_1 = (1000, -1250)\ m$, 50 receivers are placed in a counter clockwise order. The wave field is propagated using the LF scheme, cf. Chapter 3, for $T = 5\ s$ using a time step $\Delta t = 10^{-3}\ s$. All the results are compared with those obtained with a conforming SE approximation choosing $N = 4$ and $h_C = h_{HS} = 35\ m$ for all the cases (i)-(iii).
In Figure 6.8 we report the horizontal and vertical displacement recorded by the receivers along the interface, for the cases (i) and (ii), respectively obtained with the MSE approximation. Analogous results have been obtained with the DGSE method. Notice that the displacement turns out to be symmetric with respect the vertical axis. In Fig-

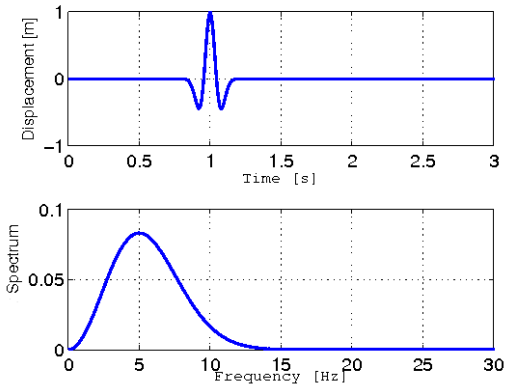

Figure 6.7: Ricker plane wave $M(t) = [1-2\beta(t-t_0)^2]\exp[-\beta(t-t_0)^2]$, $t_0 = 1$s and $\beta = 246.7401 s^{-1}$.

ure 6.9 we report the displacement recorded by the receiver $R_{11} = (239.67, -1071.1)$ m using respectively the DGSE and the MSE methods, respectively. In the same graphics we also plot the differences $(\mathbf{u}_{DG} - \mathbf{u}_{SE})$ and $(\mathbf{u}_M - \mathbf{u}_{SE})$, where $\mathbf{u}_{SE}$ is the solution obtained with the SE method. It can be observed that both methods give similar results in both the cases (i) and (ii), and reproduce accurately the wave front field for all observation times. In the third case, a much higher velocity contrast between the compliant circular inclusion and the surrounding space is considered. The incident wavefield is the same as in the previous examples and boundary conditions apply in the same way. The results shown in Figure 6.10 have been obtained with the DGSE method. Similar results have been obtained using the MSE method. In this case, it is evident the effect on the wavefield induced by the softer inclusion: the waves that travel across the circle are trapped within it and then phenomena of reflection and refraction arise. This is more evident from the snapshots of the computed solution shown in Figure 6.11.

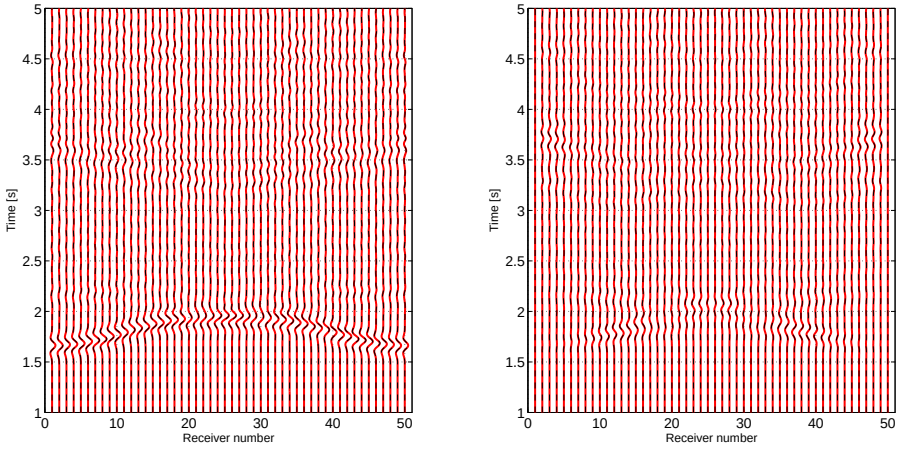

(a) Test case (i).

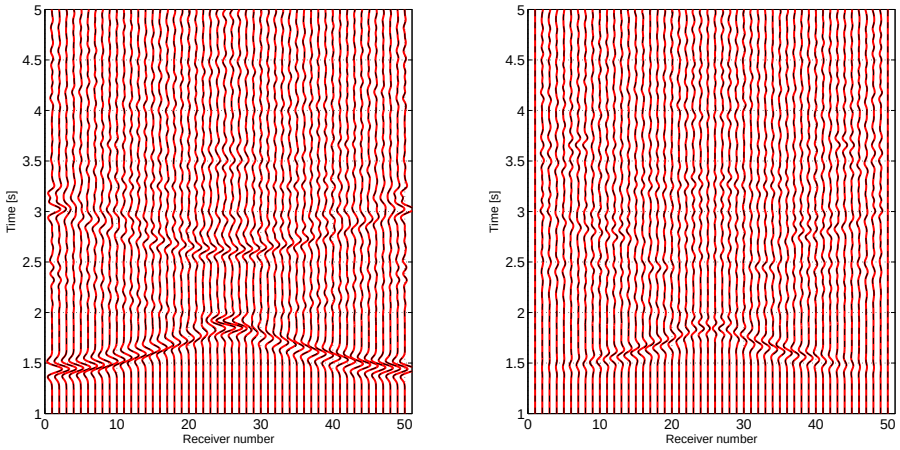

(b) Test case (ii).

Figure 6.8: Horizontal (left) and vertical (right) displacement along the circle's boundary.

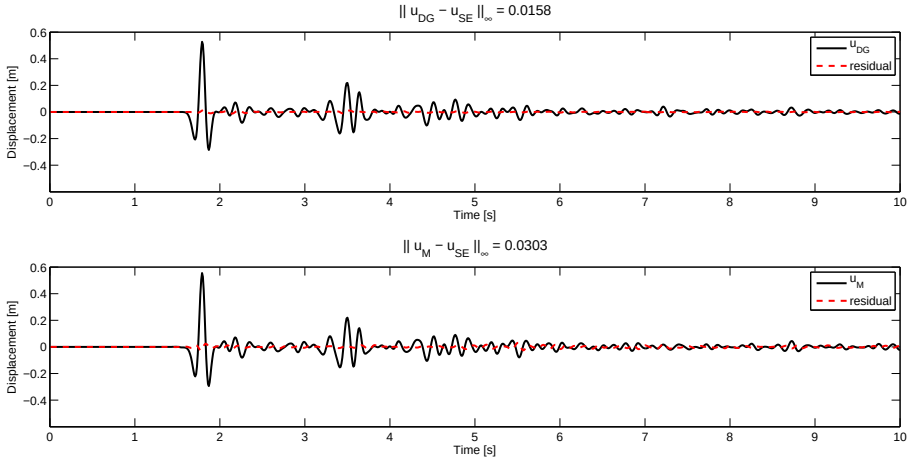

(a) Test case (i).

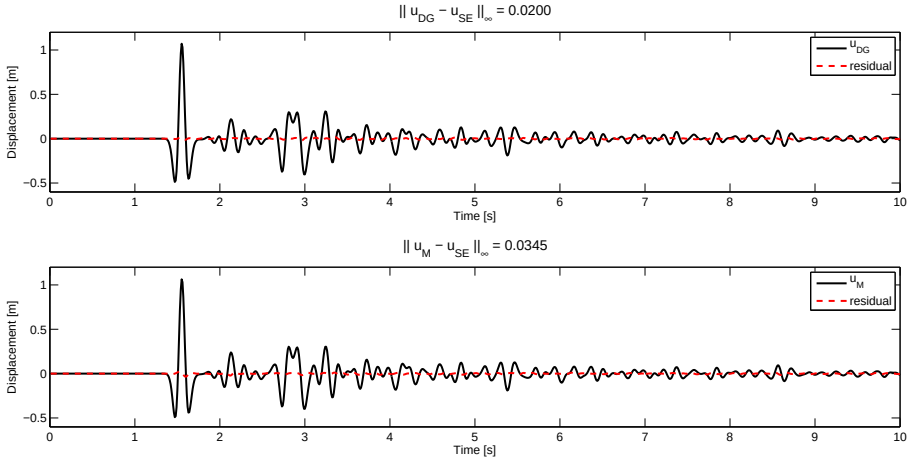

(b) Test case (ii).

Figure 6.9: Displacement recorded by R_{11} and corresponding residual.

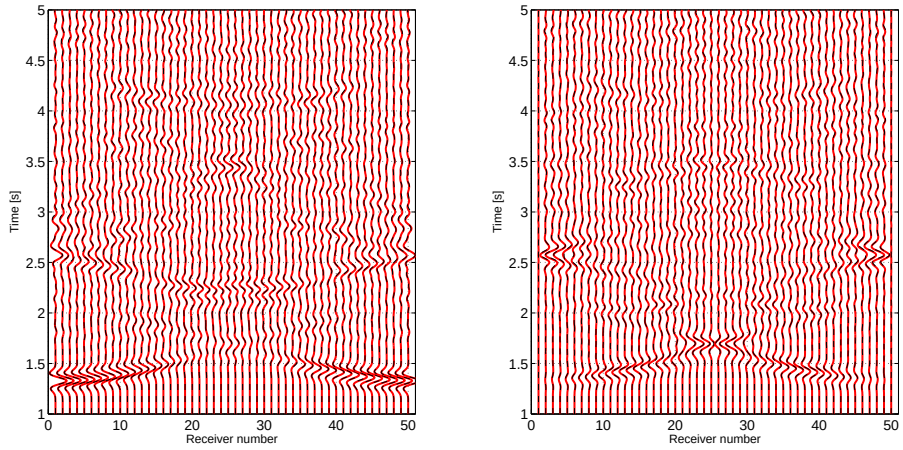

Figure 6.10: Case (iii). Horizontal and vertical displacement along the circle's boundary.

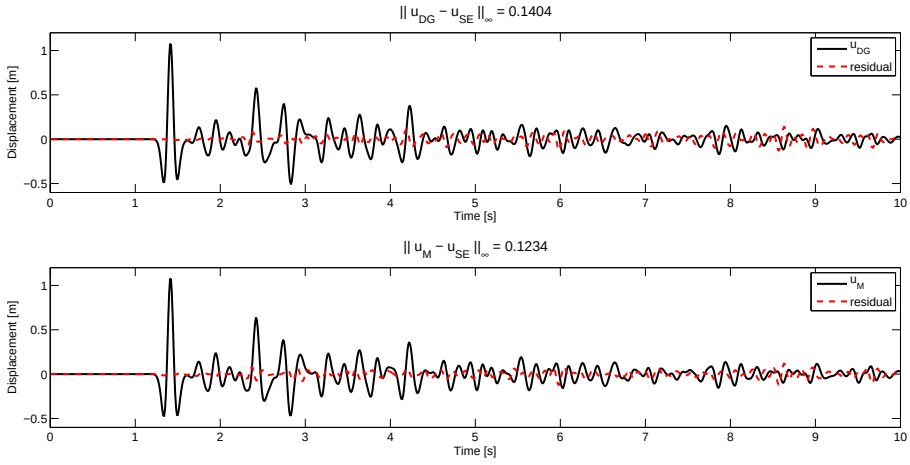

Figure 6.11: Case (iii). Displacement recorded by R_{11} and corresponding residual.

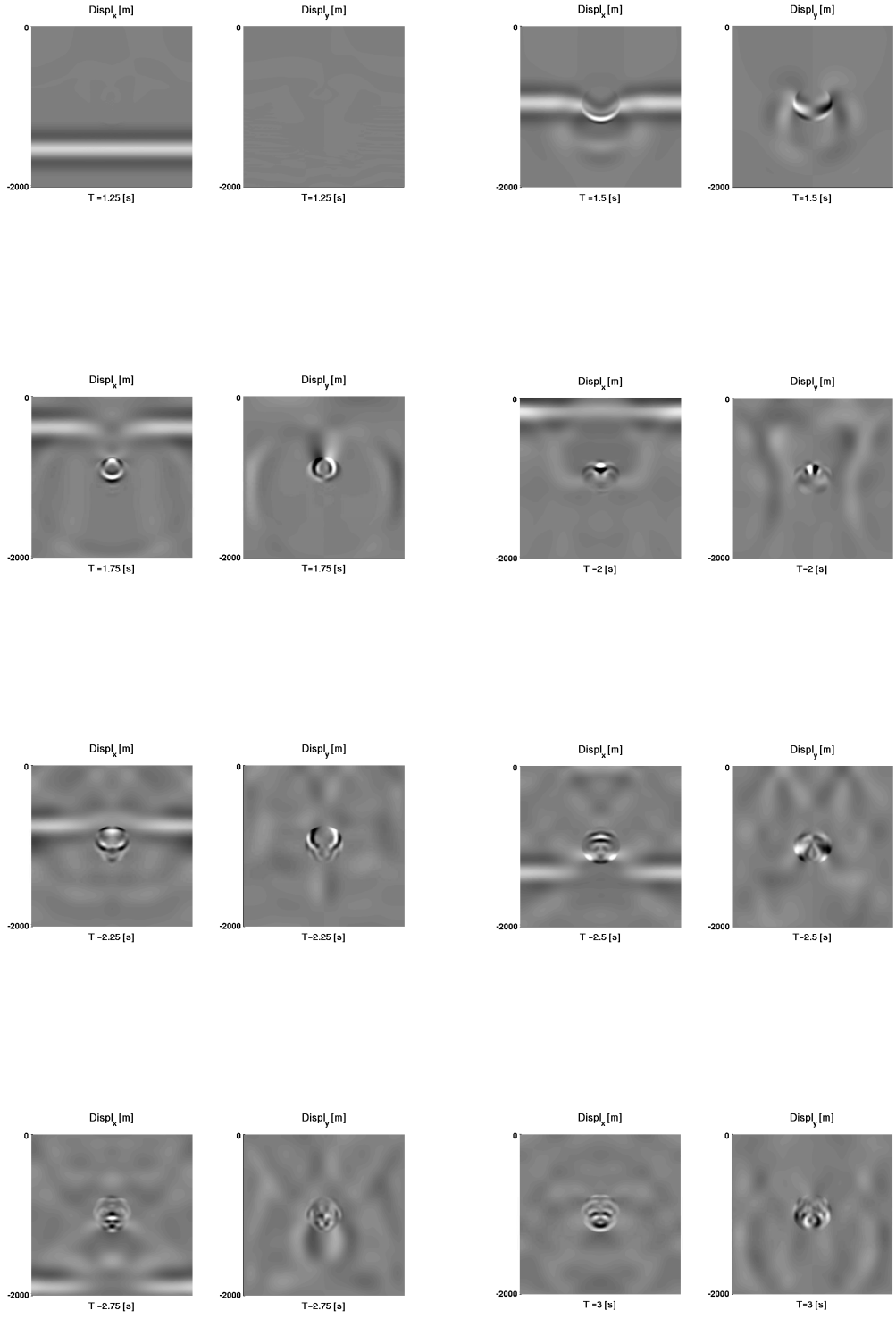

Figure 6.12: Case (iii): snapshots of the horizontal and vertical displacements obtained with DGSE method.

Layer	Depth $[m]$	$c_P[m/s]$	$c_S[m/s]$	$\rho[Kg/m^3]$
L	0-1000	4000	2000	2600
HS	1000-17000	6000	3464	2700

Table 6.2: Dynamic and mechanical parameters for the layer (L) and the halfspace (HS).

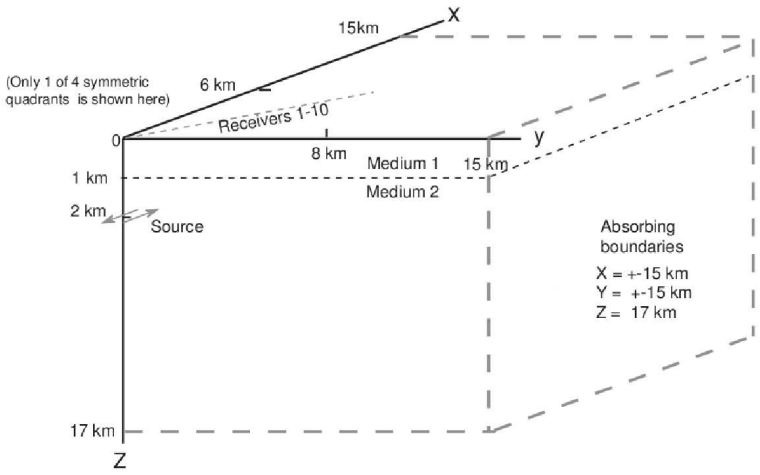

Figure 6.13: One of the four symmetric quarters of the LOH test case, consisting of a surface layer, 1 km thick. The hypocenter together with the receivers location are also shown.

6.3 Layer over a halfspace

This test case we has been proposed by [38] and it is currently a reference benchmark for the most advanced numerical codes for seismic wave propagation (see e.g., [44]). This problem is known in literature with the acronym LOH, Layer Over Halfspace. The computational domain is $\Omega = [-15, 15] \times [-15, 15] \times [17, 0]$ km, with top layer having thickness 1 km. The computational domain and the material parameters are shown in Figure 6.13 and Table 6.2, respectively.

The seismic source $\mathbf{f}(\mathbf{x}) = \delta(\mathbf{x} - \mathbf{x}_S)M(t)$ is located at the centre of Ω on the horizontal x-y plane, i.e., $\mathbf{x}_S = (0, 0, 2)$ km. The source is represented by a double couple, with amplitude $M_0 = 10^{18}$ Nm, and the moment-rate time variation is given by

$$M(t) = M_0 \frac{t}{\tau^2} \exp(-t/\tau).$$

Here τ is called smoothness parameter, and control the frequency content and amplitude of the source time function. For this test case we have set $\tau = 0.1$ s, see Figure

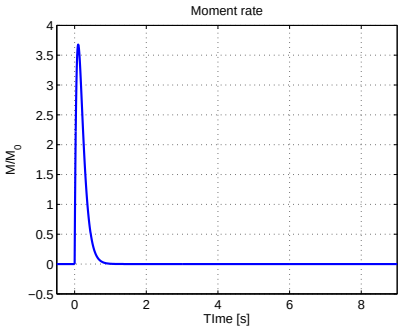

Figure 6.14: Moment rate function for the LOH test.

6.14. Further details on the problem setting as well as on the source time function can be found in [38] together with the expression of the semi-analytic solution. In order to avoid dispersion errors the non-conforming mesh is designed in order to have 5 points per wavelength for both the halfspace and the layer, with polynomial degree $N = 4$, see Chapter 4. Then, the spectral element dimension is $h_{HS} \approx 600\ m$ in the halfspace and $h_L \approx 160\ m$ in the top layer. The time step for the explicit second order leap-frog scheme is $\Delta t = 10^{-4}\ s$.

The computational grid for this problem consists in 81150 spectral element for approximately $3.6 \cdot 10^7$ degrees of freedom when using fourth order polynomial basis. In Figure 6.15 we show the three components of the computed velocity registered by the receiver located at $(6, 8, 0)\ km$. The reported results have been obtained with the DGSE method on both structured and unstructured grids (test A) as the ones shown in Figure 6.16. Figure 6.15 also shows the reference solution [38]. In each plot, we also report the relative seismogram misfit

$$E = \sum_{i=1}^{n_s} (\dot{\mathbf{u}}_{DG}(t_i) - \dot{\mathbf{u}}(t_i))^2 / \sum_{i=1}^{n_s} (\dot{\mathbf{u}}(t_i))^2 \tag{6.2}$$

where n_s is the number of time samples of the seismogram, $\mathbf{u}_{DG}(t_i)$ is the numerical value of the seismogram at sample t_i, and $\mathbf{u}(t_i)$ is the corresponding reference value.

Figure 6.15 shows that the relative misfits are under 20 percent and 26 percent for the structured (a) and unstructured case (b), respectively. We can improve the accuracy of the DGSE solutions without increasing the number of unknowns, considering a spectral element grid refined in the first quadrant of the top layer (test B) as it is shown in Figure 6.17. Indeed, setting $h_L = 100\ m$ and $N = 2$ for the positive quadrant of the

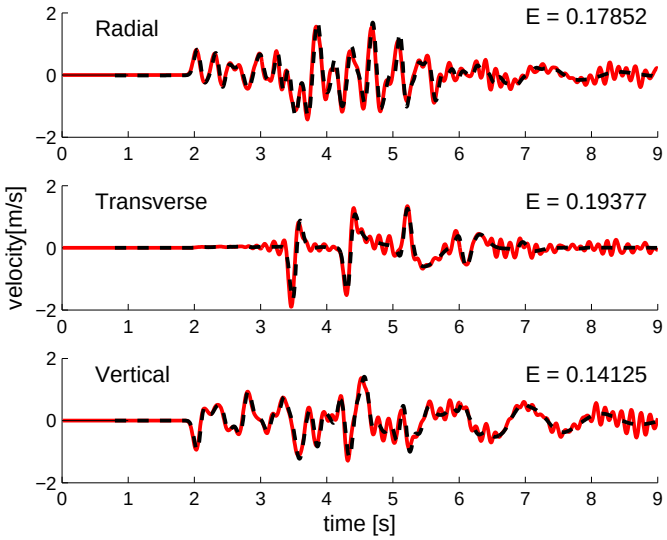

(a) Structured grid for the layer.

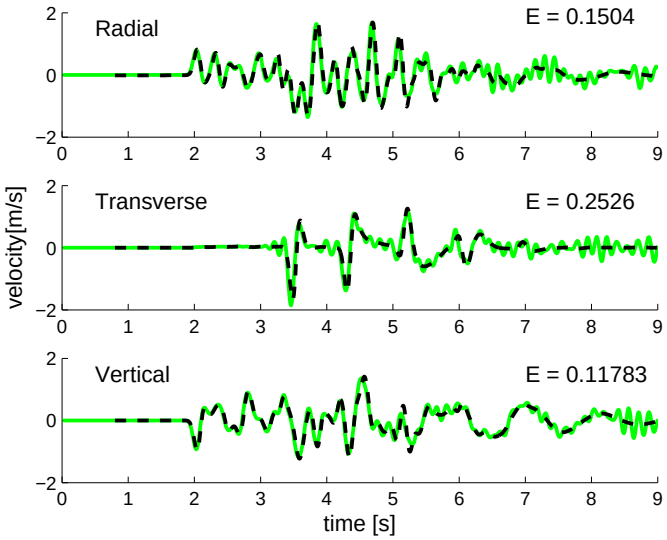

(b) Unstructured grid for the layer.

Figure 6.15: Test A: velocity field recorded at $(6, 8, 0)$ km. Comparison between the semi-analytic solution (dashed line) and the approximated one (solid line). Relative misfit computed according with (6.2).

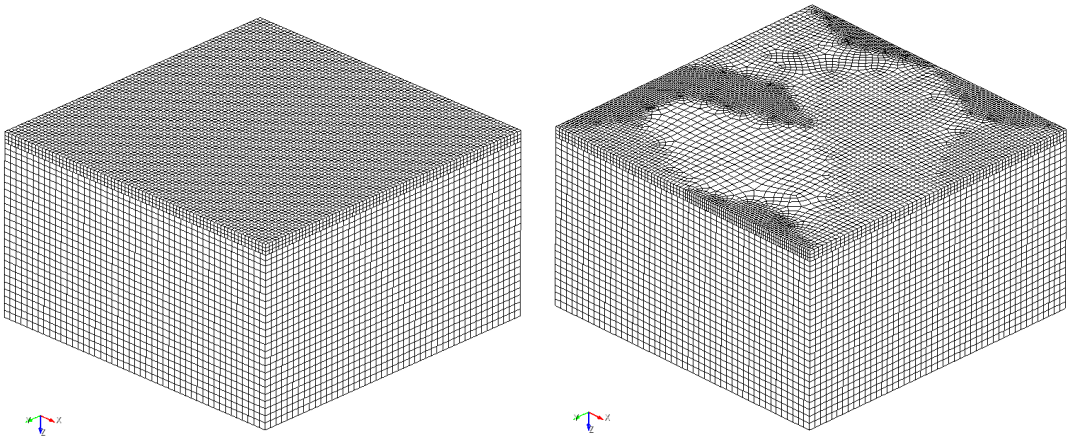

Figure 6.16: Test A: Structured (left) vs unstructured (right) grid used for the discretization of the top layer.

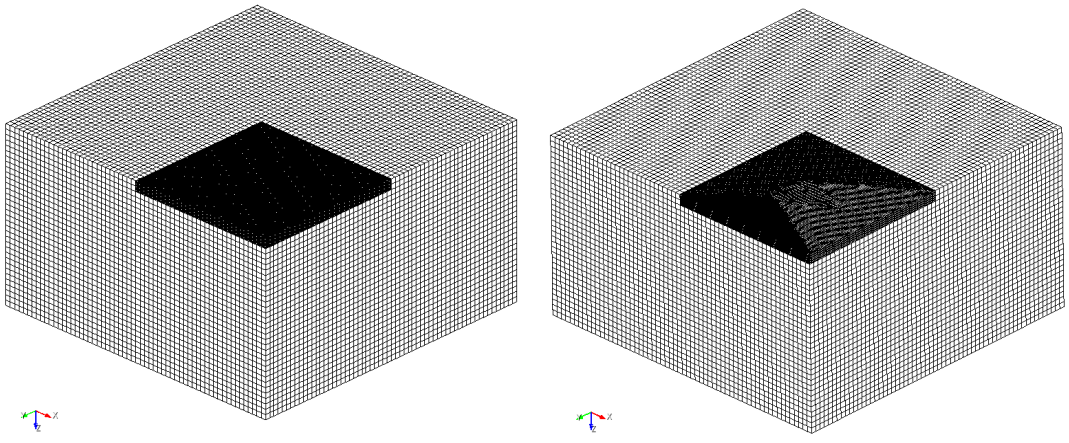

Figure 6.17: Test B: Structured (left) vs unstructured (right) refinement for the first quadrant of the top layer.

top layer and $h_{HS} = 500\ m$ and $N = 4$ for the remaining part of the domain the total number of unknowns is approximately $3.6 \cdot 10^7$. With this choice the relative misfits are under 17 percent for both a structured and an unstructured refinement as it is shown in Figure 6.18. These results are promising compared to those available in literature [110, 44]. Further improvements of the results can be achieved, for instance, choosing even higher order polynomial degrees in the first quadrant.

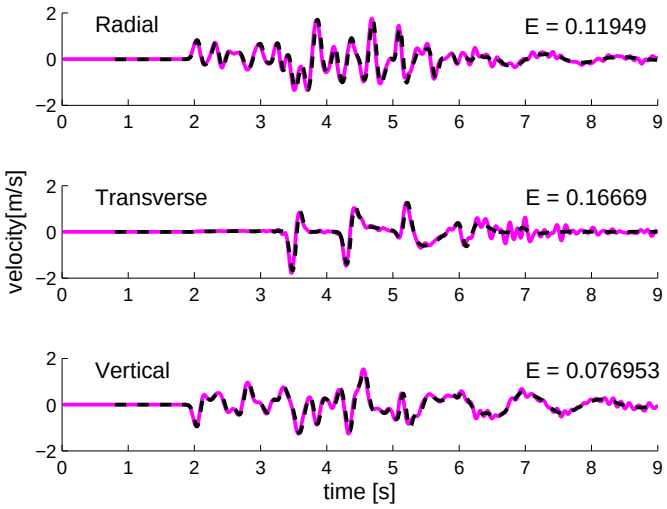

(a) Structured grid for the layer.

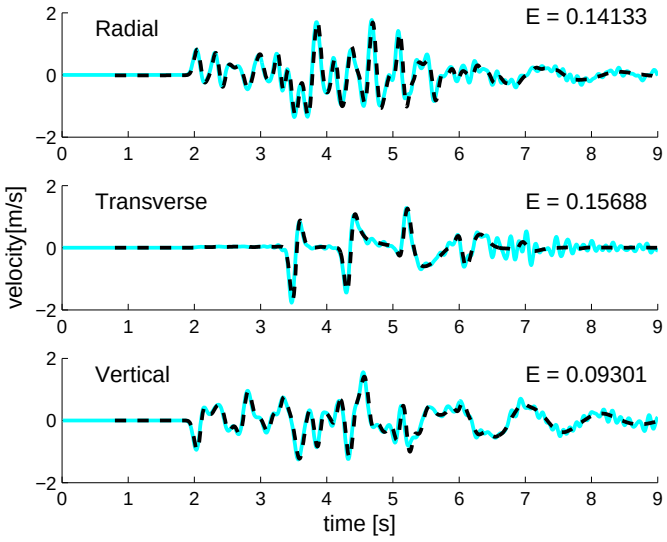

(b) Unstructured grid for the layer.

Figure 6.18: Test B: velocity field recorded at $(6, 8, 0)$ km. Comparison between the semi-analytic solution (dashed line) and the approximated one (solid line). Relative misfit computed according with (6.2).

6.4 Croissant valley

In this section we present some numerical computations obtained for the prediction of the seismic response of a three dimensional alluvial valleys under incident P and S wave [101]. We consider incidence of plane waves of the P, SH (horizontal shear) and SV (vertical shear) type with an angle of incidence of 0 degrees with respect to the vertical plane. We have computed synthetic seismograms assuming for the incoming wave a Ricker wavelet of characteristic period $t_P = 3\ s$, see Figure 6.19. The shape of the three dimensional alluvial valley can be described as follows: the soft material is, horizontally, within a region for which the conditions $r < a$ and $R > b$ hold, where $r^2 = x^2 + y^2$ and $R^2 = (x-a)^2 + y^2$. In other words the valley zone is limited by two circumferences of radii a and b, where $a > b$, (Figure 6.20). In this region the geometry of the interface between the sediment and the halfspace is given by

$$z = z(x, y) = H(b^2 - R^2)[1 - 2a(a - x)/R^2], \tag{6.3}$$

where H is a parameter that controls the valley's depth. The choice of this analytical expression is arbitrary and it is inspired by Weber's solution for the Saint-Venant stress function for the torsion of a bar of circular cross section of radius a with a circular groove of radius b. We selected $b = 0.7a$ and $H = 0.4/a$; thus, the maximum depth is approximately $0.25a$.

Figure 6.20 displays the contour levels of the interface, while Figure 6.21 shows a perspective of this profile. The free surface of both the alluvial deposit and the halfspace is assumed to be flat. The value for a is set equal to 4 km. The material properties are described in Table 6.4 This test consists of pure SH plane wave propagation through the numerical domain of Figure 6.22. The angle of incidence is orthogonal to the free surface and the excitation consists of a Ricker type wavelet. Figure 6.23 shows three detailed views of the mesh. In Figure 6.24 we show the comparison between synthetic seismograms obtained with the SE method (red line) and the DGSE discretization (black dotted line). For both the cases, the LF scheme has been employed for the time dis-

Layers	$\rho\,[Kg/m^3]$	$c_P\,[m/s]$	$c_S\,[m/s]$	$\zeta\,[1/s]$
V	2000	2082	1000	0.01472
HS	2500	3464	2000	0.01472

Table 6.3: Dynamic and mechanical parameters for the valley (V) and the halfspace (HS).

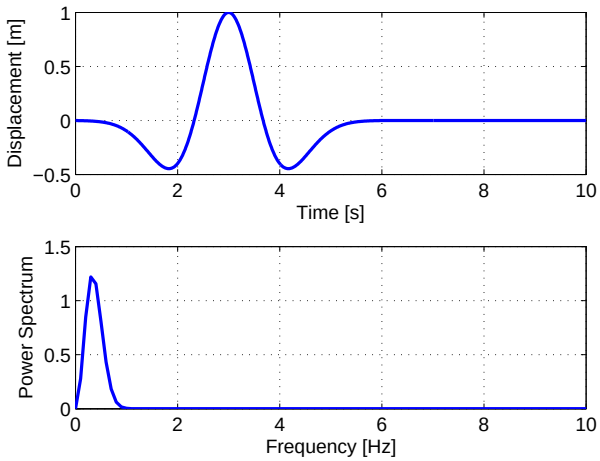

Figure 6.19: Ricker time shape function with characteristic period $t_P = 3\ s$.

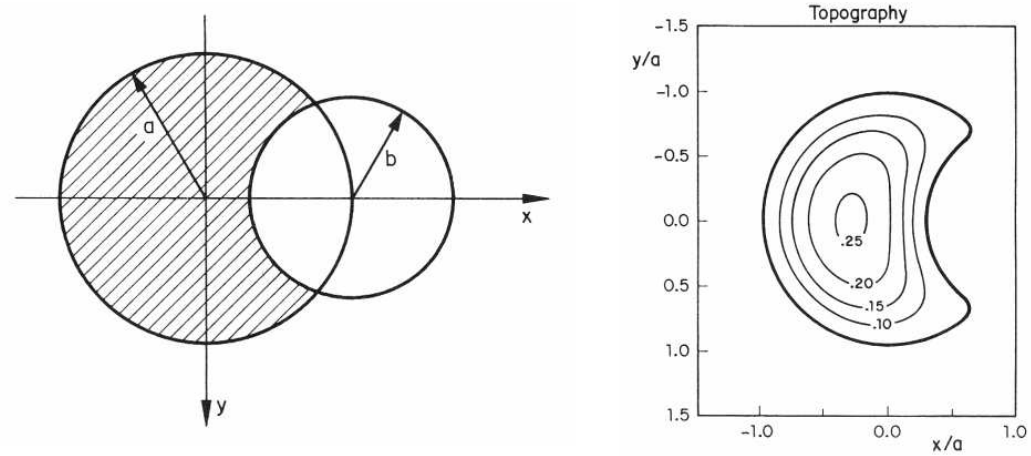

Figure 6.20: Left: the softer material (shaded area) is limited by two circumferences of radii a and b, $a > b$. Right: Topographic contour levels of the valley's basement.

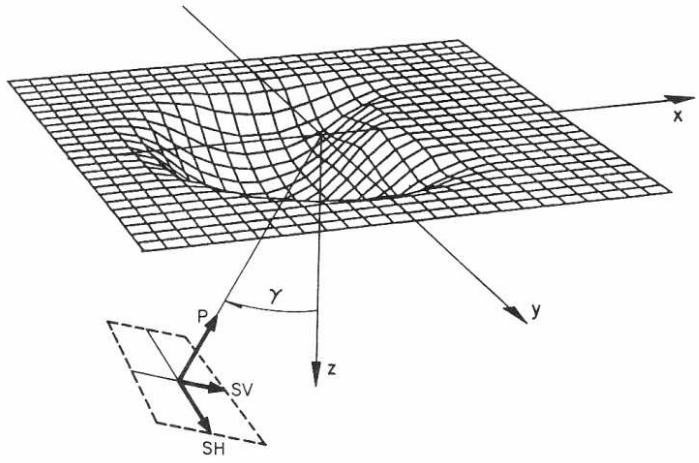

Figure 6.21: Perspective view of the irregular valley's basement. Incidence angle γ for P, SH and SV waves. Incidence angle γ with respect to the vertical for body waves.

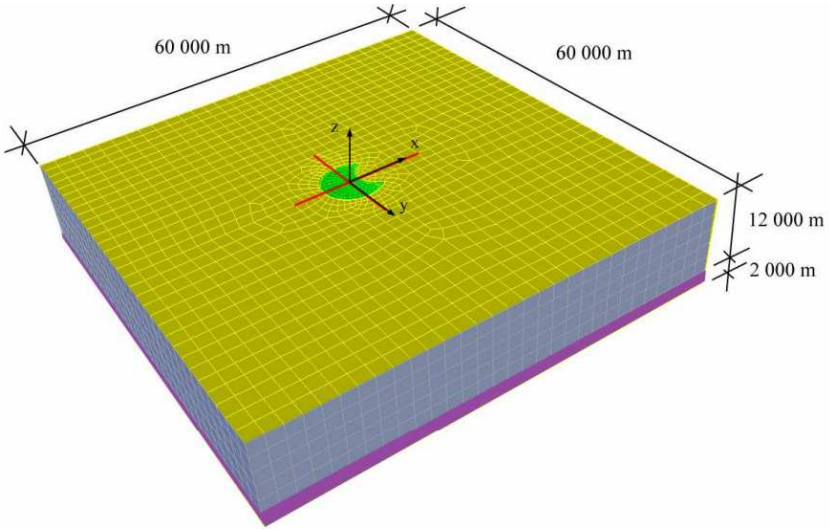

Figure 6.22: The numerical mesh for the test of plane wave load with incidence angle orthogonal to the free surface. The numerical mesh has 19254 hexahedral elements and approximately $1.3 \cdot 10^6$ nodes with polynomial approximation degree $N = 4$.

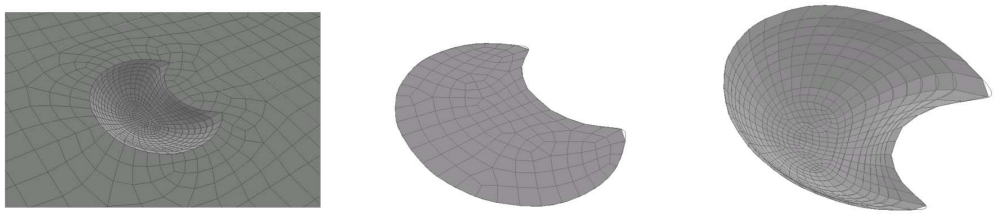

(a) (b) (c)

Figure 6.23: Detailed views of the meshes (a) near the border of the irregular alluvial valley, (b) top view of the irregular three dimensional valley area and (c) bottom view.

cretization ($\Delta t = 2 \cdot 10^{-3}$ s, final observation time $T = 40$ s). More precisely, in Figure 6.24 we compare the three components of the displacement recorded by the receivers $R_1 = (0, -7680, 0)$ m, $R_{25} = (0, 0, 0)$ and $R_{49} = (0, 7680, 0)$ m. For the DGSE method we have chosen $N = 4$ on the bedrock and $N = 3$ on the valley, while $N = 4$ is assumed for the SE discretization. In Figure 6.25 we plot the y-component of the displacement recorded by 49 receivers equally spaced along x and y axes, respectively. The range of x and y is between -7680 m and 7680 m.

A comparison between the two numerical results shows a good agreement. Computing the misfits as in (6.2) we obtain a maximum error E less than 3.10^{-3} for all the displacement components.

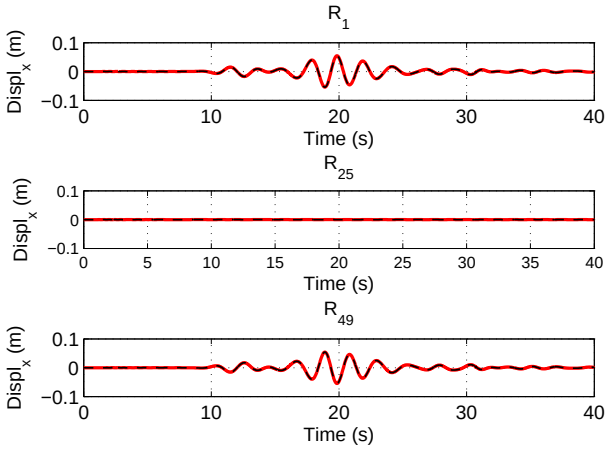

(a) First displacement component.

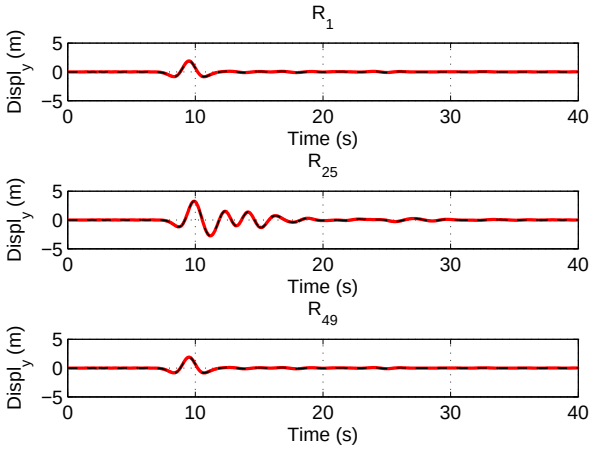

(b) Second displacement component.

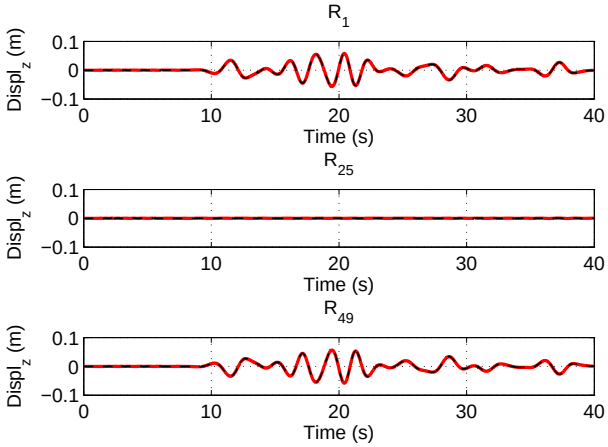

(c) Third displacement component

Figure 6.24: Displacements recorded by the receivers R_1, R_{25} and R_{49} along the y-axis. SE (continuous line) vs DGSE (dashed line) solutions.

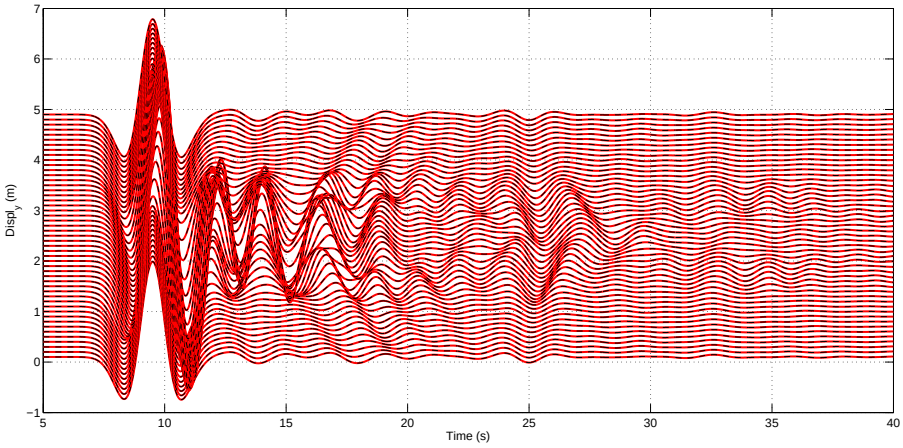

(a) Second component displacement for the receivers equally spaced between $(0, -7680, 0)$ m and $(0, 7680, 0)$ m.

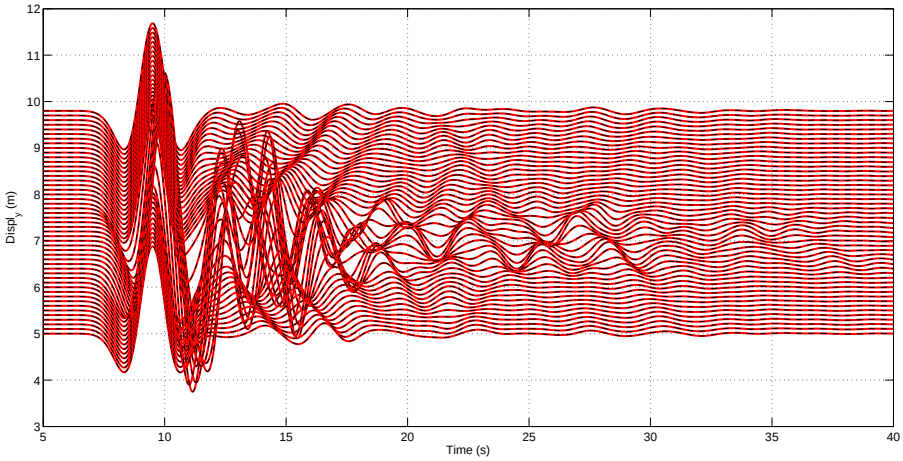

(b) Second component displacement of the 49 receivers equally spaced between $(-7680, 0, 0)$ m and $(7680, 0, 0)$ m.

Figure 6.25: Displacements recorded by 49 receivers equally spaced along x (top) and y (bottom) axes. SE (continuous line) vs DGSE solution (dashed line).

Chapter 7

Applications of geophysical interest

In this chapter we present some relevant applications of the non-conforming discretizations to problems of geophysical interest. We start presenting the seismic response of the Acquasanta railway bridge and of the Gubbio alluvial basin. The first simulation describe a soil structure interaction problem in which different scales are used for the description of the bridge and the underlying valley. With a suitable choice of the discretization parameters $\mathbf{h}$ and $\mathbf{N}$ in the non-conforming approach, we can obtain accurate results while reducing the computational cost by a factor 2 with respect to SE approximations.

The Gubbio alluvial basin is an evident example of topography amplification. Due to the different characteristic soil properties, the seismic waves that travel across the valley are amplified and trapped within the basin and reflection phenomena take place. With the non-conforming approach we can describe accurately the wave front propagating inside the valley as well as the complex geometry of the problem.

In the second part of the chapter, we propose two realistic three dimensional geophysical applications. These results are obtained with the DGSE approach. The first one concerning the valley of Grenoble (French Alps) has been the object of an international benchmark in the last years [110, 44, 35]. As for the Gubbio basin test, we can reproduce the complex interaction between the radiation mechanism and the corresponding directivity effects due to the the complicated shape of the Grenoble basin.

In the second three dimensional application we study the seismic response of the Central District Building (CBD) of Christchurch (New Zealand) during the February 22, 2011 earthquake. Here, the non conforming strategy is used to deal with different

macroscopic scales (meters for the structures and kilometers for the geophysical region) involved in the simulation. With this full-coupled analysis we can describe, at the same time, the seismic effect of the earthquake on the CDB and the wave phenomena over all the region considered. For the three dimensional simulations we make use of the software CUBIT and METIS for the mesh generation and the mesh partitioning, respectively. These commercial code are available at `http://cubit.sandia.gov/` and `http://glaros.dtc.umn.edu/gkhome/views/metis` respectively. The simulations were performed on the Lagrange cluster located at CILEA.

7.1 Acquasanta railway bridge

In this section, we aim at studying a soil-structure interaction problem, namely the seismic response of a railway viaduct (Acquasanta viaduct, Genova, Italy). We consider the viscoelastic model (1.3) in the computational domain $(x, z) \in \Omega = (0, 10^4)\ m \times (0, f(x))$, where f describes the top profile of the bridge and of the surrounding valley, see Figure 7.2. The size of the domain is chosen in order to avoid any possible interference with reflections of the waves of interest with the spurious ones eventually arising from the absorbing boundaries. The dynamic and mechanical properties of the structure and of the surrounding soil are summarized in Table 7.1. According to the mechanical properties, we subdivide the computational grid into different regions, as shown in Figure 7.2 (top panel).

We simulate a point source load of the form $\mathbf{f}(\mathbf{x}, t) = \mathbf{g}(\mathbf{x})M(t)$, where $\mathbf{f}$ is the external force introduced in (1.1). The function $\mathbf{g}$ describes the space distribution of the source $\mathbf{g}(\mathbf{x}) = \delta(\mathbf{x} - \mathbf{x}_S)\hat{\mathbf{w}}$, where δ represents the Dirac distribution, $\mathbf{x}_S$ is the source location and $\hat{\mathbf{w}}$ is the direction of the body force. The source time history $M(\cdot)$ is given by a Ricker-type time function, see Figure 7.1, defined as

$$M(t) = M_0[1 - 2\beta(t - t_0)^2] \exp[-\beta(t - t_0)^2], \tag{7.1}$$

where $M_0 = 10^6\ Nm$ is a scale factor, $t_0 = 2\ s$ is the time shift, $\nu_{\max} = 3\ Hz$ and $\beta = \pi^2\nu_{max}^2 = 9.8696\, s^{-1}$ is a parameter that determines the width of the wavelet (7.1).

In Figure 7.2 we show the two different computational grids used for the numerical simulations. The conforming grid, see Figure 7.2 (left), is used with SE discretization to produce a reference solution for the problem. It provides, in fact, a sufficiently accurate

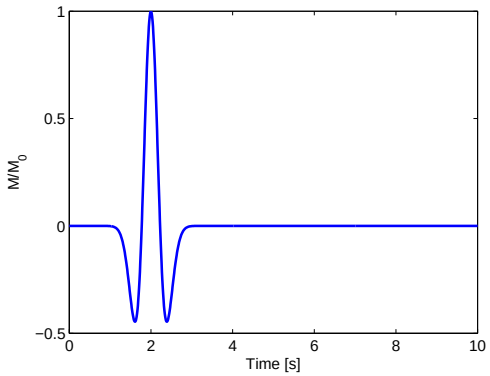

Figure 7.1: Ricker time shape fuction defined in (7.1).

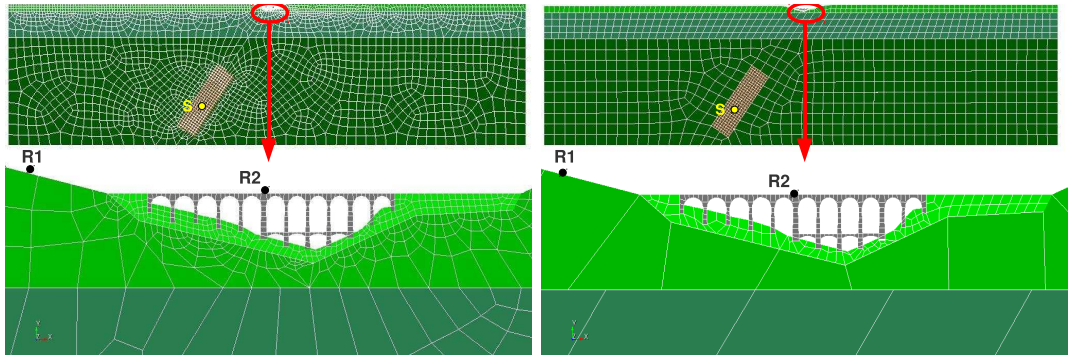

Figure 7.2: Conforming (left) and non-conforming (right) grids. The full domain is displayed on the top and a zoom of the railway bridge is displayed on the bottom. The receivers R1 (on the ground) and R2 (on the bridge) are also highlighted.

Layer	$\rho\,[Kg/m^3]$	$c_P\,[m/s]$	$c_S\,[m/s]$	$\zeta[1/s]$	N [SE]	N [MSE/DGSE]
1 (bridge)	1750	1218	716,7	0.6283	4	2
2 (stiff soil)	2400	1100	635	0.31416	4	2
3 (soft bedrock)	2400	1100	635	0.02513	4	4
4 (medium bedrock)	2600	1700	982	0.02284	4	4
5 (stiff bedrock)	2800	2300	1330	0.02094	4	4
6 (stiff bedrock)	2800	2300	1330	0.02094	4	4

Table 7.1: Dynamic and mechanical parameters and polynomial approximation degree N for each subdomain of the domain decomposition (the factor ζ takes into account the viscoelastic linear soil behaviour).

discretization, as we verified that further mesh refinements generates quasi-identical seismograms. The non-conforming grid, shown in Figure 7.2 (right), is used for both DGSE and MSE simulations. In the analysis we choose the polynomial approximation degree as described in Table 7.1. It is worth highlighting that the non-conforming approximations lead to a dramatic reduction of the size of the numerical model and, hence, of the computational costs (102.640 unknowns for the SE method vs. 41.322 for the MSE and the DGSE methods). Such an advantage will play a major role for three dimensional engineering applications. In Figure 7.3 (resp. Figure 7.4) we analyse the synthetic seismograms recorded by the receiver R1 (resp. R2) on the top of the ground (resp. bridge) using the misfits criteria introduced in [66]. With these criteria we can evaluate in the time domain the envelope (dissipation) and the phase (dispersion) misfits between the reference signals and the ones computed with DGSE and MSE methods coupled with a leap-frog time integration scheme. The results show an excellent fit of the data received by R1 and a good fit for the data registered by receiver R2. Probably, for the latter receiver, the results are affected by grid dispersion phenomena arising when low order polynomial approximation degrees are used [8, 40, 39]. Nevertheless, in both cases the error is under 20 percent.

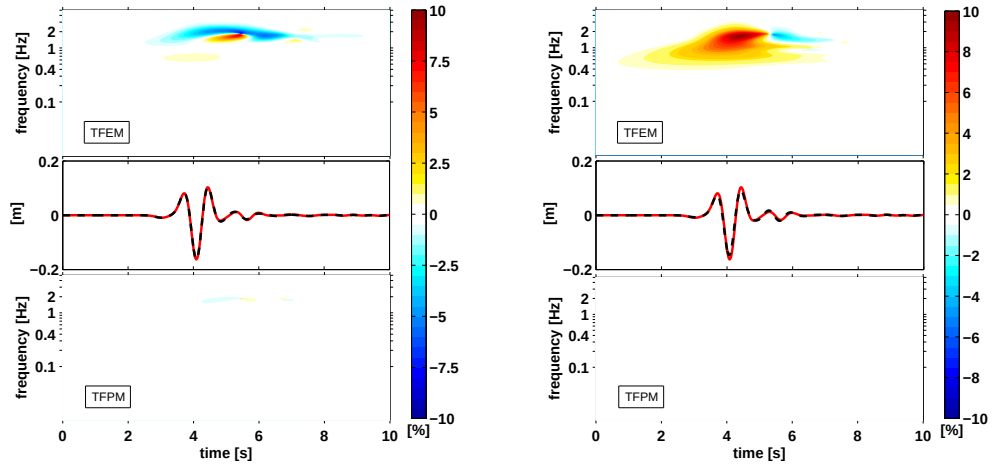

(a) DGSE vs SE methods

(b) MSE vs SE methods

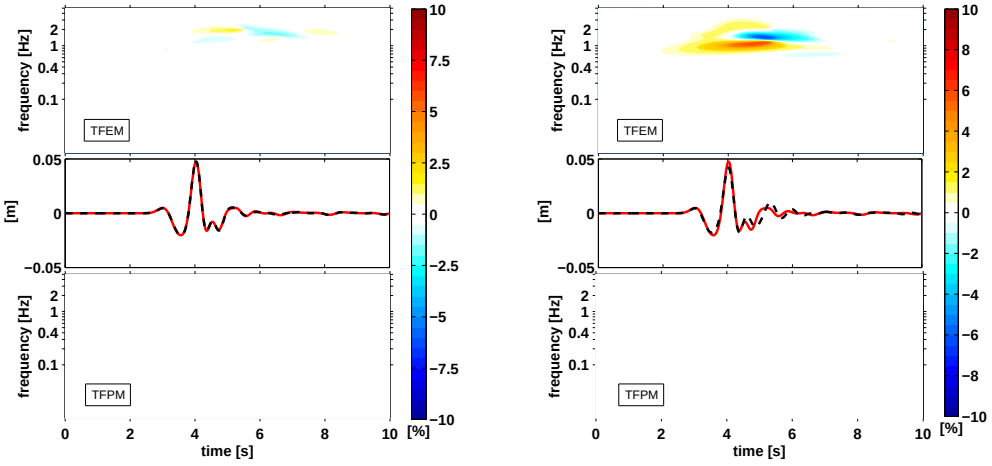

(c) DGSE vs SE methods

(d) MSE vs SE methods

Figure 7.3: Analysis of the synthetic signals recorded by receiver R1, using the misfits criteria described in [66]. The graphs in the middle of the four plots represent the computed horizontal (top) and vertical (bottom) displacements obtained using conforming (solid line) and non-conforming (dashed line) approximations. TFEM: time frequency envelope misfits. TFPM: time frequency phase misfits.

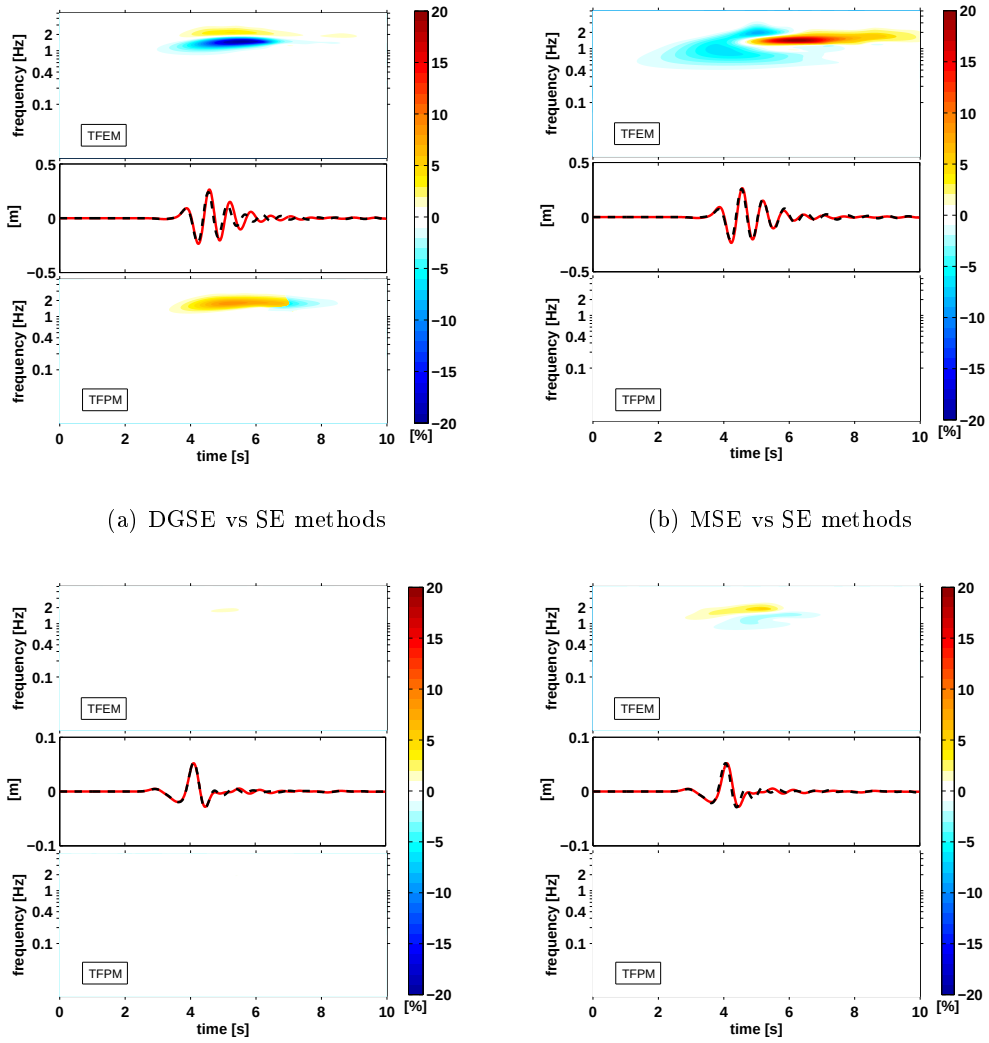

(a) DGSE vs SE methods

(b) MSE vs SE methods

(c) DGSE vs SE methods

(d) MSE vs SE methods

Figure 7.4: Analysis of the synthetic signals recorded by receiver R2, using the misfits criteria described in [66]. The graphs in the middle of the four plots represent the computed horizontal (top) and vertical (bottom) displacements obtained using conforming (solid line) and non-conforming (dashed line) approximations. TFEM: time frequency envelope misfits. TFPM: time frequency phase misfits.

7.2 Gubbio alluvial basin

In this section we analyze the seismic response of an alluvial basin. We consider the viscoelastic model (1.3) in the computational domain $(x, z) \in \Omega = (0, 2 \cdot 10^4\ m) \times (-9.6 \cdot 10^2\ m, f(x))$ where f describes the top profile of the valley, see Figure 7.5. The bottom and the lateral boundaries are set far enough from the point source to avoid any interference of possible reflections from non-perfectly absorbing boundaries with the waves of interest that are reflected, transmitted, or converted at the material or free surfaces. We simulate a point source load as described in Section 7.1. Alternative source distributions can be expressed in terms of gradient or curl of suitable potential functions, giving rise to pure pressure and shear waves: more complex and realistic source mechanisms are based on tensorial models (cf. [46]).

In Figure 7.5, we show the two different mesh configurations. Figure 7.5 (left) shows a regular, structured grid with a mesh spacing of $h \approx 40\ m$. The mesh size is chosen small enough to describe with sufficient precision the physical profile of the valley. Figure 7.5 (right) shows an irregular, overlapping quasi-structured grid with a mesh spacing $h_1 \approx 40\ m$ for layer 1 (basin) and $h_2 \approx 120\ m$ for layer 2 (bedrock). The finest mesh is used to describe the physical boundary of the valley while the coarsest mesh for the bedrock. This type of overlapping discretizations can be handled by the MSE technique described in Section 2.2. We assign constant material properties within each region as described in Table 7.2.

The regular conforming grid shown in Figure 7.5 (left) can be used to produce a reference solution for the problem with SE method and provides a sufficiently accurate discretization, since further mesh refinements generates quasi-identical seismograms. In Figures 7.6 we compare the horizontal and vertical displacement recorded by receiver R1 placed on the free surface of the valley (cf. Figure 7.5). These results have been obtained with the MSE methods coupled with the LF time integration scheme.

The high discontinuities between the mechanical properties of the materials produce high oscillations and perturbations on the wave front. All these complex phenomena

Layer	$c_P[m/s]$	$c_S[m/s]$	$\rho[Kg/m^3]$	$\zeta[1/s]$
1	700	350	1900	0.03141
2	3500	1800	2200	0.06283

Table 7.2: Dynamic and mechanical parameters.

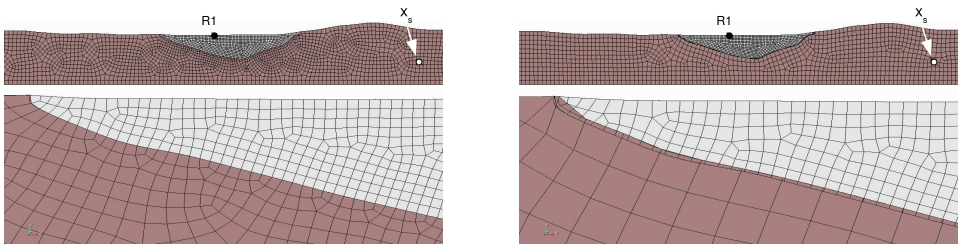

(a) Conforming, structured grid with a mesh spacing of $h \approx 40\ m$ at the interface between the two materials.

(b) Non-conforming, overlapping quasi-structured grid with a mesh spacing $h_1 \approx 40\ m$ for layer 1 (basin) and $h_2 \approx 120\ m$ for layer 2 (bedrock).

Figure 7.5: Top: receiver R1 placed on the top of the valley and point source $\mathbf{x}_S$ within the bedrock. Bottom: zoom of the valley profile.

are well captured by the MSE method using fourth order spectral elements. We remark that with MSE method we reduce the computational effort for the generation of the grid as well as the problem complexity (from 61385 spectral nodes with SE method to 48091 spectral nodes with MSE one). In Figure 7.7 we show the time histories of the seismograms recorded by some receivers on the free surface of the domain, obtained again using MSE method. It can be observed that the wave that starts travelling from the point source remains trapped into the valley, where it is amplified and where phenomena of reflection and refraction arise. This phenomenon is relevant in some geophysical contexts, e.g., it has occurred in the Gubbio valley (in Italy) on the occasion of the earthquake of September 27, 1997. We refer to [106] for a detailed analysis.

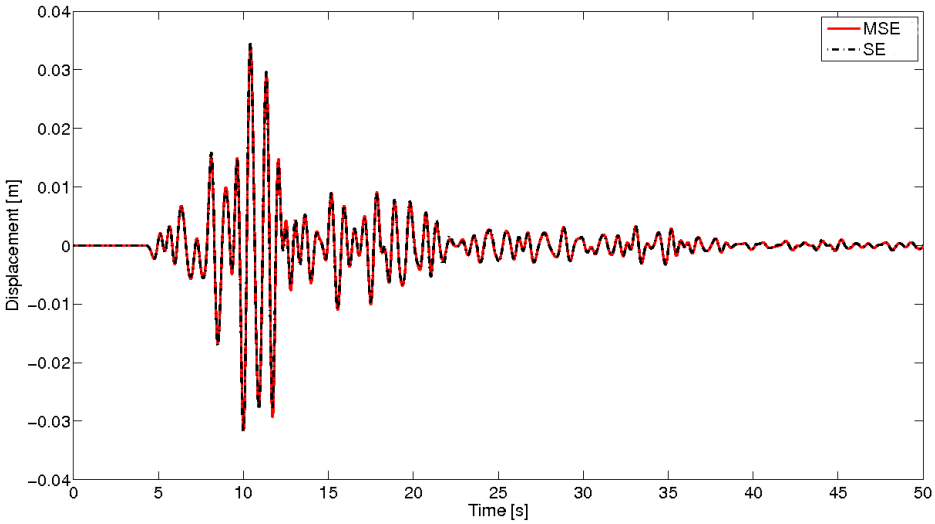

(a) Horizontal displacement.

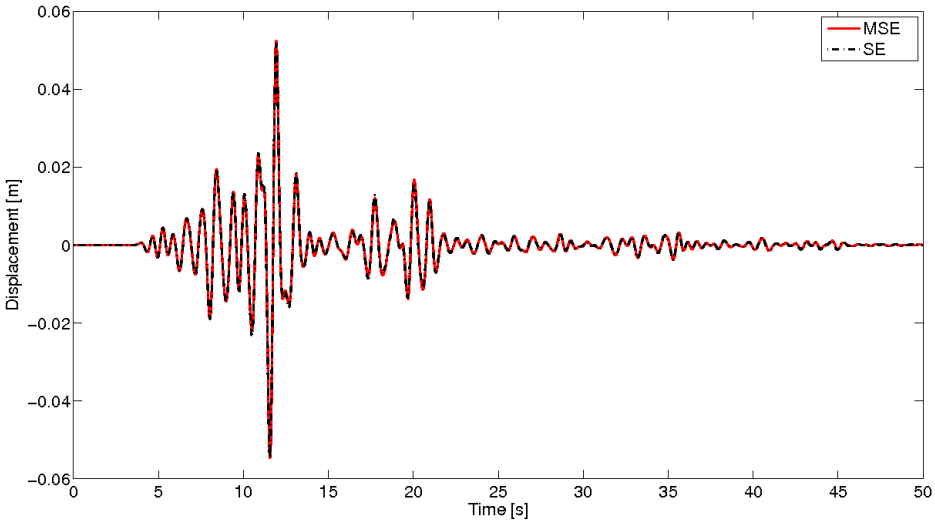

(b) Vertical displacement.

Figure 7.6: Displacements recorded by the receiver R1 on the free surface fo the valley. Comparison between SE and MSE methods, N=4.

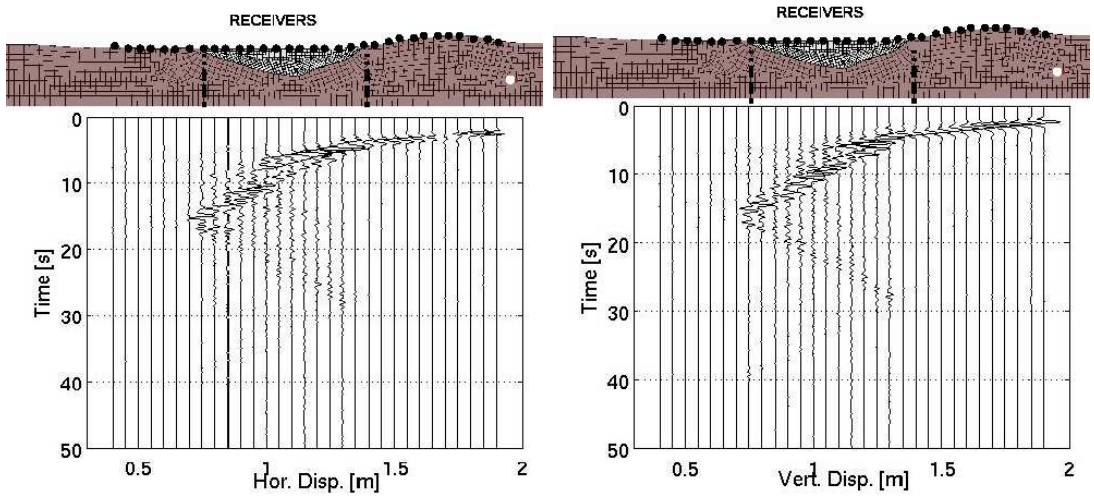

Figure 7.7: Time histories of the receivers on the top of the surface obtained with MSE method (N=4).

Layer	Depth z $[m]$	$c_P[m/s]$	$c_S[m/s]$	$\rho[Kg/m^3]$	$\zeta[1/s]$
Valley	-	1450+1.5 z	300+19 $\sqrt{z}$	2140+0.125 z	0.062832
Bedrock 1	0-3000	5600	3200	2720	0.06283
Bedrock 2	3000-27000	5920	3430	2920	0.06283

Table 7.3: Dynamic and mechanical parameters.

7.3 Grenoble valley

The Grenoble earthquake scenario has been analyzed during the last years in order to compare the performance of different numerical codes used for the numerical simulation of seismic wave propagation in near-fault conditions. We refer to [44, 35] for a more detailed description of the benchmark specifications and to [110] for the construction of the numerical model based on a 250 m resolution digital elevation model (DEM) of the surrounding topography and of the shape of the basin. We use a simplified description of the dynamic properties of the soil layers, based on the following polynomial variation with depth z, as it is shown in Table 7.3.

The spatial discretization by standard spectral elements of the Grenoble basin and the surrounding topography requires to build up a large unstructured mesh of hexahedral elements as it is described in [110]. The mesh used for SE discretization is shown in Figure 7.8 and consists of 202.477 elements, the size of which ranges from a minimum

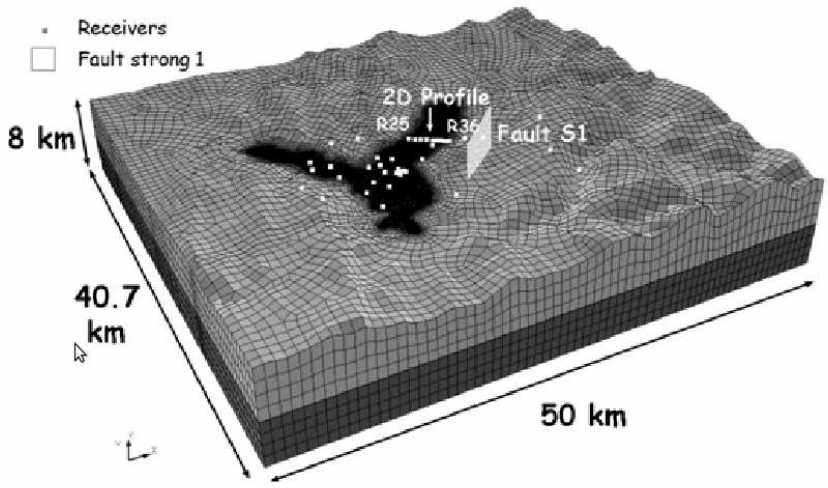

Figure 7.8: Hexahedral spectral element mesh adopted for the computation of the Grenoble benchmark, with the SE approach [110]. Belledonne Border Fault is also shown on the right of the valley along with receivers R25 to R36. Receivers R25 up to R32 are located on the alluvial basin. Receiver R36 is located on outcrop bedrock.

of about 20 m (inside the alluvial basin) up to 900 m. The mesh is designed in order to propagate correctly the signal for frequencies up to 3 Hz using fourth order polynomials. A detailed description of the meshing strategy adopted to describe the geometry of the Grenoble basin can be found in [110], while other promising strategies to tackle this problem are illustrated by [31] and [109]. The mesh generation can be simplified using the non-conforming approach. Using a mesh size ranging from 100 m to 300 m inside the valley and from 300 m to 900 m elsewhere we obtain a computational domain made by 230.900 elements, as it is shown in Figure 7.9.

The numerical simulation presented here refers to the benchmark specifications denoted as "Strong motion 1" [44] and corresponds to an earthquake scenario originated by the Eastern segment of the Belledonne Border Fault, with magnitude $M_w \approx 6$ (Figure 7.8), geometrically defined by a 9×4.5 km rectangle. The rupture mechanism is described in [110] and propagates circularly from the hypocenter, located in the centre of the rectangle, with velocity $v_r = 2.8$ km/s. The time dependency of the seismic moment source is described by an approximate Heaviside function:

$$M(t) = \frac{1}{2}\left[1 + erf\left(2\frac{t-2\tau}{\tau/2}\right)\right], \tag{7.2}$$

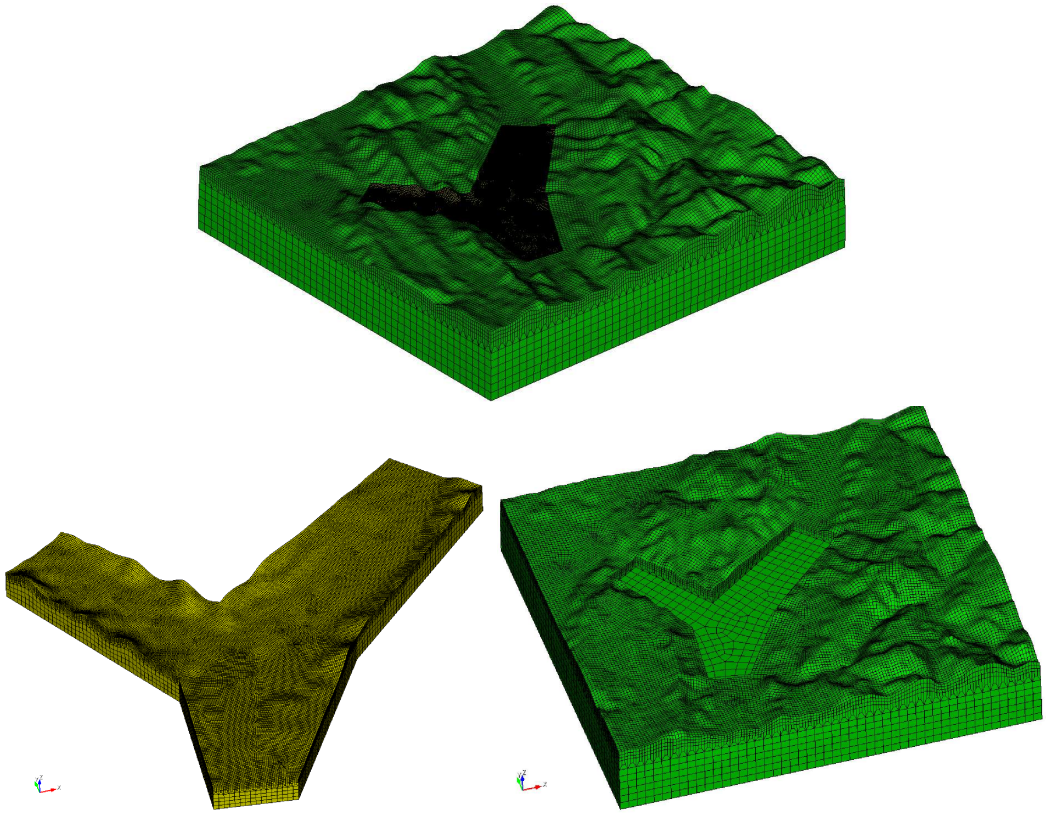

Figure 7.9: Non-conforming hexahedral spectral element mesh employed for the computation of the Grenoble benchmark, with the DGSE method (top). Mesh size ranging from 100 m to 300 m for the discretization of the valley (bottom left) and from 300 m to 900 m for the discretization of the bedrock (bottom right).

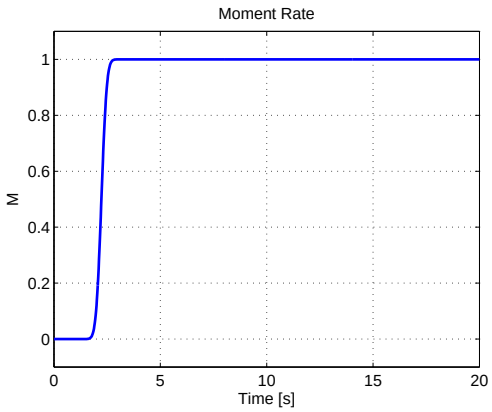

Figure 7.10: Moment rate function.

where $erf(\cdot)$ is the error function and $\tau = 1.116\ s$ is the rise time, see Figure 7.10. These values are selected for the slip velocity to be approximately 1 m/s. The total number of spectral nodes required to model the Belledonne fault is approximately 750.

Figure 7.11 shows the comparison of displacement waveforms, at receivers shown in Figure 7.8, obtained by the SE method, and the DGSE method with $N = 4$. For both the simulations, we have employed the leap-frog scheme ($\Delta t = 2.5 \cdot 10^{-4}$, $T = 20\ s$).
The numerical results obtained by SE and DGSE methods are in good agreement. Finally, in Figure 7.12 we report some snapshots of the radial velocity component ranging approximately from $-0.7\ m/s$ to $0.7\ m/s$ obtained with the DGSE discretization. The maps in Figure 7.12 clearly show the dramatic effect of the complex interaction between the radiation mechanism and the corresponding directivity effects with the complicated shape and the low wave propagation velocities of the Grenoble basin (topographic amplification effect).
Note that, as shown from the snapshots in Figure 7.12, the largest values of ground motion occur in the Grenoble basin along the fault strike direction and consist first of a large basin-edge induced amplification, followed by energy trapping inside the Southern part of the basin.

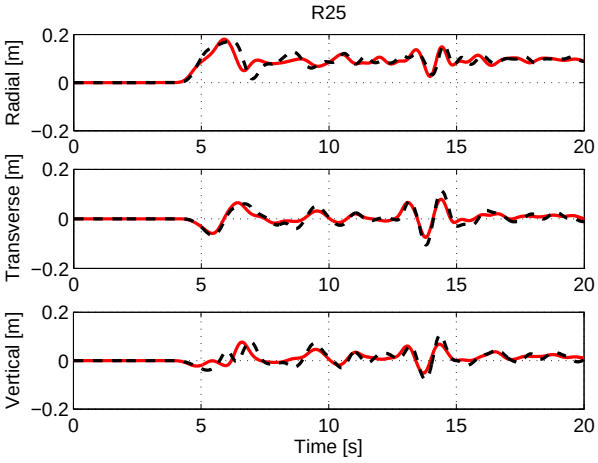

(a) Displacements recorded by R_{25}.

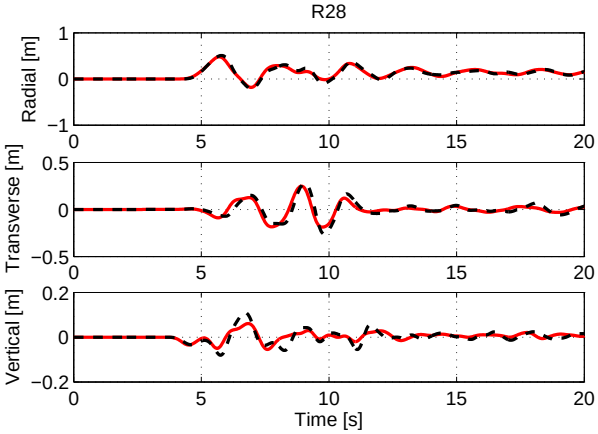

(b) Displacements recorded by R_{28}.

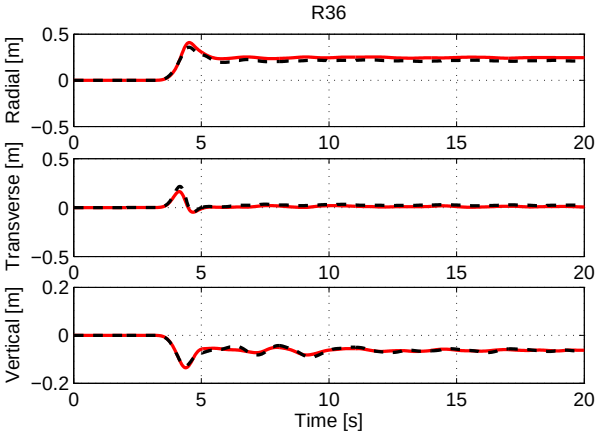

(c) Displacements recorded by R_{36}.

Figure 7.11: Displacements recorded by the receivers shown in Figure 7.8. SE (continuous line) versus DGSE (dashed line) solutions.

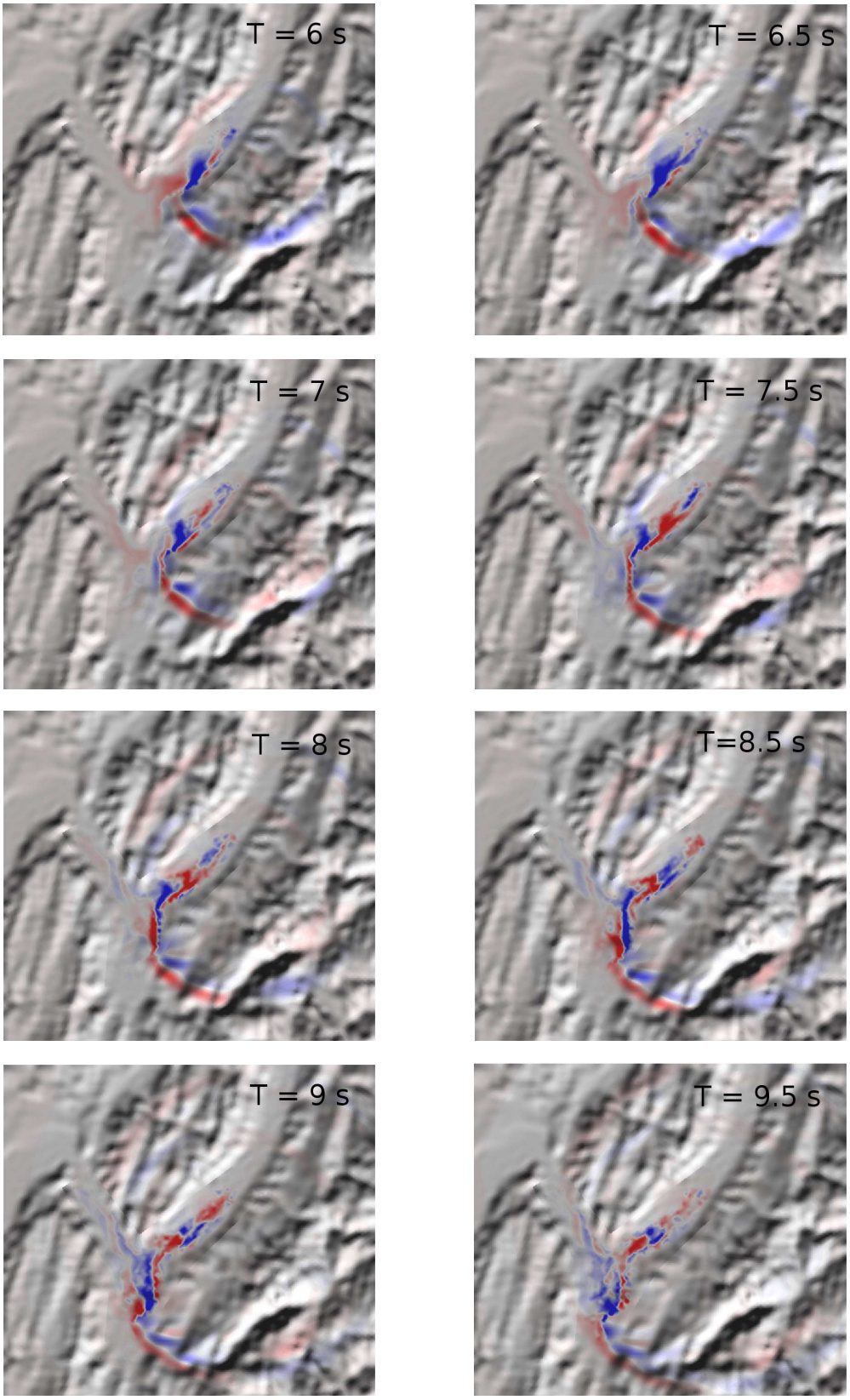

Figure 7.12: Snapshots of the fault radial velocity component in the Grenoble Valley, simulated by DGSE method.

7.4 22 February 2011 Christchurch earthquake

On 22 February 2011, an $M_w \approx 6.2$ earthquake struck the city and suburbs of the largest city on the South Island of New Zealand: Christchurch. The earthquake was generated by the Greendale fault located between the Australian and Pacific plates, within about 6 km from the city center.

During the last decade a set of seismic surveys across the Canterbury Plains had been carried out, but they did not revel any clear indication that a major earthquake was imminent in this particular region. Between September 2010 and December 2011 the Canterbury area experienced four major earthquake with $M_w \geq 6.0$ and a large number of aftershocks. The Christchurch earthquake was recorded by several digital stations of the permanent network operated by the Institute of Geological and Nuclear Sciences.

Peak ground motion accelerations in the epicentral region of the earthquake range up to 1.261 g on the horizontal component and up to 1.269 g on the vertical component. The ground accelerations recorded within the city of Christchurch are among the largest ever recorded for a New Zealand earthquake, with exceptionally high vertical ground acceleration. The unusual severity of the ground shaking can be explained as a combination of four major effects; (i) the proximity of the causative fault to the city; (ii) the directivity of the ground motion toward the urban area; (iii) the strong amplification effects of the soft alluvial sediments beneath the city; and (iv) the handing wedge effect, causing a significant increase of ground shaking on the hanging wall.

The availability on this unprecedent dataset of near-fault strong ground motion, combined with the peculiar geological configuration of the Christchurch area, makes the Christchurch earthquake a relevant benchmark to test the effectiveness of numerical tools for the prediction of the variability of strong ground motion in near-fault conditions.

In [51] different numerical models were construct for the Christchurch earthquake, to check the dependence of the results on: (a) the kinematic source model, based on the information retrieved from recent seismic source inversion studies, and (b) the shape of the alluvial-bedrock interface within the Canterbury Plains. In this work the synthetic results are compared against the strong ground motion records. The misfit between simulated and recorded waveforms are evaluated in quantitative way making use of the criteria proposed by [66]. The results show that model proposed is able to reproduce with a satisfactory level of accuracy the considered earthquake scenario.

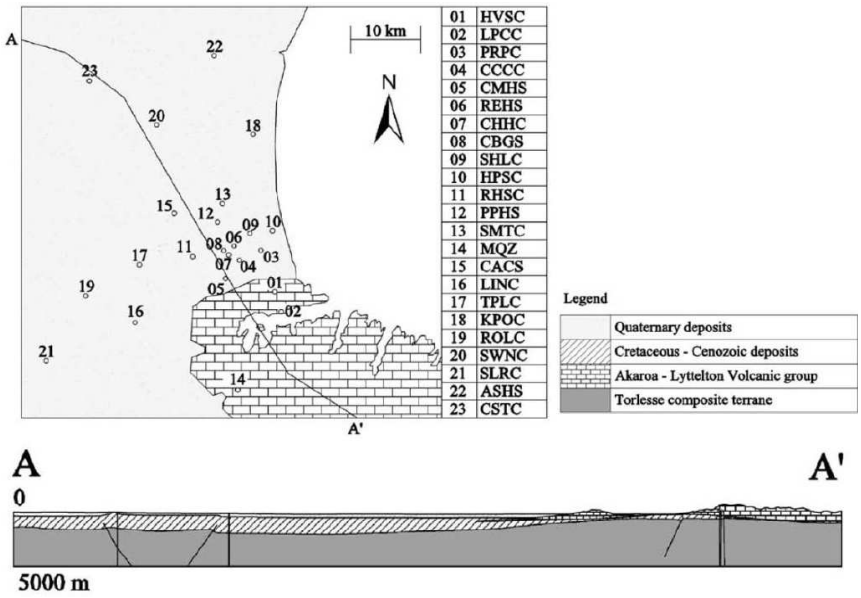

Figure 7.13: Area of the model, including part of the Canterbury Plains and the Lyttelton-Akaroa volcanic region, along with the strong ground motion stations (top). Geological A-A' cross-section (bottom).

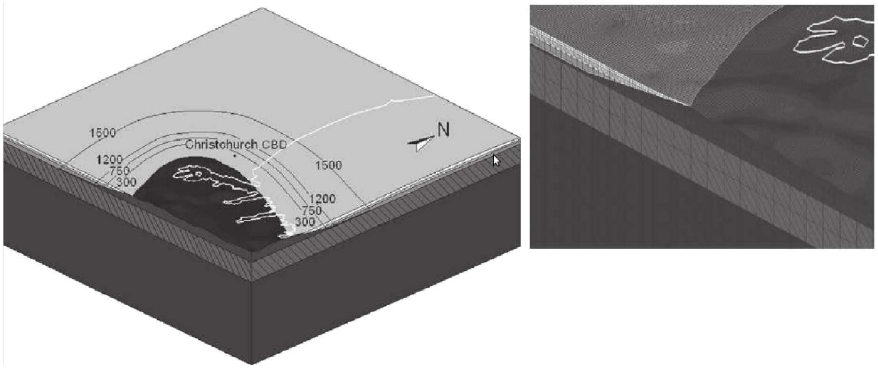

Figure 7.14: Left: three dimensional computational domain together with depth contours of the contact between the alluvial soft sediments and the grid volcano materials (in meters). Right: zoom of the corresponding hexahedral mesh for the valley.

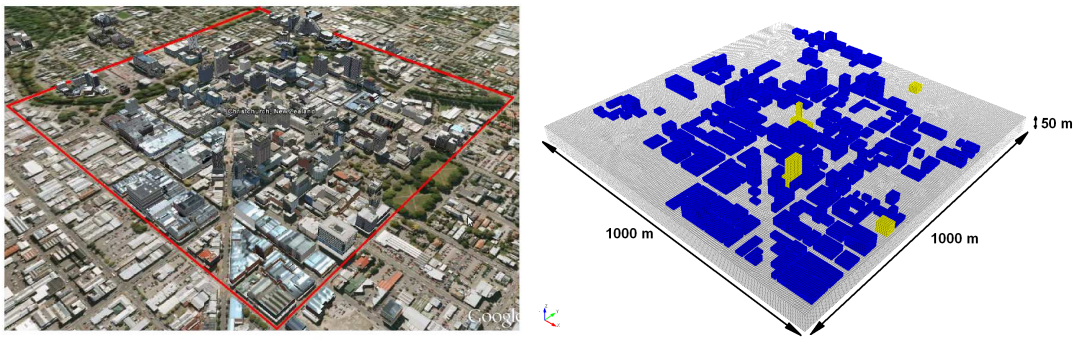

Figure 7.15: Photo of the CBD and its representation into the model.

The model of the region of the South Island of New Zealand covers an area of approximately $60 \times 60 \times 20$ km around the city of Christchurch, see Figure 7.13. In the model the shape of the interface between the soft soil and the volcanic material is improved, with constrains inferred from the topography of the volcano. The alluvial basin consist of three different layers with c_S ranging from 300 m/s in the top 300 m to 1500 m/s at the interface with the volcanic material. The volcano region, with $c_S = 3175$ m/s, extends down to a maximum depth of 5 km. Concerning the background geology, a horizontally layered crustal model was assumed, see Figure 7.14.

The viscoelastic property of the soil is taken into account choosing a suitable value of ζ in order to damp all the frequencies in the range up to 2 Hz [110]. Here, we consider the earthquake generate by the fault solution proposed by the Institute of Geological an Nuclear Science (GNS: data available by the GeoNET Data Center `http://www.geonet.org.nz/`) where the slip source time function is given as in (7.2) with rise time $\tau = 0.9$ s constant across the fault plane.

With the DGSE discretization we want to extend the results provided in [51] considering the Christchurch building district (CBD) within the same model, see Figure 7.15, occupying a 1 km^2 area of the Canterbury plains. The aim is not only to study the seismic response of the most important buildings of the city damaged by the earthquake, but also to see the influence of the city on the wave propagation problem.

We chose a mesh size h for the top layer of the valley ranging from 50 m (near the city) to 150 m, and polynomial approximation degree $N = 4$. For the CBD, h is chosen approximately equal to 5 m and $N = 1$. This choice leads to a computational domain made by $\approx 10^6$ elements and $\approx 40 \cdot 10^6$ unknowns. The mechanical parameters used for

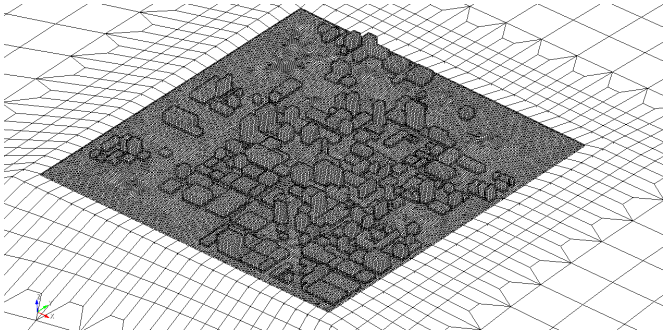

Figure 7.16: Zoom of the mesh used for the discretization of the CBD and the neighbouring valley.

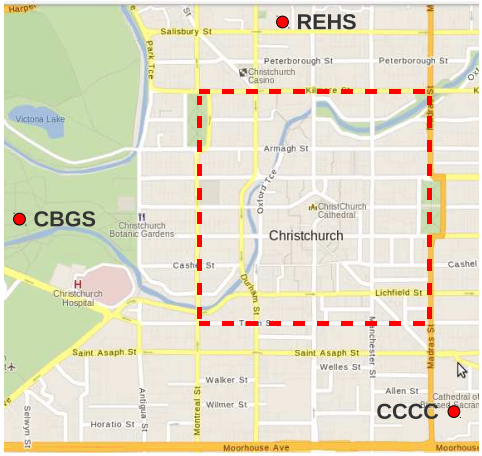

Figure 7.17: Map of Christchurch. The receivers REHS, CCCC and CBGS together with the CBD are highlighted.

Layer	$c_S[m/s]$	$c_P[m/s]$	$\rho[Kg/m^3]$	$\zeta[1/s]$
Foundation	400	650	2400	0.01472
Building	100	163	2400	0.01472

Table 7.4: Dynamic and mechanical parameters for the CBD.

the buildings and their foundations are described in Table 7.4 according to [111]. We have employed the leap-frog scheme for the time integration.

Figure 7.18 show the velocity fields obtained with the DGSE recorded by three receivers placed near the CBD, see Figure 7.17. The results are compared with those presented in [51] obtained with a SE discretization, coupled with the leap-frog time integration scheme ($\Delta t = 1.25 \cdot 10^{-4}\ s$) in absence of the CBD. The seismic wave generated by the fault under the volcano area moves from the south to the north of the Canterbury plains. On the seismograms recorded by the station REHS, placed at the north side of the CBD, it is more evident the city-site effect, especially on the final part of the signal. This result is in agreement with [114] and it will be more evident from Figure 7.19. As expected, the signals recorded by the stations CCCC and CBGS, located at the south and at the west side of the CBD respectively, do not present any substantial modifications from those obtained without the CBD.

Moreover, we present some snapshots of the radial velocity field on a neighbourhood of the CBD. In Figure 7.19 it is possible to see the influence of the city into the model. The buildings firstly retain the energy transmitted by the earthquake ($t \approx 6\ s$) and then they release it ($t \approx 6.5\ s$) onto the ground acting like a seismic source, [114].

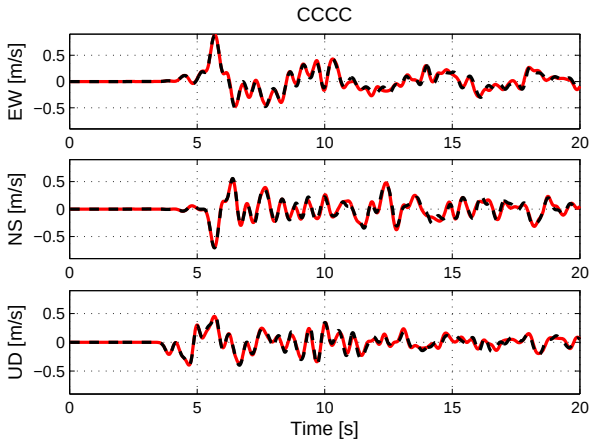

(a) Velocity fields recorded by the receiver CCCC.

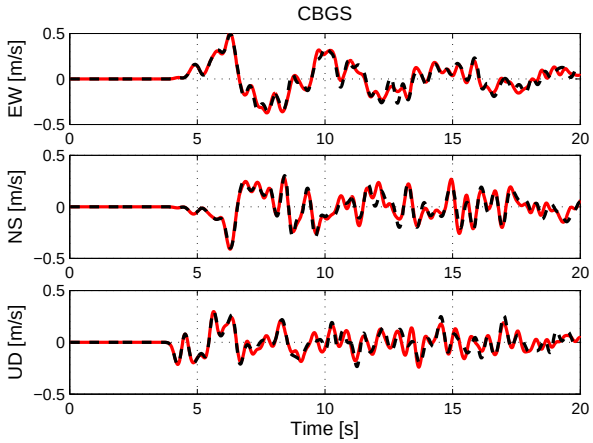

(b) Velocity fields recorded by the receiver CBGS.

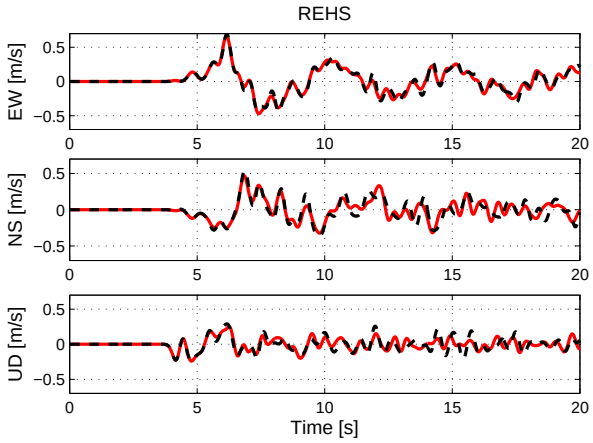

(c) Velocity fields recorded by the receiver REHS.

Figure 7.18: Velocity fields recorded by the receivers shown in Figure 7.13: East-West (EW), North-South (NS) and Up-Down (UD) components. SE (continuous line) versus DGSE solutions (dashed line).

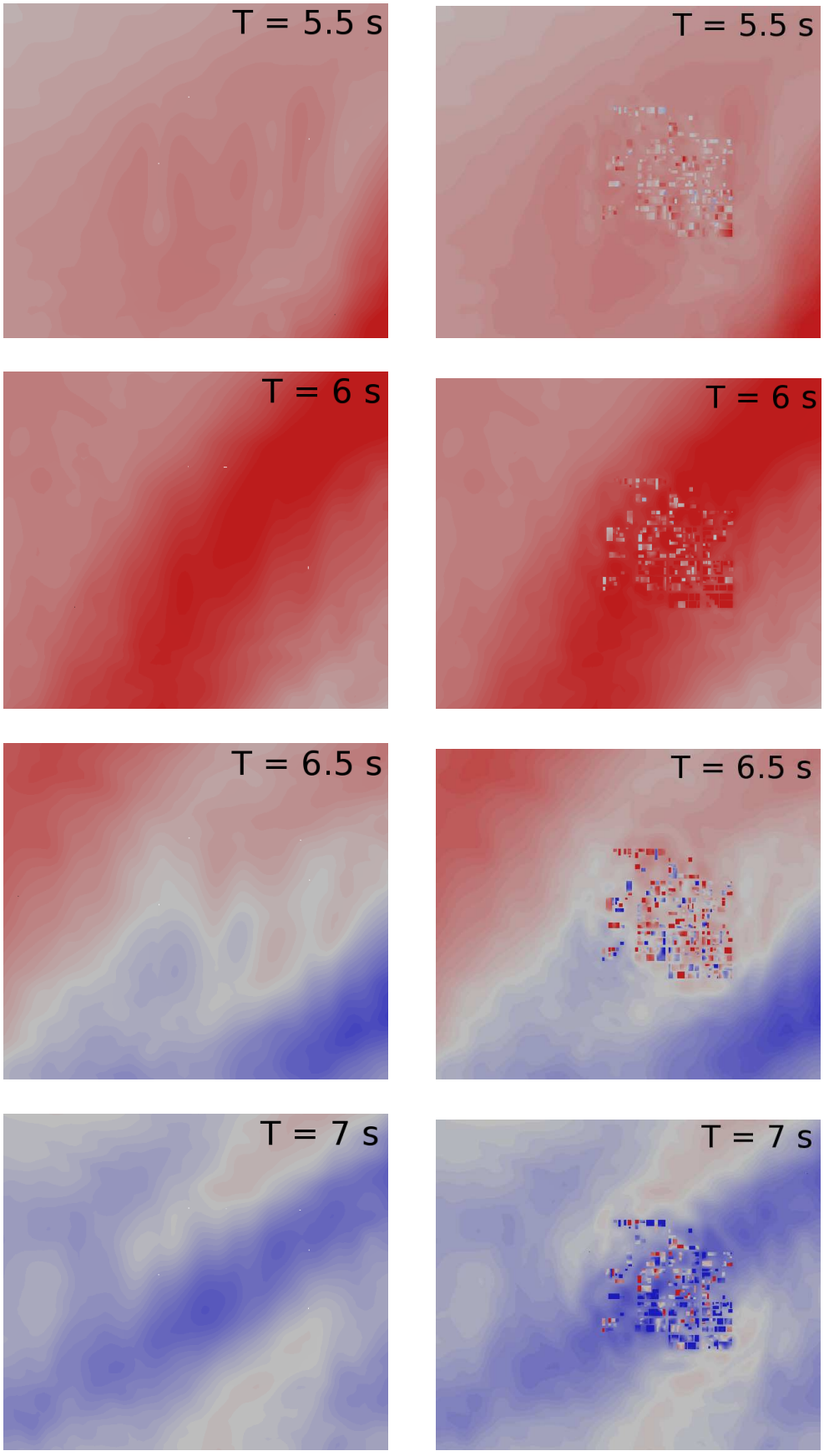

Figure 7.19: Snapshots of the fault radial velocity component in the Canterbury Plains (left) along with the CBD (right), simulated by DGSE method. Velocity field varying form $-0.75\ m/s$ to $0.75\ m/s$.

Chapter 8

Conclusions and perspectives

The Discontinuous Galerkin spectral element and the Mortar spectral element methods are high-order numerical techniques well suited for wave propagations in heterogeneous media. The possibility of treating non-conforming subdomain partitions where both the mesh size and the approximation orders can be independently tuned to the region of interest make the DGSE and MSE discretizations more flexible than standard spectral element methods.

Starting from a common weak formulation we have described and analyzed both non-conforming approaches and highlighted their analogies and their differences. The very good performance in terms of accuracy, grid dispersion/dissipation and stability of DGSE and MSE methods determine their efficacy when applied to wave propagation problems. Indeed, we have proved that DGSE and MSE exhibit optimal approximation properties, and at least five points per wavelength with spectral element approximations of order four are sufficient to make dispersion/dissipation error negligible.

Moreover, no dissipation effects arise when DGSE or MSE discretizations are employed. For the stability analysis we have derived precise bounds when explicit numerical schemes are used for time integration (leap-frog and fourth order Runge-Kutta methods). We have proved that, on the one hand, the symmetric version of the DGSE method yields optimal error decays in the grid dispersion as occurs with the SE method. On the other hand, the MSE method allows larger time steps in the time advancing scheme.

Finally, we have shown that the MSE and DGSE methods can be successfully applied to simulate realistic earthquake scenarios improving the performances of the SE dis-

cretizations in terms of computational costs. By using the numerical code developed, important progress can be made in the analysis of seismic wave propagations. Possible future developments of the present work go toward

1. the geometrical flexibility (tetrahedral meshes),
2. the accuracy (high order/implicit time integration schemes),
3. computational effort (load balancing for parallel computations).

Bibliography

[1] R.A. Adams and J.F.F. Fournier. *Sobolev Spaces*, volume 140 of *Pure and Applied Mathematics*. Academic Press, New York, second edition, 2003.

[2] M. Ainsworth. Discrete dispersion relation for *hp*-version finite element approximation at high wave number. *SIAM J. Numer. Anal.*, 42(2):553–575, 2004.

[3] M. Ainsworth. Dispersive and dissipative behaviour of high order discontinuous Galerkin finite element methods. *J. Comput. Phys.*, 198(1):106–130, 2004.

[4] M. Ainsworth, P. Monk, and W. Muniz. Dispersive and dissipative properties of discontinuous Galerkin finite element methods for the second-order wave equation. *J. Sci. Comput.*, 27(1-3):5–40, 2006.

[5] P. Ajit, K.P. Amiya, and N. Neela. Mortar element methods for parabolic problems. *Numer. Meth. Par. D. E.*, 24(6):1460–1484, 2008.

[6] P.F. Antonietti, A. Buffa, and I. Perugia. Discontinuous Galerkin approximation of the Laplace eigenproblem. *Comput. Meth. Appl. Mech. Eng.*, 195(25-28):3483–3503, 2006.

[7] P.F. Antonietti and P. Houston. A class of domain decomposition preconditioners for *hp*-Discontinuous Galerkin finite element methods. *J. Sci. Comput.*, 46:124–149, 2011.

[8] P.F. Antonietti, I. Mazzieri, A. Quarteroni, and F. Rapetti. Non-conforming high order approximations of elastodynamics equation. *Comput. Meth. Appl. Mech. Eng.*, 209-212:212–238, 2012.

[9] D.N. Arnold, F. Brezzi, B. Cockburn, and L.D. Marini. Unified analysis of discontinuous Galerkin methods for elliptic problems. *SIAM J. Numer. Anal.*, 39(5):1749–1779, 2001/02.

[10] I. Babuŝka and M. Suri. The *hp* version of the finite element method with quasi-uniform meshes. *ESAIM, Math. Model. Numer. Anal.*, 21(2):199–.238, 1987.

[11] I. Babuŝka, B.A. Szabó, and I.N. Katz. The *p* version of the finite element method. *SIAM J. Numer. Anal.*, 18:512–545, 1981.

[12] H. Bao, J. Bielak, O. Ghattas, L.F. Kallivokas, D.R. O'Hallaron, J.R. Shewchuk, and J. Xu. Large-scale Simulation of Elastic Wave Propagation in Heterogeneous Media on Parallel Computers. *Comput. Meth. Appl. Mech. Eng.*, 152(1–2):85–102, 1998.

[13] A. Bayliss, K.E. Jordan, B.J. Le Mesurier, and E. Turkel. A fourth order accurate finite-difference scheme for the computation of elastic waves. *Bull. Seismol. Soc. Am.*, 76:1115–1132, 1986.

[14] E. Bécache. A variational boundary integral equation method for an elastodynamic antiplane crack. *Int. J. Numer. Meth. Eng.*, 36(6):969–984, 1993.

[15] F. Ben Belgacem. The Mortar finite element method with Lagrange multipliers. *Numer. Math.*, 84(2):173–197, 1999.

[16] F. Ben Belgacem and Y. Maday. A spectral element methodology tuned to parallel implementations. *Comput. Meth. Appl. Mech. Eng.*, 116(1-4):59–67, 1994.

[17] F. Ben Belgacem, P. Seshaiyer, and M. Suri. Optimal convergence rates of *hp* mortar finite element methods for second-order elliptic problems. *ESAIM, Math. Model. Numer. Anal.*, 34(03):591–608, 2000.

[18] C. Bernardi, N. Debit, and Y. Maday. Coupling finite element and spectral methods: First results. *Math. Comput.*, 54(189):21–39, 1990.

[19] C. Bernardi, Y. Maday, and A.T. Patera. A new nonconforming approach to domain decomposition: the mortar element method. In *Nonlinear partial differential equations and their applications. Collège de France Seminar, Vol. XI (Paris, 1989–1991)*, volume 299 of *Pitman Res. Notes Math. Ser.*, pages 13–51. Longman Sci. Tech., Harlow, 1994.

[20] C. Bernardi, Y. Maday, and F. Rapetti. *Discrétisations variationnelles de problèmes aux limites elliptiques*, volume 45 of *Mathématiques & Applications*. Springer-Verlag, Berlin, 2004.

[21] C. Bernardi, Y. Maday, and F. Rapetti. Basics and some applications of the mortar element method. *GAMM-Mitt.*, 28(2):97–123, 2005.

[22] P.E. Bjorstad and O.B. Widlund. Iterative methods for the solution of elliptic problems on regions partitioned into substructures. *SIAM J. Numer. Anal.*, 23:1097–1120, 1986.

[23] S.C. Brenner. Korn's inequalities for piecewise H^1 vector fields. *Math. Comput.*, pages 1067–1087, 2004.

[24] S.C. Brenner and L.R. Scott. *The mathematical theory of finite element methods*, volume 15 of *Texts in Applied Mathematics*. Springer, Berlin, third edition, 2008.

[25] J.C. Butcher. *The numerical analysis of ordinary differential equations: Runge-Kutta and general linear methods*. Wiley-Interscience, New York, NY, USA, 1987.

[26] C. Canuto, M.Y. Hussaini, A. Quarteroni, and T.A. Zang. *Spectral methods - Fundamentals in single domains*. Scientific Computation. Springer-Verlag, Berlin, 2006.

[27] C. Canuto, M.Y. Hussaini, A. Quarteroni, and T.A. Zang. *Spectral methods - Evolution to complex geometries and applications to fluid dynamics*. Scientific Computation. Springer, Berlin, 2007.

[28] J.M. Carcione and P. Wang. A Chebyshev collocation method for the wave equation in generalized coordinate. *Comp. Fluid Dyn. J.*, 2:269–290, 1993.

[29] F. Casadei and E. Gabellini. Implementation of a 3D coupled spectral element/finite element solver for wave propagation and soil-structure interaction simulations. *Part I-Models, EUR 17730 EN*, 1997.

[30] F. Casadei, E. Gabellini, G. Fotia, F. Maggio, and A. Quarteroni. A mortar spectral/finite element method for complex 2D and 3D elastodynamic problems. *Comput. Meth. Appl. Mech. Eng.*, 191(45):5119–5148, 2002.

[31] E. Casarotti, M. Stupazzini, S. Lee, D. Komatitsch, A. Piersanti, and J. Tromp. Cubit and seismic wave propagation based upon the spectral-element method: An advanced unstructured mesher for complex 3d geological media. In M.L. Brewer and D. Marcum, editors, *Proc. 16th Int. Meshing Roundtable*. Springer, New York, NY, 2007.

[32] S. Chaillat, M. Bonnet, and J.F. Semblat. A multi-level fast multipole BEM for 3-D elastodynamics in the frequency domain. *Comput. Meth. Appl. Mech. Eng.*, 197:4233–4249, 2008.

[33] S. Chaillat, M. Bonnet, and J.F. Semblat. A preconditioned 3-D multi-region fast multipole solver for seismic wave propagation in complex geometries. *Commun. Comput. Phys.*, 11(2):594–609, 2012.

[34] E. Chaljub, Y. Capdeville, and J.P. Vilotte. Solving elastodynamics in a fluid-solid heterogeneous sphere: a parallel spectral element approximation on non-conforming grids. *J. Comp. Phys.*, 187(2):457–491, 2003.

[35] E. Chaljub, D. Komatitsch, J.P. Vilotte, Y. Capdeville, B. Valette, and G. Festa. Spectral element analysis in seismology. In Ru-Shan Wu and Valérie Maupin, editors, *Advances in wave propagation in heterogeneous media*, volume 48 of *Advances in Geophysics*, pages 365–419. Elsevier - Academic Press, London, UK, 2007.

[36] G.C. Cohen. *Higher-order numerical methods for transient wave equations*. Scientific Computation. Springer-Verlag, Berlin, 2002.

[37] M.A. Dablain. The application of high-order differencing to the scalar wave equation. *Geophysics*, 51:54–66, 1986.

[38] S.M. Day, J. Bielak, D. Dreger, R. Graves, S. Larsen, K.B. Olsen, and A. Pitarka. Tests of 3D elastodynamic codes: Final report for Lifelines Project 1a02. *Technical report, Pacific Earthquake Engineering Research Center, University of California, Berkeley*, 2001.

[39] J.D. De Basabe and M.K. Sen. Stability of the high-order finite elements for acoustic or elastic wave propagation with high-order time stepping. *Geophys. J. Int.*, 181(1):577–590, 2010.

[40] J.D. De Basabe, M.K. Sen, and M.F. Wheeler. The interior penalty discontinuous Galerkin method for elastic wave propagation: grid dispersion. *Geophys. J. Int.*, 175(1):83–93, 2008.

[41] J. de la Puente, M. Käser, M. Dumbser, and H. Igel. An Arbitrary High Order Discontinuous Galerkin Method for Elastic Waves on Unstructured Meshes IV: Anisotropy. *Geophys. J. Int.*, 169(3):1210–1228, 2007.

[42] M.O. Deville, P.F. Fisher, and E.H. Mund. *High-Order Methods for Incompressible Fluid Flow*. Cambridge Monographs on Applied and Computational Mathematics. Cambridge University Press, 2002.

[43] J. Diaz and M.J. Grote. Energy conserving explicit local time stepping for second-order wave equations. *SIAM J. Sci. Comput.*, 31(3):1985–2014, 2009.

[44] M. Dumbser, M. Käser, and E.F. Toro. An arbitrary high-order Discontinuous Galerkin method for elastic waves on unstructured meshes - V. Local time stepping and p-adaptivity. *Geophys. J. Int.*, 171(2):695–717, 2007.

[45] Y. Epshteyn and B. Rivière. Estimation of penalty parameters for symmetric interior penalty Galerkin methods. *J. Comput. Appl. Math.*, 206(2):843–872, 2007.

[46] E. Faccioli, F. Maggio, R. Paolucci, and A. Quarteroni. 2D and 3D elastic wave propagation by a pseudo-spectral domain decomposition method. *J. Seismol.*, 1(3):237–251, 1997.

[47] B. Flemisch, B. Wohlmuth, F. Rapetti, and Y. Maday. Scalar and vector potentials' coupling on nonmatching grids for the simulation of an electromagnetic brake. *Compel*, 24(3):1061–1070, 2005.

[48] A. Frankel. Three dimensional simulations of ground motions in San Bernardino valley, California, for hypothetical earthquakes on the San Andrea fault. *Bull. Seismol. Soc. Am.*, 84:1020–1041, 1993.

[49] V. Girault, G.V. Pencheva, M.F. Wheeler, and T.M. Wildey. Domain decomposition for linear elasticity with DG jumps and mortars. *Comput. Meth. Appl. Mech. Eng.*, 198(21-26):1751–1765, 2009.

[50] M.J. Grote, A. Schneebeli, and D. Schötzau. Discontinuous galerkin finite element method for the wave equation. *SIAM J. Numer. Anal.*, 44(6):2408–2431, 2006.

[51] R. Guidotti, M. Stupazzini, C. Smerzini, R. Paolucci, and P. Ramieri. Numerical study on the role of basin geometry and kinematic seismic source in 3D ground motion simulation of the 22 February 2011 Mw 6.2 Christchurch earthquake. *Seismol. Res. Lett.*, 82(6):767–782, 2011.

[52] J.S. Hesthaven and T. Warburton. *Nodal discontinuous Galerkin methods*, volume 54 of *Texts in Applied Mathematics*. Springer, Berlin, 2008.

[53] R. Hiptmair, A. Moiola, and I. Perugia. Plane wave discontinuous galerkin methods for the 2D Helmholtz equation: Analysis of the p-version. *SIAM J. Numer. Anal.*, 49(1):264–284, 2011.

[54] F.Q. Hu, M.Y. Hussaini, and J.L. Manthey. Low-dissipation and low-dispersion Runge-Kutta schemes for computational acoustics. *J. Comput. Phys.*, 124(1):177..191, 1996.

[55] T.J.R. Hughes. *The Finite Element Method*. Prentice-Hall, 1987.

[56] T.J.R. Hughes and J.E. Marsden. Classical elastodynamics as a linear symmetric hyperbolic system. *J. Elasticity*, 8:97–110, 1978.

[57] M. Käser and M. Dumbser. An Arbitrary High Order Discontinuous Galerkin Method for Elastic Waves on Unstructured Meshes I: The Two-Dimensional Isotropic Case with External Source Terms. *Geophys. J. Int.*, 166(2):855–877, 2006.

[58] P. Klin, E. Priolo, and G. Seriani. Numerical simulation of seismic wave propagation in realistic 3-D geo-models with a Fourier pseudo-spectral method. *Geophys. J. Int.*, 1(183):905 – 922, 2010.

[59] D. Komatitsch, F. Coutel, and P. Mora. Tensorial formulation of the wave equation for modeling curved interfaces. *Geophys. J. Int.*, 127:156–168, 1996.

[60] D. Komatitsch, J. Ritsema, and J. Tromp. The spectral-element method, Beowulf computing, and global seismology. *Science*, 298(5599):1737–1742, 2002.

[61] D. Komatitsch and J. Tromp. Introduction to the spectral-element method for 3-D seismic wave propagation. *Geophys. J. Int.*, 139(3):806–822, 1999.

[62] D. Komatitsch, S. Tsuboi, and J. Tromp. The spectral-element method in seismology. In Alan Levander and Guust Nolet, editors, *Seismic Earth: Array Analysis of Broadband Seismograms*, volume 157 of *Geophysical Monograph*, pages 205–228. American Geophysical Union, Washington DC, USA, 2005.

[63] D. Komatitsch and J.P. Vilotte. The spectral-element method: an efficient tool to simulate the seismic response of 2D and 3D geological structures. *Bull. Seismol. Soc. Am.*, 88(2):368–392, 1998.

[64] D. Kosloff, A.Q. Filho, E. Tessmer, and A. Behle. Numerical solution of the acoustic and elastic wave equations by a new rapid expansion method. *Geophys. Prospect.*, 37(4):383–394, 1989.

[65] D. Kosloff, D. Kessler, A.Q. Filho, E. Tesssmer, A. Behle, and R. Strahilevitz. Solution of the equation of dynamic elasticity by a Chebyshev spectral method. *Geophysics*, 55:748–754, 1990.

[66] M. Kristeková, J. Kristek, and P. Moczo. Time-frequency misfit and goodness-of-fit criteria for quantitative comparison of time signals. *Geophys. J. Int.*, 178(2):813–825, 2009.

[67] D.J.P. Lahaye, F. Maggio, and A. Quarteroni. Hybrid finite element–spectral element approximation of wave propagation problems. *East-West J. Numer. Math.*, 5(4):265–289, 1997.

[68] J.D. Lambert. *Numerical methods for ordinary differential systems: the initial value problem.* John Wiley & Sons, Inc., New York, NY, USA, 1991.

[69] B.P. Lamichhane, R.P. Stevenson, and B.I. Wohlmuth. Higher order mortar finite element methods in 3D with dual Lagrange multiplier bases. *Numer. Math.*, 102:93–121, 2005.

[70] A.R. Levander. Fourth order finite difference P-SV seismograms. *Geophysics*, 53:1425–1436, 1988.

[71] D. Levy and E. Tadmor. From semi-discrete to fully-discrete: Stability of Runge-Kutta schemes by the Energy Method. *SIAM J. Numer. Anal.*, 40(1):1–27, 1998.

[72] R. Madariaga. Dynamics of an expanding circular fault. *Bull. Seismol. Soc. Am.*, 65:163–182, 1976.

[73] Y. Maday, C. Mavriplis, and A.T. Patera. Nonconforming mortar element methods: application to spectral discretizations. In *Domain decomposition methods (Los Angeles, CA, 1988)*, pages 392–418. SIAM, Philadelphia, PA, 1989.

[74] Y. Maday and A.T. Patera. Spectral element methods for the incompressible Navier-Stokes equations. *in State of the Art Survey in Computational Mechanics A. K. Noor and J. T. Oden (Editors) ASME*, pages 71–143, 1989.

[75] Y. Maday, F. Rapetti, and B.I. Wohlmuth. Mortar element coupling between global scalar and local vector potentials to solve eddy current problems. In *Numerical mathematics and advanced applications*, pages 847–865. Springer Italia, Milan, 2003.

[76] K.J. Marfurt. Accuracy of finite-difference and finite-element modeling of the scalar and elastic wave equations. *Geophysics*, 49(5):533–549, 1984.

[77] P. Massimi, R. Tezaur, and C. Farhat. A discontinuous enrichment method for three-dimensional multiscale harmonic wave propagation problems in multi-fluid and fluid-solid media. *Int. J. Numer. Meth. Eng.*, 76(3):400–425, 2008.

[78] I. Mazzieri, C. Smerzini, P.F. Antonietti, F. Rapetti, M. Stupazzini, R. Paolucci, and A. Quarteroni. Non-conforming spectral approximations for the elastic wave equation in heterogeneous media. In *Proceedings of COMPDYN 2011 - 3rd International Conference in Computational Methods in Structural Dynamics and Earthquake Engineering*. 2011.

[79] E.D. Mercerat, J.P. Vilotte, and F.J. Sánchez-Sesma. Triangular spectral-element simulation of two-dimensional elastic wave propagation using unstructured triangular grids. *Geophys. J. Int.*, 166(2):679–698, 2006.

[80] P. Moczo and J. Kristek. Seismic wave propagation in viscoelastic media with material discontinuities : a 3D fourth-order staggered-grid finite-difference modeling. *Bull. Seismol. Soc. Am.*, 93:2273–2280, 2003.

[81] P. Moczo, J. Kristek, V. Vavrycuk, R.J. Archuleta, and L. Halada. 3D heterogeneous staggered-grid finite-difference modeling of seismic motions with volume harmonic and arithmetic averaging of elastic moduli and densities. *Bull. Seismol. Soc. Am.*, 92:3042–3066, 2002.

[82] P. Moczo, J.O.A. Robertsson, and L. Eisner. The finite-difference time-domain method for modeling of seismic wave propagation. In *Advances in Wave Propagation in Heterogenous Earth*, volume 48 of *Advances in Geophysics*, pages 421–516. Elsevier, 2007.

[83] A. Moiola, R. Hiptmair, and I. Perugia. Plane wave approximation of homogeneous Helmholtz solutions. *Z. Angew. Math. Phys.*, 62:809–837, 2011.

[84] R. Mullen and T. Belytschko. Dispersion analysis of finite element semidiscretizations of the two-dimensional wave equation. *Int. J. Numer. Meth. Eng.*, 18(1):11–29, 1982.

[85] T. Nissen-Meyer, A. Fournier, and F.A. Dahlen. A 2-D spectral-element method for computing spherical-earth seismograms - II. Waves in solid-fluid media. *Geophys. J. Int.*, 174(3):873–888, 2008.

[86] T. Ohminato and B.A. Chouet. A free-surface boundary condition for including 3D topography in the finite difference method. *Bull. Seismol. Soc. Am.*, 87:494–515, 1997.

[87] K.B. Olsen and R.J. Archuleta. 3-D simulation of earthquakes on the Los Angeles fault system. *Bull. Seismol. Soc. Am.*, 86:575–596, 1996.

[88] A.T. Patera. A spectral element method for fluid dynamics: laminar flow in a channel expansion. *J. Comp. Phys.*, 54:468–488, 1984.

[89] A. Pitarka and K. Irikura. Basin structure effects on long period strong motions in the San Fernando valley and the Los Angeles basin from the 1994 Northridge earthquake and aftershocks. *Bull. Seismol. Soc. Am.*, 86:126–137, 1996.

[90] E. Priolo, J.M. Carcione, and G. Seriani. Numerical simulation of interface waves by high-order spectral modeling techniques. *J. Acoust. Soc. Am.*, 95(2):681–693, 1994.

[91] A. Quarteroni, R. Sacco, and F. Saleri. *Numerical mathematics*, volume 37 of *Texts in Applied Mathematics*. Springer-Verlag, Berlin, second edition, 2007.

[92] A. Quarteroni and A. Valli. *Numerical approximation of partial differential equations*, volume 23 of *Springer Series in Computational Mathematics*. Springer-Verlag, Berlin, 1994.

[93] F. Rapetti. An overlapping mortar element approach to coupled magneto-mechanical problems. *Math. Comput. Simulat.*, 80(8):1647–1656, 2010.

[94] P.A. Raviart and J.M. Thomas. *Introduction à l'analyse numérique des équations aux dérivées partielles*. Collection Mathématiques Appliquées pour la Maîtrise. Masson, Paris, 1983.

[95] B. Rivière. *Discontinuous Galerkin methods for solving elliptic and parabolic equations - Theory and implementation*, volume 35 of *Frontiers in Applied Mathematics*. Society for Industrial and Applied Mathematics (SIAM), Philadelphia, PA, 2008.

[96] B. Rivière, S. Shaw, M. F. Wheeler, and J. R. Whiteman. Discontinuous Galerkin finite element methods for linear elasticity and quasistatic linear viscoelasticity. *Numer. Math.*, 95(2):347–376, 2003.

[97] B. Rivière, S. Shaw, and J.R. Whiteman. Discontinuous Galerkin finite element methods for dynamic linear solid viscoelasticity problems. *Numer. Meth. Par. D. E.*, 23(5):1149–1166, 2007.

[98] B. Rivière and M.F. Wheeler. Discontinuous finite element methods for acoustic and elastic wave problems. In *Current trends in scientific computing (Xi'an, 2002)*, volume 329 of *Contemp. Math.*, pages 271–282. Amer. Math. Soc., Providence, RI, 2003.

[99] J.O.A. Robertsson. A numerical free-surface condition for elastic / viscoelastic finite-difference modeling in the presence of topography. *Geophysics*, 61:1921–1934, 1996.

[100] F.J. Sanchez-Sesma and M. Campillo. Topographic effects for incident P, SV and Rayleigh waves. *Tectonophysics*, 218:113–125, 1993.

[101] F.J. Sánchez-Sesma and F. Luzon. Seismic response of three-dimensional alluvial valleys for incident P, S, and Rayleigh waves. *Bull. Seismol. Soc. Am.*, 85(1):269–284, 1995.

[102] D. Sármány, M.A. Botchev, and J.J.W. van der Vegt. Dispersion and dissipation error in high-order Runge-Kutta discontinuous Galerkin discretisations of the Maxwell equations. *J. Sci. Comput.*, 33(1):47–74, 2007.

[103] G. Seriani and S.P. Oliveira. Dispersion analysis of spectral element methods for elastic wave propagation. *Wave Motion*, 45(6):729–744, 2008.

[104] G. Seriani, E. Priolo, and A. Pregarz. Modelling waves in anisotropic media by a spectral element method. In G. Cohen, editor, *Proceedings of the third international conference on mathematical and numerical aspects of wave propagation*, pages 289–298. SIAM, Philadephia, PA, 1995.

[105] J.C. Simo, N. Tarnow, and K.K. Wong. Exact energy-momentum conserving algorithms and symplectic schemes for nonlinear dynamics. *Comput. Meth. Appl. Mech. Eng.*, 100(1):63–116, 1992.

[106] C. Smerzini, R. Paolucci, and M. Stupazzini. Comparison of 3D, 2D and 1D numerical approaches to predict long period earthquake ground motion in the Gubbio plain, Central Italy. *B. Earthq. Eng.*, 9:2007–2029, 2011.

[107] R. Stacey. Improved transparent boundary formulations for the elastic-wave equation. *Bull. Seismol. Soc. Am.*, 78(6):2089–2097, 1988.

[108] D. Stanescu, D.A. Kopriva, and M.Y. Hussaini. Dispersion analysis for discontinuous spectral element methods. *J. Sci. Comput.*, 15(2):149–171, 2000.

[109] M.L. Staten, R.A. Kerr, S.J. Owen, T.D. Blacker, M. Stupazzini, and K. Shimada. Unconstrained plastering-Hexahedral mesh generation via advancing-front geometry decomposition. *Int. J. Numer. Meth. Eng.*, 81(2):135–171, 2010.

[110] M. Stupazzini, R. Paolucci, and H. Igel. Near-fault earthquake ground-motion simulation in the Grenoble valley by a high-performance spectral element code. *Bull. Seismol. Soc. Am.*, 99(1):286–301, 2009.

[111] R. Taborda and J. Bielak. Three Dimensional Nonlinear Soil and Site-City Effects in Earthquake Simulations. *AGU Fall Meeting Abstracts*, page A1923, 2010.

[112] N. Tarnow and J.C. Simo. How to render second order accurate time-stepping algorithms fourth order accurate while retaining the stability and conservation properties. *Comput. Meth. Appl. Mech. Eng.*, 115(3-4):233–252, 1994.

[113] T. Toshinawa and T. Ohmachi. Low wave propagation in three dimensional sedimentary basin. *Bull. Seismol. Soc. Am.*, 82:1661–1667, 1992.

[114] M.D. Trifunac. The role of strong motion rotations in the response of structures near earthquake faults. *Soil Dyn. Earthq. Eng.*, 29(2):382–393, 2009.

[115] J. Virieux. P - SV wave propagation in heterogeneous media : velocitystress finite difference method. *Geophysics*, 51:589–901, 1986.

[116] D. Wang, R. Tezaur, J. Toivanen, and C. Farhat. Overview of the discontinuous enrichment method, the ultra-weak variational formulation, and the partition of unity method for acoustic scattering in the medium frequency regime and performance comparisons. *Int. J. Numer. Meth. Eng.*, 89(4):403–417, 2012.

[117] B.I. Wohlmuth. *Discretization Methods and Iterative Solvers Based on Domain Decomposition*, volume 17 of *Lecture Notes in Computational Science and Engineering*. Springer-Verlag, Berlin, 2001.

[118] E. Zampieri and A. Tagliani. Numerical approximation of elastic waves equations by implicit spectral methods. *Comput. Meth. Appl. Mech. Eng.*, 144(1-2):33–50, 1997.

[119] L. Zhang, R. Tezaur, and C. Farhat. The discontinuous enrichment method for elastic wave propagation in the medium-frequency regime. *Int. J. Numer. Meth. Eng.*, 66(13):2086–2114, 2006.

Acknowledgements

I would like to express my deepest gratitude to my advisor Prof. Alfio Quarteroni for his kindness, his advices and his precious suggestions (pearls of wisdom). I am grateful to him because he gave me the opportunity to study new challenging fields of applied mathematics and despite his crazy agenda was always able to find a spot for answering my questions.

I spent more than six months of my three years PhD at the Université de Nice at the Laboratoire de Mathématiques J.A. Dieudonné. That was a wonderful experience I had in my life. My heartfelt thanks Dr. Francesca Rapetti. She taught me almost everything I know about Mortar methods and gave me the opportunity to grow up as a researcher and as a person. I also would like to thank her for the support, the kindness and the helpfulness.

I am truly grateful to Dr. Paola Antonietti. I had the chance to work with her and it was a very great pleasure. She aided me to clarify so many doubts and she gave me important suggestions during these last three years.

A special thank to Dr. Marco Stupazzini, who introduced me to the "new" world of computational seismology. He provided me a valid scientific support. This work greatly benefited from his experience and from the ideas were born during night phone calls.

I also would like to acknowledge Dr. Chiara Smerzini and Dr. Roberto Guidotti for their friendship and their collaboration. They were incredibly kind when I need help and work in team with them was great.

I thank all the people of the high performance computing team at CILEA. Their support and experience were fundamental for the development of the parallel code. This work has been supported by Regione Lombardia and CILEA Consortium through a LISA Initiative (Laboratory for Interdisciplinary Advanced Simulation) 2010 grant.

I can not forget to thank all the people (professors, colleagues, friends) at the MOX laboratory that contributed to this work with their suggestions and/or support.

Finally, my family deserves special thanks for all effort it made to give me encouragement every

day. In particular, I would like to deeply thank Irene for always being close to me. She always supported me and convinced me to never give up, even when I filled with difficulties.